THE UTILITY OF LOW-VALENT NIOBIUM IN SMALL MOLECULE ACTIVATION AND THE STUDY OF FIRST ROW TRANSITION METAL COMPLEXES SUPPORTED BY TETRADENTATE REDOX ACTIVE LIGANDS

A Dissertation

Presented to the Faculty of the Graduate School

of Cornell University

In Partial Fulfillment of the Requirements for the Degree of

Doctor of Philosophy

by

Valerie Anne Williams

August 2014

THE UTILITY OF LOW-VALENT NIOBIUM IN SMALL MOLECULE ACTIVATION AND THE STUDY OF FIRST ROW TRANSITION METAL COMPLEXES SUPPORTED BY TETRADENTATE REDOX ACTIVE LIGANDS

Valerie Anne Williams, Ph. D.

Cornell University 2014

The low-valent complex $(silox)_3NbPMe_3$ (silox = $^tBu_3SiO$) was synthesized and tested for reactivity towards small molecules. It was discovered that exposure to CO generated the complexes $(silox)_3Nb{=}C{=}C{=}O$ (**3**-Nb), $(silox)_3Nb{=}O$ (**2**-Nb), and $[(silox)_3Nb]_2(\mu\text{-}C_2)$ (**4**-Nb) in various ratios depending on reaction stoichiometry. The formation of $[(silox)_3Nb]_2(\mu\text{-}CO)$ (**5**-Nb) was discovered as a byproduct in most reactions. Treatment of $(silox)_3NbPMe_3$ with potassium under a dinitrogen atmosphere afforded the dinitrogen complex $(silox)_3NbNNNb(silox)_3$ (**8**-Nb). Reaction of $(silox)_3NbCl$ (**10**-Nb) with NH_3 afforded $(silox)_3Nb^{IV}(NH_3)Cl$, with ammonia binding parameters of $\Delta H = 20.4 \pm 2.3$ kcal/mol and $\Delta S = 39 \pm 7$ e.u.

The nickel complex $\{dmp(PI)_2\}Ni$ ($dmp(PI)_2 = Me_2C(CH_2{=}Npy)_2$) was synthesized and subjected to chemical oxidation and reduction to synthesize a 5-membered redox series. Through electronic structure study, it was determined that in these complexes the metal center typically remained Ni^{II}, with the possible exception of the cationic complex $[\{dmp(PI)_2\}Ni](OTf)$, and redox changes were primarily ligand-centered. The chemistry of $dmp(PI)_2$ was extended to iron, and $\{dmp(PI)_2\}FePMe_3$ was synthesized. As with the nickel analogue, the complex was

determined to be a M^{II} center bound to a dianionic ligand framework, with similar redox behavior as the nickel species.

A related tetradentate β-diketiminate-based ligand incorporating two pyridine-methylene units, 2,4-bis[(E)-(2-pyridyl)methylideneamino]pentane (H{nn(PM)$_2$}), was synthesized and metallated to form {nn(PM)$_2$}FeN(TMS)$_2$ (**1**-N(TMS)$_2$). **1**-N(TMS)$_2$ could be further derivatized to form {nn(PM)$_2$}FeX (X = Cl, N_3). One of the methylene fragments of the ligand backbone was prone to facile deprotonation and allowed synthesis of {nn(PM)(PI)}FeLL' (LL' = $(PMe_3)_2$, $(PMe_2Ph)_2$, $(PMe_3)CO$; **2**-LL') and {nn(PM)(PI)}FeL (L = PMe_3, $PMePh_2$, PPh_3, CO; **3**-L). Electronic structure studies suggested **2**-LL' and **3**-L existed as Fe^{II} metal centers bound to dianionic {nn(PM)(PI)}$^{2-}$, with strong metal-ligand covalency in **3**-L. Oxidation studies on **2**-$(PMe_3)_2$ showed two successive ligand-based $1e^-$ oxidations. The same tetradentate β-diketiminate-based ligand was applied to other transition metals of the first row and allowed synthesis of {nn(PM)$_2$}VCl_2 (**1**-VCl_2) and {nn(PM)$_2$}Co (**1**-Co), both of which formed through unusual ligand exchange or disproportionation events, and {nn(PM)(PI)}M (M = Cr, **4**-Cr; M = Ni, **4**-Ni), which were generated through double deprotonation of the H{nn(PM)$_2$} ligand.

BIOGRAPHICAL SKETCH

Valerie Anne Williams was born in San Jose, CA to Robert Williams, a computer engineer, and Irene Tran, a former chemist and stay-at-home mom. Valerie grew up as the younger of two children and, because her older sister chose to follow a career in engineering, had no choice but to pursue a future in chemistry, aided by her very supportive high school chemistry teacher Mr. Ken Porush. Valerie applied to several universities within California to study chemistry, all of which shared a common application form, and decided in 2005 to attend UC Berkeley. At Berkeley, Valerie first learned the basics of chemical research through the study of biosensors with Professor Marcin Majda, and discovered her true love of organometallic chemistry in her third year when she joined the laboratory of Professor John Arnold. Under the supervision of her friend and mentor Dr. Stefan Minasian in the Arnold group, she further discovered an interest in everything uranium, as well as the unique bonding characteristics of group 13 metals. While at Berkeley Valerie managed to obtain a minor concentration in chemical engineering, but decided to follow a path in synthetic organometallic chemistry because "Money Isn't Everything". In 2009, Valerie applied and was accepted to the chemistry department at Cornell University where she had the great fortune to join the laboratory of Peter T. Wolczanski, and had the pleasure of spending every day in the lab with her closest friends and coconspirators. After 5 years at Cornell which simultaneously felt longer and shorter than they actually were, Valerie finally completed her doctoral studies in May 2014.

To my family and friends,
Who have supported me unconditionally.

ACKNOWLEDGMENTS

First I would like to thank my advisor and mentor Pete Wolczanski, who has guided me both scientifically and personally these past five years, and has patiently tolerated my rather numerous quirks throughout. From this day forth, I will never forget the most important life lesson I have learned, “Men are Pigs, and Girls are Weird.” Wiser and truer words have never been uttered.

My sincere thanks go also to my remaining committee members, Dave Collum and Geoff Coates. Dave has been very helpful throughout the years, and I have been fortunate to have his input in all matters of organic synthesis. His instinct on all things, scientific and otherwise, never ceases to amaze me, and it has been a true pleasure to interact with him. Geoff has also been very helpful, and his reactions and witty comments whenever he looked for Pete in his office before noon on Thursdays were always entertaining. I would also like to extend my gratitude to Kyle Lancaster, who has been a valuable friend and collaborator in the years since he first came to Cornell. Kyle has always been willing to take the time to plug a molecule into his computer for our group on short notice, even if he didn’t always get credit for it, and is responsible for the calculations and EPR fits that appear in Chapter 2. Tom Cundari is also thanked for his computational support, which appears in Chapters 1 and 3. A great many thanks go to Karsten Meyer and his group members Jörg Sutter and Johannes Hohenberger, who have very kindly acquired SQUID, Mössbauer, EPR, and elemental analysis data for our group throughout the years. Without their support this work would not have been possible. Gabriel Rodriguez-Calero was a tremendous help with electrochemistry, which appears in Chapter 2. Emil Lobkovsky is thanked for his

crystal structure determination, which has been of immeasurable worth throughout the course of this work. The most interesting results have come out of Emil stopping by the lab with, “It is different from what you thought.”

I would also like to thank Josh Wakeman and Denise Wurtenburg, who made trips to the stockroom both productive and enjoyable. Dave Neish and Larry Stull were also always helpful and kept the lab running behind the scenes, and were always willing to stop and strike up a conversation. I would also like to thank Pat Hine, Dan Lorey, John Terry, and Cynthia Kinsland for the various interactions I have had with them through the years, and Tom Ruttledge, who has been a reliable friend and source of advice on a number of topics.

A special thanks goes to the Wolczanski group, past, present, and future. Brenda Frazier, Emily Volpe, and Elliott Hulley together ensured that I had a very unique first year in the lab, and kindly put me in my place when I thought I knew more than I did. In particular, Elliott was a great mentor with more ideas than one person could handle in a lifetime, some of which transitioned into rewarding projects in my own Ph.D. work. I would also like to thank my undergrad Marty Roskoff, whose positive attitude and perseverance in the face of negative results was remarkably inspiring. I see the same positive attitude in our newest group member Spencer Heins, who has been a pleasure to work with and to guide through the first few months in lab. I have no doubt that he will keep the group lively and interesting.

My fellow yearmate Wes Morris, along with Erika Bartholomew and Brian Lindley, have been with me through the good times and the bad, and without them I would never have made it far in my scientific career. Erika, as a fellow member of

Team Estrogen©, guided me many of the perils of graduate school and ensured that I never got *too* boring. Wes was always willing to talk about anything, and many of life's problems in the last five years were solved through a late-night conversation. His ingenuity as a scientist is only exceeded by his strength as a person, for which I will always be grateful. Brian has always been a reliable friend who never failed to call me out when I said something strange, often in the most entertaining way possible. His ironic humor and sharp wit have eased many uncomfortable situations, and I have been truly fortunate to know and work alongside him these last four years. Undoubtedly, his presence will keep the lab classy yet fresh.

Finally, I would like to thank my family for supporting me these past few years. My older sister, who has always been willing to listen to my problems and offer advice, my mother, who unfailingly called me every week to ensure I did not suffer a tragic lab accident, and my father, who still does not quite grasp why I haven't made a battery yet, have always been there for me. My boyfriend and closest friend Carsten has been my strength and inspiration since we met. More than anyone, he has put up with my eccentricities and, at the expense of his own sanity, has always encouraged me to be myself. I am a better scientist and a better person for knowing him.

TABLE OF CONTENTS

LIST OF FIGURES

LIST OF SCHEMES

LIST OF TABLES

Chapter 1

Small Molecule Activation With $(silox)_3NbPMe_3$ (silox = $^tBu_3SiO$)

Introduction

In 2008 the world consumption of energy was 16.4 TW, and energy consumption is predicted to double in the next 30 years.[1-6] Over 80% of the energy obtained in 2008 was derived from fossil fuels, with nuclear energy accounting for roughly 6% and renewable sources comprising the remaining 12%.[7] While renewable energy will certainly see increased popularity in the coming years, it is undeniable that carbon-based energy sources will continue to dominate the energy economy in the foreseeable future.[8]

The primary product of fossil fuel combustion, CO_2, is thought to be a major contributor to global climate change; hence, it would be desirable to convert CO_2 back to useable fuels through reduction with dihydrogen produced through water splitting (Scheme 1.1a).[9-12] Currently, ~80% of dihydrogen production arises from hydrocarbon-derived steam reforming processes (Scheme 1.1b), the reverse of the desired CO_2 reduction. Consequently, use of H_2 generated from these processes is nonsensical. To develop a carbon-neutral process, dihydrogen must be derived from solar-powered water splitting (Scheme 1.1c). On an industrial scale carbon monoxide

(a) $(3n+1)\,H_2 + n\,CO_2 \rightleftharpoons C_nH_{2n+2} + 2n\,H_2O$

(b) $C_nH_{2n+2} + 2n\,H_2O \rightleftharpoons (3n+1)\,H_2 + n\,CO_2$

(c) $H_2O \rightleftharpoons H_2 + \tfrac{1}{2}\,O_2$

(d) $(2n+1)\,H_2 + n\,CO \rightleftharpoons C_nH_{2n+2} + n\,H_2O$

Scheme 1.1. Carbon dioxide reduction (a); steam reforming (b); water splitting (c); Fischer-Tropsch process (d).

is currently reduced with dihydrogen to generate liquid hydrocarbons in the presence of metal catalysts through Fischer-Tropsch chemistry (Scheme 1.1d).[13-16] The study of the deoxygenation of CO_2[17-40] to generate CO and subsequent C-O bond splitting is quite valuable,[41-45] and one can model these chemistries through use of low-valent early transition metals to synthesize stable CO_2-derived metal compounds.

It has previously been shown by Neithamer *et al.*[46] that treatment of $(silox)_3Ta$ (**1**-Ta) with excess carbon dioxide resulted in formation of the oxo complex $(silox)_3Ta{=}O$ (**2**-Ta) and release of a stoichiometric amount of carbon monoxide (Eq. 1.1). When treated with a substoichiometric amount of CO_2, the CO byproduct was further reduced by **1**-Ta. To study this carbonylation process, **1**-Ta was treated with

$$\underset{\textbf{1}\text{-Ta}}{(silox)_3Ta} + \text{excess } CO_2 \xrightarrow[23\ ^\circ C]{C_6H_6} \underset{\textbf{2}\text{-Ta}}{(silox)_3Ta{=}O} + CO \qquad \textbf{(1.1)}$$

carbon monoxide to yield $(silox)_3Ta{=}O$ (**2**-Ta), $(silox)_3Ta{=}C{=}C{=}O$ (**3**-Ta), and $(silox)_3Ta{=}C{=}C{=}Ta(silox)_3$ (**4**-Ta) in various product distributions (Eq. 1.2 and 1.3). When $(silox)_3Ta$ (**1**-Ta) was treated with an excess of CO at low temperature, the oxo complex **2**-Ta and $(silox)_3Ta{=}C{=}C{=}O$ (**3**-Ta) were formed as given in Eq. 1.2. Ketenylidene **3**-Ta was characterized by a strong infrared band at 2076 cm^{-1} that shifted to 2011 cm^{-1} when ^{13}CO was used. Exposure of **1**-Ta to a 1:1 mixture of CO and ^{13}CO resulted in bands of equal intensity at 2076, 2065, 2022, and 2011 cm^{-1}, corresponding to a statistical mixture of the four isotopomers $(silox)_3Ta{=}C{=}C{=}O$, $(silox)_3Ta{=}{}^{13}C{=}C{=}O$, $(silox)_3Ta{=}C{=}{}^{13}C{=}O$, and $(silox)_3Ta{=}{}^{13}C{=}{}^{13}C{=}O$. The ^{13}C NMR spectrum of $(silox)_3Ta{=}{}^{13}C{=}{}^{13}C{=}O$ showed two doublets ($^1J_{CC}$ = 100 Hz) at δ 135.96 (Ta*C*CO) and δ 142.51 (Ta*C*CO), in addition to silox resonances (Table 1.1).

$$(\text{silox})_3\text{Ta} + \text{excess CO} \xrightarrow[-78 \rightarrow 23\ ^\circ\text{C}]{\text{toluene}} \tfrac{1}{2}\,(\text{silox})_3\text{Ta=O} + \tfrac{1}{2}\,(\text{silox})_3\text{Ta=C=C=O} \quad \textbf{(1.2)}$$

1-Ta **2**-Ta **3**-Ta

$$(\text{silox})_3\text{Ta} + \tfrac{1}{2}\,\text{CO} \xrightarrow[23\ ^\circ\text{C}]{C_6H_6} \tfrac{1}{2}\,(\text{silox})_3\text{Ta=O} + \tfrac{1}{4}\,[(\text{silox})_3\text{Ta}]_2(\mu\text{-}C_2) \quad \textbf{(1.3)}$$

1-Ta **2**-Ta **4**-Ta

In contrast, treatment of $(\text{silox})_3\text{Ta}$ (**1**-Ta) with 1.00 equiv carbon monoxide in benzene resulted in immediate reaction and uptake of 0.47 equiv carbon monoxide to form **2**-Ta and a red precipitate identified as the dicarbide complex, $(\text{silox})_3\text{Ta=C=C=Ta(silox)}_3$ (**4**-Ta) (Eq. 1.3). Infrared spectra of **4**-Ta generated from either CO or $C^{18}O$ exhibited a band at 709 cm^{-1}, assigned to the Ta=C stretch. When ^{13}CO was used, the Ta=C stretch of **4**-Ta shifted to 682 cm^{-1}, and when a 1:1 mixture of CO to ^{13}CO was used, three bands at 709, 695, and 682 cm^{-1} appeared in an approximate 1:2:1 ratio, indicative of a two-carbon bridge. Raman spectra of **4**-Ta and the isotopically labeled **4**-Ta$^{13}C_2$ revealed strong absorptions at 1617 cm^{-1} and 1549 cm^{-1} respectively, corresponding to the symmetric C–C stretch (Table 1.2). Infrared spectra of **2**-Ta derived from $C^{16}O$ revealed a band at 905 cm^{-1}, assigned to the Ta=O stretch of **2**-Ta, which shifted to a position obscured by silox absorptions (750 – 900 cm^{-1}) when $C^{18}O$ was used instead.

A single-crystal X-ray structure determination of **4**-Ta confirmed an approximately linear two-carbon bridge, with a Ta–C bond length (1.95 (2) Å) within the range expected for tantalum alkylidenes (1.89 – 2.07 Å)[47-49] and a C–C bond distance (1.37 (4) Å) similar to that of a typical double bond (1.34 Å).[50] It is important to note that these distances have fairly high standard deviations due to the difficulty of precisely locating light atoms near significantly heavier atoms via X-ray

crystallography.

Hydrolysis of **3**-Ta at elevated temperatures resulted in production of ethylene and H(silox) as the only NMR-identifiable products, although presumably, Ta_2O_5 was also generated (Eq. 1.4). Under conditions designed to optimize formation of **3**-Ta (Eq. 1.2) trace amounts of **4**-Ta were observed, and under optimal condition for formation of **4**-Ta, trace amounts of **3**-Ta were observed. These results implicate the

$$\underset{\textbf{4}\text{-Ta}}{[(\text{silox})_3\text{Ta}]_2(\mu\text{-}C_2)} + \text{excess } H_2O \xrightarrow[110\ ^\circ\text{C, 15 h}]{\text{THF-}d_8} C_2H_4 + \text{H(silox)} + Ta_2O_5 \quad \textbf{(1.4)}$$

intermediacy of **3**-Ta in the formation of **4**-Ta, perhaps via formation of a $(silox)_3TaCO$ adduct.[51] At low temperatures in the presence of a coordinating solvent such as THF or DME, a thermally unstable solvent adduct of the carbonyl compound (**1**-TaCO(THF)) was formed and characterized via ^1H NMR spectroscopy (Eq. 1.5). Additional labeling experiments supported the existence of **1**-TaCO(THF) as a

$$\underset{\textbf{1}\text{-Ta}}{(\text{silox})_3\text{Ta}} + CO \xrightarrow[-78\ ^\circ\text{C}]{\text{THF}} \underset{\textbf{1}\text{-TaCO(THF)}}{(\text{silox})_3(\text{THF})\text{TaCO}} \quad \textbf{(1.5)}$$

monomeric carbonyl adduct. In the presence of non-coordinating solvents such as toluene, benzene, hexane, and Et_2O, treatment of **1**-Ta with carbon monoxide at low temperature resulted in formation of a red precipitate proposed as the solvent-free carbonyl adduct, $(silox)_3TaCO$ (**1**-TaCO). However, these carbonyl adducts, although characterized spectroscopically, could not be isolated for further study.

Because $(silox)_3Ta$ was shown to be highly competent for activation of small molecules such as CO_2 and CO, due to the tendency to undergo oxidative addition, the activation of dinitrogen was pursued.[52-53] The propensity for early transition metals to

achieve a high oxidation state through formation of strong metal-ligand bonds provides a large thermodynamic driving force for cleavage of the dinitrogen triple bond, resulting in very stable early transition metal (groups 5 – 7) bisimido or nitride complexes. Activation of dinitrogen through reductive bond cleavage by soluble early transition metal complexes has been demonstrated by several laboratories in recent years, following the general method of treating a metal complex with reducing equivalents in the presence of dinitrogen to activate a molecule of N_2 bound to the metal center.[54-80] Figure 1.1 shows two recent examples of N_2 bond cleavage by tantalum and niobium to generate the corresponding metal nitrides as dimeric, diamond-core structures. In the latter case, the resulting niobium nitride (Figure 1.1b) could further be protonated by lutidinium chloride to release ammonia (61% yield) and regenerate the niobium chloride starting material. Because the strengths of the metal-nitride bonds formed are quite high, the functionalization and extrusion of nitrogen-containing species from early-metal complexes is typically difficult.

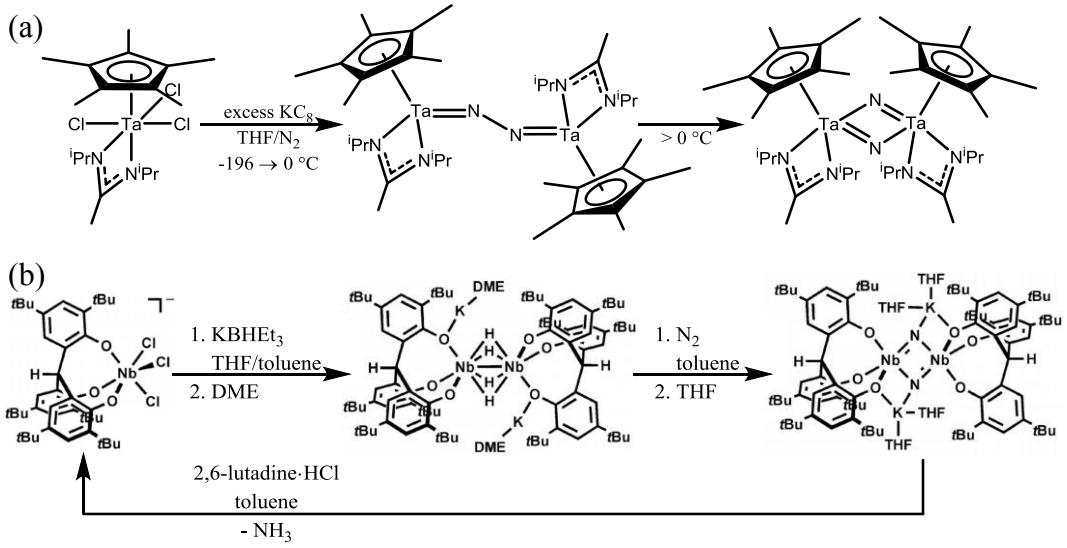

Figure 1.1. Selected examples from the literature of dinitrogen activation with tantalum[77] (a) and niobium[54] (b).

Although it is highly unlikely that protonation of activated dinitrogen complexes to generate ammonia will replace the highly efficient Haber-Bosch process for synthesis of ammonia from N_2 and H_2, study of ammonia production from dinitrogen utilizing early transition metal complexes is presumed to provide significant mechanistic information.

In an effort to achieve similar reactivity with $(silox)_3Ta$ (**1**-Ta), the formation of a dinitrogen complex, $(silox)_3TaNNTa(silox)_3$ (**8**-Ta) was targeted. However, although **1**-Ta has been shown in this laboratory to facilitate bond cleavage of a variety of small molecules including the C-N bonds of electron-deficient anilines, C-O bonds, and E-H (E = N, P, As) bonds,[81-84] as well as CO_2 and CO as shown above, **1**-Ta is unreactive with respect to N_2. It has been shown in related studies that compounds of the form $L_nX_3Ta=N-N=TaX_3L_n$ can be synthesized through reduction of X_nM in the presence of L and N_2,[85-94] yet **1**-Ta does not bind dinitrogen to form $(silox)_2Ta(N_2)$ or the reduced species $(silox)_3Ta=N-N=Ta(silox)_3$ (**8**-Ta).[81,95-98] Although the transformation is calculated to be exergonic by 55.6 kcal/mol, these transformations are orbital symmetry forbidden. Figure 1.2[95] illustrates the calculated linear reaction coordinate for reaction of two equiv **1**-Ta with N_2 to form $(silox)_3TaNNTa(silox)_3$ via the intermediate $(silox)_3Ta(N_2)$. In its ground state, **1**-Ta exists as a singlet with two electrons in the d_{z^2} orbital. To undergo dinitrogen binding, intersystem crossing to a triplet state is necessary, as $(silox)_3Ta(N_2)$ has a triplet ground state that is 5.5 kcal/mol lower in energy than the corresponding singlet. Therefore, one of the **1**-Ta molecules must undergo excitation to a triplet state $\{(d_{z^2})^1(d_{xz} \text{ or } d_{yz})^1\}$ which is calculated to be approximately 19 kcal/mol uphill (solid

red line). Furthermore, the calculated triplet configuration of $(silox)_3Ta(N_2)$, $\{(d_{xz})^1(d_{yz})^1\}$, doesn't correlate with the first excited state of $(silox)_3Ta$ $\{(d_{z2})^1(d_{xz}$ or $d_{yz})^1\}$; thus, excitation to a higher energy excited triplet state likely must occur for dinitrogen binding (dashed red line).

The second step of dinitrogen binding, in which another equivalent of **1**-Ta binds to $(silox)_3Ta(N_2)$, again requires intersystem crossing to occur. A possible pathway is one in which the second equivalent of **1**-Ta undergoes excitation to a triplet state to bind the triplet $(silox)_3Ta(N_2)$. The resulting quintet $(silox)_3TaNNTa(silox)_3$ may then undergo electronic reorganization to achieve the singlet ground state. Thus, although binding of N_2 is very thermodynamically favorable, the reaction is not observed because both steps require intersystem crossing, rendering the transformations orbital symmetry forbidden.

In contrast, synthesis of a tantalum imido compound from ammonia and **1**-Ta is quite facile (Scheme 1.2). This can be viewed as a study of the microscopic reverse of ammonia formation from the desired $(silox)_3TaNNTa(silox)_3$ species, and was initially perused as a route to synthesis of the dinitrogen compound.

Treatment of **1**-Ta with NH_3 resulted in rapid oxidative addition of an N-H bond to tantalum to form the corresponding hydride $(silox)_3Ta(H)(NH_2)$ (Scheme 1.2),[65,97-98] which underwent facile 1,2-H_2-elimination at room temperature to form the

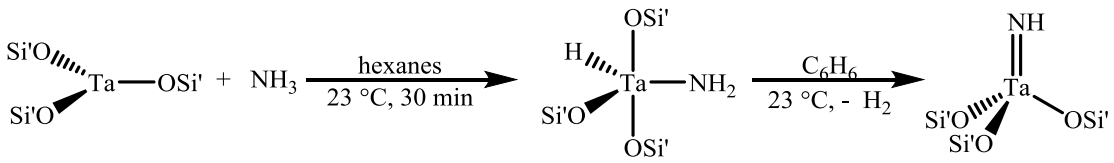

Scheme 1.2. Formation of tantalum imido from **1**-Ta and ammonia.

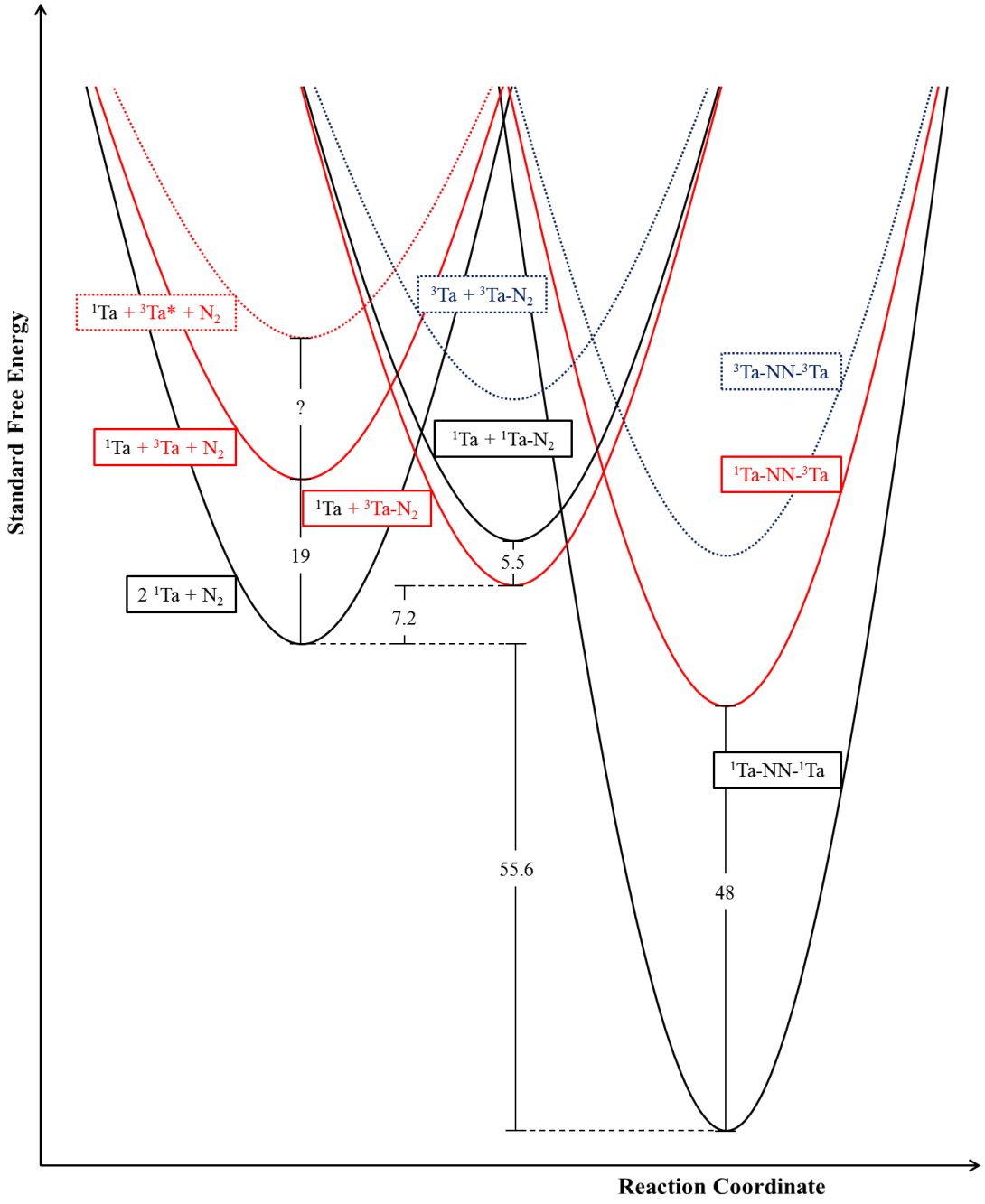

Figure 1.2. Plausible linear reaction coordinate vs. standard free energy diagram for 2 **1**-Ta + N_2 to the hypothetical $(silox)_3$Ta-NN-Ta$(silox)_3$ via $(silox)_3$Ta(N_2). Calculated standard free energies are in kcal/mol, and all surface representations are parabolically equivalent. The energies pertaining to dashed surfaces have been estimated.[90]

corresponding imido complex $(silox)_3Ta{=}NH$. Although the synthesis of $(silox)_3Ta{=}NH$ was straightforward, conversion to the desired $(silox)_3TaNNTa(silox)_3$ through a variety of routes was unsuccessful. Formation of the dinitrogen adduct is predicted to be highly thermodynamically exergonic and despite substantial efforts from this laboratory, $(silox)_3TaNNTa(silox)_3$ has thus far remained elusive.

Results and Discussion

1.1 Activation of CO_2 and CO with Low-Valent Niobium

As shown with tantalum, treatment of the analogous low-valent $(silox)_3NbPMe_3$ (**1**-$NbPMe_3$)[99-100] with excess carbon dioxide resulted in the formation of $(silox)_3Nb{=}O$ (**2**-Nb), with concomitant release of CO and free PMe_3 (Eq. 1.6).[101] When **1**-$NbPMe_3$ was instead treated with 1/3 equiv CO_2, evidence of formation of **2**-Nb and the dicarbide $(silox)_3Nb{=}C{=}C{=}Nb(silox)_3$ (**4**-Nb) was observed; however, the chemistry was not as clean as observed for the related tantalum system. As such, the direct carbonylation of **1**-$NbPMe_3$ was studied.

$$\underset{\textbf{1}\text{-NbPMe}_3}{(silox)_3NbPMe_3} + \text{excess } CO_2 \xrightarrow[23\ ^\circ C]{C_6H_6} \underset{\textbf{2}\text{-Nb}}{(silox)_3Nb{=}O} + CO + PMe_3 \qquad \textbf{(1.6)}$$

Treatment of **1**-$NbPMe_3$ with an excess of carbon monoxide resulted in formation of **2**-Nb and ketenylidene **3**-Nb (Eq. 1.7). Unlike the tantalum system, solid-state IR spectra of the reaction mixture revealed two sharp bands at 2068 and 2053 cm^{-1}.[102] When ^{13}CO was used instead, both bands shifted to 2003 and 1987 cm^{-1}, and with a 1:1 mixture of CO and ^{13}CO, two sets of four bands were observed: one set at 2068, 2057, 2013, and 2003 cm^{-1}, and the other set at 2053, 2042, 1999, and 1987 cm^{-1} (Figure 1.3a). Based on isotopic labeling studies, while one set of bands certainly corresponded to the expected ketenylidene **3**-Nb, the second set of bands also corresponded to a dicarbon fragment. Additionally, although both sets of bands were

$$\underset{\textbf{1}\text{-NbPMe}_3}{(silox)_3NbPMe_3} + \text{excess } CO \xrightarrow[23\ ^\circ C]{C_6H_6} \tfrac{1}{2}\ \underset{\textbf{2}\text{-Nb}}{(silox)_3Nb{=}O} + \tfrac{1}{2}\ \underset{\textbf{3}\text{-Nb}}{(silox)_3Nb{=}C{=}C{=}O} \qquad \textbf{(1.7)}$$

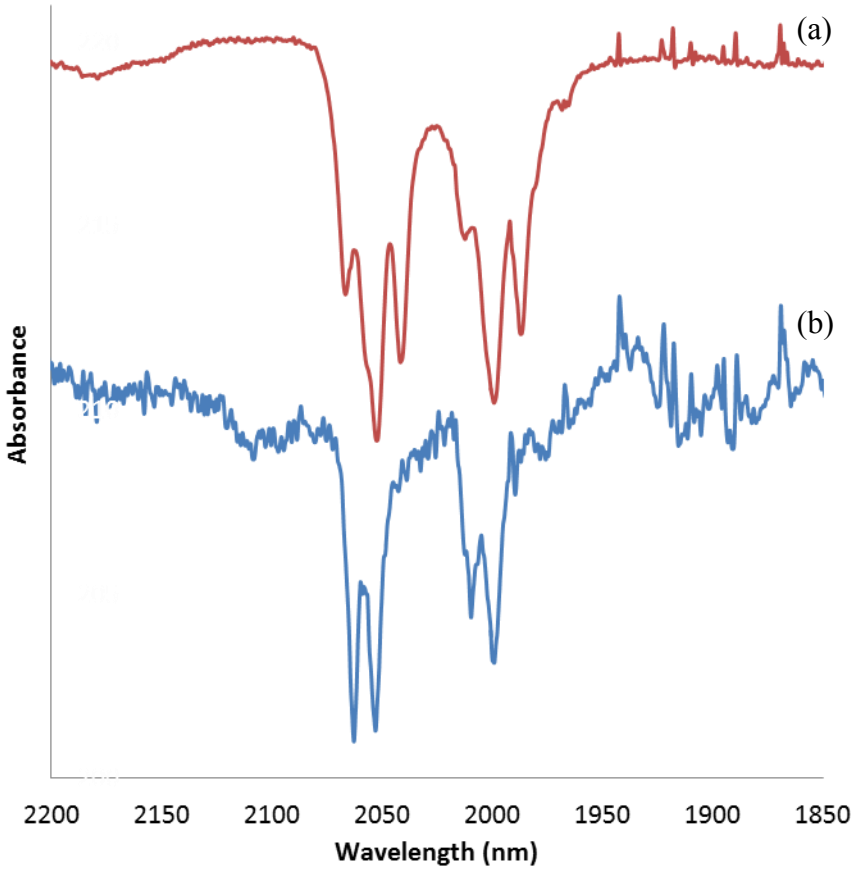

Figure 1.3. IR spectra of **3**-Nb generated from a 1:1 mixture of CO and ^{13}CO prepared as a Nujol mull between KBr plates (a) and as a solution in toluene (b).

always present in reactions to form **3**-Nb, the relative ratios of the bands differed from reaction to reaction.

A solution IR spectrum resolved this conflict: in toluene, only four bands of approximately equal intensity were observed at 2063, 2053, 2010, and 1999 cm^{-1} (Figure 1.3b), representing a statistical distribution of the four different isotopomers (silox)$_3$Nb=C=C=O, (silox)$_3$Nb=^{13}C=C=O, (silox)$_3$Nb=C=^{13}C=O, and (silox)$_3$Nb=^{13}C=^{13}C=O. Since the solution bands appear as an average of the solid-state bands, it is reasonable to propose that the two sets of bands arise from either (a) coupling of the ketenylidene chromophores in the solid state to yield one high-energy

band and one low-energy band, or (b) that the ketenylidene is somewhat soluble in Nujol and the solvated **3**-Nb exhibits slightly altered IR stretches relative to **3**-Nb in the solid state. Given that the relative ratios of the two bands in the solid state differ from sample to sample within the same batch of **3**-Nb, it is likely that the two bands arise due to differing amounts of Nujol in each sample, (b).

The ^{13}C NMR spectrum of (silox)$_3$Nb=^{13}C=^{13}C=O (**3**-Nb^{13}C$_2$) revealed a single resonance at δ 76.0 (NbC*C*O), with a J_{CC} = 76 Hz, within the range expected for a two-carbon bridge. The α-carbon (Nb*C*CO) was not observed, presumably due to a large degree of quadrupolar broadening from the Nb metal center. ^{93}Nb NMR revealed a doublet at δ -687, with a J_{NbC} ~ 500 Hz. Selected spectroscopic parameters for **3**-Nb and **3**-Ta are compared in Table 1.1 and due to a substantially smaller J_{CC}, suggest a greater degree of CO triple bond character in **3**-Nb.

Table 1.1. Comparison of selected spectroscopic parameters of **3**-Nb and **3**-Ta (n. d. = not determined).

	^{13}C NMR				Infrared
	δ MC*C*O	δ M*C*CO	J_{CC} (Hz)	J_{MC} (Hz)	ν_{CO} (cm^{-1})
3-Nb	76.0	n. d.	76	~500	2063
3-Ta	142.5	136.0	100	n. d.	2076

When **3**-Nb was treated with two equiv **1**-NbPMe$_3$ a purple precipitate was observed, identified as the dicarbide (silox)$_3$Nb=C=C=Nb(silox)$_3$ (**4**-Nb), along with production of **2**-Nb and free PMe$_3$ (Eq. 1.8). As with the tantalum analogue, it is reasonable to propose **3**-Nb as a mechanistic precursor to formation of **4**-Nb.

$$\underset{\textbf{3}\text{-Nb}}{(\text{silox})_3\text{Nb=C=C=O}} + 2\ \underset{\textbf{1}\text{-NbPMe}_3}{(\text{silox})_3\text{NbPMe}_3} \xrightarrow[23\ ^\circ\text{C}]{C_6H_6} \underset{\textbf{4}\text{-Nb}}{[(\text{silox})_3\text{Nb}]_2(\mu\text{-}C_2)} + \underset{\textbf{2}\text{-Nb}}{(\text{silox})_3\text{Nb=O}} + 2\ \text{PMe}_3 \quad \textbf{(1.8)}$$

When **1**-$NbPMe_3$ and exactly 0.5 equiv carbon monoxide were mixed at low temperatures and slowly allowed to warm to room temperature over several hours, formation of an insoluble dark purple solid, consistent with dicarbide **4**-Nb, and **2**-Nb, was observed (Eq. 1.9). The solid was isolated in 42% yield and the pale yellow material in the filtrate was isolated in 49% yield. Based on ^1H NMR spectroscopy the filtrate contained primarily **2**-Nb, so the reaction occurred mostly according to the stoichiometry indicated in Eq. 1.9. IR analysis of the solid, however, indicated the presence of an impurity with a characteristic band at 1208 cm^{-1} which shifted to 1172 cm^{-1} with ^{13}CO. When a 1:1 mixture of CO and ^{13}CO was used, only the two bands at 1208 and 1172 cm^{-1} were observed in roughly equivalent intensities, consistent with an absorption arising from a single carbon unit derived from carbon monoxide.

$$\underset{\textbf{1}\text{-NbPMe}_3}{(\text{silox})_3\text{NbPMe}_3} + \tfrac{1}{2}\,\text{CO} \xrightarrow[-78 \rightarrow 23\ ^\circ\text{C}]{\text{toluene}} \tfrac{1}{2}\,\underset{\textbf{2}\text{-Nb}}{(\text{silox})_3\text{Nb=O}} + \tfrac{1}{4}\,\underset{\textbf{4}\text{-Nb}}{[(\text{silox})_3\text{Nb}]_2(\mu\text{-C}_2)} \quad \textbf{(1.9)}$$

Due to the poor solubility of **4**-Nb NMR analysis could not be carried out, but solid-state magnetic data could be collected. Because **4**-Ta was shown to be an S = 1 system, it was expected that **4**-Nb might display analogous magnetic behavior. SQUID magnetometry measurements on two independently prepared samples displayed vastly different results, shown in Figure 1.4. The two sets of data exhibit a μ_{eff} of between 1.5 and 4.0 μ_B at 300 K, bracketing the value expected for an S = 1 system (spin-only value for S = 1 is 2.82 μ_B). Chemically sensible fit parameters could not be obtained for either set of data without inclusion of a diamagnetic impurity that comprised >90% of the sample; however, representative parameters *are* given in Figure 1.4. Unfortunately, fits with a similar temperature-independent paramagnetism (TIP) value

for both sets of data could not be obtained, perhaps due to a very small amount of ferromagnetic material in sample (a) that would manifest in SQUID data as an unusually large TIP contribution. The variability between samples, as well as the difficulty in obtaining a reasonable fit, most likely arises from differing amounts of a magnetically dissimilar impurity in each sample.

To further probe the insoluble solid identified as primarily **4**-Nb, Raman spectra were acquired for **4**-Nb and **4**-Nb$^{13}C_2$. A ν_{CC} of 1612 cm^{-1} was obtained for **4**-Nb and a $\nu_{^{13}C^{13}C}$ of 1555 cm^{-1} was obtained for **4**-Nb$^{13}C_2$. These data were compelling

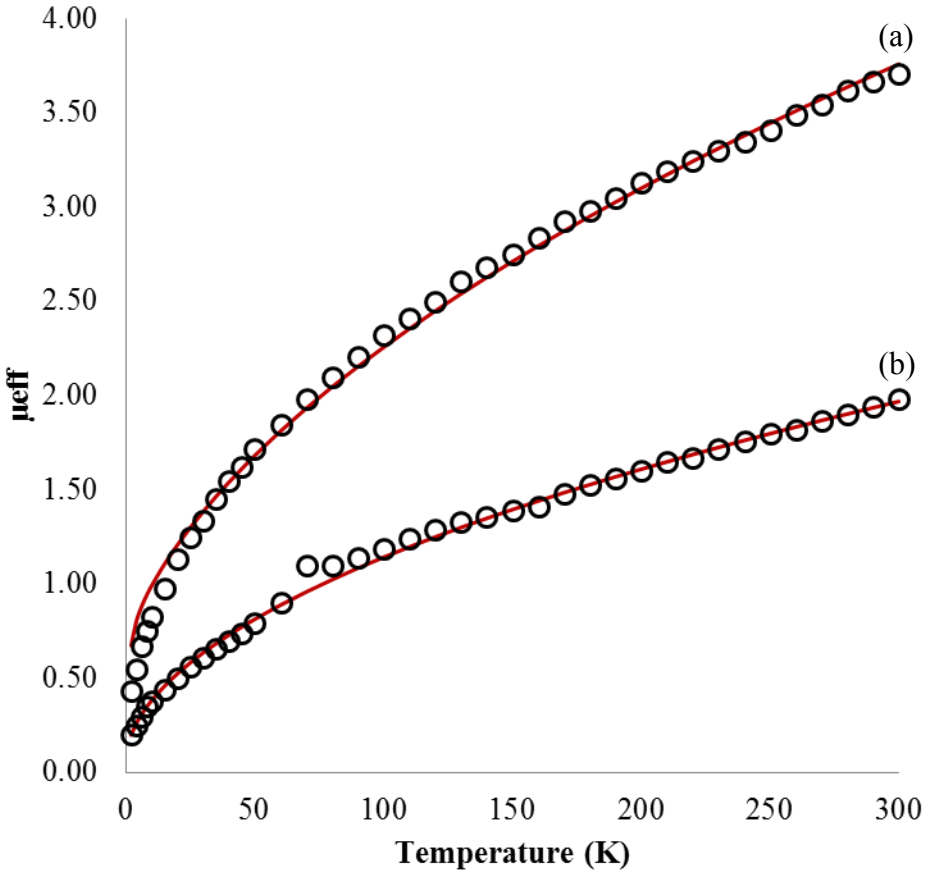

Figure 1.4. Representative SQUID data for **4**-Nb. Fit parameters: (a) g = 2.00, D = -3.92 cm^{-1}, E/D = 0, TIP = 5656.9 x 10^{-6} emu, DI = 92.8%, TW = -0.619 K; (b) g = 2.00, D = -3.92 cm^{-1}, E/D = 0, TIP = 1609.2 x 10^{-6} emu, DI = 99.8%, TW = -0.010 K (b).

Table 1.2. Comparison of selected spectroscopic parameters for **4**-Nb and **4**-Ta (n. d. = not determined).

	Raman		Infrared
	ν_{CC} (cm^{-1})	$\nu_{^{13}C^{13}C}$ (cm^{-1})	ν_{MC} (cm^{-1})
4-Nb	1612	1555	n. d.
4-Ta	1617	1549	709

evidence for the presence of **4**-Nb in the insoluble solid, and match up well to the Raman data collected for **4**-Ta (Table 1.2).[103] Unfortunately, although a ν_{MC} of 709 cm^{-1} was obtained from IR spectra of 4-Ta, the analogous stretch could not be observed for **4**-Nb with the appropriate labeling studies.

Crystals suitable for X-ray analysis were obtained through thermal digestion of the insoluble material containing **4**-Nb, and the resulting structure is shown in Figure 1.5 with relevant parameters presented in Table 1.3. The niobium-oxygen distances are normal (1.905 Å avg.) and a tetrahedral geometry is observed about each metal center. Surprisingly, the structure refined better when nitrogen atoms were placed in

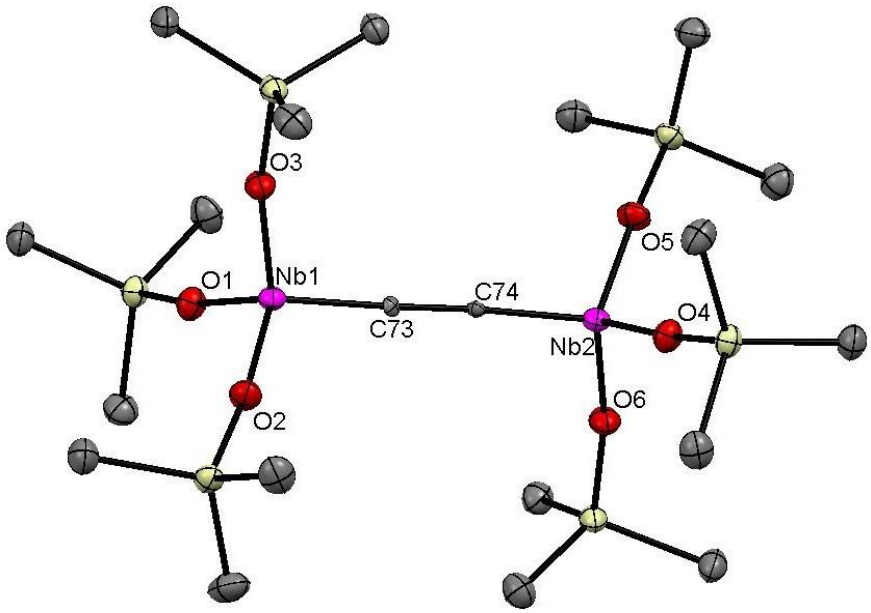

Figure 1.5. Molecular Structure of **4**-Nb. Methyl groups have been omitted for clarity.

Table 1.3. Selected interatomic distances and bond angles for **4**-Nb.

Selected Bond Distances (Å)		Selected Bond Angles (°)	
Nb1-O1	1.9011 (19)	O1-Nb1-C73	109.80 (9)
Nb1-O2	1.9087 (19)	O2-Nb1-C73	110.51 (9)
Nb1-O3	1.9036 (17)	O3-Nb1-C73	107.13 (9)
Nb1-O4	1.9053 (19)	O4-Nb2-C74	108.02 (9)
Nb1-O5	1.9086 (19)	O5-Nb2-C74	110.93 (9)
Nb1-O6	1.9005 (17)	O6-Nb1-C74	107.61 (9)
Nb1-C73	1.876 (2)	Nb1-C73-C74	177.9 (2)
Nb1-C74	1.873 (2)	Nb2-C74-C73	176.4 (2)
C73-C74	1.324 (3)		

Table 1.4. Structural data for **4**-Nb and **8**-Nb.

Crystal Data

Formula	$C_{74}H_{162}Nb_2O_6Si_6$	$C_{72}H_{162}N_2Nb_2O_6Si_6$
Formula Weight	1502.40	1506.40
Crystal System	Triclinic	Orthorhombic
Space Group	P-1	C222(1)
Z	2	4
a, Å	12.9421(7)	22.6485(9)
b, Å	16.1735(9)	24.6140(10)
c, Å	21.2969(11)	17.3420(6)
α, deg	75.271(2)	90
β, deg	87.305(2)	90
γ, deg	88.024(2)	90
Volume, $Å^3$	4305.4(4)	9667.6(6)
D (calc.), g/cm^3	1.159	1.035
Absorption coeff., mm^{-1}	0.393	0.351
F(000)	1640	3288
Crystal Size, mm	0.25 x 0.10 x 0.05	0.40 x 0.30 x 0.15

Data Collection and Refinement

Temp, K	173(2)	193(2)
Wavelength (λ), Å	0.71073	0.71073
θ limits, deg	1.30 to 27.10	2.03 to 26.36
Index Ranges	$-16 \le h \le 16, -20 \le k \le 20, -19 \le l \le 27$	$-28 \le h \le 26, -30 \le k \le 29, -21 \le l \le 14$
Reflections Collected	68634	37004
Absorption Correction	Semi-empirical from equivalents	Semi-empirical from equivalents
Max. and Min. Transmission	0.9806 and 0.9081	0.9492 and 0.8724
Refinement Method	Full-matrix least-squares on F^2	Full-matrix least-squares on F^2
Data/Restraints/Params.	18766 / 0 / 847	9828 / 0 / 407
Goodness-of-Fit on F^2	1.014	1.036
R Indices (all data)	R1 = 0.0747, wR2 = 0.1191	R1 = 0.0401, wR2 = 0.0846
Largest Diffraction Peak and Hole (e^- Å)	0.784 and -0.568	0.353 and -0.245

the bridge of the molecule instead of carbon atoms; however, as the synthesis of **4**-Nb was performed with careful exclusion of N_2, incorporation of a dinitrogen unit into the

dimer was improbable. Rather, this result suggests a greater degree of electron density present in the bridge than would be expected for a pure dicarbide unit. In addition, the *d*(Nb-C) distances (1.875 Å avg.) are shorter than expected for niobium alkylidenes and significantly shorter than the corresponding tantalum dicarbide **4**-Ta (*d*(Ta-C) = 1.95 Å).

An IR spectrum of the crystalline material used to obtain the crystal structure shown in Figure 1.5 revealed weak bands characteristic of ketenylidene **3**-Nb, as well as a small band at 1208 cm^{-1}, indicative of the impurity with one carbon derived from CO. It has been proposed[51] that a plausible intermediate in the reduction of CO with $(silox)_3Ta$ is the dimer $(silox)_3TaCOTa(silox)_3$. The related $(silox)_3NbCONb(silox)_3$ (**5**-Nb) is a potential impurity containing one carbon derived from CO that could exhibit a relatively low-energy IR band. The apparent increased electron density in the dicarbide bridge of **4**-Nb can be explained in two ways. If a small amount (~15%) of **3**-Nb, known to be present via IR analysis, co-crystallized with **4**-Nb, the apparent electron density of the dicarbide bridge would be increased. Alternatively, a crystal of the proposed **5**-Nb may appear very similar to the structure of **4**-Nb. If the molecule were disordered, the electron density corresponding to the carbon and oxygen in the bridge of **5**-Nb would average and appear crystallographically like a dinitrogen unit, consistent with the observation that the obtained structure refined better with nitrogen rather than carbon. IR analysis indicated the presence of the putative **5**-Nb as only a minor component of the bulk. If a crystal composed primarily or exclusively of **5**-Nb was chosen, the crystal structure does not represent the bulk material.

To further explore the abnormalities presented in the structure of **4**-Nb, calculations were carried out on **4**-Nb, **5**-Nb, and **4**-Ta. All calculated structures indicated a tetrahedral geometry about the metal centers as expected. Both **4**-Nb and **4**-Ta were calculated to be ground state triplets, and the computed structures are shown in Figure 1.6. The calculated *d*(Nb-C) values of 2.01 Å are quite elongated relative to the observed average *d*(Nb-C) value of 1.875 Å, and the calculated *d*(C-C) for **4**-Nb of 1.29 Å is contracted relative to the observed value of 1.324 (3) Å. These data further support the assertion that the structure presented in Figure 1.5 is compromised, either by cocrystalized impurities or by a compound (presumably **5**-Nb) not representative of the bulk material. In contrast, the calculated metric parameters for **4**-Ta match up well to those previously reported[51] (*d*(Ta-C) = 1.95 Å and *d*(C-C) = 1.30 Å). Additionally, the computed spin density of the ground state (74% Ta and 26% C) is consistent with that previously reported (80% Ta and 20% C). The data support the veracity of the calculations.

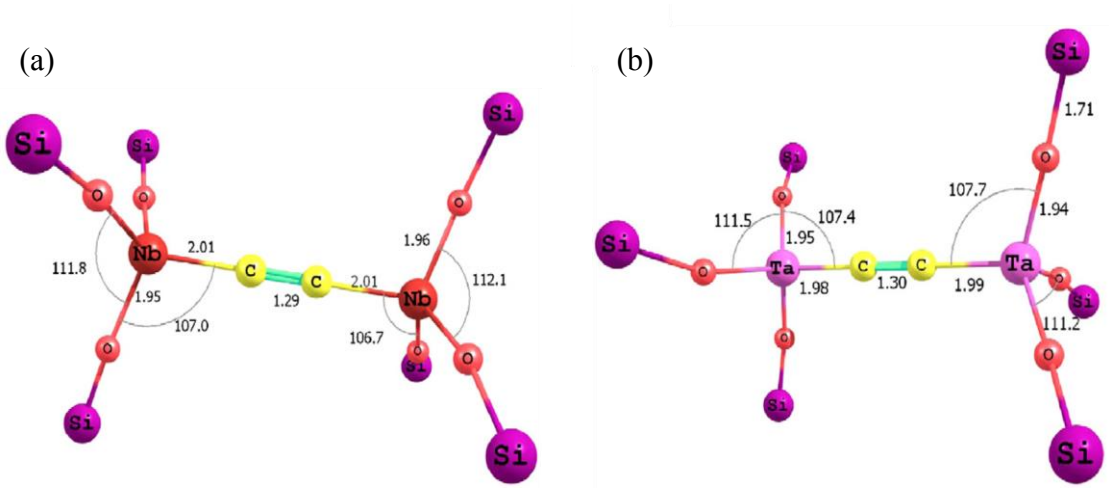

Figure 1.6. Calculated structures of **4**-Nb (a) and **4**-Ta (b). ^{t}Bu groups have been removed for clarity.

A computed Raman spectrum of **4**-Nb indicated a ν_{CC} of 1677 cm^{-1}, in line with the experimentally observed value of 1612 cm^{-1}. The calculated ν_{CC} for **4**-Ta of 1668 cm^{-1} is also consistent with the observed frequency of 1617 cm^{-1}. The computed ν_{NbC} of 676 cm^{-1} for **4**-Nb should correspond to an experimental stretch of about 650 cm^{-1}, yet no shifted bands upon ^{13}C labeling were observed in this region in the infrared spectrum. If a ν_{NbC} stretch exists in this region, the intensity must be quite low.

In the reaction of **1**-$NbPMe_3$ with carbon monoxide, two different impurities containing a one-carbon unit exhibiting a band at 1208 cm^{-1} are possible: the aforementioned dimer $(silox)_3NbCONb(silox)_3$ (**5**-Nb), or a PMe_3-containing compound $(silox)_3NbCPMe_3$ (**6**-Nb). Possible pathways to generate these compounds are given in Scheme 1.3. Considering the relative solubilities of monomeric versus dimeric silox species, **5**-Nb is more reasonable than **6**-Nb as a proposed impurity similar to dimeric **4**-Nb; however, calculations on the proposed **6**-Nb *did* reveal an absorption at 1227 cm^{-1} corresponding to a ν_{PC}/ν_{NbC} stretching vibration.

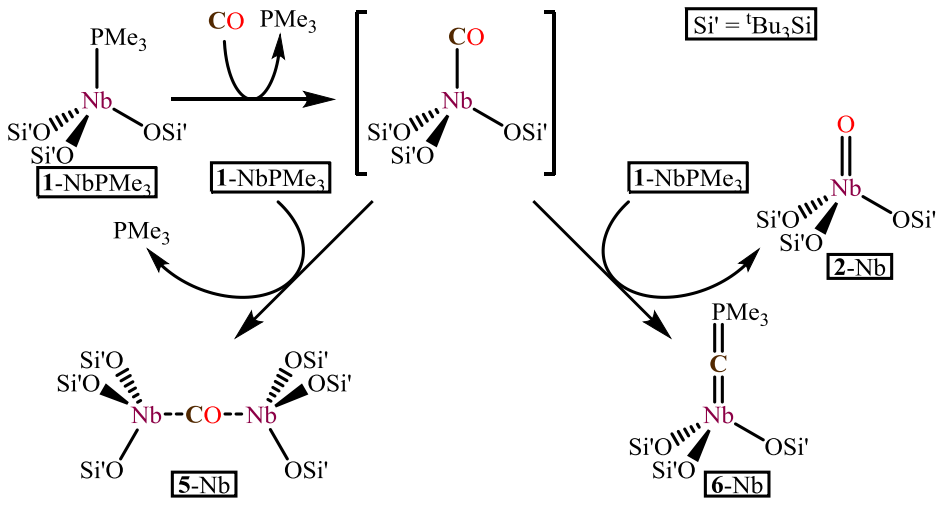

Scheme 1.3. Possible pathways for formation of **5**-Nb and **6**-Nb.

To rule out the possibility of the phosphine-containing **6**-Nb, a Nb^{III} phosphine-free precursor was utilized. Treatment of $[(silox)_3Nb]_2(\mu\text{-}C_6H_6)$ (**7**-Nb)[104] with one equiv CO resulted in the formation of **2**-Nb and a purple insoluble solid (Eq. 1.10). IR analysis of the solid revealed a spectrum strikingly similar to that of **4**-Nb prepared as given in Eq. 1.9, with an intense absorption at 1208 cm^{-1} (Figure 1.7).

$$\underset{\textbf{7}\text{-Nb}}{[(silox)_3Nb]_2(\mu\text{-}C_6H_6)} + CO \xrightarrow[23\ ^\circ C]{C_6H_6} \underset{\textbf{5}\text{-Nb}}{[(silox)_3Nb]_2(\mu\text{-}CO)} + \underset{\textbf{4}\text{-Nb}}{[(silox)_3Nb]_2(\mu\text{-}C_2)} + \underset{\textbf{2}\text{-Nb}}{(silox)_3Nb{=}O} + C_6H_6 \quad \textbf{(1.10)}$$

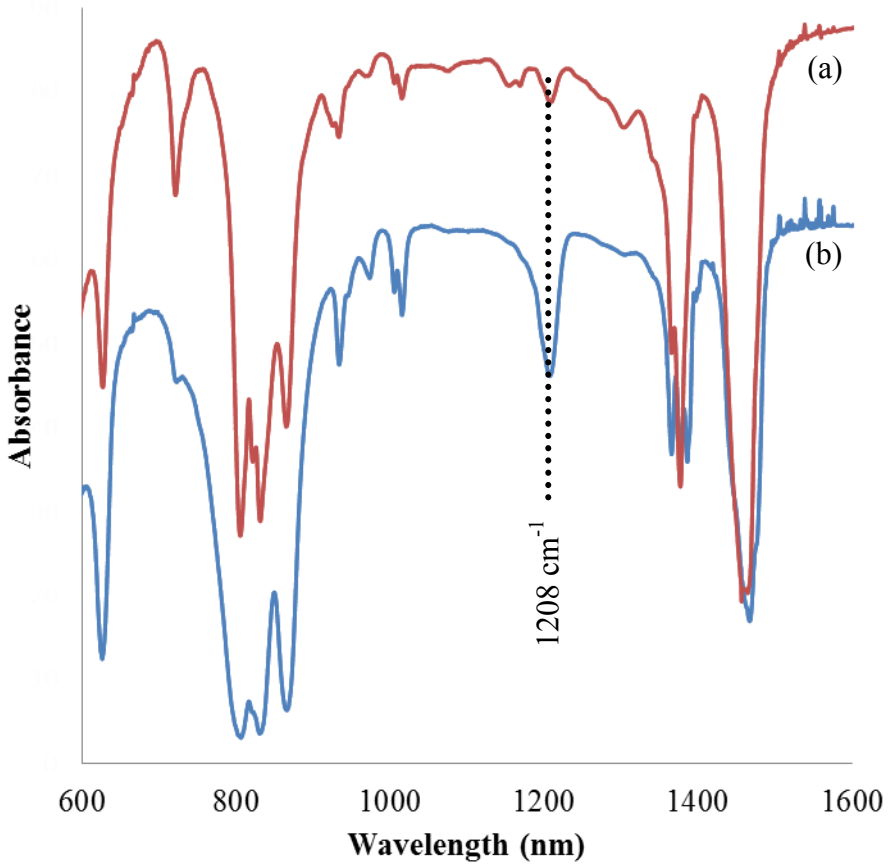

Figure 1.7. IR spectra of purple insoluble solid generated from carbonylation of **1**-$NbPMe_3$ (a) and **7**-Nb (b).

Because phosphine was rigorously excluded in preparation of this sample, it is reasonable to conclude that the 1208 cm^{-1} absorption does *not* arise from **6**-Nb.

Calculations on **5**-Nb, illustrated in Figure 1.8, revealed a singlet ground state with a significantly shorter *d*(Nb-Nb) than the corresponding **4**-Nb. The sum of the computed bridge distances in **5**-Nb is 5.08 Å, as compared to 5.31 Å (calculated) for **4**-Nb. The crystallographically determined bridge length of 5.073 Å is more consistent with the computed structure for **5**-Nb. Although it can be difficult to precisely locate light atoms between two heavy atoms crystallographically, the distance between the niobium centers should be very accurate. The calculated frequency for the CO stretch in **5**-Nb is 1358 cm^{-1}, quite a bit higher than the experimental value (1208 cm^{-1}). Computed frequencies from DFT calculations are typically ~3% high; however the calculated value is 13% greater than experimental and hence does not offer support for the presence of **5**-Nb. Nevertheless, as **5**-Nb is calculated to be diamagnetic, presence of varying amounts of **5**-Nb in dicarbide **4**-Nb prepared as shown in Eq. 1.9 would

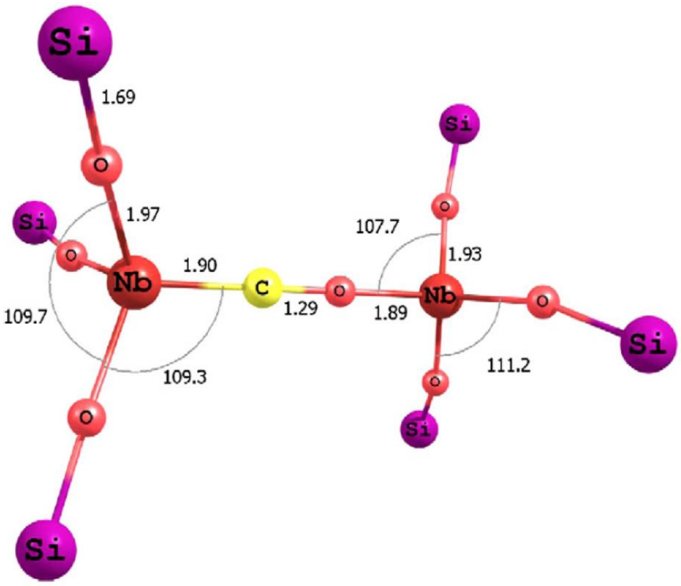

Figure 1.8. Calculated structure of **5**-Nb. ^{t}Bu groups have been removed for clarity.

explain the highly variant magnetic moments obtained in magnetism studies of **4**-Nb (Figure 1.4).

A quenching study was carried out on ^{13}C-labeled material from Eq. 1.10, in which the purple insoluble material was treated with an excess of D_2O (Eq. 1.11). Proton-decoupled ^{13}C NMR of the quench products revealed a septet (J_{CD} = 18 Hz) at δ 49.2 ppm, identified as methanol-^{13}C-d_4. The presence of $D_3{}^{13}COD$ was confirmed through a D_3COD spike to the NMR sample. This result is consistent with hydrolysis of **5**-Nb, in which D^+ protolytically cleaves an oxycarbene. Although DFT frequency calculations do not offer support for the existence of **5**-Nb, perhaps the molecule

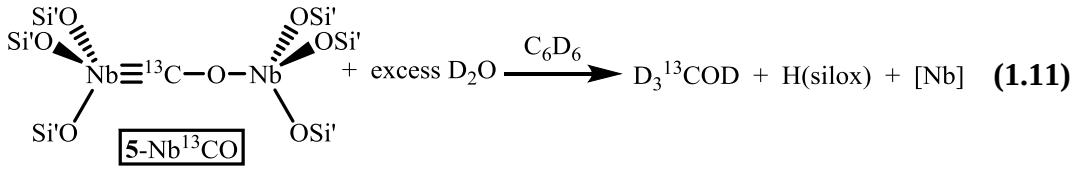

(1.11)

suffers from a high degree of excited state mixing such that extremely accurate calculations are difficult to carry out.[104] In the quench mixture shown in Eq. 1.11 ethane was not identified, unlike in the analogous quench of **4**-Ta (Eq. 1.4); however, **4**-Nb was almost certainly present in the purple insoluble material. It is reasonable to propose that the small amount of ethylene produced from a NMR-scale quench (30 – 60 torr) would mostly exist in the headspace of the sealed tube rather than in solution and not be easily seen via NMR spectroscopy.

The thermodynamics of dicarbide formation for both niobium and tantalum were investigated computationally, and results are presented in Figure 1.9. As expected, in both reactions ΔS has the same value regardless of metal identity, but niobium has a more favorable enthalpy of reaction than tantalum. For simple binding

of a C_2 unit, formation of $(silox)_3NbCCNb(silox)_3$ **(4**-Nb**)** is enthalpically 7.2 kcal/mol more favorable than formation of $(silox)_3TaCCTa(silox)_3$ **(4**-Ta**)**. Similarly, formation of **4**-Nb via cleavage of CO is 5.8 kcal/mol more enthalpically favorable than the analogous reaction to generate **4**-Ta. Generation of the oxo **2**-M is roughly 1 kcal/mol more favorable for M = Ta than M = Nb ($\Delta\Delta H$ = 1.4 kcal/mol).

Based on periodic properties, one might predict the formation of **4**-Ta would be more favorable than the formation of **4**-Nb due to the stronger M-C bonds expected for a third row transition metal, but the opposite is calculated. In both these reactions, two electrons from a d_{z^2} orbital in **1**-M must first be excited to a high-energy triplet state. For the third row metal tantalum, the d_{z^2} orbital is lower in energy than for niobium due to a greater degree of $6s\text{-}5d_{z^2}$ mixing in the third row compared with

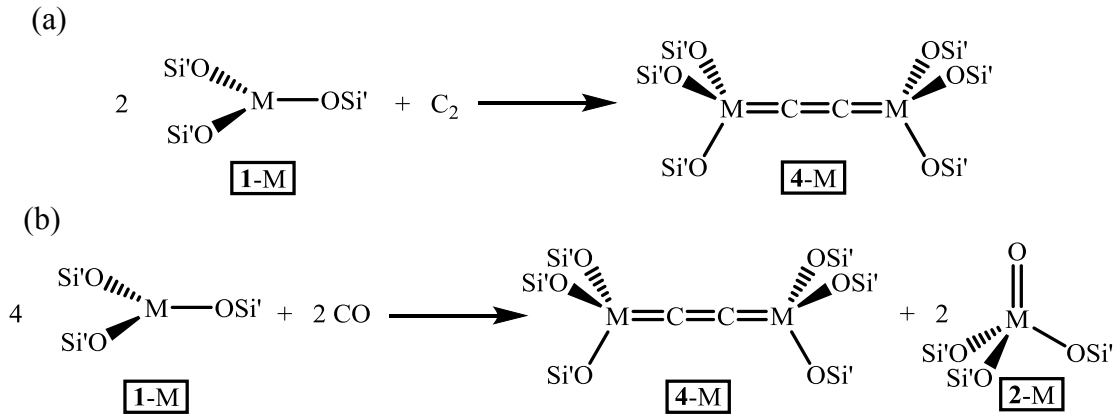

	Dicarbide Binding (a)			CO Cleavage (b)		
	ΔH (kcal/mol)	ΔS (kcal/mol)	ΔG (kcal/mol)	ΔH (kcal/mol)	ΔS (kcal/mol)	ΔG (kcal/mol)
M = Nb	-223.7	-109	-191.3	-211.8	-158	-164.8
Ta	-216.5	-109	-184.0	-206.0	-158	-159.0

Figure 1.9. Calculated thermodynamic parameters for dicarbide binding (a) and carbon monoxide cleavage (b) by $(silox)_3M$ (M = Nb, Ta).

5s-4d_{z^2} mixing in the second row. This s-d orbital mixing reduces the amount of σ* character of d_{z^2} via attenuation of its toroidal component, dropping the d_{z^2} orbital in energy relative to the pure d-orbital. Because this attenuation is less for niobium, the triplet state is more energetically accessible and, as shown computationally, the promotional energy necessary for excitation to a $\{(d_{xz})^1(d_{yz})^1\}$ state is approximately 30 kcal/mol less for niobium than tantalum.[105-106] When both M-C bond strengths and relative orbital energies are taken into account, the formation of **4**-Nb is slightly more favorable than **4**-Ta.

1.2 Activation of N_2 with Low-Valent Niobium

Attempts were made to generate a group 5 metal nitride through reaction of dinitrogen with the corresponding low-valent group 5 starting material in conjunction with a reducing agent. Unfortunately, treatment of $(silox)_3Ta$ (**1**-Ta) with potassium or cesium metal in the presence of N_2, with or without various chelating agents present, resulted in intractable mixtures of products. Gratifyingly, although treatment of $(silox)_3NbPMe_3$ (**1**-$NbPMe_3$) with Cs^0 or NaK resulted in similar reaction mixtures as seen for **1**-Ta, reaction of **1**-$NbPMe_3$ with elemental potassium in the presence of N_2 resulted in the formation of a sparingly soluble yellow precipitate (Eq. 1.12).

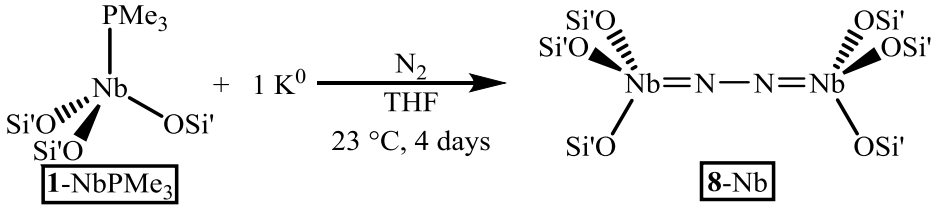

(1.12)

Addition of potassium chelating agents resulted in the same yellow precipitate, which showed a characteristic sharp singlet in the ^1H NMR spectrum at δ 1.21 ppm, signifying a diamagnetic silox-containing compound. The ^{93}Nb NMR spectrum

indicated a broad peak at δ -570 ($\nu_{1/2}$ ~4500 Hz), consistent with other reported $(silox)_3Nb^{V}$=NR compounds.[96]

X-ray crystallography was used to identify the compound as a dimeric dinitrogen complex, $(silox)_3NbNNNb(silox)_3$ (**8**-Nb). The molecular structure of **8**-Nb is shown in Figure 1.10, and relevant parameters are presented in Table 1.5. The molecule is orthorhombic, crystallizing in the C222(1) space group. As with **4**-Nb/**5**-Nb, the niobium-oxygen bond distances are normal with an average length of 1.9093 Å (1.905 Å for **4**-Nb) and are arranged in a tetrahedral geometry about each metal

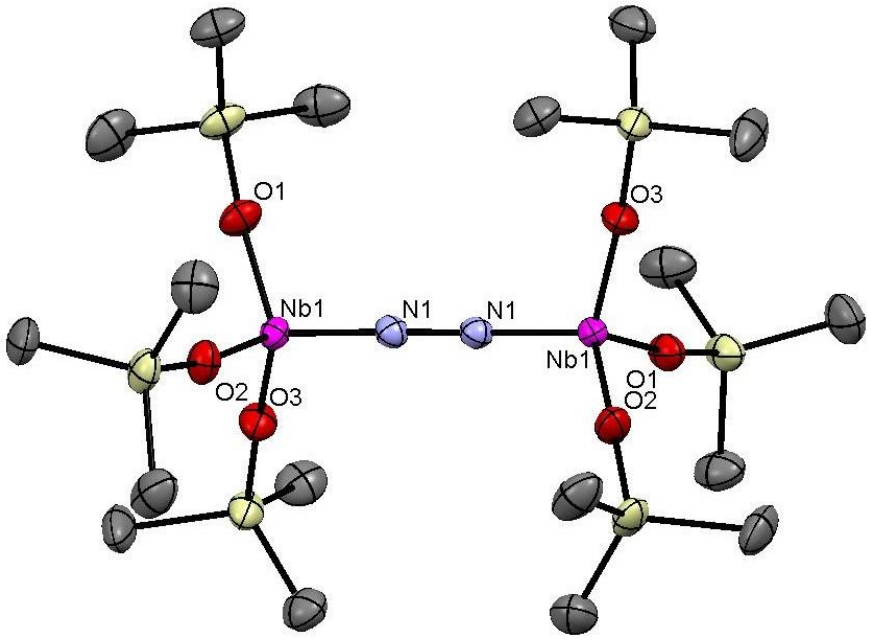

Figure 1.10: Molecular Structure of **8**-Nb. Methyl groups have been omitted for clarity.

Table 1.5: Selected interatomic distances and bond angles for **8**-Nb.

Selected Bond Distances (Å)		Selected Bond Angles (°)	
Nb1-O1	1.9144 (18)	O1-Nb1-N1	109.69 (9)
Nb1-O2	1.9085 (17)	O2-Nb1-N1	109.42 (9)
Nb1-O3	1.9050 (18)	O3-Nb1-N1	108.76 (8)
Nb1-N1	1.8039 (19)	Nb1-N1-N1$^{\#1}$	178.5 (2)
N1-N1$^{\#1}$	1.310 (4)		

center. The Nb1-N1bond distance lies within the range expected for a niobium imido, and the d(N1-N1$^{\#1}$) of 1.310 (4) Å is between that expected for a double bond (1.25 Å) and a single bond (1.45 Å). The molecule has an essentially linear bridge, with a Nb1-N1-N1$^{\#1}$ angle of 178.5 (2)°. The d(Nb1-Nb1$^{\#1}$) for **8**-Nb of 4.918 Å is slightly contracted relative to that of **4**-Nb (5.073 Å).

The synthesis of (silox)$_3$NbNNNb(silox)$_3$ (**8**-Nb) is particularly unusual in that potassium metal is required for product formation, yet does not appear in the final product. In a control reaction, a mixture of **1**-NbPMe$_3$ in THF at room temperature in the presence of N_2 did not result in the generation of any **8**-Nb over the course of weeks. However, treatment of **1**-NbPMe$_3$ with 0.25 equiv K^0 in THF resulted in formation of **8**-Nb in comparable yield, albeit with a longer reaction time (1 week). Presumably, potassium activates **1**-NbPMe$_3$ through reduction of one equiv **1**-NbPMe$_3$ to promote formation of a dinitrogen adduct K[(silox)$_3$Nb(N_2)], which could then react with a second equivalent of **1**-NbPMe$_3$ to generate K[(silox)$_3$NbNNNb(silox)$_3$]

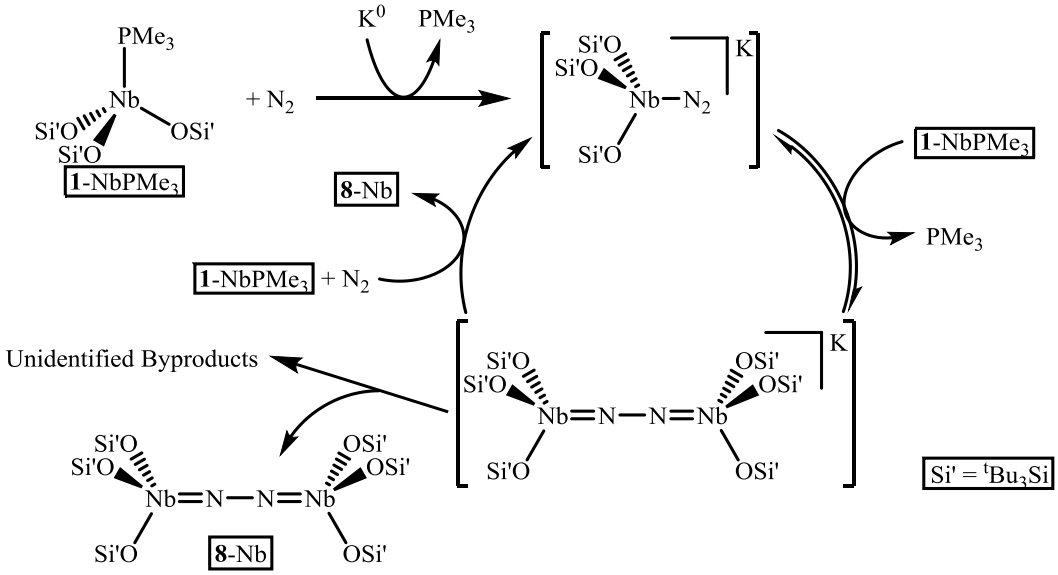

Scheme 1.4. Possible pathways for the formation of (silox)$_3$NbNNNb(silox)$_3$ (**8**-Nb).

(Scheme 1.4). K[(silox)$_3$NbNNNb(silox)$_3$] could then react with another equivalent of **1**-NbPMe$_3$ and N_2 to release **8**-Nb and regenerate K[(silox)$_3$Nb(N_2)]. Alternatively, the anion K[(silox)$_3$Nb=N-N=Nb(silox)$_3$]could undergo an oxidation event to release **8**-Nb and unidentified potassium-containing byproducts. Given that **1**-NbPMe$_3$ produced a similar amount of **8**-Nb regardless of whether stoichiometric or substoichiometric K^0 was used, the former pathway is most likely dominant.

It is intriguing that **8**-Nb forms under any conditions, given that exhaustive efforts to synthesize the analogous (silox)$_3$TaNNTa(silox)$_3$ (**8**-Ta) were unsuccessful. It is proposed that **8**-Ta does not form from **1**-Ta because the transformation requires several intersystem crossings that are orbital-symmetry forbidden, resulting in prohibitively high reaction barriers (Figure 1.2). Niobium experiences a lesser degree of s-d_{z^2} mixing than tantalum does, so the d_{z^2} orbital of Nb is closer in energy to its lowest unoccupied orbitals (d_{xz}/d_{yz}) and, correspondingly, the promotional energy required to excite Nb from a singlet ground state to a triplet excited state is less than that for Ta (Figure 1.2). Because **8**-Nb is not observed in the absence of K^0, although the barrier to reaction may be lower than that of **8**-Ta, it is still prohibitively high and addition of K^0 allows for formation of **8**-Nb through an alternate pathway (Scheme 1.4).

In an effort to generate a niobium nitride compound **8**-Nb was treated with additional reducing equivalents, but exposure to KC_8 or NaK resulted only in decomposition to a variety of silox-containing products, including H(silox), K(silox), and (silox)$_3$Nb=O (**2**-Nb). Furthermore, treatment of **8**-Nb with acids such as HCl(g) or $HBAr_4^F \cdot 2\ Et_2O$ (BAr_4^F = B[C_6H_3-3,5-(CF_3)$_2$]$_4$) did not result in isolation of

nitrogen-derived products such as hydrazine or ammonia, but decomposition products were observed. No reaction occurred with TMSCl even at elevated temperatures, and treatment with alkylating agents such as MeI at elevated temperatures again generated a mixture of silox-containing products.

1.3 Activation of NH_3 with Low-Valent Niobium

Attempts were also made to synthesize a niobium imido compound from NH_3, a reaction which could be viewed as the microscopic reverse of ammonia formation from **8**-Nb. Unfortunately, although there is precedence for similar reactivity in the analogous tantalum system (Scheme 1.2),[65,97-98] treatment of **1**-$NbPMe_3$ with 1.00 equiv NH_3 resulted in a reaction mixture containing H(silox), $(silox)_3Nb{=}O$, and a variety of other unidentified silox-containing products. No niobium hydride species were observed by IR or ^1H NMR spectroscopy. Although the ligand-free **1**-Nb has a proposed singlet ground state, the ligand-bound **1**-$NbPMe_3$ displays a triplet ground state. It is conceivable that **1**-$NbPMe_3$ does not react with ammonia as cleanly as **1**-Ta because a singlet ground state is required. A niobium starting material with a singlet ground state was sought to test this approach. Unfortunately, treatment of the S = 0 complex $(silox)_3Nb(2\text{-pic})$ with ammonia resulted in no reaction, and at elevated temperatures, only decomposition of the Nb starting material was observed.

Although the $(silox)_3Nb^{III}(NH_3)$ adduct or subsequent complexes along the reaction pathway, $(silox)_3Nb(H)(NH_2)$ or $(silox)_3Nb{=}NH$, were not observed, the pale teal complex $(silox)_3Nb^{IV}(NH_3)Cl$ (**10**-Nb) could be readily prepared through treatment of $(silox)_3NbCl$ (**9**-Nb) with ammonia (Eq. 1.13). X-ray diffraction data were collected to ascertain the identity of **10**-Nb. **10**-Nb displayed a characteristic

broad singlet in the ^{1}H NMR spectrum at δ 1.86 ($\nu_{1/2}$ = 15 Hz), which did not shift in spectrometers of different magnetic field strength. If a paramagnetic complex

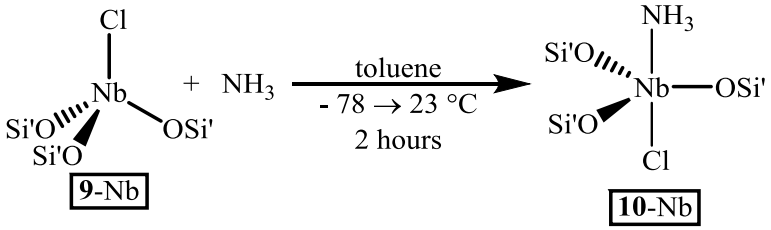

(1.13)

displayed a high degree of temperature-independent paramagnetism (TIP) one might predict a field-dependent chemical shift, but for an S = ½ species TIP would not be expected. Accordingly, the SQUID magnetometry data for **10**-Nb indicated a μ_{eff} (300 K) = 1.54 μ_β (avg.), as expected for an S = ½ early transition metal center (spin-only

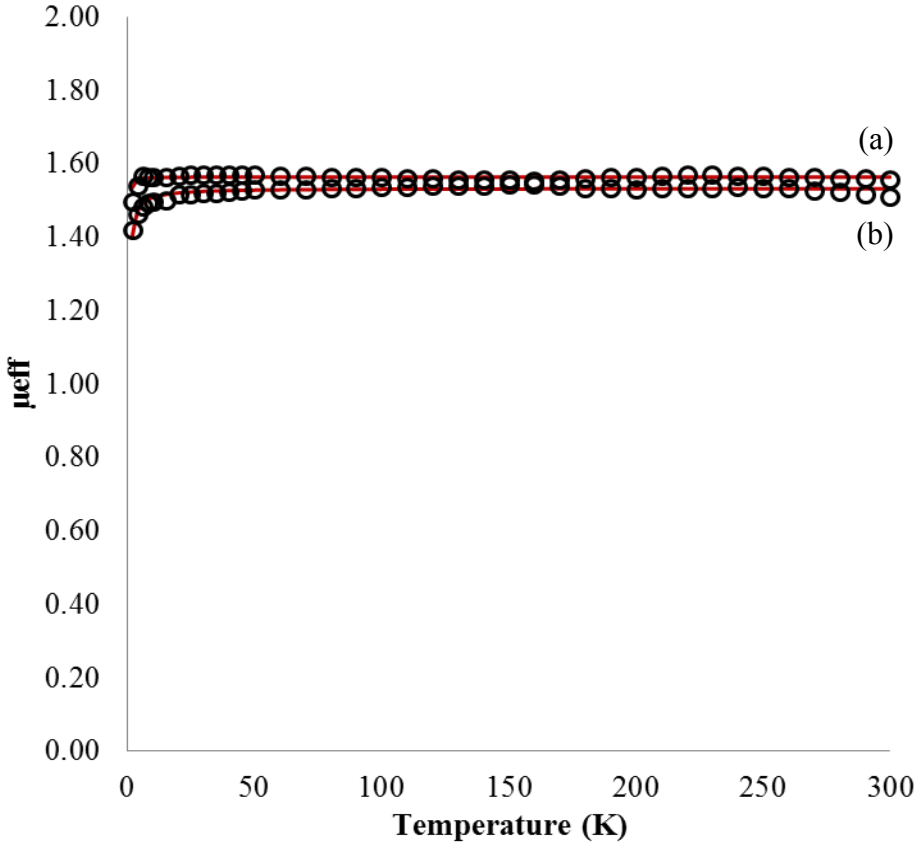

Figure 1.11. SQUID data for **10**-Nb. Fit parameters: (a) g = 2.00, D = 0 cm^{-1}, E/D = 0, TIP = 238.1 x 10^{-6} emu (subtracted), DI = 18.5%, TW = 0 K; (b) g = 2.00, D = 0 cm^{-1}, E/D = 0, TIP = -223.5 x 10^{-6} emu (subtracted), DI = 21.6%, TW = -0.323 K.

value = 1.73 μ_β), with negligible TIP (Figure 1.11). With g set to 2.00, the data fit well to d = 0 cm^{-1} and an average TIP of ~0 emu. Both fits required addition of ~20% diamagnetic impurity, indicating the presence of S = 0 impurities arising from decomposition of **10**-Nb.

UV-visible data for **10**-Nb showed two absorptions at 430 nm (ε = 95 $M^{-1}cm^{-1}$) and 630 nm (ε = 130 $M^{-1}cm^{-1}$), as might be expected for d-d transitions in a d^1 complex with roughly trigonal bipyramidal geometry (Figure 1.12). Upon heating, the absorptions corresponding to **10**-Nb gradually decreased in intensity and a new absorption at 515 nm grew in, as solutions of **10**-Nb slowly lost their teal hue and took on a light purple color. By ^{1}H NMR spectroscopy, a new broad resonance at δ 1.66

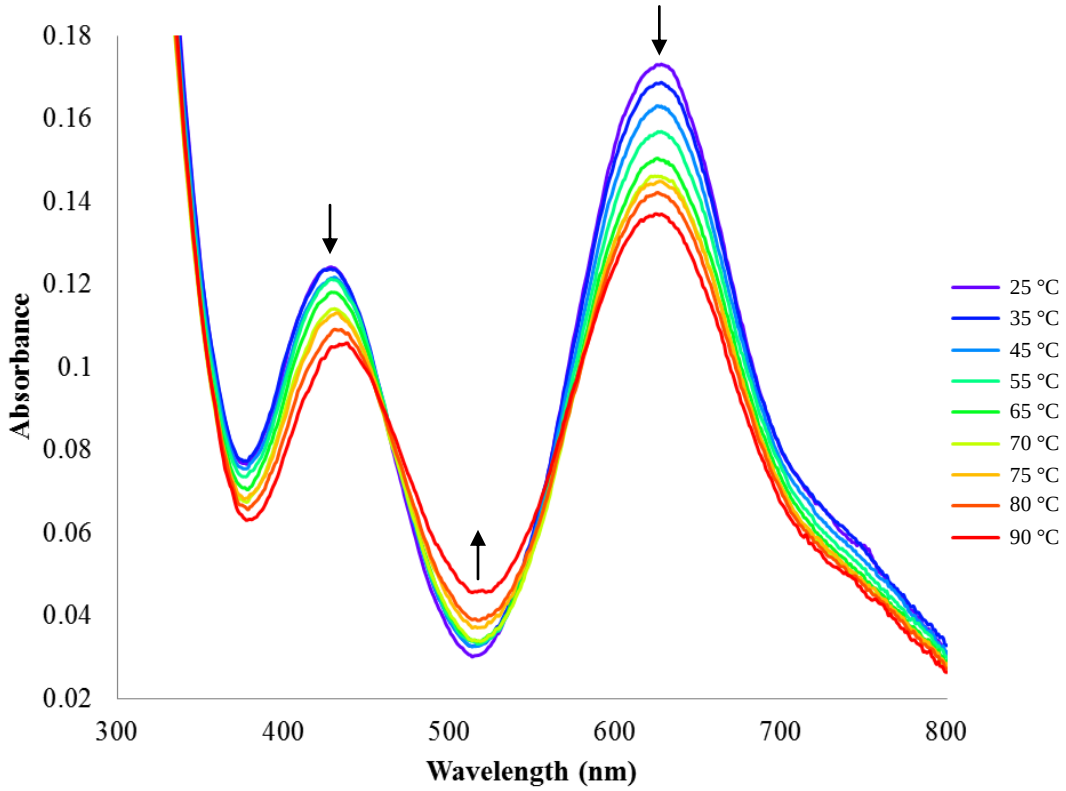

Figure 1.12. UV-visible data for **10**-Nb in C_6H_6 as a function of temperature. Arrows indicate spectral changes upon temperature increase.

($\nu_{1/2}$ = 23 Hz) appeared at elevated temperatures, consistent with the NH_3-free $(silox)_3NbCl$ (**9**-Nb). Upon cooling, **9**-Nb disappeared to quantitatively regenerate **10**-Nb, indicating a binding equilibrium that lies strongly towards formation of the ammonia complex **10**-Nb at room temperature but shifts towards formation of **9**-Nb + NH_3 at elevated temperatures.

By ^1H NMR spectroscopy solutions of **10**-Nb contain negligible amounts of **9**-Nb at 25 °C, so the UV-visible data acquired at 25 °C can be assumed to represent pure **10**-Nb. Using absorption data measured at 630 nm, the concentration of **10**-Nb at each temperature was estimated. With the assumption that all **10**-Nb lost converted to **9**-Nb and NH_3, the concentrations of **9**-Nb and NH_3 were also calculated, along with a corresponding equilibrium constant K_{eq} at each temperature (Figure 1.13). It should be noted that the data acquired near or above the boiling point of benzene (80.1 °C)

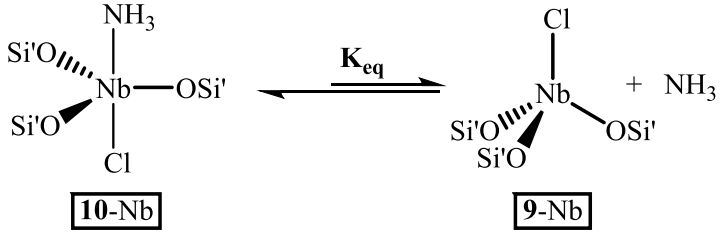

Temp. (°C)	[**10**-Nb] x 10^3 (M)	[**9**-Nb] x 10^4 (M)	K_{eq} x 10^5 (M^{-1})
25	1.26 (13)	0	----------
35	1.23 (12)	0.31 (3)	0.077 (13)
45	1.19 (12)	0.74 (7)	0.46 (8)
55	1.15 (11)	1.17 (12)	1.20 (2)
65	1.01 (11)	1.65 (17)	2.49 (4)
70	1.07 (11)	1.94 (19)	3.50 (6)
75	1.06 (11)	2.01 (20)	3.79 (7)
80	1.04 (10)	2.23 (22)	4.77 (8)
90	1.01 (10)	2.58 (26)	6.64 (11)

Figure 1.13. Selected parameters extracted from UV-visible data at 630 nm for the equilibrium between **10**-Nb and **9**-Nb + NH_3.

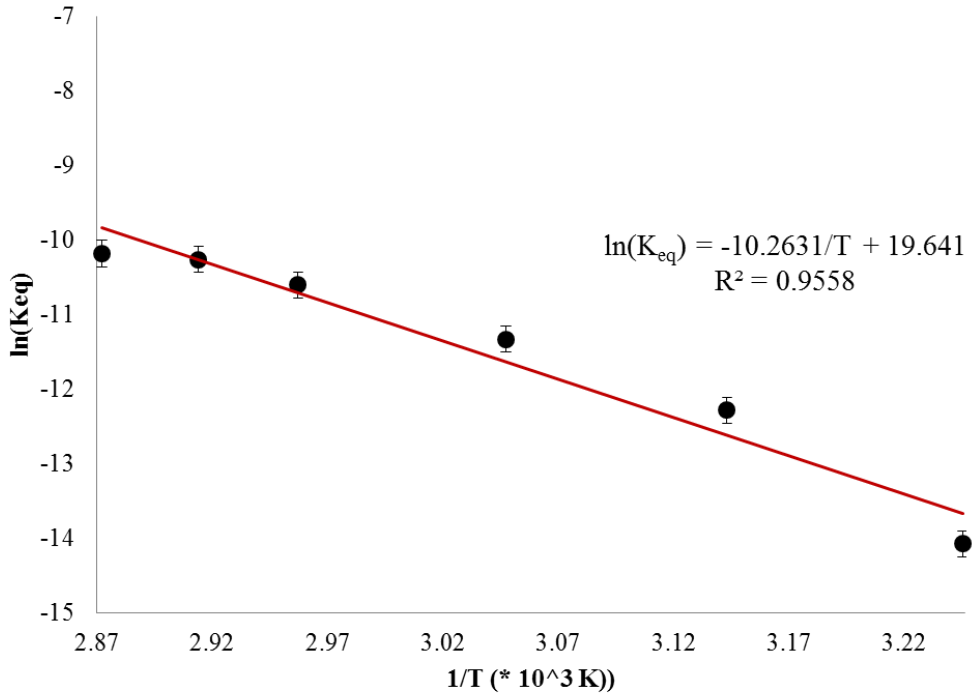

Figure 1.14. Van't Hoff plot for the formation of **9**-Nb and NH_3 from **10**-Nb.

are somewhat suspect. Although UV-visible data were collected in a sealed cuvette, vaporization of solvent could potentially skew the data. Given this, a plot of $\ln(K_{eq})$ vs. 1/T from 35 °C to 75 °C allowed for extraction of thermodynamic parameters (Figure 1.14). For the reaction of **10**-Nb to form **9**-Nb and NH_3, ΔH was determined to be 20.4 ± 2.3 kcal/mol and ΔS was determined to be 39 ± 7 e.u. The enthalpy of reaction is on par with what might be expected for reactions of this sort, but ΔS is fairly high, even when taking into account the conversion of one molecule of reactant to two products. Trigonal bipyramidal **10**-Nb is quite sterically constricted and therefore highly ordered. Loss of NH_3 to form **9**-Nb then relieves some steric rigidity, resulting in a ΔS larger than expected.

The IR data for **10**-Nb show characteristic broad N-H absorptions centered at 3376 cm^{-1}. When **10**-$NbND_3$ was synthesized from **1**-PMe_3 and ND_3, the absorptions

shifted to lower energies centered at 2518 cm^{-1} (Figure 1.15), in line with the expected energy shift upon isotopic labelling.

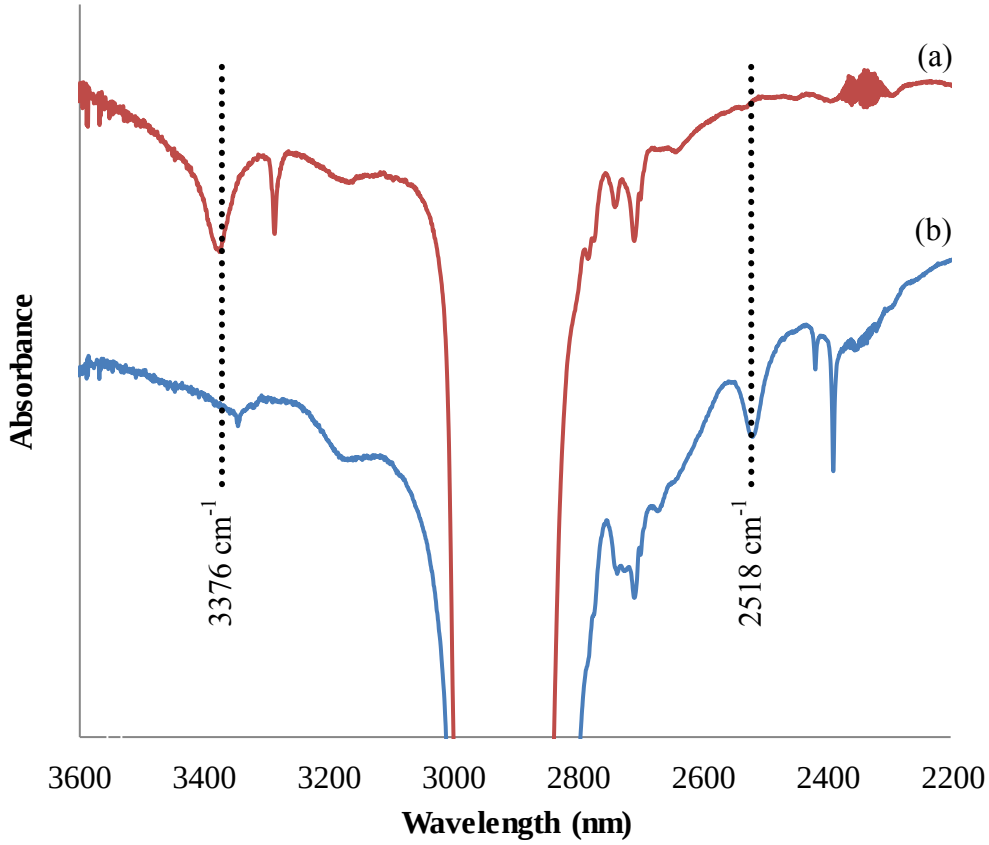

Figure 1.15. IR spectra of **10**-Nb (a) and **10**-$NbND_3$ (b), prepared as Nujol mulls between $CaCl_2$ plates.

Attempts at further reduction of **10**-Nb to transiently synthesize $(silox)_3NbNH_3$, which could then undergo oxidative addition/1,2-H_2-elimation to generate $(silox)_3Nb{=}NH$, were largely unsuccessful. Treatment of **10**-Nb with KC_8, Na(Hg), or NaK resulted in intractable reaction mixtures, with formation of H(silox) and K(silox) alongside a host of unidentified silox-containing decomposition products, much like the direct reaction of $(silox)_3Nb^{III}$ starting materials with NH_3. As it is difficult to imagine that facile N-H oxidative addition to Nb^{III} does not occur, and

hydrogen is *not* observed in these reaction mixtures, it is likely that $(silox)_3Nb(H)(NH_2)$ forms transiently and undergoes rapid unspecific degradation to produce the intractable reaction mixtures.

Conclusion

It was determined that formation of $(silox)_3Nb{=}C{=}C{=}O$ (**3**-Nb) and $[(silox)_3Nb]_2(\mu\text{-}C_2)$ (**4**-Nb) with concomitant formation of $(silox)_3Nb{=}O$ (**2**-Nb) occurred as observed in these laboratories for the analogous $(silox)_3Ta$ systems, but the chemistry was not as clean as that for tantalum. Instead, upon synthesis of **4**-Nb, a μ-CO byproduct was formed in varying amounts. Spectroscopic, magnetochemical, and computational techniques have been employed to study these compounds, and a theoretical study of the thermodynamics of dicarbide formation was carried out to determine that formation of **4**-Nb was thermodynamically more favorable than formation of the analogous **4**-Ta.

It was discovered that synthesis of a dinitrogen-bridged niobium compound, $(silox)_3NbNNNb(silox)_3$ (**8**-Nb) was possible through treatment of $(silox)_3NbPMe_3$ with elemental potassium. Although the fate of the reducing equivalent is as of yet unknown, it was discovered that K^0 was necessary for the reaction to occur. Analogous reactivity was not seen for $(silox)_3Ta$, presumably due to a greater HOMO-LUMO gap observed for third row transition metals as compared to second row transition metals. Unfortunately, protonation of **8**-Nb did not result in production of nitrogen-derived products such as hydrazine or ammonia. Study of the reverse reaction, formation of **8**-Nb through reaction of $(silox)_3Nb^{III}$ starting materials with ammonia, were unsuccessful, but the ammonia adduct $(silox)_3Nb^{IV}(NH_3)Cl$ (**10**-Nb) was synthesized, isolated, and characterized. Variable-temperature UV-visible spectroscopy was used to determine thermodynamic parameters of NH_3 binding (ΔH = 20.4 ± 2.3 kcal/mol; ΔS = 39 ± 7 e.u.).

Experimental

General Considerations. All manipulations of air sensitive materials were performed using glove box and high vacuum techniques under an inert atmosphere. Hydrocarbon and ethereal solvents were refluxed over sodium and vacuum transferred from sodium benzophenone ketyl (with 3–6 mL tetraglyme/L added to hydrocarbons). Benzene-d_6 was heated to reflux over sodium to dry and vacuum transferred from freshly cut sodium prior to use. THF-d_8 was dried over sodium and vacuum transferred from sodium benzophenone ketyl. All glassware was oven dried for a minimum of 4 h. NMR tubes for sealed tube experiments and glass bombs were flame dried under dynamic vacuum prior to use. $(silox)_3Ta$ (**1**-Ta), $(silox)_3NbPMe_3$ (**1**-$NbPMe_3$), $(silox)_3NbO$ (**2**-Nb),[99] $[(silox)_3Nb(\mu\text{-}C_6H_6)]_2$ (**7**-Nb),[104] have been described previously. CO and CO_2 (Matheson) were dried via passage through dry ice traps and NH_3 was dried over Na^0 prior to use.

^1H, $^{13}C\{^1H\}$, ^{13}C, $^{31}P\{^1H\}$, and ^{93}Nb NMR spectra were obtained on Varian INOVA 400, Varian INOVA 500, Varian Mercury 300, and Bruker ARX 300 spectrometers, and chemical shifts are reported relative to benzene-d_6 (^1H, δ 7.15; $^{13}C\{^1H\}$, δ 128.00), THF-d_8 (^1H, δ 3.58; $^{13}C\{^1H\}$, δ 67.57), external VCl_5 (^{93}Nb, δ 0.00), or external H_3PO_4 (^{31}P, δ 0.00). IR spectra were recorded on a Mattson FT-IR, Perkin-Elmer 299B grating IR, or PE 377 grating IR. Raman spectra were recorded on a Renishaw InVia Confocal Raman microscope with a 785 nm laser. UV-visible spectra were obtained on a Cary 60 UV/Vis spectrometer. Elemental analyses were performed by Complete Analysis Laboratories, Inc., Parsippany, New Jersey, or by the

laboratory of Professor Karsten Meyer, University of Erlangen – Nuremberg, Department of Chemistry & Pharmacy, Egerlandstr. 1, D-91058 Erlangen, Germany.

Small pot reactions: general. For the reactions shown in Eq. 1.6 – 1.13, small pot and NMR tube scale reactions were employed. For small pot reactions, the Nb-containing reagent and any solid substrate were loaded into a round bottom flask (typically a 10 or 25 mL) equipped with a stir bar, and fitted with either a calibrated gas bulb or a needle valve adapter. Solvent was distilled into the flask on the vacuum line, and gases were then admitted to the attached bulb at the prescribed pressure.

NMR tube scale reactions: general. An NMR tube was loaded with solid reagents (sometimes deuterated solvent was added at this point, typically 0.4 mL) in a N_2 glove box and attached to either a calibrated gas bulb or needle valve adapter (14/20 joints). Deuterated solvent was distilled into the tube on the vacuum line, and gases were admitted via the vacuum line or via the attached bulb. The tube was sealed with a torch and monitored.

Synthesis. 1. Formation of $(silox)_3NbCCNb(silox)_3$ (4-Nb) and $(silox)_3NbO$ (2-Nb). To a 25 mL flask charged with $(silox)_3NbPMe_3$ (**1**-$NbPMe_3$, 550. mg, 0.675 mmol) was added 10 mL of toluene at −78 °C. The flask was warmed to 23 °C and opened to a calibrated gas bulb containing CO (0.337 mmol, 0.50 equiv). The initial blue color discharged to give a dark purple-brown precipitate within 1 h. After stirring an additional 8 h at 25 °C, the mixture was evaporated to dryness to yield a pale purple powder. The solid was slurried in 10 mL benzene and filtered to separate the purple solid from an orange-brown solution. The solid was washed with six 8 mL portions of benzene, dried *in vacuo*, and collected to give 210. mg of material (42%

based on Nb; **4**-Nb and **5**-Nb, see text). Raman: ν(C=C/^{13}C=^{13}C) = 1612/1555 cm^{-1}. Crystals of [(silox)$_3$Nb]$_2$(μ-C$_2$) used for X-ray analysis were obtained from benzene heated to reflux for 1 day. The filtrate was concentrated to dryness to give 243 mg of brown solid (49% based on Nb; **2**-Nb).

2. Formation of (silox)$_3$NbCCO (3-Nb) and (silox)$_3$NbO (2-Nb). A 35 mL glass bomb reactor containing (silox)$_3$NbPMe$_3$ (**1**-NbPMe$_3$, 200. mg, 0.245 mmol) and 10 mL toluene at 77 K was exposed to 1 atm CO. While the solution was warmed to −78 °C over 2 h, a color change from navy blue to deep red was observed. After warming to 23 °C and stirring an additional 12 h, the resulting yellow-brown solution was concentrated to dryness. ^{1}H NMR ((silox)$_3$NbCCO, C$_6$D$_6$) δ 1.26. ^{93}Nb NMR ((silox)$_3$NbCCO, C$_6$D$_6$) δ -652.8. ^{93}Nb NMR ((silox)$_3$NbO, C$_6$D$_6$) δ -947.1. IR (Nujol) ν(^{12}C^{12}CO) = 2068, 2053; ν(^{13}C^{12}CO) = 2057, 2042; ν(^{12}C^{13}CO) = 2013, 1999; ν (^{13}C^{13}CO) = 2003, 1987 cm^{-1}. IR (toluene) ν(^{12}C^{12}CO) = 2063, ν(^{13}C^{12}CO) = 2053, ν(^{12}C^{13}CO) = 2010, ν (^{13}C^{13}CO) = 1999 cm^{-1}.

3. Alternative preparation of [(silox)$_3$Nb]$_2$(μ-C$_6$H$_6$) (7-Nb). A 25 mL flask was charged with (silox)$_3$NbPMe$_3$ (**1**-NbPMe$_3$, 196 mg, 0.240 mmol) and attached to a 180° needle valve. Benzene (10 mL) was vacuum transferred into the flask at −78 °C and the resulting purple solution was heated to 50 °C for 1.5 h while stirring, during which the initial purple color was discharged and formation of a brown precipitate was observed. Benzene was removed under vacuum, and the resulting brown solid was triturated twice with 10 mL portions of pentane, slurried in 2 mL pentane, and filtered to yield **7**-Nb as a brown solid (85 mg, 45%).

4. Carbonylation of [(silox)$_3$Nb]$_2$(μ-C$_6$H$_6$) (7-Nb). A 35 mL glass bomb reactor was charged with [(silox)$_3$Nb]$_2$(μ-C$_6$H$_6$) (**7**-Nb, 75 mg, 0.048 mmol) and 3 mL toluene. The solution was freeze-pump-thaw degassed three times and exposed to 280 torr CO (1.0 equiv). The bomb was sealed, heated to 50 °C for 14 h, then 90 °C for 7 h. Volatiles were removed under vacuum, and the remaining brown solid was taken up in 4 mL pentane, filtered, and washed twice with 2 mL pentane to afford 40. mg (55% as **5**-Nb). IR (Nujol) 1208 cm^{-1}.

5. Small pot example: CO/^{13}CO labeling study. A 25 mL flask containing (silox)$_3$NbPMe$_3$ (**1**-NbPMe$_3$, 50. mg, 0.061 mmol) and toluene (5 mL) was attached to two calibrated gas bulbs containing CO (0.015 mmol, 0.25 equiv) and ^{13}CO (0.015 mmol, 0.25 equiv). The two gas bulbs were opened to each other and the gas was allowed to effuse for 10 h. The flask was opened to the gas bulbs, and the initial blue color discharged over 2 h to give a dark brown precipitate. After stirring an additional 8 h at 23 °C, toluene was removed *in vacuo*. The resulting solid was taken up in 3 mL benzene, filtered, and washed with three 2 mL portions of benzene. The solid obtained from removal of the solvent from the filtrate was assayed as isotopologues of **3**-Nb, and the insoluble purple-brown precipitate was assayed as **4**-Nb and **5**-Nb.

6. NMR studies to find J_{NbC} in (silox)$_3$NbCCO (3-Nb). An NMR tube sealed to a 14/20 joint was charged with (silox)$_3$NbPMe$_3$ (**1**-NbPMe$_3$, 20. mg, 0.025 mmol) and ~0.4 mL toluene-d_8. The tube was attached to a gas bulb (14.5 mL) and the resulting solution was freeze–pump–thaw degassed three times. The gas bulb was charged with 105 torr ^{13}CO, which was admitted into the NMR tube at 77 K. After

sealing with a torch, the tube was allowed to warm to −78 °C overnight to maximize ketenylidene formation. ^{93}Nb NMR data were acquired at 93 °C. ^{1}H NMR ((silox)$_3$NbCCO (**3**-Nb), toluene-d_8) δ 1.26; ^{13}C NMR (toluene-d_8) δ 76.0 (d, J_{CC} = 76 Hz, C*C*O), 31.8 (C(*C*H$_3$)$_3$), 24.5 (*C*(CH$_3$)$_3$); ^{93}Nb NMR (C_6D_6): δ −687 (d, J_{NbC} = 500 Hz).

7. D_2O quench of (silox)$_3$NbCONb(silox)$_3$ (5-Nb). An NMR tube sealed to a 14/20 joint was charged with (silox)$_3$NbCONb(silox)$_3$ (**5**-Nb, 30. mg, 0.020 mmol) and ~0.4 mL C_6D_6. The solution was freeze–pump–thaw degassed and ~0.2 mL D_2O was vacuum transferred to the tube. The NMR tube was heated to 50 °C for 2 h, during which a thick white precipitate formed. NMR spectra were consistent with the formation of ^{t}Bu$_3$SiOH and ^{13}C-methanol-d_4. ^{1}H NMR (C_6D_6) δ 1.08 (^{t}Bu$_3$SiOH); ^{13}C NMR (C_6D_6) δ 23.05 (*C*(CH$_3$)$_3$), 30.10 (C(*C*H$_3$)$_3$), 49.16 (septet, J_{CD} = 18 Hz, D$_3$*C*OD).

8. Formation of (silox)$_3$NbNNNb(silox)$_3$ (8-Nb). *a.* To a 20 mL vial charged with (silox)$_3$NbPMe$_3$ (**1**-NbPMe$_3$, 150. mg, 0.184 mmol) and K^0 (7 mg, 0.2 mmol) in a N_2 glove box was added 10 mL THF at room temperature. The vial was capped and stirred for 4 d, over which the deep purple solution turned brown and a yellow precipitate formed. The solution was filtered and the filtrate was washed three times with 2 mL portions of THF. The yellow power was recrystallized from hot THF to yield bright yellow plates (50. mg, 0.033 mmol, 37%). ^{1}H NMR (THF-d_8): δ 1.21. ^{93}Nb NMR (THF-d_8): δ -570 ($\nu_{1/2}$ ~4500 Hz). Anal. calcd for $C_{72}H_{162}N_2Nb_2O_6Si_6$: C, 57.41%; H, 10.84%; N, 1.86%. Found: C, 55.99%; H, 10.56%; N, 1.74%. *b.* To a 20 mL vial charged with (silox)$_3$NbPMe$_3$ (**1**-NbPMe$_3$, 400. mg, 0.491 mmol) and K^0 (5

mg, 0.1 mmol) in a N_2 glove box was added 10 mL THF at room temperature. The vial was capped and stirred for 8 d, over which the deep purple solution turned brown and a yellow precipitate formed. The solution was filtered and the filtrate was washed three times with 2 mL portions of THF. The yellow power was recrystallized from hot THF to yield bright yellow plates (120. mg, 0.080 mmol, 33%). Anal. calcd for $C_{72}H_{162}N_2Nb_2O_6Si_6$: C, 57.41%; H, 10.84%; N, 1.86%. Found: C, 57.55%; H, 11.01%; N, 1.66%.

9. Formation of (silox)$_3$Nb(NH$_3$)Cl (10-Nb). A 25 ml flask containing (silox)$_3$NbCl (**9**-Nb, 100. mg, 0.129 mmol) was attached to a calibrated gas bulb. Toluene (10 mL was vacuum transferred into the flask at -78 °C and the gas bulb was charged with dry NH_3 (0.13 mmol, 1 equiv). The flask was then opened to the gas bulb at -78 °C and slowly allowed to warm to room temperature while stirring, over which the initial purple color slowly turned pale teal. Stirring was maintained for 2 h, and toluene was removed *in vacuo*. The crude mixture was washed with two 2 mL portions of Et_2O and crystallized from Et_2O to yield turquoise needles of **10**-Nb (80. mg, 0.10 mmol, 77%). ^{1}H NMR (THF-d_8): δ 1.79 ($\nu_{1/2}$ =13 Hz). ^{13}C NMR (THF-d_8): δ 39.73 ($\nu_{1/2}$ =3 Hz, C(*C*H$_3$)$_3$), 30.29 ($\nu_{1/2}$ =2 Hz, *C*(CH$_3$)$_3$). ^{1}H NMR (C_6D_6): δ 1.86 ($\nu_{1/2}$ = 15 Hz). Anal. calcd for $C_{36}H_{84}ClNNbO_3Si_3$: C, 54.62%; H, 10.10%; N, 1.77%. Found: C, 55.48%; H, 10.67%; N, 1.51%.

Calculations. Calculations were performed on full silox models using the Gaussian09 code.[107] Density functional theory (DFT), specifically the BLYP functional, was utilized for the quantum portion of all calculations described herein, this choice being motivated by previous research with related complexes.

The transition metals and heavy main group atoms (Si and P) were described with the Stevens effective core potentials (ECPs) and attendant valence basis sets (VBSs).[108] This scheme, dubbed CEP-121G, entails a valence triple zeta description for both transition metals and heavy main group elements (viz S and P). For the latter, polarization and diffuse functions are added to improve the valence description of these elements. The 6–311+G(d) all-electron basis set was used to describe C, H, and O atoms.

These full silox models are studied using hybrid quantum mechanics/molecular mechanics (QM/MM) techniques with the ONIOM methodology.[109] The QM region consisted of the transition metal, the O and Si atoms of the silox group, and any pertinent ligands such as C, C_2, PMe_3, etc. The QM level of theory employed is that just described. The *tert*-butyl groups of silox are modeled with the Universal Force Field (UFF).[110]

Full geometry optimizations were employed without any symmetry constraint. All of the resultant stationary points were characterized as true minima (i.e., no imaginary frequencies) via calculation of the energy Hessian. Enthalpic and entropic corrections to the total electronic energy were calculated using harmonic vibrational frequencies determined at the same level of theory employed for geometry optimization, and are calculated at 1 atm and 298.15 K using unscaled vibrational frequencies. Closed- and open-shell species were described with the restricted and unrestricted Kohn–Sham formalisms, respectively, with no evidence of spin contamination for the latter.

Single-Crystal X-ray Diffraction Studies. Upon isolation, crystals were covered in polyisobutenes and placed under a 173 K N_2 stream on the goniometer head of a Siemens P4 SMART CCD area detector (graphite-monochomated Mo Kα radiation, λ = 0.71073 Å). The structures were solved by direct methods (SHELXS). All non-hydrogen atoms were refined anisotropically unless otherwise stated, and hydrogen atoms were treated as idealized contributions (Riding model).

Crystal data for (silox)$_3$NbCCNb(silox)$_3$ (4-Nb). A purple plate measuring 0.25 x 0.10 x 0.05 mm^3 was obtained from a hot benzene solution. $C_{74}H_{162}Nb_2O_6Si_6$, M = 1502.40, Triclinic, P-1, a = 12.9421(7), b = 16.1735(9), c = 21.2969(11)Å, α = 75.271(2)°, β = 87.305(2)°, γ = 88.024(2)°, V = 4305.4(4) Å^3, T = 173(2), Z = 2, R_{int} = 0.0608, 68634 reflections, 18766 independent, R_1(all data) = 0.0747, wR_2 = 0.1191, GOF = 1.014. The electron density of the bridging atoms and corroborative IR data suggested that **3**-Nb and **5**-Nb were incorporated in the crystal (see text).

Crystal data for (silox)$_3$NbNNNb(silox)$_3$ (8-Nb). A yellow plate measuring 0.40 x 0.30 x 0.15 mm^3 was obtained from a hot THF solution. $C_{72}H_{162}N_2Nb_2O_6Si_6$, M = 1506.40, Orthorhombic, C222(1), a = 22.6485(9), b = 24.6140(10), c = 17.3420(6) Å, $\alpha = \beta = \gamma$ = 90°, V = 9667.6(6) Å^3, T = 193(2), Z = 4, R_{int} = 0.0465, 37004 reflections, 9828 independent, R_1(all data) = 0.0401, wR_2 = 0.0846, GOF = 1.036.

REFERENCES

1. Lewis, N. S.; Nocera, D. G. *Proc. Natl. Acad. Sci.* **2006,** *103,* 15729 – 15735.

2. Annual Energy Outlook 2014 with projections to 2040, U.S. Energy Information Administration (EIA), U.S. Department of Energy, December 16, 2013.

3. Deffeyes, K. S.; Beyond Oil: The View from Hubbert's Peak, Hill and Wang, New York, 2005.

4. Deffeyes, K. S.; Hubbert's Peak: The Impending World Oil Shortage, Princeton University Press, Princeton, New Jersey, 2001.

5. Simmons, M. R.; Twilight in the Desert; The Coming Saudi Oil Shock and the World Economy, John Wiley & Sons, Hoboken, New Jersey, 2005.

6. Huber, P. W.; Mills, M. P.; The Bottomless Well: The Twilight of Fuel, the Virtue of Waste, and Why We Will Never Run Out of Energy, Basic Books, New York, 2005.

7. World Energy Outlook 2012: Executive Summary, International Energy Agency, 2012.

8. Nocera, D. G. On the future of global energy, *Daedalus* **2006,** *135*, 112 – 115.

9. Rostrup-Nielsen, J. R.; Sehested, J.; Nørskov, J. K.; *Adv. Catal.* **2002,** *47*, 65 – 139.

10. Ferreira-Aparicio, P.; Benito, M. J.; Sanz, J. L. *Catal. Rev. Sci. Eng.* **2005,** *47*, 491 – 588.

11. The Hydrogen Economy: Opportunities, Costs, Barriers, and R&D Needs, National Academy of Engineering, National Academies Press, Washington, DC, 2004.

12. Hu, Y. H.; Ruckenstein, E. *Adv. Catal.* **2004,** *48*, 297 – 345.

13. Van Der Laan, G. P.; Beenackers, A. A. C. M. *Catal. Rev. Sci. Eng.* **1999,** *41*, 255 – 318.

14. Bromfield, T. C.; Vosloo, A. C. *Macromol. Symp.* **2003,** *193*, 29 – 34.

15. Chen, J. Q.; Bozzano, A.; Glover, B.; Fuglerud, T.; Kvisle, S. *Catal. Today* **2005,** *106*, 103 – 107.

16. Shen, J.; Schmetz, E.; Kawalkin, G. J.; Steigel, G. J.; Noceti, R. P.; Winslow, J. C.; Kornosky, R. M.; Krastman, D.; Venkataraman, V. K.; Driscoll, D. J.;

Cicero, D. C.; Haslebacher, W. F.; Hsieh, B. C. B.; Jain, S. C.; Tennant, J. B. *Top. Catal.* **2003,** *26*, 13 – 16.

17. Jessop, P. G.; Joó, F.; Tai, C. C. *Coord. Chem. Rev.* **2004,** *248*, 2425 – 2442.

18. Tanaka, K.; Ooyama, D. *Coord. Chem. Rev.* **2002,** *226*, 211 – 218.

19. Yin, X.; Moss, J. R. *Coord. Chem. Rev.* **1999,** *181*, 27 – 59.

20. Benson, E. E.; Kubiak, C. P.; Sathrum, A. J.; Smieja, J. M. *Chem. Soc. Rev.* **2009,** *38*, 89 – 99.

21. Matsuo, T.; Kawaguchi, H. *J. Am. Chem. Soc.* **2006,** *128*, 12362 – 12363.

22. Chatani, N.; Shinohara, M.; Ikeda, S.; Murai, S. *J. Am. Chem. Soc.* **1997,** *119*, 4303 – 4304.

23. Laitar, D. S.; Mueller, P.; Sadighi, J. P. *J. Am. Chem. Soc.* **2005,** *127*, 17196 – 17197.

24. Berthet, J. -C.; Ephritikhine, M. *New J. Chem.* **1992,** *16*, 767.

25. Rankin, M. A.; Cummins, C. C. *J. Am. Chem. Soc.* **2010,** *132*, 10021 – 10023.

26. Hanna, T.; Baranger, A.; Bergman, R. G. *J. Am. Chem. Soc.* **1995,** *117*, 11363 – 11364.

27. Silvia, J. S.; Cummins, C. C. *J. Am. Chem. Soc.* **2010,** *132*, 2169 – 2171.

28. Castro-Rodriguez, I.; Meyer, K. *J. Am. Chem. Soc.* **2005,** *127*, 11242 – 11243.

29. Lam, O. P.; Bart, S. C.; Kameo, H.; Heinemann, F. W.; Meyer, K. *Chem. Commun.* **2010,** *46*, 3137 – 3139.

30. Fullmer, B. C.; Fan, H.; Pink, M.; Caulton, K. G. *Inorg. Chem.* **2008,** *47*, 1865 – 1867.

31. Whited, M. T.; Grubbs, R. H. *J. Am. Chem. Soc.* **2008,** *130*, 5874 – 5875.

32. Allen, O. R.; Dalgarno, S. J.; Field, L. D. *Organometallics* **2008,** *27*, 3328 – 3330.

33. Lee, C. H.; Laitar, D. S.; Müller, P.; Sadighi, J. P. *J. Am. Chem. Soc.* **2007,** *129*, 13802 – 13803.

34. Tardif, O.; Hashizume, D.; Hou, Z. *J. Am. Chem. Soc.* **2004,** *126*, 8080 – 8081.

35. Lu, C. C.; Saouma, C. T.; Day, M. W.; Peters, J. C. *J. Am. Chem. Soc.* **2007,** *129,* 4 – 5.

36. Savéant, J. -M. *Chem. Rev.* **2008,** *108,* 2348 – 2378.

37. Raebiger, R. J.; Turner, J. W.; Noll, B. C.; Curtis, C. J.; Miedaner, A.; Cox, B.; DuBois, D.L. *Organometallics* **2006,** *25,* 3345 – 3351.

38. Simón-Manso, E.; Kubiak, C. P. *Organometallics* **2005,** *24,* 96 – 102.

39. Hayashi, H.; Ogo, S.; Abura, T.; Fukuzumi, S. *J. Am. Chem. Soc.* **2003,** *125,* 14266 – 14267.

40. Grodkowski, J.; Neta, P.; Fujita, E.; Mahammed, A.; Simkhovich, L.; Gross, Z. *J. Phys. Chem. A* **2002,** *106,* 4772 – 8381.

41. LaPointe, R. E.; Wolczanski P. T. *J. Am. Chem. Soc.* **1986,** *106,* 3535 – 3537.

42. Cummins, C. C.; Van Duyne, G. D.; Schaller, C. P; Wolczanski, P. T. *Organometallics* **1991,** *10,* 164 – 170.

43. Wolczanski, P. T.; Bercaw, J. E.; *Acc. Chem. Res.* **1980,** *13,* 121 – 127.

44. Overett, M. J.; Hill, R. O.; Moss, J. R. *Coord. Chem. Rev.* **2000,** *206,* 581 – 605.

45. Miller, R. L.; Wolczanski, P. T.; Rheingold, A. L. *J. Am. Chem. Soc.* **1993,** *115,* 10422 – 10423.

46. Neithamer, D. R.; LaPointe, R. E.; Wheeler, R. A.; Richeson, D. S.; Van Duyne, G. D.; Wolczanski, P. T. *J. Am. Chem. Soc.* **1989,** *111,* 9056 – 9072.

47. Schrock, R. R. *Acc. Chem. Res.* **1979,** *12,* 98 – 104.

48. Schultz, A. J.; Brown, R. K.; Williams, J. M.; Schrock, R. R. *J. Am. Chem. Soc.* **1981,** *103,* 169 – 176.

49. Chamberlin, L.; Rothwell, I. P.; Huffman, J. C. *Ibid.* **1982,** *104,* 7338 – 7340.

50. Wade, L. G.; Organic Chemistry, Pearson Prentice Hall, New Jersey, 2006.

51. Brookes, N. J.; Ariafard, A.; Stranger, R.; Yates, B. F. *Chem. Eur. J.* **2010,** *16,* 8117 – 8132.

52. Wolczanski, P. T. *Chem. Commun.* **2009,** 740 – 757.

53. Wolczanski, P. T. *Polyhedron* **1995,** *14,* 3335 – 3362.

54. Akagi, F.; Suzuki, S.; Ishida, Y.; Hatanaka, T.; Matsuo, T.; Kawaguchi, H. *Eur. J. Inorg. Chem.* **2013,** 3930 – 3936.

55. Akagi, F.; Matsuo, T.; Kawaguchi, H. *Angew. Chem.* **2007**, *119*, 8934 – 8937; *Angew. Chem. Int. Ed.* **2007**, *46*, 8778 – 8781.

56. Kawaguchi, H.; Matsuo, T. *Angew. Chem.* **2002**, *114*, 2916 – 2918; *Angew. Chem. Int. Ed.* **2002**, *41*, 2792 – 2794.

57. Curley, J. J.; Cook, T. R.; Reece, S. Y.; Müller, P.; Cummins, C. C. *J. Am. Chem. Soc.* **2008**, *130*, 9394 – 9405.

58. Figueroa, J. S.; Piro, N. A.; Clough, C. R.; Cummins, C. C. *J. Am. Chem. Soc.* **2006**, *128*, 940 – 950.

59. Mindiola, D. J.; Meyer, K.; Cherry, J.-P. F.; Baker, T. A.; Cummins, C. C. *Organometallics* **2000,** *19*, 1622 – 1624.

60. Laplaza, C. E.; Johnson, M. J. A.; Peters, J. C.; Odom, A. L.; Kim, E.; Cummins, C. C.; George, G. N.; Pickering, I. J. *J. Am. Chem. Soc.* **1996**, *118*, 8623 – 8638.

61. Laplaza, C. E.; Cummins, C. C. *Science* **1995**, *268*, 861 – 863.

62. Solari, E.; Da Silva, C.; Iacono, B.; Hesschenbrouck, J.; Rizzoli, C.; Scopelliti, R.; Floriani, C. *Angew. Chem.* **2001**, *113*, 4025 – 4027; *Angew. Chem. Int. Ed.* **2001**, *40*, 3907 – 3909.

63. Caselli, A.; Solari, E.; Scopelliti, R.; Floriani, C.; Re, N.; Rizzoli, C.; Chiesi-Villa, A. *J. Am. Chem. Soc.* **2000**, *122*, 3652 – 3670.

64. Zanotti-Gerosa, A; Solari, E.; Giannini, L.; Floriani, C.; Chiesi-Villa, A.; Rizzoli, C. *J. Am. Chem. Soc.* **1998,** *120*, 437 – 438.

65. Shaver, M. P.; Fryzuk, M. D. *J. Am. Chem. Soc.* **2005,** *127*, 500 – 501.

66. Morello, L.; Yu, P.; Carmichael, C. D.; Patrick, B. O.; Fryzuk, M. D. *J. Am. Chem. Soc.* **2005**, *127*, 12796 – 12797.

67. MacKay, B. A.; Patrick, B. O.; Fryzuk, M. D. *Organometallics* **2005,** *24*, 3836 – 3841.

68. Fryzuk, M. D.; Kozak, C. M.; Bowdridge, M. R.; Patrick, B. O.; Rettig, S. J. *J. Am. Chem. Soc.* **2002**, *124*, 8389 – 8397.

69. Nikiforov, G. B.; Vidyaratne, I.; Gambarotta, S.; Korobkov, I. *Angew. Chem.* **2009,** *121*, 7551 – 7555; *Angew. Chem. Int. Ed.* **2009,** *48*, 7415 – 7419.

70. Vidyaratne, I.; Crewdson, P.; Lefebvre, E.; Gambarotta, S. *Inorg. Chem.* **2007**, *46*, 8836 – 8842.

71. Vidyaratne, I.; Scott, J.; Gambarotta, S.; Budzelaar, P. H. M. *Inorg. Chem.* **2007,** *46*, 7040 – 7049.

72. Korobkov, I.; Gambarotta, S.; Yap, G. P. A. *Angew. Chem.* **2003**, *115*, 5108 – 5111; *Angew. Chem. Int. Ed.* **2003**, *42*, 4958 – 4961.

73. Korobkov, I.; Gambarotta, S.; Yap, G. P. A. *Angew. Chem.* **2002,** *114*, 3583 – 3586; *Angew. Chem. Int. Ed.* **2002,** *41*, 3433 – 3436.

74. Tayebani, M.; Feghali, K.; Gambarotta, S. *Organometallics* **1997,** *16*, 5084 – 5088.

75. Jubb, J.; Scoles, L.; Jenkins, H.; Gambarotta, S. *Chem. Eur. J.* **1996**, *2*, 767 – 771.

76. Berno, P.; Gambarotta, S. *Angew. Chem.* **1995**, *107*, 871 – 873; *Angew. Chem. Int. Ed. Engl.* **1995**, *34*, 822 – 824.

77. Hirotsu, M.; Fontaine, P. P.; Epshteyn, A.; Zavalij, P. Y.; Sita, L. R. *J. Am. Chem. Soc.* **2007,** *129*, 9284 – 9285.

78. Hebden, T. J.; Schrock, R. R.; Takase, M. K.; Müller, P. *Chem. Commun.* **2012**, *48*, 1851 – 1853.

79. Clentsmith, G. K. B.; Bates, V. M. E.; Hitchcock, P. B.; Cloke, F. G. N. *J. Am. Chem. Soc.* **1999**, *121*, 10444 – 10445.

80. Rodriguez, M. M.; Bill, E.; Brennessel, W. W.; Holland, P. L. *Science* **2011,** *334*, 780 – 783.

81. Bonanno, J. B.; Wolczanski, P. T.; Lobkovsky, E. B. J. *Am. Chem. Soc.* **1994,** *116*, 11159 – 11160.

82. Chadeayne, A. R.; Wolczanski, P. T.; Lobkovsky, E. B. *Inorg. Chem.* **2004,** *43*, 3421 – 3432.

83. Bonanno, J. B.; Henry, T. P.; Neithamer, D. R.; Wolczanski, P. T.; Lobkovsky, E. B. *J. Am. Chem. Soc.* **1996,** *118*, 5132 – 5133.

84. Covert, K. J.; Neithamer, D. R.; Zonnevylle, M. C.; LaPointe, R. E.; Schaller, C. P.; Wolczanski, P. T. *Inorg. Chem.* **1991,** *30*, 2494 – 2508.

85. Turner, H. W.; Fellmann, J. D.; Rocklage, S. M.; Schrock, R. R.; Churchill, M. R.; Wasserman, H. *J. J. Am. Chem. Soc.* **1980,** *102*, 7809 – 7811.

86. Rocklage, S. M.; Turner, H. W.; Fellmann, J. D.; Schrock, R. R. *Organometallics* **1982,** *2,* 703 – 707.

87. Rocklage, S. M.; Schrock, R. R. *J. Am. Chem. Soc.* **1982,** *104,* 3077 – 3081.

88. Fryzuk, M. D. *Acc. Chem. Res.* **2009,** *42,* 127 – 133.

89. Fryzuk, M. D.; Johnson, S. A.; Patrick, B. O.; Albinati, A.; Mason, S. A.; Koetzle, T. F. *J. Am. Chem. Soc.* **2001,** *123,* 3960 – 3973.

90. Gambarotta, S.; Scott, J. *Angew. Chem., Int. Ed.* **2004,** *43,* 5298 – 5308.

91. Gambarotta, S. J. *Organomet. Chem.* **1995,** *500,* 117 – 126.

92. Chirik, P. J. *Organometallics* **2010,** *29,* 1500 – 1517.

93. Lee, T.-Y.; Wooten, A. J.; Luci, J. J.; Swenson, D. C.; Messerle, L. *Chem. Commun.* **2005,** 5444 – 5446.

94. Dilworth, J. R.; Henderson, R. A.; Hills, A.; Hughes, D. L.; MacDonald, C.; Stephens, A. N.; Walton, D. R. M. *J. Chem. Soc., Dalton Trans.* **1990,** 1077 – 1085.

95. Hulley, E. B.; Bonanno, J. B.; Wolczanski, P. T.; Cundari, T. R.; Lobkovsky, E. B. *Inorg. Chem.* **2010,** *49,* 8524 – 8544.

96. Hulley, E. B. Ph.D. Thesis, Cornell University, Ithaca, NY, 2011.

97. Neithamer, D. R. Ph.D. Thesis, Cornell University, Ithaca, NY, 1989.

98. Zhao, J.; Goldman, A. S.; Hartwig, J. F. *Science* **2005,** *307,* 1080 – 1082.

99. Veige, A. S.; Slaughter, L. M.; Lobkovsky, E. B.; Wolczanski, P. T.; Matsunaga, N.; Decker, S. A.; Cundari, T. R. *Inorg. Chem.* **2003,** *42,* 6204 – 6224.

100. Veige, A. S.; Slaughter, L. M.; Wolczanski, P. T.; Matsunaga, N.; Decker, S. A.; Cundari, T. R. *J. Am. Chem. Soc.* **2001,** *123,* 6419 – 6420.

101. Williams, V. A.; Manke, D. R.; Wolczanski, P. T.; Cundari, T. R. *Inorg. Chim. Acta* **2011,** *369,* 203 – 214.

102. Zhou, M.; Andrews, L. *J. Phys. Chem. A* **1999,** *103,* 7785 – 7794.

103. Colebatch, A. L.; Cordiner, R. L.; Hill, A. F.; Nguyen, K. T. H. D.; Shang, R.; Willis, A. C. *Organometallics* **2009,** *28,* 4394 – 4399.

104. Veige, A. S.; Kleckley, T. S.; Chamberlin, R. L. M.; Neithamer, D. R.; Lee, C. E.; Wolczanski, P. T.; Lobkovsky, E. B.; Glassey, W. V. *J. Organomet. Chem.* **1999,** *591*, 194 – 203.

105. Drago, R. S. *J. Phys. Chem.* **1958,** *62*, 353 – 357.

106. Power, P. P. *Chem. Rev.* **1999,** *99*, 3463 – 3503.

107. Frisch, M. J. *et al.* Gaussian 09, Revision A.1 **2009,** Gaussian, Inc., Wallingford, CT.

108. Stevens, W. J.; Krauss, M.; Basch, H.; Jasien, P. G. *Can. J. Chem.* **1992,** *70*, 612 – 630.

109. Svensson, M.; Humbel, S.; Froese, R. D. J.; Matsubara, T.; Sieber, S.; Morokuma, K. *J. Phys. Chem.* **1996,** *100*, 19357 – 19363.

110. Rappé, A. K.; Casewit, C. J.; Colwell, K. S.; Goddard, W. A.; Skiff, W. M. *J. Am. Chem. Soc.* **1992,** *114*, 10024 – 10035.

Chapter 2

Exploitation of the Redox Non-Innocence Properties of Pseudo Square Planar [{κ^4-$Me_2C(CH_2N{=}CHpy)_2$}M^n

Introduction

A long-standing goal of this laboratory has been to generate complexes of the first-row transition metals featuring supporting ligands that impart a strong field on the metal center. The resulting complexes could potentially facilitate 2-electron chemical processes. During the study of tripodal ligands designed to promote M-C bond formation, a ligand fragmentation was discovered to yield the very stable 1,3-dipyridyl-2-azapropenylide anion (smif) (Eq. 2.1).[1] The protonated ligand, (smif)H,

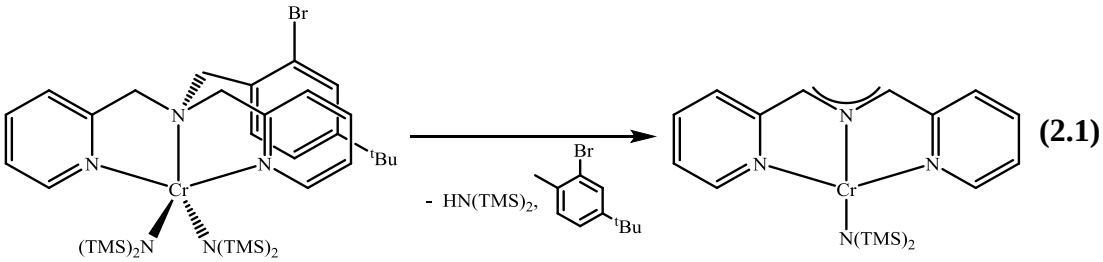

(2.1)

could be synthesized rationally through condensation of 2-picolylamine and pyridine-2-carboxaldehyde in nearly quantitative yields, and treatment with $M(NR_2)_2$ (M = Fe, Cr) precursors afforded the octahedral $(smif)_2M$ complexes. Employment of a variety of synthetic methodologies allowed for preparation of the analogous $(smif)_2M$ (M = V, Mn, Co, Ni) complexes.[2] In particular, $(smif)_2Fe$ was intriguing because of its diamagnetic ground state, indicating that the smif ligand was capable of imparting a strong field on first-row transition metals.

The smif ligand displays reactivity characteristic of both a closed-shell azaallyl

anion and a singlet diradical. For example, $(smif)_2Fe$ reacts with polar substrates such as organic isocyanates through nucleophilic attack by $(smif)_2Fe$ on the isocyanate carbon, characteristic of closed-shell anionic behavior. However, $(smif)FeN(TMS)_2$ and $(^oMe_2Smif)FeN(TMS)_2$ both exist as monomers in solution and undergo reversible dimerization when in the solid-state, indicative of diradical character (Scheme 2.1).[3] This dipolar/diradical character has been often observed in azomethine ylides, and electronic structure calculations have shown that both representations are important contributions to the ground state of the molecule.[4]

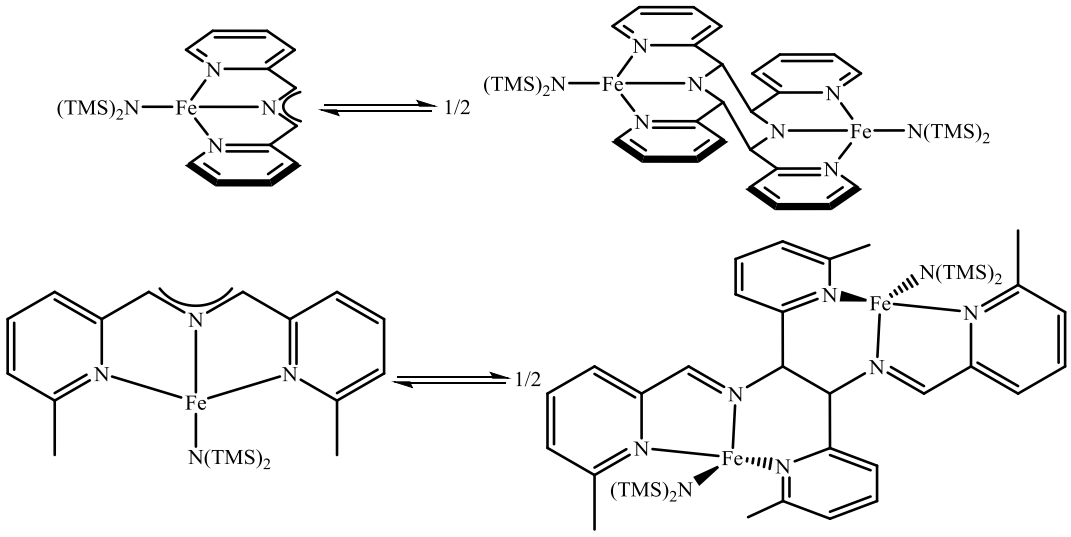

Scheme 2.1. Solid-state dimerization of $(smif)FeN(TMS)_2$ (top) and $(^oMe_2Smif)FeN(TMS)_2$ (bottom).[3]

Simultaneously in this laboratory, through attempts to extend azaallyl chemistry to M-C bond-containing complexes, a series of organometallic iron(III) and iron(II) azaallyl complexes were prepared (Figure 2.1 left, center).[5] Unfortunately, although installation of one aryl-iron bond was facile, the diarylimine azaallyl metal species could not be easily synthesized (Figure 2.1 right), highlighting the importance of an electron-withdrawing group to stabilize the azaallyl fragment.

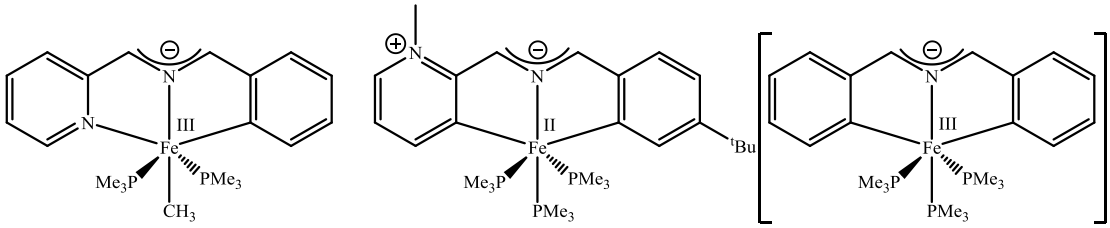

Figure 2.1. Organometallic azaallyl-containing iron(III) (left) and iron(II) (center) complexes, and proposed iron(III) azaallyl complex (right).

A series of pyridine-containing polydentate ligands were designed containing the desired azaallyl architecture, some of which were capable of irreversible C-C coupling. It was shown that treatment of $Me_2C(CH{=}NCH_2Py)_2$ with $M(NR_2)_2$ (M = Cr, Co, Ni) precursors resulted in ligand deprotonation, metallation, and dimerization, concurrent with the formation of three new carbon-carbon bonds (Eq. 2.2).[6] This dimerization yields a formally dianionic ligand framework chelated to two reduced

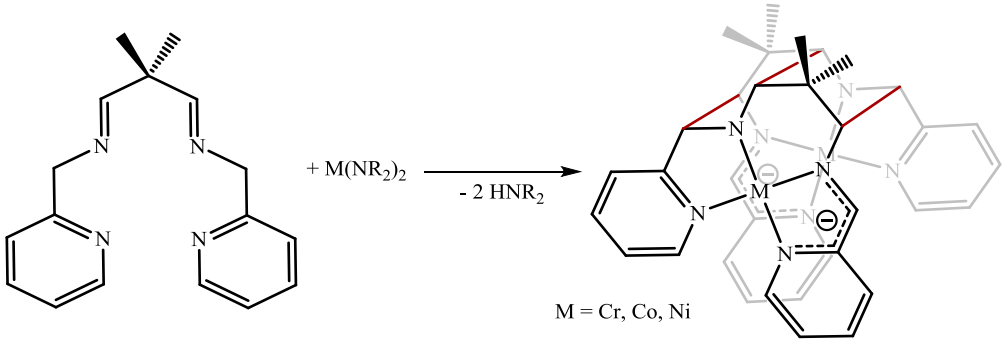

(2.2)

M(I) metal centers. However, pyridine-imine frameworks have been shown to be easily reduced, and metal complexes of these ligands often exhibit structural parameters consistent with one- or two-electron reduced ligands.[7-16] A thorough study on pseudo-tetrahedral $(\alpha\text{-iminopyridine})_2M^{0/+}$ (M = Cr, Mn, Fe, Co, Ni, Zn) has been conducted, and metric parameters for the α-iminopyridine ligand in the 0, -1, and -2 oxidation states have been tabulated (Figure 2.2).[7]

Use of supporting ligands capable of shuttling electrons to and from a metal

center, termed redox non-innocent ligands, has seen widespread use in recent years.[17-20] These ligands have been shown to electronically buffer metal centers,

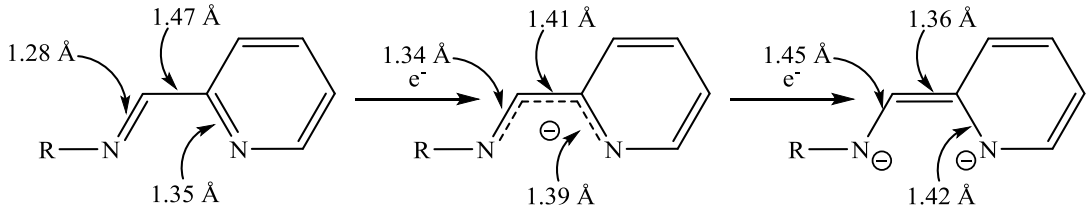

Figure 2.2. Metric parameters of pyridine-imine moieties in the 0 (left), -I (center), and -II (right) oxidation states.[7]

effectively expanding the electron cloud about the metal center. This electronic buffering has been proposed to promote unique reactivity of the first row transition metals, allowing for mediation of formally two-electron processes characteristic of second- and third-row transition metals.[21-53]

In particular, the groups of Chirik and Heyduk have utilized metal complexes supported by redox non-innocent ligands to promote a range of catalytic transformations, including hydrosilylations,[30,34-37] hydroborations,[45-47] hydrogenations,[27,29,31-33] olefin polymerizations,[38-40] [2+2] cycloadditions,[23-25] and

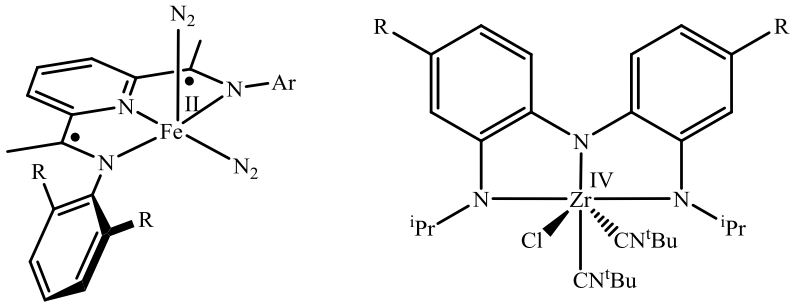

Figure 2.3. Precatalysts developed by Chirik *et al.* (left) and Heyduk *et al.* (right).

group transfer reactions[48-53] (Figure 2.3). In most of these reactions, the redox non-innocence of the supporting ligand has been implicated in key steps of the reaction mechanism.

Similarly, the redox non-innocence of supporting ligands has been implicated in many of the C-C couplings observed by this laboratory. Metric parameters of the C-C coupled metal dimers $[\{Me_2C(CHNCHPy)_2\}M]_2$ (M = Cr, Co, Ni) illustrated in Eq. 2.2 are consistent with a ligand framework containing two singly reduced pyridine imine fragments and two M^{II} centers, and metric parameters of the solid-state $[(^oMe_2Smif)FeN(TMS)_2]_2$ dimer shown in Scheme 2.1 (bottom) are indicative of two metal centers each coupled to a radical anionic pyridine imine fragment.[6]

In attempt to extend the chemistry of $Me_2C(CH=NCH_2Py)_2$ a more readily synthesized chelate, $Me_2C(CH_2N=CHpy)_2$ ($dmp(PI)_2$) was prepared. Unlike the system shown in Eq. 2.2, $dmp(PI)_2$ did *not* undergo metallation and C-C bond formation when treated with various $M(NR_2)_2$ precursors, presumably because initial deprotonation was not as facile. The protons adjacent to the imines in $Me_2C(CH=NCH_2Py)_2$ are fairly acidic (*p*Ka(est) ~ 28), but the corresponding protons adjacent to the imines in $dmp(PI)_2$ are less acidic (*p*Ka(est) ~ 35), rendering the deprotonation more difficult. Instead, a M^0 starting material was chosen in an effort to induce C-H activation to generate the same transient azaallyl fragments, which would then be expected to undergo C-C bond formation.

Synthesis and Electronic Structure Study of $\{dmp(PI)_2^{2-}\}Ni^{II}$ *(**Ni**[0])*[54]

The M^0 precursor $Ni(COD)_2$ (COD = 1,5-cyclooctadiene)[55] was exposed to 1.0 equiv $dmp(PI)_2$ and, rather than the expected C-H activation, formation of a diamagnetic, forest green coordination compound $\{\kappa^4\text{-}Me_2C(CH_2N=CHpy)_2\}Ni^0$ (**Ni**[0]) was observed (Eq. 2.3). **Ni**[0] was fully characterized by ^1H and ^{13}C NMR spectroscopy, and exhibited resonances consistent with the expected C_{2v} symmetry.

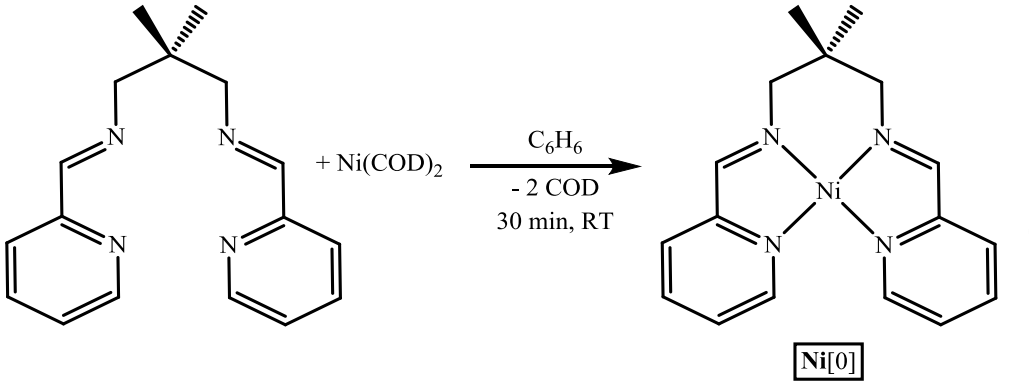

(2.3)

The proton *ortho* to the pyridine nitrogen was shifted significantly downfield (δ 9.29) relative to the free ligand (δ 8.59) and the imine C-H proton was shifted significantly upfield (δ 7.67) relative to the free ligand (δ 8.59). X-ray analysis confirmed the identity of **Ni**[0] and the resulting structure is presented in Figure 2.4 with relevant parameters displayed in Table 2.1. The compound is monomeric, with a distorted square-planar geometry about the metal center. The imine C-N bond lengths (1.303(3)

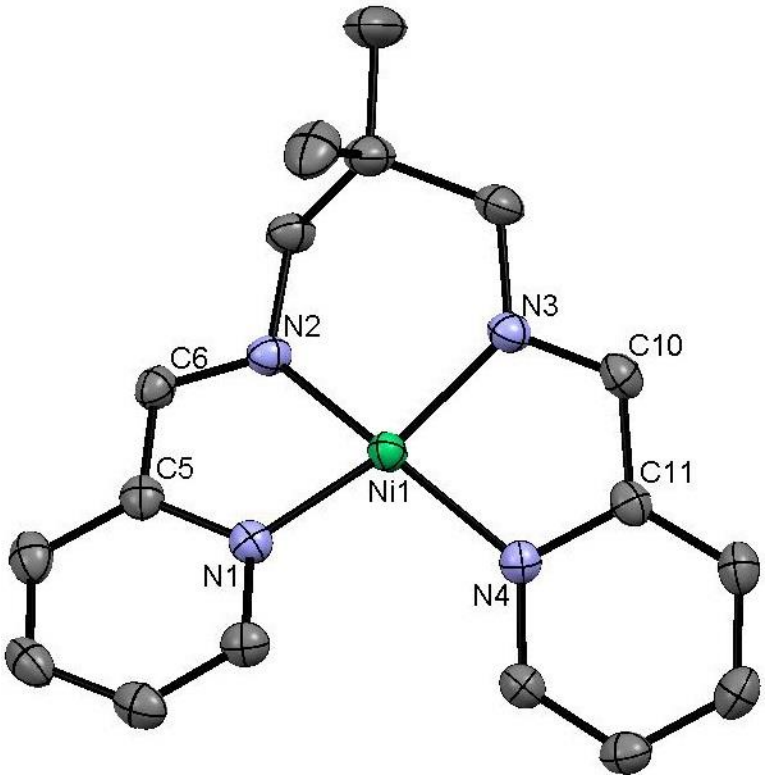

Figure 2.4. Molecular structure of **Ni**[0]. Hydrogens have been omitted for clarity.

Table 2.1: Selected interatomic distances and bond angles for **Ni**-[0].

Selected Bond Distances (Å)		Selected Bond Angles (°)	
Ni1-N1	1.9091(12)	N1-Ni1-N2	79.68(5)
Ni1-N2	1.8670(12)	N2-Ni1-N3	94.67(5)
Ni1-N3	1.8754(12)	N3-Ni1-N4	79.68(5)
Ni1-N4	1.9038(12)	N4-Ni1-N1	104.55(5)
N2-C6	1.3780(18)	N1-Ni1-N3	104.41(5)
C6-C5	1.411(2)	N2-Ni1-N4	89.71(5)
C5-N1	1.3186(18)	N1-N2-N3-N4	33.59(10)
N3-C10	1.3269(19)	(dihedral)	
C10-C11	1.410(2)		
C11-N4	1.3827(18)		

Å ave), imine-pyridine C-C bond lengths (1.411(2) ave) and pyridine C-N bond lengths (1.411(3) Å ave) are consistent with a molecule containing two mono-reduced pyridine-imine fragments (Figure 2.2).[7] The Ni-N bond distances are consistent with a low-spin Ni^{II} complex with a slight chelate twist (N1-N2-N3-N4 (dihedral) = 33.59°) reducing overlap with the torus of d_{z^2} and attenuating its σ^* character.

Based on X-ray crystallography, **Ni**[0] is predicted to possess two noninteracting radical anions on the ligand periphery and a low-spin d^8 metal center, resulting in an S = 1 complex. Experimentally, ^{1}H NMR spectroscopy of **Ni**[0] is indicative of a diamagnetic (S = 0) compound, so to rationalize this discrepancy coupling between the two radical anions must be present. Two mono-reduced ligands of the same symmetry could interact as illustrated in Figure 2.5 (left), where the radical anions are in close spatial proximity and orbital interaction leads to formation of bonding and antibonding orbitals. The two electrons would then pair and reside in the lower-lying bonding orbital, resulting in an S = 0, closed-shell electronic

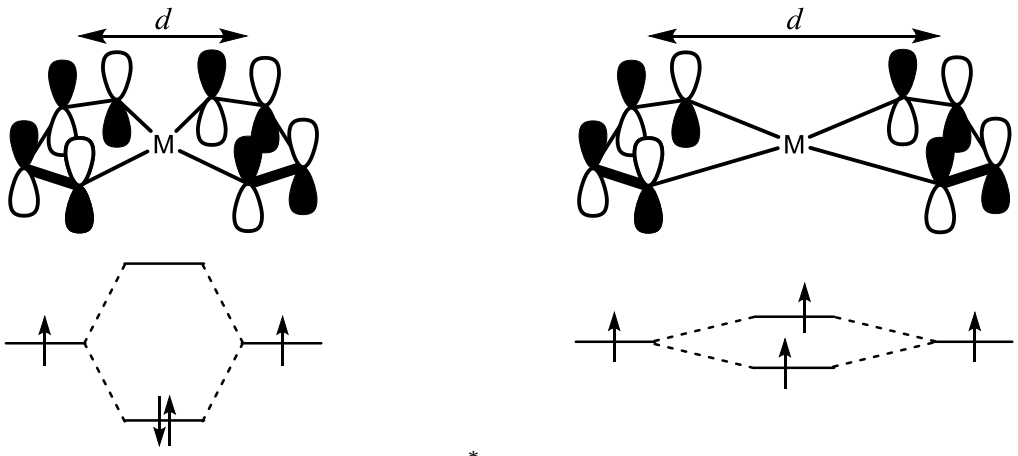

Figure 2.5. Interaction of two ligand π^* orbitals in the limits of large spatial overlap (left) and small spatial overlap (right).[56]

configuration. Alternatively, as the distance between the two ligand orbitals increases the spatial overlap and degree of interaction decreases, resulting in the S = 1 ground state shown in Figure 2.5 (right). The distance between the pyridine imine fragments in **Ni**[0] is large ($d \sim 3$ Å) and favors the latter description, in which the two π^* systems have very little overlap and the electronic structure approaches an open-shell S = 1 configuration.

Due to the large spatial separation between the radical anions in **Ni**[0], an additional interaction must be considered to rationalize the observed S = 0 ground state. Because there are filled metal-based orbitals of appropriate symmetry and energy to interact with the ligand π^* orbitals, the electronic structure of **Ni**[0]cannot be fully described by the simple molecular orbital (MO) depiction shown in Figure 2.5. Instead, as first proposed by Goodenough and Kanamori,[57-59] the interaction of a filled metal orbital spatially located between two half-filled orbitals may lead to the stabilization of an S = 0 ground state. Although the two pyridine imine fragments of **Ni**[0] are likely too spatially separated to interact directly (Figure 2.6 left), the

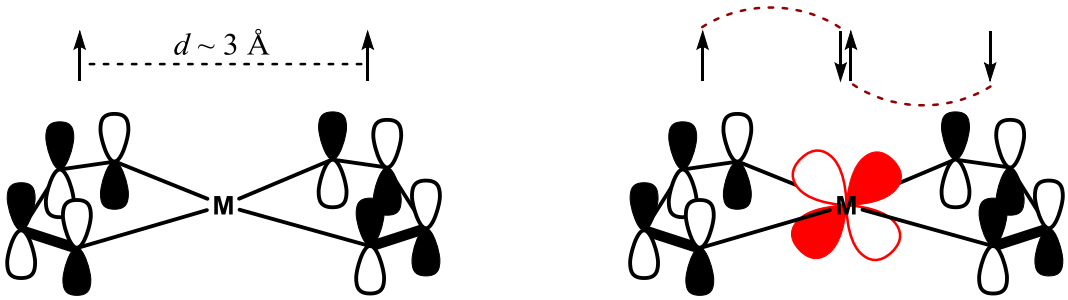

Figure 2.6. Interaction of two spatially separated ligand π^* orbitals in the absence of an intermediate metal orbital (left) and in the presence of a filled metal orbital (right).

presence of an intermediate filled Ni orbital of the correct symmetry facilitates interaction between the two radical anions. One can visualize this interaction as coupling between an unpaired electron on one ligand fragment with a paired electron of opposite spin on the metal center, and coupling of the remaining electron on the metal center with an unpaired electron on the remaining ligand fragment, illustrated by the dashed red lines in Figure 2.6 (right). In this way, coupling between two spatially separated unpaired electrons, termed antiferromagnetic coupling, may be mediated by an intermediate filled metal orbital. It is important to note that this is a valence-bond model, not a MO-based model, and may be applied only when the intermediate orbital is filled.

Broken symmetry (BS) calculations were carried out on **Ni**[0] and are presented in Figure 2.7. BS calculations, in contrast to single-determinant DFT calculations, allow two paired electrons of similar energy to spatially separate into one-electron α and β orbitals localized on different atoms.[60-62] This in turn allows for a single configuration to approximate the electronic structure of complexes with low-lying excited states that would otherwise have to be treated using computationally expensive multi-configuration techniques. In BS solutions, each one-electron orbital

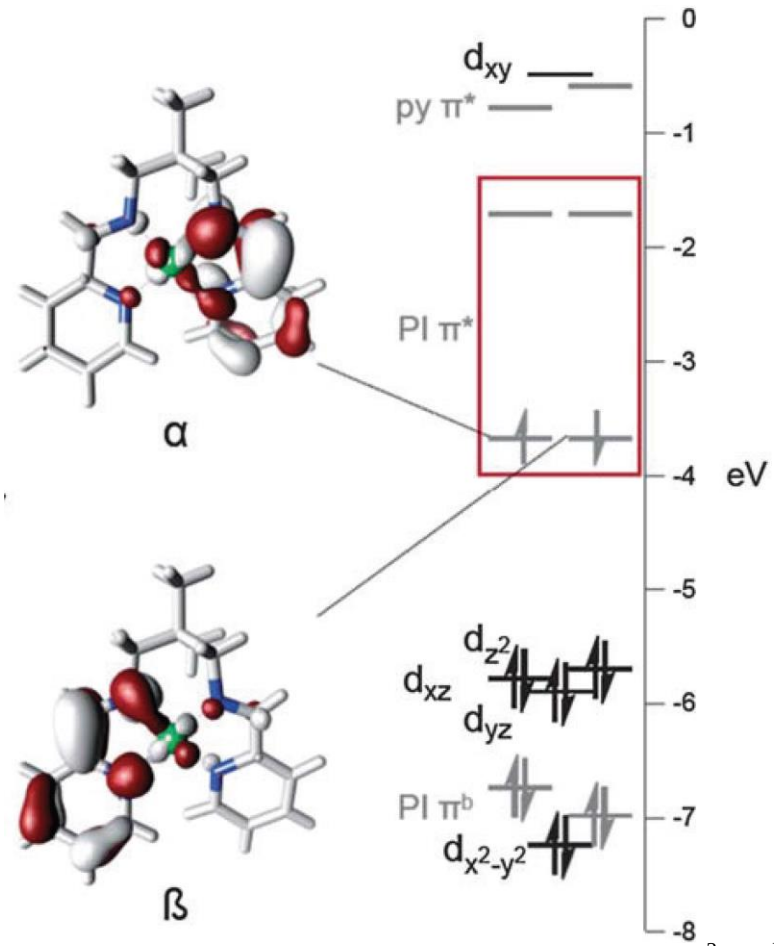

Figure 2.7. Broken Symmetry (BS[1,1]) calculations on $[dmp(PI)_2^{2-}]Ni^{II}$ showing α and β magnetic orbitals with S = 0.497, and a d-orbital splitting diagram infused with critical BS pyridine-imine (PI) based orbitals boxed (red) as α and β sets.

has a different energy and spatial distribution, but often α and β orbitals are quite similar in energy and are very nearly spin-paired. In Figure 2.7, the one-electron α and β orbitals, boxed in red, compose a high-lying ligand-based HOMO containing two pyridine-imine radical anions. The two unpaired electrons are antiferromagnetically coupled, with a coupling constant of J_{cald} = -1499 cm^{-1}. The metal-based orbitals are split as expected for a standard d^8 square planar complex and ligand π^b orbitals within the *d*-block are substantially mixed, indicating a high degree of covalency between metal and ligand.

2.1 Electrochemical Behavior of {dmp$(PI)_2^{2-}$}Ni^{II} (Ni[0])

Cyclic voltammetry studies were carried out on **Ni**[0] and are shown in Figure 2.8. The compound exhibits two reversible waves centered at -1.21 V and -2.28 V *vs.*

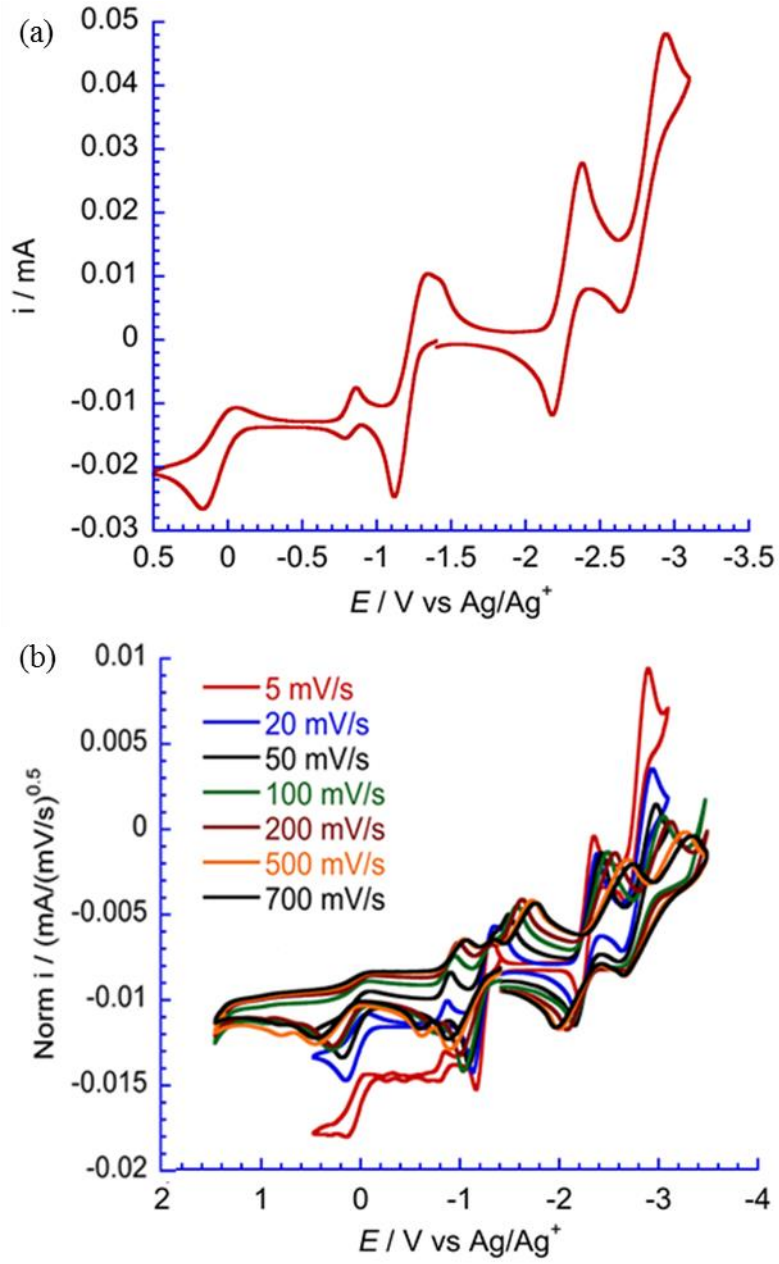

Figure 2.8. Cyclic Voltammettry with a sweep rate of 20 mV/s (a) and variable sweep rates (b) of a 5 mM {dmp$(PI)_2^{2-}$}Ni^{II} / 0.1 M $^{n}Bu_4NPF_6$ / THF solution at a glassy carbon electrode; *vs.* Ag^0/Ag^+.

Ag^0/Ag^+, and two quasi-reversible waves at 0.08 V and -2.77 V, indicating that the compound can be oxidized by two electrons and reduced by two electrons (Figure 2.8a).[63-69] A smaller, reversible wave centered at -0.83 V and an irreversible wave at -1.47 V increased in current with increasing sweep rate (Figure 2.8b) and were observed only after initial oxidation of **Ni**[0], indicating that both features may arise from a compound generated chemically upon oxidation.

2.2 Synthesis and Electronic Structure of $[\{dmp(PI)_2\}Ni]^+$ (Ni[+])

Hulley demonstrated that a one-electron chemical oxidation could be achieved through mixture of **Ni**[0] with 1.0 equiv AgOTf (OTf = OSO_2CF_3) in acetonitrile (Eq. 2.4).[56] The resulting brick red compound was paramagnetic, with a magnetic moment of $\mu_{eff} = 2.1\ \mu_\beta$ (Evan's method),[70,71] and the reversible cyclic voltammetry wave at -1.21 V is attributed to the reaction shown in Eq. 2.4. The solution-state EPR

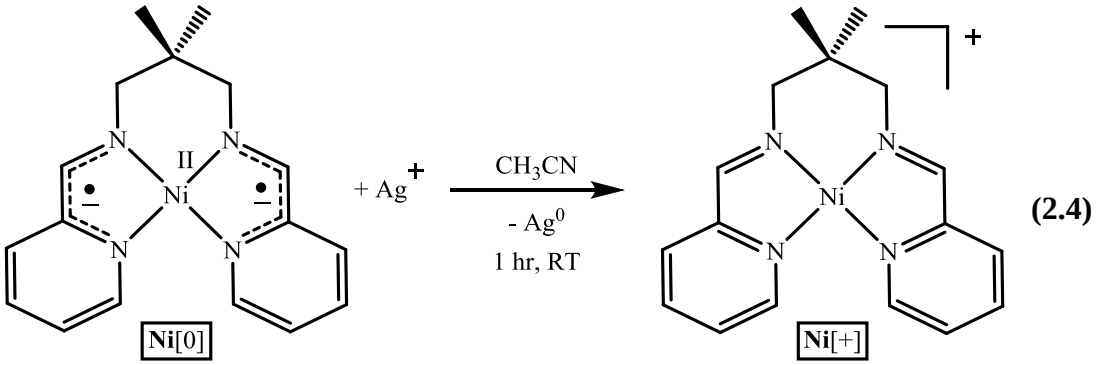

(2.4)

spectrum of **Ni**[+] is shown in Figure 2.9, and a fit of the data revealed a rhombic field with $g_1 = 2.104$, $g_2 = 2.146$, and $g_3 = 2.242$. The average g value of $g_{iso} = 2.164$ is indicative of a Ni-localized unpaired electron, which may be rationalized by three possible electronic configurations. Two potential Ni^{II} d^8 configurations are illustrated in Figure 2.10 (left, center), with either a low-spin Ni^{II} center and a single ligand-

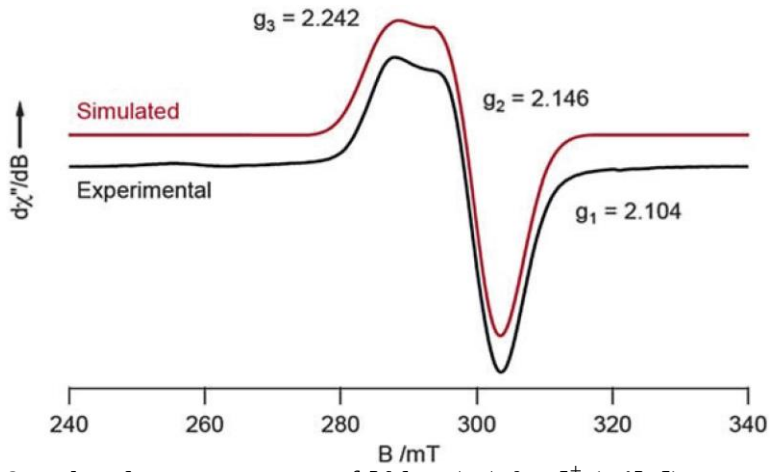

Figure 2.9. X-band EPR spectrum of $[\{dmp(PI)_2\}Ni]^+$ (**Ni**[+]), generated from dissolution of $[\{dmp(PI)_2\}_2Ni^{II}Ni^0]^{2+}$ (**Ni**[2+]**Ni**[0]) in THF glass at 10 K; simulation *via* SPINCOUNT (*g*-strain parameters: $\sigma g_1 = \sigma g_2 = 0.023$, $\sigma g_3 = 0.024$.

based radical anion (Figure 2.10 left) or a high-spin Ni^{II} center and a ligand-based radical anion antiferromagnetically coupled to one of the unpaired electrons on the Ni metal center (Figure 2.10 center). In addition, a Ni^I d^9 configuration is possible, in which the ligand remains neutral (Figure 2.10 right).

Quasi-restricted DFT and *ab initio* (multi-reference) calculations were carried out on the monomeric cation, with the computed electronic structure shown in

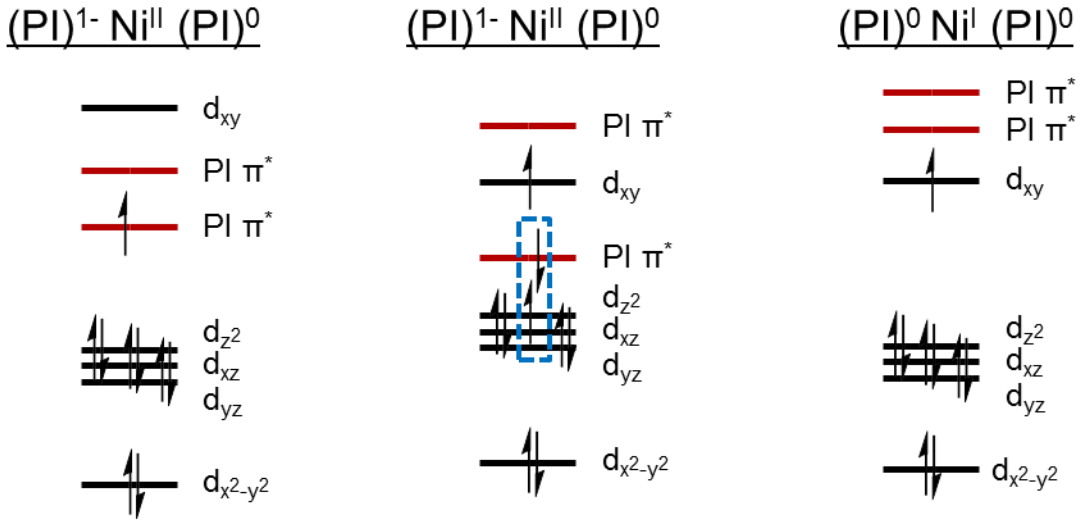

Figure 2.10. Possible electronic configurations of **Ni**[+]. Ligand-based orbitals are shown in red, and antiferromagnetically coupled electrons are indicated by a dashed box (blue).

Figure 2.11. The SOMO is fairly covalent, with a weak interaction between a Ni d_{xy} orbital and the roughly orthogonal ligand π^* system which results in a spin density that is ~50% metal-based and ~50% ligand π^*-based.[72] The configuration shown in Figure 2.11 contributes 70% to the ground state in the multi-reference calculations, and affords EPR *g* values of 2.032, 2.044, and 2.181, in agreement with, but offset from experiment. This primary configuration does not correspond to any of the pure orbital depictions illustrated in Figure 2.10. Instead, the appropriate depiction is a covalent one in which the HOMO is ~50% ligand-based and ~50% metal-based, and the

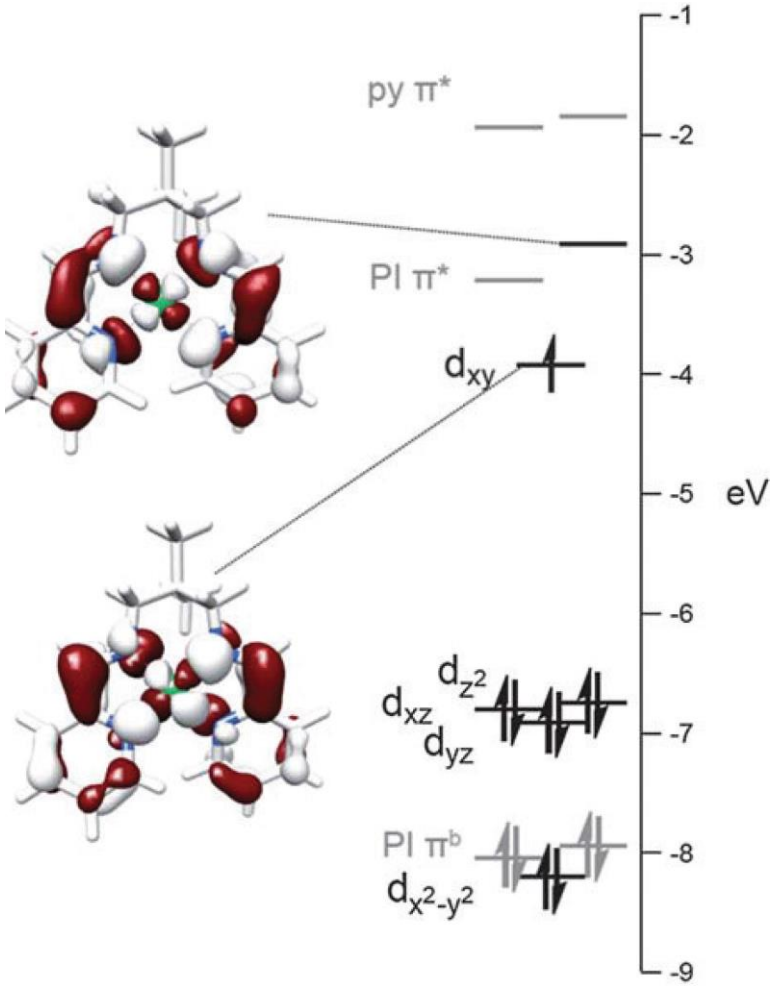

Figure 2.11. Quasi-restricted orbital transformation of the unrestricted Kohn-Sham solution for $[\{dmp(PI)_2Ni]^+$. The SOMO is comprised of 50% Ni and 50% ligand π^*.

oxidation state of Ni is approximately Ni(1.5). Broken symmetry calculations carried out on **Ni**[+] resulted in a solution ~5000 cm^{-1} higher in energy, so a broken symmetry model was not employed in the description of the electronic structure of **Ni**[+]. In addition, as calculations of a THF adduct of **Ni**[+] did not converge in geometry optimization, the possibility of monomeric **Ni**[+] existing as a THF adduct in solution was discarded.

Attempts were made to obtain crystalline **Ni**[+], but X-ray analysis of crystals isolated from $MeCN/Et_2O$ revealed formation of an asymmetric dimer in the solid state, $[\{dmp(PI)_2\}_2Ni^{II}Ni^{0}]^{2+}(OTf^{-})_2$ (**Ni**[2+]**Ni**[0]). The solid-state structure of **Ni**[2+]**Ni**[0] is illustrated in Figure 2.12, and relevant parameters are presented in Tables 2.2 and 2.3. The molecule consists of a distorted octahedral metal center with six nitrogen chelates (90.2(5)° ave, 166.7(5)° ave), linked to a distorted tetrahedral metal site comprised of two nitrogen chelates and two C=N units bound in an η^2 fashion to the nickel center. The *d*(Ni-N) for the octahedral metal center are indicative

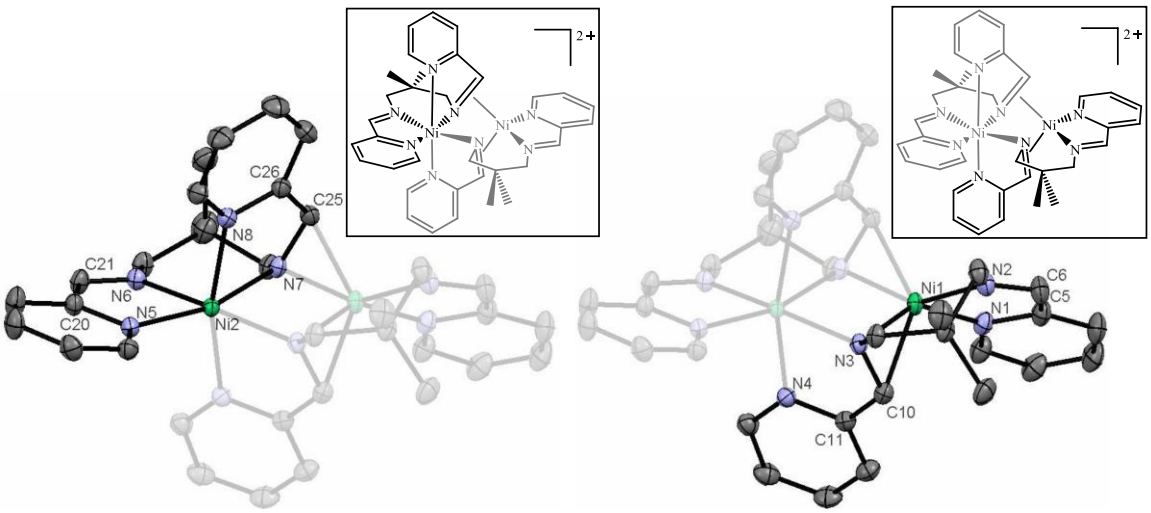

Figure 2.12. Molecular structure of **Ni**[2+]**Ni**[0], containing an S = 1 octahedral metal center (left) and an S = 0 tetrahedral metal center (right). Two triflate counterions and hydrogens have been omitted for clarity.

Table 2.2. Selected interatomic distances for **Ni**[2+]**Ni**[0].

Selected Bond Distances (Å)		Selected Bond Distances (Å)	
Ni2-N5	2.0738(13)	Ni1-N1	1.9871(14)
Ni2-N6	2.0629(13)	Ni1-N2	1.9274(14)
Ni2-N7	2.0368(13)	Ni1-N3	1.9679(13)
Ni2-N8	2.1021(14)	Ni1-N7	1.9666(13)
Ni2-N3	2.1373(13)	Ni1-C10	2.0582(16)
Ni2-N4	2.0743(14)	Ni1-C25	2.0401(16)
N6-C21	1.273(2)	N2-C6	1.278(2)
C21-C20	1.469(2)	C6-C5	1.456(3)
C20-N5	1.353(2)	C5-N1	1.360(2)
N7-C25	1.361(2)	N3-C10	1.356(2)
C25-C26	1.463(2)	C10-C11	1.463(2)
C26-N8	1.354(2)	C11-N4	1.350(2)
Ni1-Ni2	2.9607(3)		

Table 2.3. Selected bond angles for **Ni**[2+]**Ni**[0].

Selected Bond Angles (°)		Selected Bond Angles (°)	
N5-Ni2-N6	80.13(5)	N1-Ni1-N2	82.54(6)
N6-Ni2-N7	89.52(5)	N2-Ni1-N3	98.80(6)
N7-Ni2-N3	83.01(5)	N3-Ni1-N7	89.39(5)
N3-Ni2-N5	108.51(5)	C10-Ni1-N7	102.11(6)
N5-Ni2-N4	99.91(5)	C25-Ni1-N3	102.50(6)
N5-Ni2-N8	91.28(5)	C10-Ni1-N1	103.93(6)
N6-Ni2-N4	92.27(5)	C20-Ni1-N2	105.34(6)
N6-Ni2-N8	99.16(5)	C25-Ni1-N2	105.95(6)
N7-Ni2-N4	90.18(5)	N1-Ni1-N7	110.66(6)
N7-Ni2-N8	80.66(5)	C25-Ni1-N1	113.21(6)
N3-Ni2-N4	79.83(5)	C10-Ni1-C25	133.71(6)
N3-Ni2-N8	87.54(5)	N1-Ni1-N3	142.50(6)
N5-Ni2-N7	165.76(5)	N2-Ni1-N7	145.50(6)
N3-Ni2-N6	169.07(5)		
N4-Ni2-N8	165.24(5)		

of a high-spin Ni^{II} (2.08(3) Å ave), and the metal-ligand distances for the tetrahedral site are indicative of a Ni^{0} center (*d*(Ni-N) = 1.962(2) Å ave, *d*(Ni-C) = 2.0492(16) Å ave). The imine C-N (1.276(2) Å ave), imine-pyridine C-C (1.463(3) ave) and pyridine C-N bond lengths (1.357(2) Å ave) of the two unperturbed pyridine imine moieties are consistent with two neutral fragments, with the two remaining pyridine imine fragments elongated (1.356(2) Å ave) due to a substantial interaction with the π-bound tetrahedral Ni center.[7]

SQUID magnetometry was carried out on **Ni**[2+]**Ni**[0], and resulting data are shown in Figure 2.13. Two realistic electronic configurations exist for the dimer. If

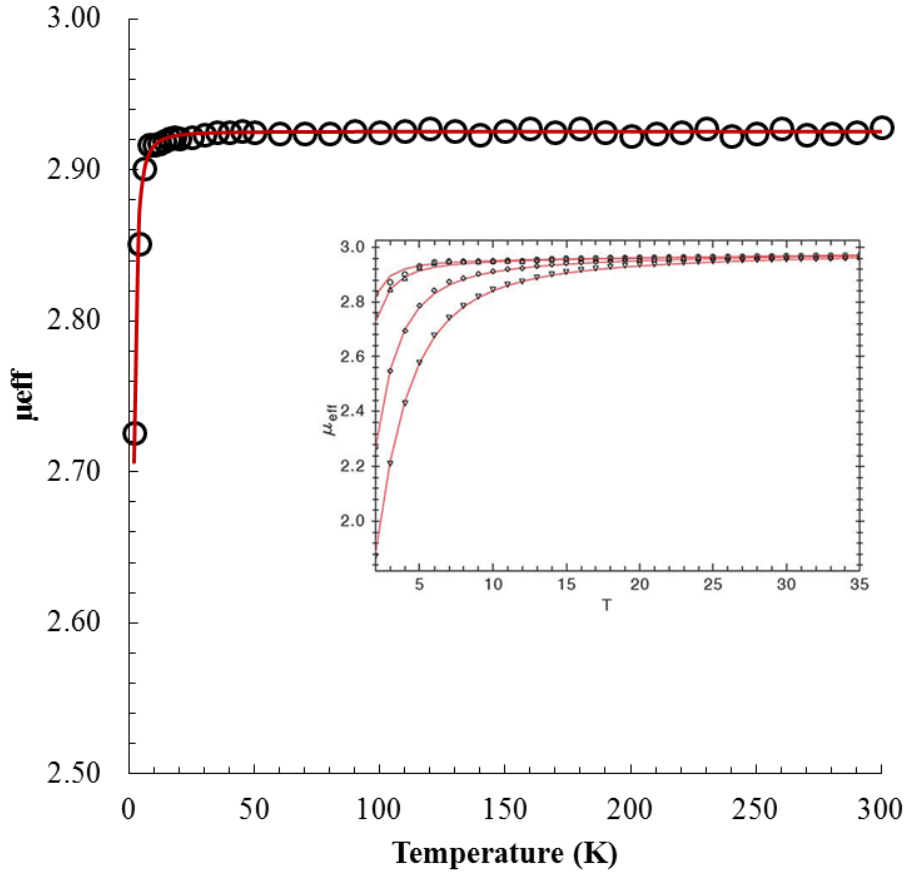

Figure 2.13. SQUID data for **Ni**[2+]**Ni**[0]. Inset: Variable field (0.100, 1.000, 3.000, 5.000 T) SQUID data from 2 to 35 K. Fit parameters: g = 2.085, D = 1.650 cm^{-1}, E/D = 0 cm^{-1}, TIP = 462.5 x 10^{-6} emu (subtracted), TW = 0 K. At 300 K, μ_{eff} = 2.93 μ_{β}.

$[\{dmp(PI)_2\}_2Ni_2]^{2+}$ had one unpaired electron on each Ni center (two uncoupled S = ½ spin centers), a spin-only μ_{eff} of 2.45 μ_β would be predicted. If, however, $[\{dmp(PI)_2\}_2Ni_2]^{2+}$ consists of two unpaired electrons on one Ni center and a second, fully paired Ni center (consistent with a single S = 1 spin system), as indicated by the structural data given in Table 2.2, a spin-only μ_{eff} of 2.83 μ_β would be predicted. At 300 K, the μ_{eff} was determined as 2.93 μ_β, which further supports the assignment of the Ni^{II}/Ni^0 system implicated by the structural data.

It is likely that the electrochemical waves observed at -0.83 V and -1.47 V (Figure 2.8) are attributable to this dimeric complex. These features are only observed after an initial oxidation cycle, consistent with a compound formed chemically upon electrochemical oxidation of **Ni**[0]. Presumably, initial oxidation generates **Ni**[+], some of which dimerizes in solution to form **Ni**[2+]**Ni**[0]. The limited solubility of **Ni**[2+]**Ni**[0] in THF may account for the low current observed. Because the current of these two waves was proportional to sweep rate, an increase in sweep rate would allow for detection before **Ni**[2+]**Ni**[0] precipitated from solution. The reversible wave at -0.83V likely corresponds to oxidation of the dimer **Ni**[2+]**Ni**[0] to $[\{dmp(PI)_2\}_2Ni_2]^{3+}$ (**Ni**[2+]**Ni**[+]), which remains dimeric in solution and may undergo electrochemical reduction back to **Ni**[2+]**Ni**[0]. The wave at -1.47 V would then correspond to reduction of **Ni**[2+]**Ni**[0] to $[\{dmp(PI)_2\}_2Ni_2]^{+}$ (**Ni**[+]**Ni**[0]), which would likely deaggregate to generate **Ni**[+] and **Ni**[0] or undergo disproportionation to **Ni**[2+]**Ni**[0] and monomeric **Ni**[0], accounting for the observed electrochemical irreversibility of this wave.

2.3 Synthesis and Electronic Structure of $[\{dmp(PI)_2\}(CH_3CN)_2Ni^{II}]^{2+}$ (Ni[2+])

Upon treatment of **Ni**[+] with an oxidizing agent, or treatment of **Ni**[0] with 2 equiv of an oxidizing agent, rapid formation of pale yellow $[\{dmp(PI)_2\}(CH_3CN)_2Ni^{II}]^{2+}$ was observed (Eq. 2.5). **Ni**[2+] is paramagnetic, and an

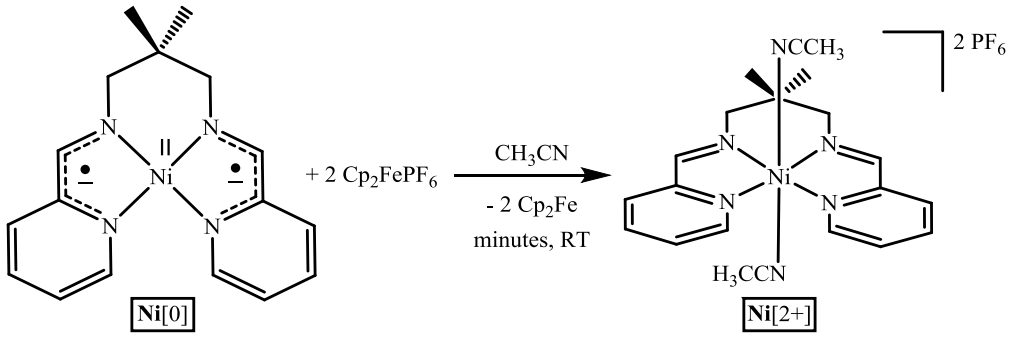

(2.5)

Evans' method magnetic measurement[70,71] revealed μ_{eff} = 2.91 (8) μ_β, consistent with an S = 1 spin center (spin-only μ_{eff}= 2.82 μ_β). X-ray analysis of **Ni**[2+] indicated a pseudo-octahedral metal center with two bound acetonitrile molecules, the structure of

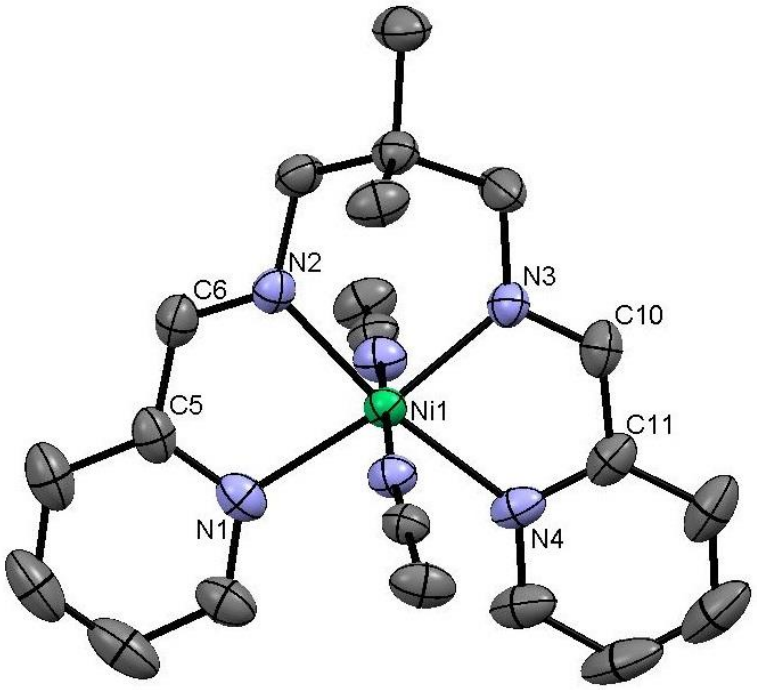

Figure 2.14. Molecular Structure of **Ni**[2+]. Two hexafluorophosphate counterions, one molecule of acetonitrile in the outer coordination sphere, and hydrogens have been omitted for clarity.

Table 2.4: Selected interatomic distances and bond angles for **Ni**[2+].

Selected Bond Distances (Å)		Selected Bond Angles (°)	
Ni1-N1	2.1109(18)	N1-Ni1-N2	79.45(8)
Ni1-N2	2.041(2)	N2-Ni1-N3	91.08(7)
Ni1-N3	2.0421(17)	N3-Ni1-N4	80.08(8)
Ni1-N4	2.102(2)	N4-Ni1-N1	109.61(8)
N2-C6	1.260(3)	N1-Ni1-N3	168.91(7)
C6-C5	1.467(3)	N2-Ni1-N4	170.78(8)
C5-N1	1.356(3)	N1-N2-N3-N4	6.64(16)
N3-C10	1.273(3)	(dihedral)	
C10-C11	1.462(3)		
C11-N4	1.352(4)		

which is given in Figure 2.14, with relevant parameters presented in Table 2.4. Metric parameters for the N_{im}-C_{im} bonds (1.267 (3) Å ave), C_{im}-C_{py} bonds (1.465 (3) Å ave), and C_{py}-N_{py} bonds (1.354 (4) Å ave) are clearly indicative of neutral pyridine imine moieties with a Ni^{II} metal center.[7] This octahedral high-spin Ni^{II} dication is responsible for the quasi-reversible wave seen at +0.08 V in the cyclic voltammetry data (Figure 2.8). The electrochemical quasi-reversibility is attributable to the limited solubility of **Ni**[2+] in THF.

2.4 Synthesis and Electronic Structure of $[\{dmp(PI)_2\}^{3-}Ni^{II}]^-$ (Ni[-])

Treatment of $\{dmp(PI)_2^{2-}]Ni^{II}$ with 1.0 equiv of reducing agents such as K^0 or Cs^0 in THF resulted in one-electron reduction to the anion $[\{dmp(PI)_2^{3-}\}Ni^{II}]^-$ $(K(THF)_2)^+$, **Ni**[-], in moderate (58%) isolated yield (Eq. 2.6). Addition of 1.0 equiv oxidizing agent to **Ni**[-] quantitatively regenerated **Ni**[0], confirming the chemical reversibility of this transformation. An Evans' method magnetic measurement[70,71] on **Ni**[-] indicated a magnetic moment of μ_{eff} = 1.7 μ_β, consistent with the predicted S = ½ spin state (spin-only μ_{eff} = 1.73 μ_β).

Table 2.5. Structural comparison of **Ni**[2+]**Ni**[0], **Ni**[2+], **Ni**[-] (polymer chain), **Ni**[-] (ion pair), and **Ni**[AcPP].

Crystal Data					
Formula	$C_{36}H_{40}F_6N_8Ni_2O_6S_2$	$C_{23}H_{29}F_{12}N_7NiP_2$	$C_{25}H_{36}KN_4NiO_2$	$C_{35}H_{56}KN_6NiO_6$	$C_{70}H_{106}K_2N_{12}NiO_{12}$
Formula Weight	976.30	752.18	522.39	754.67	1444.58
Crystal System	Triclinic	Monoclinic	Monoclinic	Monoclinic	Monoclinic
Space Group	P-1	Cc	P2(1)/n	P2(1)/c	C2/c
Z	2	4	4	8	4
a, Å	10.0760(7)	9.2230(4)	10.5982(8)	12.7277(11)	34.460(7)
b, Å	10.6657(7)	23.7522(8)	12.3634(8)	21.000(2)	10.852(5)
c, Å	19.6623(14)	15.2139(6)	19.8165(13)	28.837(3)	23.144(4)
α, deg	90.050(3)	90	90	90	90
β, deg	97.940(3)	107.3500(10)	95.155(3)	99.126(4)	100.903(4)
γ, deg	105.384(3)	90	90	90	90
Volume, $Å^3$	2016.3(2)	3181.2(2)	2586.0(3)	7610.2(13)	8499(4)
D (calc.), g/cm^3	1.608	1.571	1.342	1.317	1.129
Absorption coeff., mm^{-1}	1.121	0.808	0.939	0.670	0.384
F(000)	1004	1528	1108	3224	3088
Crystal Size, mm	0.60 x 0.20 x 0.03	0.60 x 0.40 x 0.30	0.50 x 0.30 x 0.04	0.40 x 0.10 x 0.02	0.20 x 0.10 x 0.03
Data Collection and Refinement					
Temp, K	173(2)	173(2)	173(2)	173(2)	243(2)
Wavelength (λ), Å	0.71073	0.71073	0.71073	0.71073	0.71073
θ limits, deg	1.05 to 28.28	2.47 to 29.13	2.54 to 28.28	1.43 to 21.26	1..20 to 23.26
Index Ranges	$-13 \le h \le 13$, $-14 \le k \le 14$, $-25 \le l \le 26$	$-11 \le h \le 12$, $-30 \le k \le 32$, $-20 \le l \le 20$	$-8 \le h \le 14$, $-14 \le k \le 16$, $-26 \le l \le 25$	$-12 \le h \le 11$, $-21 \le k \le 21$, $-29 \le l \le 29$	$-38 \le h \le 37$, $-10 \le k \le 12$, $-25 \le l \le 25$
Reflections Collected	33779	15695	25673	35129	24183
Absorption Correction	Semi-empirical from equivalents	Semi-empirical from equivalents	Semi-empirical from equivalents	Semi-empirical from equivalents	Semi-empirical from equivalents
Max. and Min. Transmission	0.9725 and 0.5527	0.7935 and 0.6427	0.9634 and 0.6509	0.9867 and 0.7755	0.9886 and 0.9271
Refinement Method	Full-matrix least-squares on F^2	Full-matrix least-squares on F^2	Full-matrix least-squares on F^2	Full-matrix least-squares on F^2	Full-matrix least-squares on F^2
Data/Restraints/Params.	9861 / 0 / 545	7932 / 158 / 448	6390 / 6 / 366	8405 / 0 / 883	6091 / 0 / 506
Goodness-of-Fit on F^2	1.016	1.051	1.016	1.012	0.989
Final R Indices [$I>2\sigma(I)$]	R1 = 0.0280, wR2 = 0.0676	R1 = 0.0282, wR2 = 0.0781	R1 = 0.0355, wR2 = 0.0864	R1 = 0.0695, wR2 = 0.1682	R1 = 0.0413, wR2 = 0.0942
R Indices (all data)	R1 = 0.0385, wR2 = 0.0733	R1 = 0.0303, wR2 = 0.0796	R1 = 0.0511, wR2 = 0.0952	R1 = 0.1258, wR2 = 0.2094	R1 = 0.0676, wR2 = 0.1027
Largest Diffraction Peak and Hole (e^- Å)	0.406 and -0.379	0.421 and -0.295	1.227 and -0.548	2.159 and -0.626	0.202 and -0.214

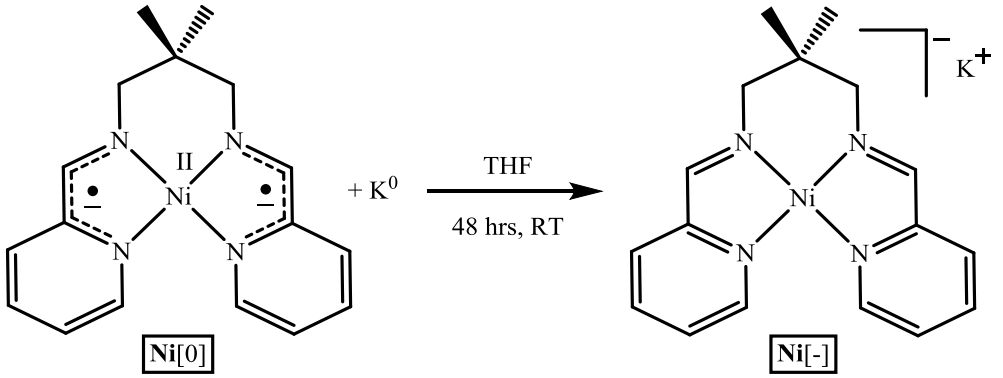

(2.6)

Solution EPR measurements were carried out and the resulting data are shown in Figure 2.15. A fit of the data revealed a rhombic field with $g_1 = 2.045$, $g_2 = 2.003$, and $g_3 = 1.977$, and an average $g_{iso} = 2.008$. As this is quite close to the value of a free electron ($g_e = 2.0023$), EPR data are indicative of a ligand-localized spin, consistent with the electronic configuration [{dmp(PI)$_2^{3-}$}Ni^{II}]$^-$.[73]

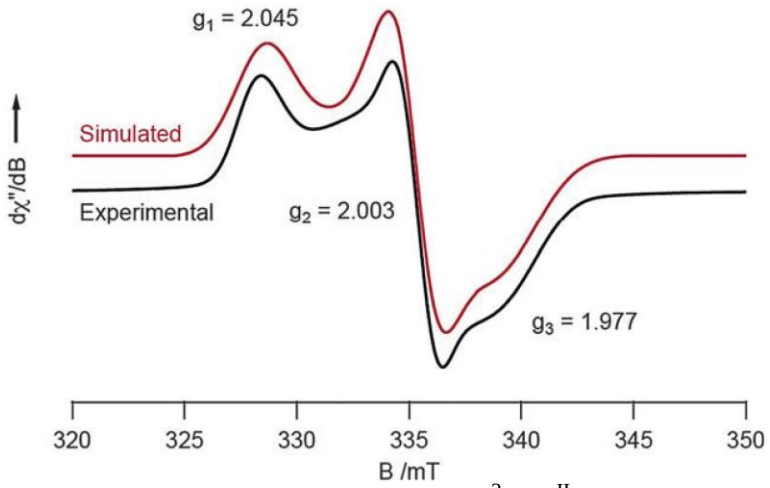

Figure 2.15. X-band EPR spectrum of [{dmp(PI)$_2^{3-}$}Ni^{II}]$^-$ (**Ni**[-]) in THF glass at 10 K; simulation *via* SPINCOUNT (*g*-strain parameters: $\sigma g_1 = 0.010$, $\sigma g_2 = 0.006$, $\sigma g_3 = 0.008$).

X-ray analysis was carried out on **Ni**[-] and revealed a 1-dimensional polymeric chain, with alternating [{dmp(PI)$_2^{3-}$}Ni^{II}]$^-$ and (K(THF)$_2$)$^+$ units (Figure 2.16). A close interaction between the pyridine imine fragments of [{dmp(PI)$_2^{3-}$}Ni^{II}]$^-$ and the bridging potassium ions was observed, with d(K-N$_{im}$) = 3.115 Å and 3.063 Å,

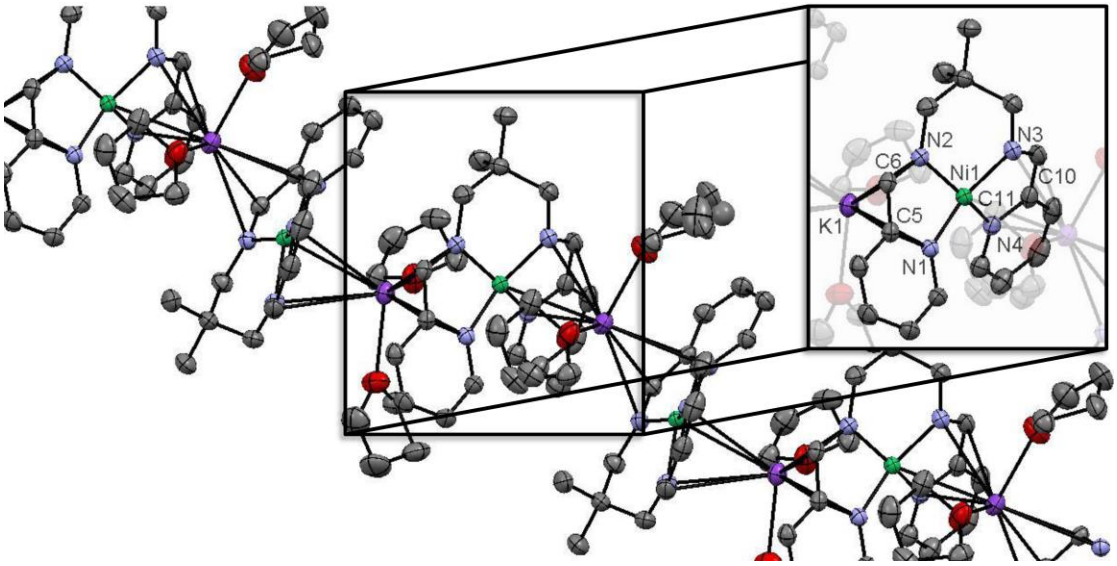

Figure 2.16. Molecular structure of **Ni**[-] as a 1-dimensional polymeric chain, with alternating $[\{dmp(PI)_2^{3-}\}Ni^{II}]^-$ and $(K(THF)_2)^+$ units. Inset: one $[\{dmp(PI)_2^{3-}\}Ni^{II}]^-$ anionic unit with numbering shown.

$d(K\text{-}C_{im})$ = 3.046 Å and 3.362 Å, $d(K\text{-}C_{py})$ = 3.024 Å and 3.460 Å, and $d(K\text{-}N_{py})$ = 3.196 Å and 3.329 Å. Attempts towards extraction of the potassium cation from the polymeric chain were carried out to remove the potential of bond length perturbation of $[\{dmp(PI)_2^{3-}\}Ni^{II}]^-$ through delocalization of charge onto potassium. Treatment of **Ni**[-] with 1.0 equiv crypt-2.2.2 in THF at room temperature resulted in the precipitation of long brown needles suitable for X-ray analysis. The resulting structure is shown in Figure 2.17, and relevant parameters for both polymeric and separated ion-pair $[\{dmp(PI)_2^{3-}\}Ni^{II}]^-$ are presented in Table 2.6. Bond lengths and angles are quite similar for both structures, indicating that the potassium ion in the polymeric chain does not have a major perturbative effect to metric parameters.

The $[\{dmp(PI)_2^{3-}\}Ni^{II}]^-$ anion in both structures has a distorted square planar geometry about the metal center, with pyridine imine distances indicative of an intermediate state between a radical anion and a dianion ($d(N_{im}\text{-}C_{im})$ = 1.357 Å ave,

$d(C_{im}\text{-}C_{py})$ = 1.378 Å ave, $d(C_{py}\text{-}N_{py})$ = 1.416 Å ave).[7] This is again consistent with the electronic assignment of three electrons in the ligand framework and a Ni^{II} metal center. The Ni-N distances are quite similar to those observed for **Ni**[0], and are fully consistent with a low-spin Ni^{II} center in a pseudo square-planar environment. Although one can predict reduced core distances for **Ni**[-] relative to **Ni**[0] due to increased covalency arising from a greater amount of charge on the $\{dmp(PI)_2^{3-}\}$ moiety, this effect is apparently attenuated by a greater degree of intraligand electron repulsion on the trianionic fragment. As with **Ni**[0], a slight chelate twist (N1-N2-N3-

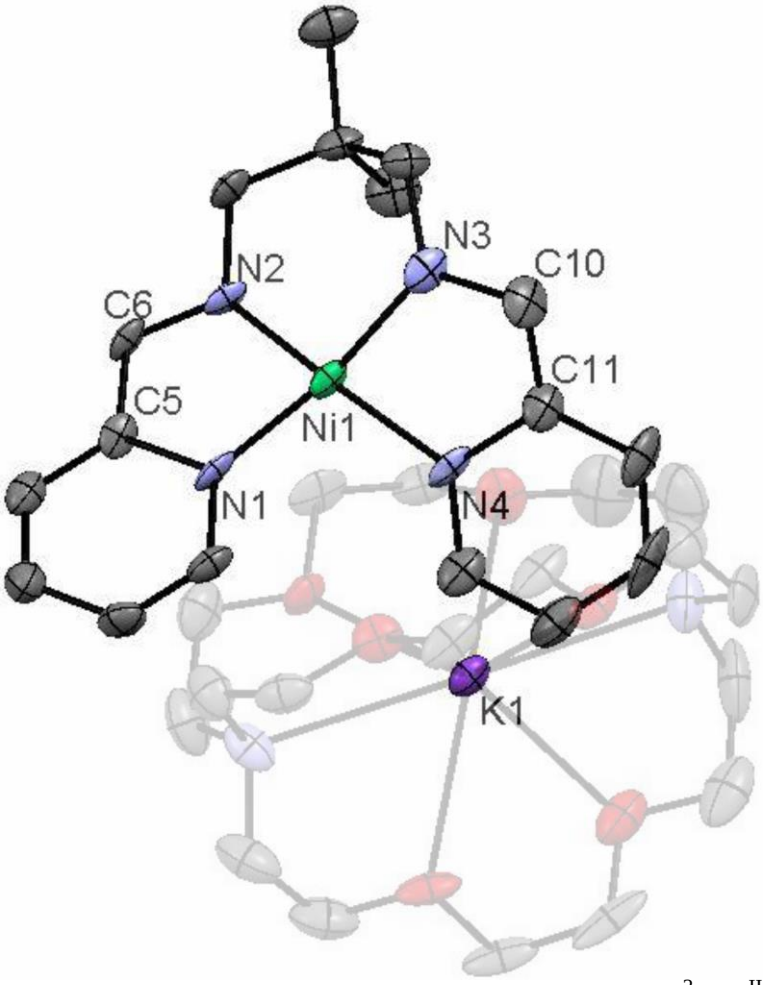

Figure 2.17. Molecular Structure of one molecule of $[\{dmp(PI)_2^{3-}\}Ni^{II}]^-$ $[K(crypt\text{-}2.2.2)]^+$ in the asymmetric unit. Hydrogens have been omitted for clarity.

Table 2.6: Selected interatomic distances and bond angles for the anion $[\{dmp(PI)_2^{3-}\}Ni^{II}]^-$ $(K(THF)_2)^+$. Parameters shown in bold are for the isolated ion-pair and are an average of the two molecules in the asymmetric unit, which are equivalent within 3σ.

Selected Bond Distances (Å)			Selected Bond Angles (°)		
Ni1-N1	1.8995(15)	**1.918(6)**	N1-Ni1-N2	84.54(7)	**85.0(3)**
Ni1-N2	1.8728(15)	**1.873(6)**	N2-Ni1-N3	97.05(7)	**95.3(3)**
Ni1-N3	1.8704(15)	**1.878(6)**	N3-Ni1-N4	84.03(7)	**84.1(3)**
Ni1-N4	1.9203(16)	**1.909(6)**	N4-Ni1-N1	104.36(7)	**103.3(3)**
N2-C6	1.367(2)	**1.365(9)**	N1-Ni1-N3	157.17(7)	**159.9(3)**
C6-C5	1.377(3)	**1.375(11)**	N2-Ni1-N4	154.25(7)	**157.4(2)**
C5-N1	1.418(2)	**1.403(9)**	N1-N2-N3-N4	36.10(10)	**31.7(1)**
N3-C10	1.352(3)	**1.342(9)**	(dihedral)		
C10-C11	1.389(3)	**1.372(11)**			
C11-N4	1.411(2)	**1.431(9)**			
K1-N2	3.1149(16)				
K1-C6	3.0463(19)				
K1-C5	3.0238(19)				
K1-N1	3.1958(16)				

N4 (dihedral) ~ 34°) allows for reduced ligand overlap with the torus of d_{z^2} and attenuation of its σ^* character.

Calculations carried out on $[\{dmp(PI)_2^{3-}\}N\mathbf{i}^{II}]^-$ further support the electronic assignment of **Ni**[-] as a Ni^{II} metal center with three ligand-based π-electrons. A truncated molecular diagram is illustrated in Figure 2.18. The molecule exhibits substantial covalency, as even the filled "pure" nickel d_{xz}, d_{yz}, and d_{z^2} orbitals and the pyridine imine π^b orbitals possess a fair amount of metal and ligand character. The highest energy orbitals, a filled pyridine imine π^* orbital and a half-filled pyridine imine π^* SOMO, have greater than 80% ligand character and represent the three electrons in the trianionic $\{dmp(PI)_2^{3-}\}$. This anionic species is responsible for the

reversible wave observed at -2.28 V in the cyclic voltammetry data (Figure 2.8), and the full chemical reversibility is consistent with the observed electrochemical reversibility. As **Ni**[-] is fully soluble in THF, no current attenuation was observed.

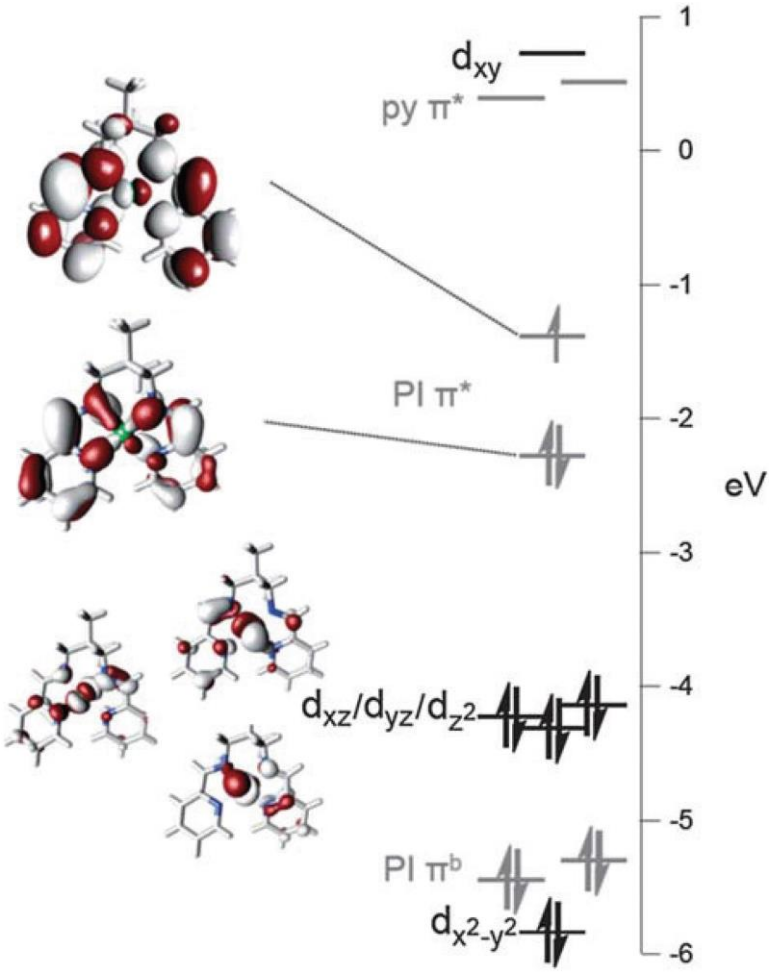

Figure 2.18. Quasi-restricted orbital transformation of the unrestricted Kohn-Sham solution for $[\{dmp(PI)_2\}^{3-}Ni^{II}]^-$, implicating a d^8 metal core with 2 electrons in a pyridine imine π^* orbital and a pyridine imine π^*-based SOMO.

2.5 Synthesis and Electronic Structure of $[\{dmp(PI)_2\}^{4-}Ni^{II}]^{2-}$ (Ni[2-])

A second reduction of **Ni**[0] could be achieved through treatment of neutral **Ni**[0] with 2.0 equiv K^0 or Cs^0. In the case of potassium, an excess of reducing agent was required to prepare a red-brown diamagnetic complex with seven ^1H NMR resonances and nine ^{13}C resonances, consistent with the expected C_s-symmetric

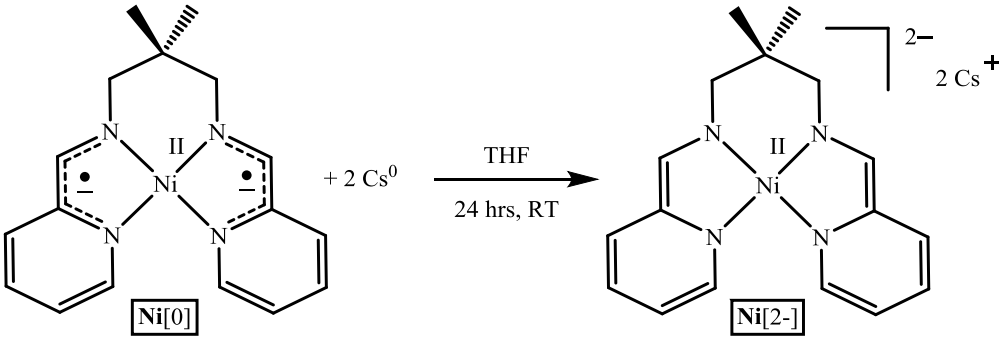

(2.7)

dianion. Unfortunately, the amount of oxidant required to regenerate **Ni**[0] was inconsistent between reactions, indicating an uncertain and potentially variable stoichiometry. However, when elemental cesium was used as a reducing agent, **Ni**[0] cleanly consumed 2.0 equiv to generate $[\{dmp(PI)_2^{4-}\}Ni^{II}]^{2-}[Cs^+(THF)_n]_2$ (**Ni**[2-]), which exhibited the same NMR spectra as the material generated from reduction with K^0 (Eq. 2.7). The ^{1}H NMR spectrum of **Ni**[2-] is shown in Figure 2.19 (left), revealing significantly upfield-shifted resonances assigned to protons within the pyridine imine π-system when compared to neutral **Ni**[0] (right). The aromatic and imine protons are shifted almost 3 ppm (6.5 – 4.0 ppm) relative to **Ni**[0] (9.5 – 6.5 ppm), indicating a much greater degree of pyridine imine-based electron density for

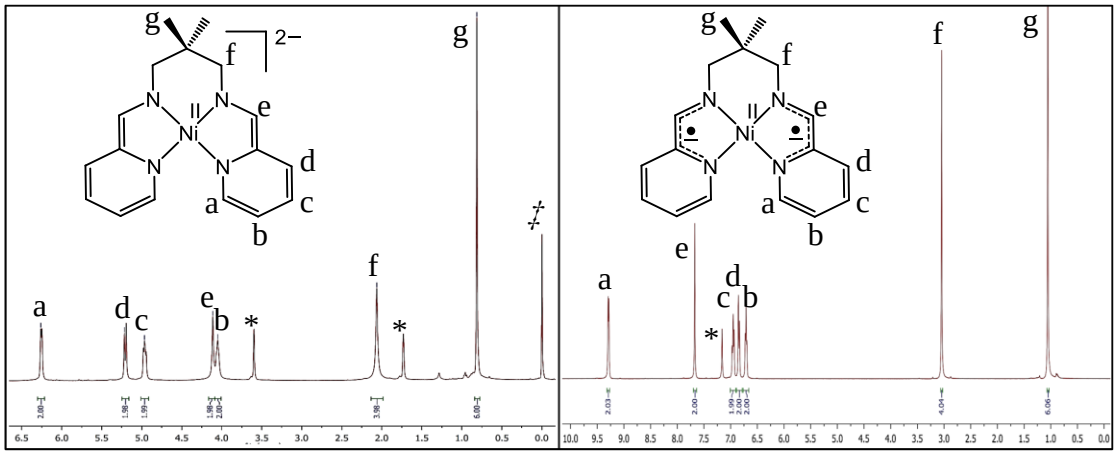

Figure 2.19. ^{1}H NMR spectrum of $[\{dmp(PI)_2^{4-}\}Ni^{II}]^{2-}[Cs^+(THF\text{-}d_8)_n]_2$ in THF-d_8 (left) and ^{1}H NMR spectrum of $\{dmp(PI)_2^{2-}\}Ni^{II}$ in C_6D_6 (right). Solvent is indicated by (*) and TMS is indicated by (‡).

Ni[2-]. The dianion **Ni**[2-] was prone to oxidation to **Ni**[-] or **Ni**[0], so X-ray analysis on suitable crystals was elusive and reasonable elemental analysis data were not obtained. However, the molecule was fully characterized via 2-dimensional NMR correlation techniques.

To gain insight into the electronic structure of **Ni**[2-], calculations on the geometry-optimized dianion were carried out and the resulting truncated molecular orbital diagram is illustrated in Figure 2.20. As with **Ni**[-] the orbitals are substantially covalent, and the filled metal orbitals and pyridine imine π^b orbitals possess a

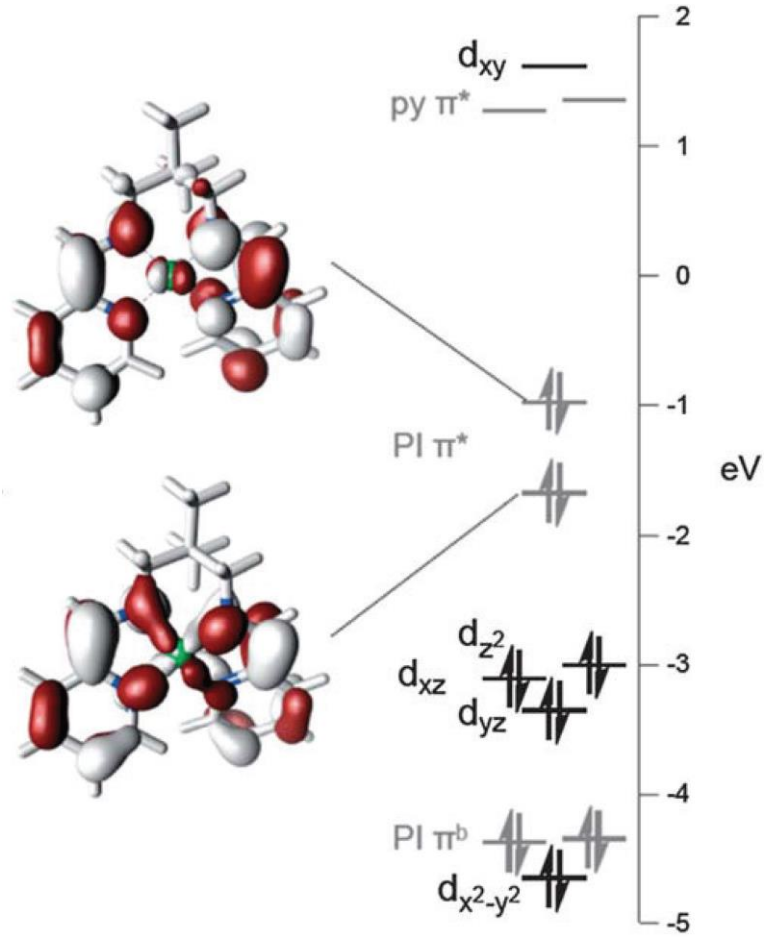

Figure 2.20. Quasi-restricted orbital transformation of the unrestricted Kohn-Sham solution for $[\{dmp(PI)_2^{4-}Ni^{II}]^{2-}$, implicating a d^8 metal core with 4 electrons in two filled pyridine imine π^* orbitals.

significant degree of both metal and ligand character. As **Ni**[0] undergoes ligand-based reduction, the pyridine imine orbitals increase in energy and allow for a greater degree of mixing with metal orbitals, resulting in a greater degree of covalency. The tetraanionic nature of $\{dmp(PI)_2^{4-}\}$ is further supported in Figure 2.20, as the two highest-occupied pyridine imine π^* orbitals are now each doubly occupied.

2.6 UV-visible data for $[\{dmp(PI)_2\}Ni]^n$ Complexes

UV-visible data were acquired for $[\{dmp(PI)_2\}Ni]^n$ (n = 2+, 1+, 0, 1-) and are presented in Figure 2.21. The pale yellow **Ni**[2+] exhibits only weak d-d absorptions in the UV-visible region, as expected for a high-spin d^8 pseudo-octahedral complex. **Ni**[+], **Ni**[0], and **Ni**[-] display similar spectroscopic behavior, and absorption data are summarized in Table 2.7. All three complexes exhibit several intense charge transfer bands in the UV-visible region. To distinguish between metal-to-ligand, ligand-to-metal, or intraligand charge transfer bands, the UV-visible spectrum of $\{dmp(PI)_2\}Mg(THF)_n$ was acquired and is given in Figure 2.21.

The low energy bands of **Ni**[+], **Ni**[0], and **Ni**[-] from 10,000–16,000 cm^{-1} are absent in the spectrum of $\{dmp(PI)_2\}Mg(THF)_n$, suggesting these bands are likely ligand-to-metal or metal-to-ligand charge transfer bands. The intense absorptions from 22,000–27,000 cm^{-1} for **Ni**[0] and **Ni**[-] are intraligand charge transfer bands that match up well to those of $\{dmp(PI)_2\}Mg(THF)_n$, but are blue-shifted due to chelation of a Ni^{II} center. The low-energy features from 17,000–21,000 cm^{-1} for $\{dmp(PI)_2\}Mg(THF)_n$ may correspond to a vibronic progression, where the 17,640, 18,980, and 20,400 cm^{-1} bands are the $\nu_{GS} = 0$ to $\nu_{ES} = 0$, 1, and 2 vibrational components. Because the highest-energy band is the one of greatest intensity, the

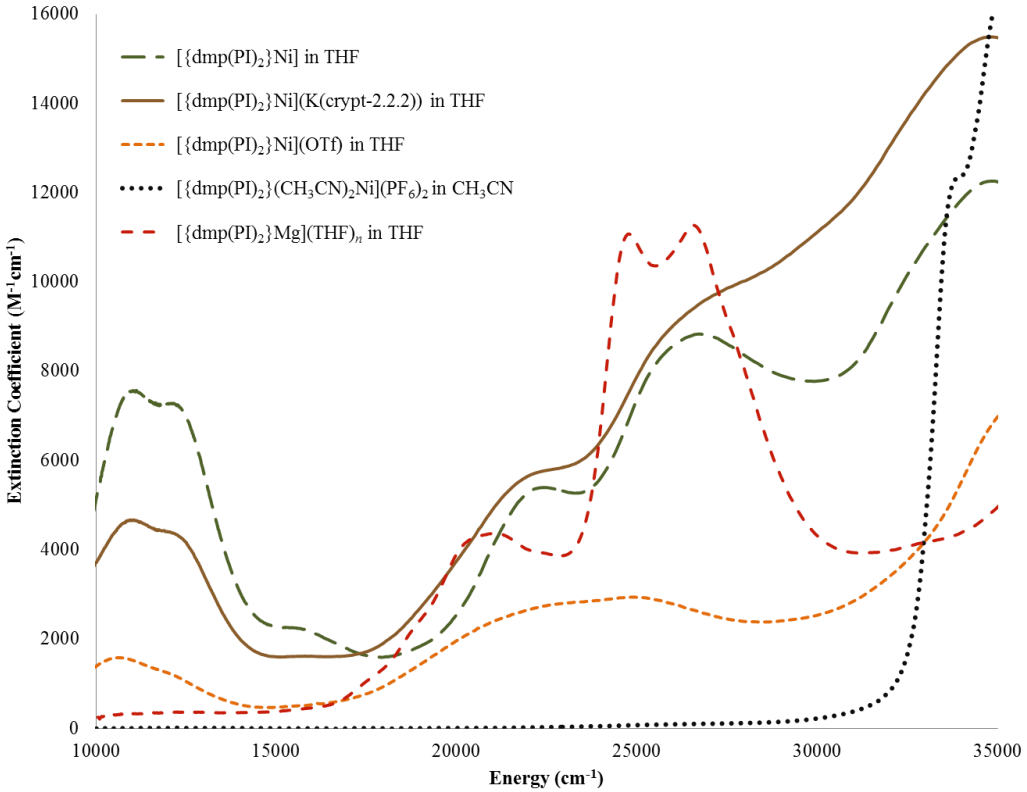

Figure 2.21. UV-visible spectra of $[\{\kappa_4\text{-}Me_2C(CH_2N{=}CHpy)_2\}Ni]^n$(n = 2+, 1+, 0,-1) and $[\{\kappa_4\text{-}Me_2C(CH_2N{=}CHpy)_2\}Mg]$.

Table 2.7. Extinction coefficient (ε) values for **Ni**[+], **Ni**[0], **Ni**[-], and $\{dmp(PI)_2\}Mg(THF)_n$.

Ni[+]		**Ni**[0]		**Ni**[-]		$\{dmp(PI)_2\}Mg(THF)_n$	
ν (cm^{-1})	ε ($M^{-1}cm^{-1}$)	ν (cm^{-1})	ε ($M^{-1}cm^{-1}$)	ν (cm^{-1})	ε ($M^{-1}cm^{-1}$)	ν (cm^{-1})	ε ($M^{-1}cm^{-1}$)
10620	1560	11100	7560	11080	4670	17640	1125
12020	1235	12140	7270	12270	4340	18980	2700
16000	540	15920	2190	15820	1620	20400	5180
22400	2740	22470	5390	22520	5780	21050	5350
25000	2930	26670	8830	27100	9620	22370	4700
						24690	13490
						36380	14090

excited state potential energy surface must be substantially displaced relative to the ground state surface. The difference of ~1,400 cm^{-1} is comparable to ground state

stretches observed in the infrared spectrum of dmp(PI)$_2$}Mg(THF)$_n$, corroborating the assignment of a vibronic progression.

The spectrum of **Ni**[-] is remarkably similar to that of **Ni**[0], and may indicate a minor degree of sample contamination arising from oxidation of **Ni**[-] to **Ni**[0]. Although **Ni**[-] did not visually appear contaminated, it is feasible that the deep brown color of **Ni**[-] could successfully mask a small amount of the forest green color characteristic of **Ni**[0]. However, the UV-visible spectrum of **Ni**[-] *was* reproducible from multiple samples so if **Ni**[0] was present, it was a minor component. The similarity of the spectra presented in Figure 2.21 further illustrates the similarity in electronic structure of **Ni**[+], **Ni**[0], and **Ni**[-].

2.7 Degradation Reaction to form [{2-py,3-(=NCHpy),4-Me$_2$-aza-cyclopent-2-ene^{2-}}$_2$Ni]$^{2-}$[K$^+$(crypt-2.2.2)]$_2$ (Ni[AcPP])

During attempts to obtain crystalline **Ni**[2-] for X-ray analysis, various chelating agents were utilized. Surprisingly, treatment of **Ni**[2-] with 2.0 equiv crypt-2.2.2 triggered degradation, and a new bis-ligand complex [{2-py,3-(=NCHpy),4-Me$_2$-aza-cyclopent-2-ene^{2-}}$_2$Ni]$^{2-}$[K$^+$(crypt-2.2.2)]$_2$ (**Ni**[AcPP]) was isolated in low (~7%) yield (Scheme 2.2).

NMR data for **Ni**[AcPP] could not be obtained due to insolubility in organic solvents, but the molecular structure was confirmed via X-ray analysis and is illustrated in Figure 2.22 with relevant metric parameters listed in Table 2.8. Carbon-carbon coupling occurs between the methylene and imine positions on each ligand to generate a new pyrroline ring, and each Ni center binds two C-C coupled ligands. It is likely this species forms through deprotonation at the methylene position adjacent to a

pyridine imine fragment, which would lead to formation of a transient azaallyl fragment that could undergo C-C coupling.[6,74] As indicated in Scheme 2.2, formation

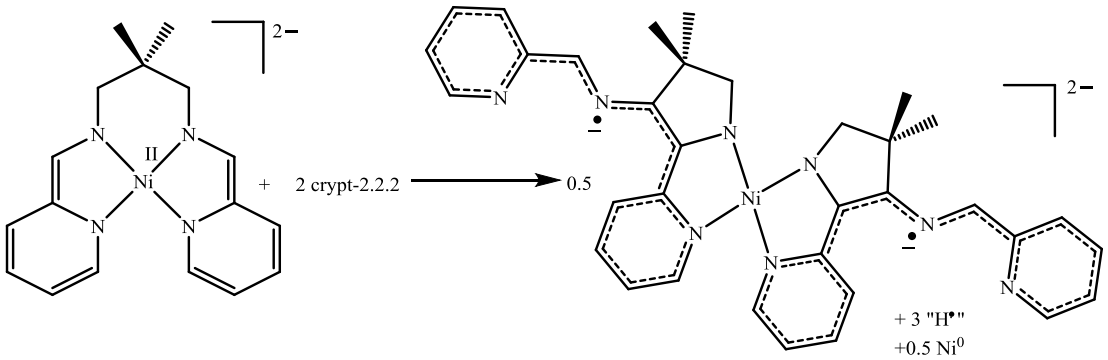

Scheme 2.2. Degradation of **Ni**[2-] to generate [{2-py,3-(=NCHpy),4-Me_2-aza-cyclopent-2-ene^{2-}}$_2$Ni]$^{2-}$[K^+(crypt-2.2.2)]$_2$ (**Ni**[AcPP]).

of **Ni**[AcPP] occurs with the formal loss of 0.5 equiv Ni^0 and three hydrogens per equiv **Ni**[2-]. The nickel center is pseudo square planar, with a slight chelate twist (N1-N2-N2'-N1' (dihedral) ~ 28°), similar to that observed in **Ni**[0] and **Ni**[-], which allows for reduction of σ^* character of the Ni d_{z^2} orbital. The Ni-N distances are indicative of a Ni^{II} metal center, and the metric parameters of the non-coordinated

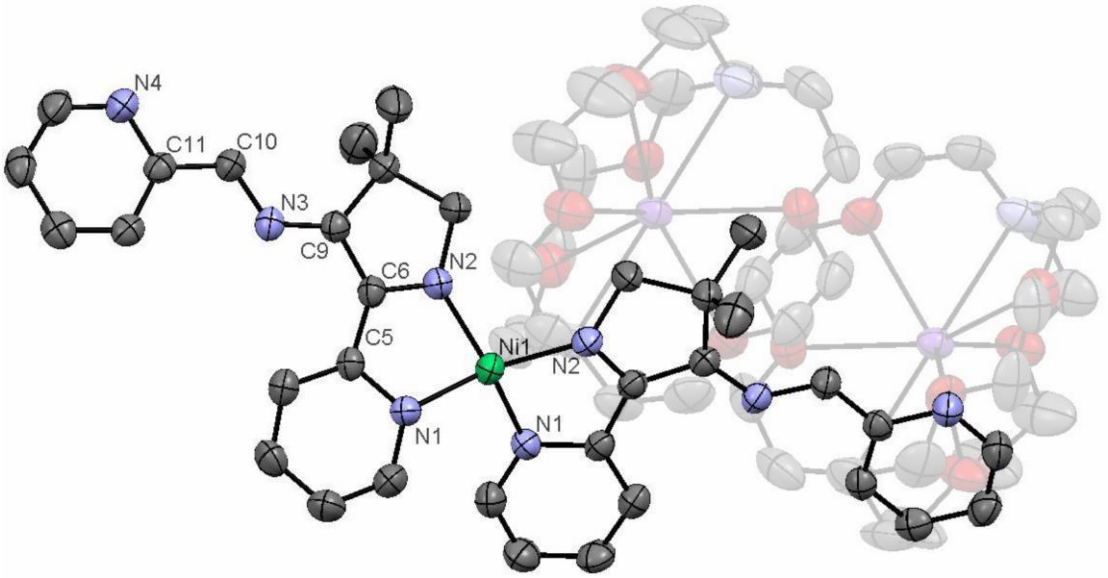

Figure 2.22. Molecular Structure of [{2-py,3-(=NCHpy),4-Me_2-aza-cyclopent-2-ene^{2-}}$_2$Ni]$^{2-}$[K^+(crypt-2.2.2)]$_2$ (**Ni**[AcPP]). Hydrogens have been omitted for clarity.

Table 2.8. Selected interatomic distances and bond angles for **Ni**[AcPP].

Selected Bond Distances (Å)		Selected Bond Angles (°)	
Ni1-N1	1.930(2)	N1-Ni1-N2	81.88(9)
Ni1-N2	1.909(2)	N2-Ni1-N2’	105.53(12)
N1-C5	1.395(3)	N1’-Ni1-N1	102.13(12)
C5-C6	1.430(3)	N1-Ni1-N2’	154.40(8)
C6-C9	1.429(3)	N1-N2-N2’-N1’	28.91(9)
C9-N3	1.325(3)	(dihedral)	
N3-C10	1.336(3)		
C10-C11	1.419(3)		
C11-N4	1.368(3)		

pyridine imine fragments are consistent with a radical anion ($d(N_{im}\text{-}C_{im})$ = 1.336 Å, $d(C_{im}\text{-}C_{py})$ = 1.419 Å, $d(C_{py}\text{-}N_{py})$ = 1.368 Å).[7,75] However, because the bound and unbound pyridine imine fragments of each ligand linked by the newly formed C=C bond constitute an essentially planar π-network, it is likely the radical anion is delocalized over the entire ligand as illustrated in Scheme 2.2.

2.8 Reactivity of Ni[*n*] Complexes

In the electronic structure calculations of **Ni**[+], **Ni**[0], and **Ni**[-] radical character was implicated on the ligand framework or metal center, so one might predict these compounds would exhibit traditional radical reactivity. Surprisingly, H-atom sources such as $^{n}Bu_3SnH$, 9,10-dihydroanthracene, or 1,3-cyclohexadiene were unreactive with **Ni**[0], and H-atom abstraction agents such as $[Ph_3C]_2$ or various peroxides were similarly unreactive. Treatment of **Ni**[0] with halide sources resulted in either nonspecific decomposition or a lack of reaction even at elevated temperatures. Radical sources such as NO triggered decomposition of **Ni**[0]. Treatment of **Ni**[0] with reagents capable of 2 e^- chemistry gave similar results. The

reaction of **Ni**[0] with traditional hydride sources such as KH, $LiBH_4$, or $LiAlH_4$ led to nonspecific decomposition, as did treatment with alkylating agents such as CH_3I or Et_3OBF_4. Reaction of **Ni**[0] with excess TEMPO resulted in the uptake of 4 equiv TEMPO and formation of a new diamagnetic C_2-symmetric compound identified by ^{1}H NMR, but the species underwent decomposition at room temperature over 24 hrs. As isolation proved difficult, complete characterization of this new species was not pursued.

Similarly, **Ni**[+] was unreactive with respect to H-atom transfer reagents or H-atom abstractors, and underwent decomposition when exposed to various halide sources. In contrast to **Ni**[0], TEMPO was unreactive towards **Ni**[+], and treatment of **Ni**[+] with hydride sources capable of single-electron transfer such as KH or $KHBEt_3$ resulted in reduction to **Ni**[0] with concomitant formation of unidentified insoluble byproducts. **Ni**[-] proved even more sensitive than **Ni**[0] or **Ni**[+], and treatment of **Ni**[-] with H-atom transfer reagents or even relatively benign reagents such as acetonitrile, butadiene, 1,3-cyclohexadiene, 9,10-dihydroanthracene, CO_2, or bis(triphenylphosphine)iminium chloride (PPNCl) resulted in oxidation to **Ni**[0] with formation of unidentified insoluble byproducts.

2.9 Synthesis and Electronic Structure Study of {dmp(PI)$_2^{2-}$}Fe^{II}PMe$_3$ (Fe[0])

In an effort to expand the chemistry of $dmp(PI)_2$ to different transition metals of the first row, $Fe(PMe_3)_4$[76,77] was combined with 1.0 equiv $dmp(PI)_2$ in C_6H_6 to generate the deep brown iron complex [{κ^4-$Me_2C(CH_2N{=}CHpy)_2$}$FePMe_3$ (**Fe**[0]), which exhibited eight resonances in the diamagnetic region of the ^{1}H NMR spectrum and ten resonances in the ^{13}C NMR spectrum, indicative of C_{2v} geometry (Eq. 2.8).

The proton *ortho* to the pyridine nitrogen was shifted downfield (δ 9.51) relative to both **Ni**[0] (δ 9.29) and the free ligand (δ 8.59), and the imine C-H proton was shifted

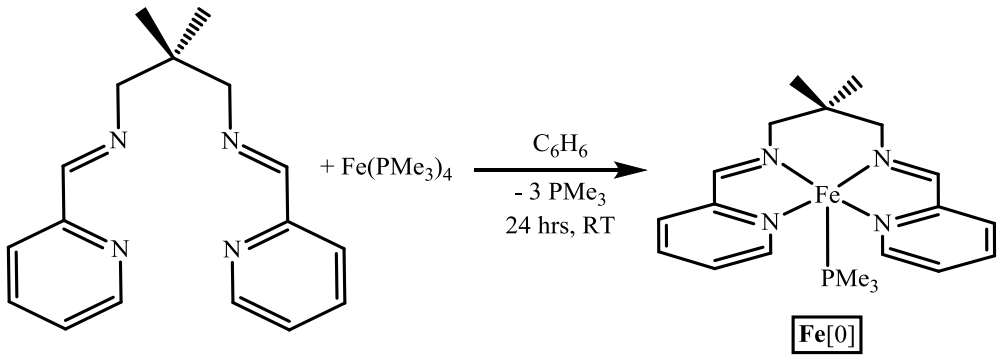

(2.8)

slightly upfield (δ 8.31) relative to free ligand (δ 8.59), but appeared significantly downfield of the imine C-H proton of **Ni**[0] (δ 7.67).

Suitable crystals were subjected to X-ray analysis, and the resulting structure in presented in Figure 2.23 with relevant parameters displayed in Table 2.9. The imine

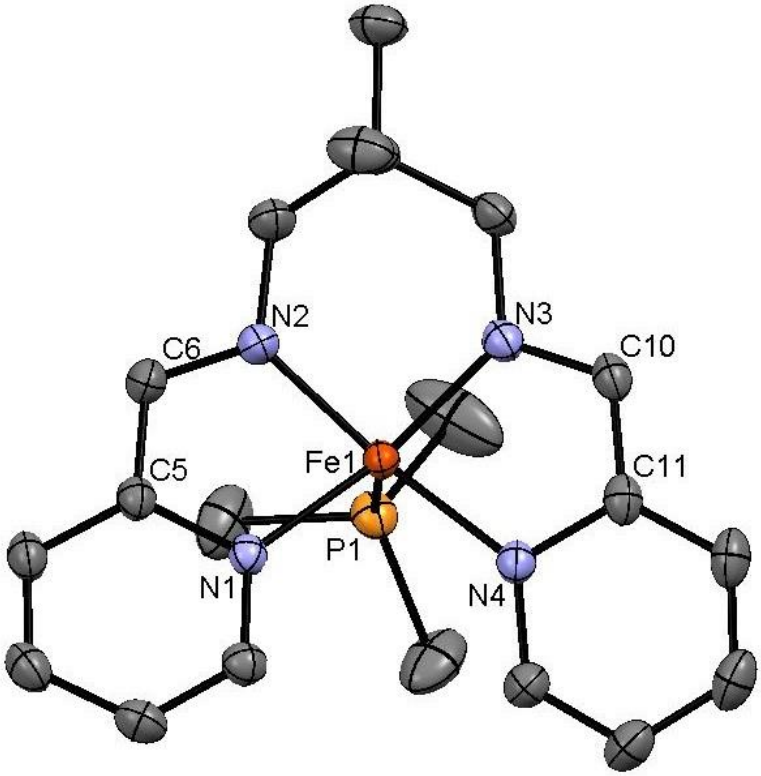

Figure 2.23. Molecular Structure of **Fe**[0]. Hydrogens have been omitted for clarity.

Table 2.9. Selected interatomic distances and bond angles for **Fe**[0].

Selected Bond Distances (Å)		Selected Bond Angles (°)	
Fe1-N1	1.9574(11)	N1-Fe1-N2	81.21(5)
Fe1-N2	1.8812(12)	N2-Fe1-N3	92.72(5)
Fe1-N3	1.8862(11)	N3-Fe1-N4	81.56(5)
Fe1-N4	1.9438(12)	N4-Fe1-N1	100.29(5)
Fe1-P1	2.1952(4)	N1-Fe1-N3	155.80(5)
N2-C6	1.3293(17)	N2-Fe1-N4	169.22(5)
C6-C5	1.3940(19)	N1-Fe1-P1	99.86(3)
C5-N1	1.3959(16)	N2-Fe1-P1	94.65(4)
N3-C10	1.3299(17)	N3-Fe1-P1	103.99(4)
C10-C11	1.393(2)	N4-Fe1-P1	95.59(3)
C11-N4	1.3889(17)	N1-N2-N3-N4 (dihedral)	10.98(5)

C-N bond lengths (1.330 (2) Å ave), imine-pyridine C-C bond lengths (1.394 (2) ave) and pyridine C-N bond lengths (1.392 (2) Å ave) are consistent with a molecule containing two mono-reduced pyridine-imine fragments bound to an iron(II) metal center. Because **Fe**[0] is diamagnetic, the two radical anions are likely antiferromagnetically coupled through a filled iron d-orbital (Figure 2.6) to yield an overall S = 0 complex. The geometry about the metal center is distorted square

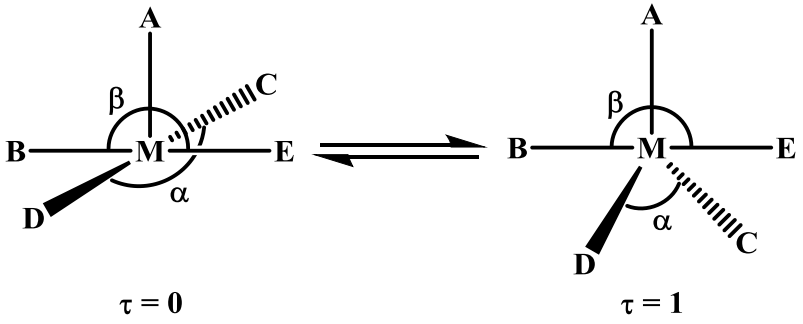

Figure 2.24. Determination of τ as a measure of deviation from ideal geometry. α is defined as the lesser of the basal angles and β is defined as the greater of the basal angles. For square pyramidal geometry τ approaches 0 (left) and for trigonal bipyramidal geometry τ approaches 1 (right).[78]

pyramidal. To quantify the degree of distortion from ideal square pyramidal geometry for 5-coordinate compounds, it is useful to determine the Addison parameter, τ.[78] τ is defined as (α-β)/60°, and ranges from a value of $\tau = 0$ for pure square pyramidal geometry to a value of $\tau = 1$ for pure trigonal bipyramidal geometry (Figure 2.24). In **Fe**[0], α is defined as ∠N1-Fe1-N3 (155.80°) and β is defined as ∠N2-Fe1-N4 (169.22°), with $\tau = 0.22$.

2.10 Redox Chemistry of $\{dmp(PI)_2^{2-}\}Fe^{II}PMe_3$ (Fe[0])

$\{dmp(PI)_2^{2-}\}Fe^{II}PMe_3$ was probed for redox chemistry analogous to that seen for **Ni**[0]. It is conceivable that **Fe**[0] could undergo two chemical reductions and three chemical oxidations as shown in Figure 2.25, with each reduced and oxidized species capable of several different electronic configurations. To synthesize these species, **Fe**[0] was first treated with 1.0 equiv KC_8 in THF to generate a turquoise

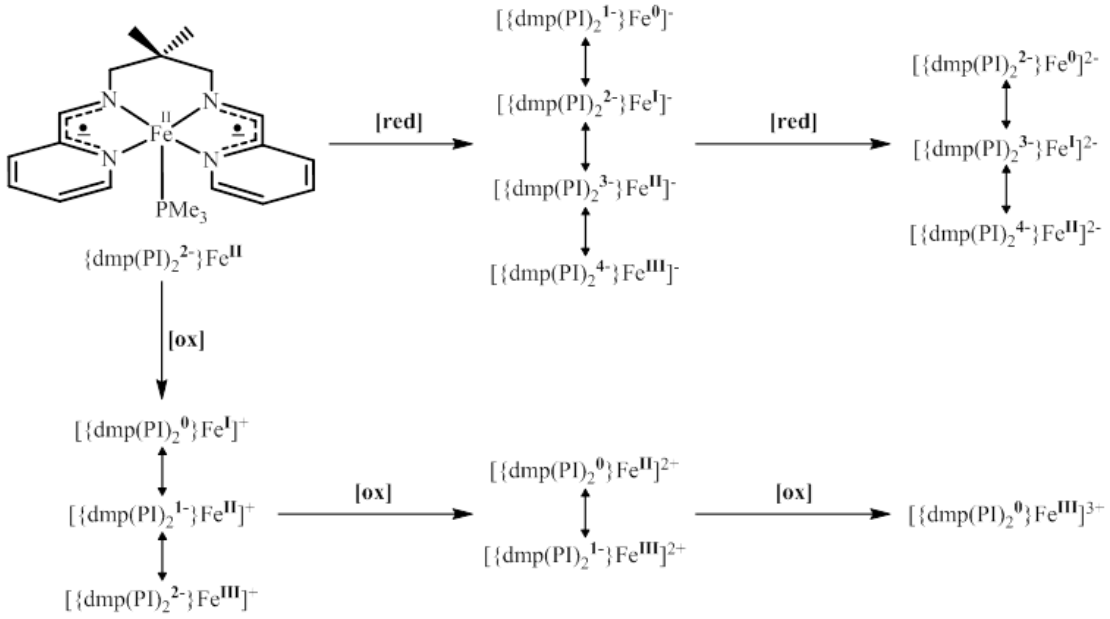

Figure 2.25. Various reductions and oxidations available to **Fe**[0]. The possible electronic configurations for each hypothetical reduced and oxidized species are given as resonance forms.

solution containing a paramagnetic compound, consistent with [{dmp(PI)$_2$}Fe(PMe$_3$)$_n$][K(THF)$_m$] (**Fe**[-]), with a magnetic moment of μ_{eff} = 1.4 μ_β (Evans' method),[70,71] consistent with an S = ½ species ($\mu_{spin\text{-}only}$ = 1.73 μ_β) (Scheme 2.3). Treatment of **Fe**[-] with 1.0 equiv of an oxidant such as Cp_2Fe^+ regenerated **Fe**[0]. ^{1}H NMR spectroscopy of the paramagnetic **Fe**[-] revealed a broad peak ($\nu_{1/2}$ = 365 Hz) centered at δ -13.16 that integrated to ~18 H relative to the 6 methyl protons of **Fe**[-], suggesting the coordination of two PMe_3 units to the metal center. Additionally, treatment of **Fe**[0] with KC_8 in the presence of excess PMe_3 resulted in a cleaner crude reaction mixture than without excess phosphine. Assuming two bound phosphines, the electronic structure of **Fe**[-] would necessarily be [{dmp(PI)$_2^{3-}$}Fe^{II}]$^-$ to maintain an 18-electron count at the pseudo-octahedral metal center.

Exposure of **Fe**[-] to a second equivalent of KC_8 in THF resulted in a color change from turquoise to brown and formation of a new paramagnetic complex by ^{1}H NMR, characterized by five broad singlets (2H, py-C*H*, Im-C*H*) and one broad singlet

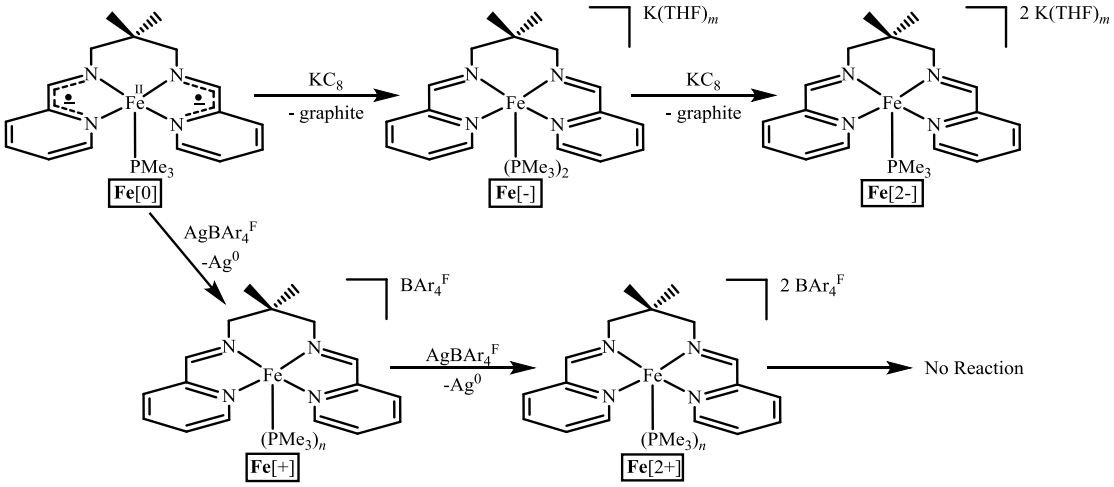

Scheme 2.3. Redox activity of **Fe**[0]. Note that the electronic structures of **Fe**[-], **Fe**[2-], **Fe**[+], and **Fe**[2+] have *not* been determined and are illustrated for convenience here with neutral pyridine imine fragments. For possible electronic configurations of each compound, refer to Figure 2.25.

at δ -6.72 (9H, P(CH_3)$_3$). Additional resonances attributable to the methyl and methylene protons were not found, but could have been obstructed by residual solvent signals in the diamagnetic region. By analogy to the related reductive chemistry observed for **Ni**[0] (*vide supra*), the new species is likely [{dmp(PI)$_2$}Fe(PMe$_3$)][K(THF)$_m$]$_2$, (**Fe**[2-]) (Scheme 2.3). As seen with the doubly-reduced **Ni**[2-], **Fe**[2-] was quite sensitive and prone to oxidation to **Fe**[-] or **Fe**[0]. Indeed, addition of 2.0 equiv oxidant to **Fe**[2-] cleanly regenerated **Fe**[0].

Treatment of **Fe**[0] with 1.0 equiv AgBAr$_4^F$ (BAR$_4^F$ = B[3,5-CF$_3$(C$_6$H$_3$)]$_4$)[79] resulted in a color change from brown to deep forest green and a loss of resonances in the diamagnetic region and formation of a new set of paramagnetically shifted and broadened resonances in ^{1}H NMR spectrum, consistent with generation of [{dmp(PI)$_2$}Fe(PMe$_3$)$_n$][BAr$_4^F$], **Fe**[+]. Evans' Method magnetic measurements[70,71] resulted in a μ_{eff} = 1.5 μ_β, consistent with an S = ½ complex.

Addition of a second equiv AgBAr$_4^F$ to **Fe**[+] resulted in formation of a diamagnetic, magenta compound consistent with the C_2-symmetric [{dmp(PI)$_2$}Fe(PMe$_3$)$_2$][BAr$_4^F$]$_2$, **Fe**[2+] (Scheme 2.3). The ^{1}H NMR spectrum of **Fe**[2+] revealed an imine C-H proton shifted significantly downfield (δ 9.21) relative to free ligand (δ 8.59), arising from a large deshielding effect and indicative of a non-reduced ligand. Consequently, although **Fe**[2+] has two possible electronic configurations (Figure 2.25), the most probable configuration is [{dmp(PI)$_2^0$}Fe^{II}]$^{2+}$.

One could envision a last oxidation available to **Fe**[0] to generate [{dmp(PI)$_2^0$}Fe^{III}]$^{3+}$, as it is known that dmp(PI)$_2$ can exist in the +0 oxidation state

and Fe^{III} complexes are ubiquitous in coordination chemistry. Unfortunately, exposure of **Fe**[2+] to excess $AgBAr_4^F$ resulted in no reaction, indicating that the **Fe**[2+]/**Fe**[3+] redox couple must be greater than 0.41 V (vs. Fc/Fc^+, THF).[80]

2.11 Reactivity of Fe[0]

As **Fe**[0] is similar to some group-transfer catalysts known in the literature,[48-52,81] efforts towards mediating group-transfer reactions were carried out. Unfortunately, **Fe**[0] was unreactive with respect to carbene-transfer reagents such as Ph_2CN_2[82] or Ph_2SCPh[83] and organic azides such as 1-adamantyl azide and trimethylsilyl azide. Possibly the presence of a strongly donating phosphine *trans* to the open coordination site of **Fe**[0] disfavors coordination and subsequent reaction with group-transfer reagents, so attempts to remove the PMe_3 from **Fe**[0] were carried out. Treatment of **Fe**[0] with O-atom transfer reagents such as pyridine-N-oxide in the presence of group transfer reagents led to formation of a highly insoluble, diamagnetic, species with C_1 symmetry, with concomitant formation of unidentified insoluble byproducts. Treatment of **Fe**[0] with tosyl azide in the presence of styrene, alkyne, or isocyanide substrates led to immediate release of N_2 and precipitation of a thick lime green solid. The same reaction mixture was generated in the absence of substrate, indicating that tosyl azide was competent in triggering the decomposition of **Fe**[0].

Efforts were made to generate a $\{dmp(PI)_2\}$-coordinated iron complex in the absence of phosphine through treatment of FeX_2 (X = Br, Cl) with $\{dmp(PI)_2\}$ followed by reduction in the presence of a weakly-coordinating L-type ligand. The bright teal $\{dmp(PI)_2\}FeBr_2$ and magenta $\{dmp(PI)_2\}FeCl_2$ compounds could be

readily synthesized through mixture of a THF solution of {dmp(PI)$_2$} with a THF slurry of the appropriate FeX_2 salt at room temperature. The resulting coordination compounds were virtually insoluble in THF and discolored in strongly coordinating solvents such as CH_3CN, rendering characterization via NMR spectroscopy difficult. In order to increase solubility {dmp(PI)$_2$}FeX_2 was treated with 2.0 equiv ^{neo}PeLi to facilitate characterization, but intractable reaction mixtures were generated. Similarly, a soluble {dmp(PI)$_2$}Fe(alk)$_2$ (alk = CH_3, ^{neo}Pe) complex could not be isolated from reaction of {dmp(PI)$_2$} with $Fe(PMe_3)_2(Me)_2$ or $Fe(py)_4(^{neo}Pe)_2$, but fortunately an H_2O quench of {dmp(PI)$_2$}FeX_2 allowed for quantitative recovery of {dmp(PI)$_2$}, offering indirect evidence for clean formation of {dmp(PI)$_2$}FeX_2 (Scheme 2.4).

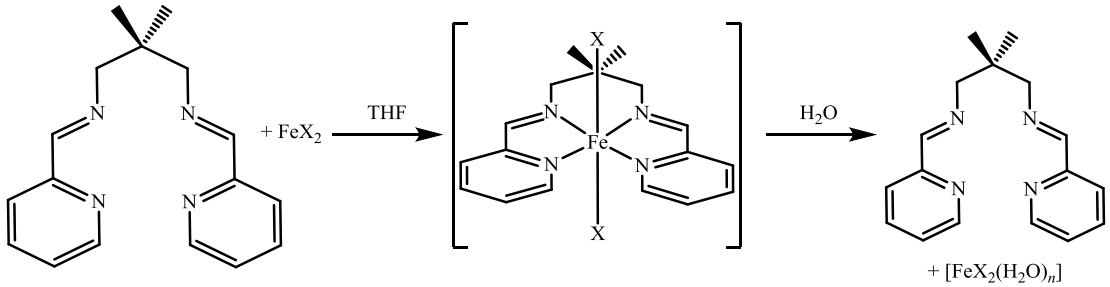

Scheme 2.4. Synthesis and quench of {dmp(PI)$_2$}FeX_2.

Treatment of a THF slurry of {dmp(PI)$_2$}FeX_2 (X = Br, Cl) with 2.0 equiv Na(Hg) or KC_8 in the presence of excess PMe_3 generated **Fe**[0], with concomitant formation of a small amount of uncharacterized, virtually insoluble brown byproduct, demonstrating the viability of {dmp(PI)$_2$}FeX_2 reduction to access complexes of the form {dmp(PI)$_2$}FeL. However, while exposure of {dmp(PI)$_2$}FeX_2 to reducing equivalents in the presence of PMe_2Ph and $PMePh_2$ produced the corresponding iron phosphine compounds, use of more weakly-donating ligands such as pyridine, cyanides, alkynes, or PPh_3 did not result in formation of {dmp(PI)$_2$}FeL. Instead, the

same highly insoluble, diamagnetic species with C_1 symmetry, formed previously during phosphine abstraction from **Fe**[0], was observed in low yield. Additionally, the same product was detected during the reduction of {dmp(PI)$_2$}FeX$_2$ in the presence of 2,3-dihydrofuran or 3,3-diphenylcyclopropene, suggesting that initial reduction of {dmp(PI)$_2$}FeX$_2$ may produce [{dmp(PI)$_2$}Fe] transiently, which in the absence of strongly-donating phosphine traps will undergo further reaction to generate the observed C_1-symmetric product.

Exposure of **Fe**[0] to CO resulted in ligand exchange to form forest green {dmp(PI)$_2$}FeCO, which could also be produced through reduction of {dmp(PI)$_2$}FeX$_2$ under a CO atmosphere (Scheme 2.5). {dmp(PI)$_2$}FeCO is a diamagnetic compound, and ^{1}H NMR assignments are given in Table 2.10. While

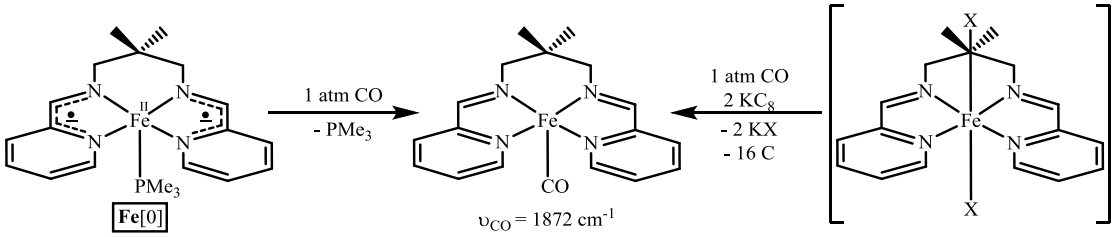

Scheme 2.5. Synthesis of {dmp(PI)$_2$}FeCO. Note that the electronic structure of {dmp(PI)$_2$}FeCO has *not* been determined and is illustrated for convenience here with neutral pyridine imine fragments.

most of the proton chemical shifts of {dmp(PI)$_2$}FeCO were quite similar to those of **Fe**[0], the imine C-H protons of {dmp(PI)$_2$}FeCO were shifted somewhat upfield ($\Delta\delta$ = 0.75) relative to **Fe**[0]. While this could indicate a greater amount of electron density on the ligand backbone, the presence of the carbonyl ligand would also alter the electronics at the metal center and could account for the variation in chemical shift. One would predict that substitution of PMe$_3$ for the more π-withdrawing CO ligand would decrease the electron density at the metal center, which would in turn decrease

the electron density on the {dmp(PI)$_2$} ligand backbone. Hence, the differences in chemical shift between {dmp(PI)$_2$}FePMe$_3$ and {dmp(PI)$_2$}FeCO are likely a reflection of different coordination environments rather than an indication of formal ligand oxidation state change. The IR stretching frequency of the CO fragment (ν_{CO} = 1872 cm^{-1}) is quite reduced relative to free CO (ν_{CO} = 2143 cm^{-1}),[84] suggesting a substantial amount of π-backdonation from the metal center to CO and further supporting a highly covalent interaction between CO and the Fe^{II} metal center. Unfortunately, {dmp(PI)$_2$}FeCO was stable with respect to CO loss under thermolytic or photolytic conditions, so reactivity presumably mirrored that of **Fe**[0] and further studies were not carried out.

Table 2.10. ^{1}H NMR data (δ, coupling (mult, *J*) in Hz) of {dmp(PI)$_2$}FeCO and {dmp(PI)$_2$}FePMe$_3$ (**Fe**[0]) acquired in C_6D_6 in a 400 MHz spectrometer.

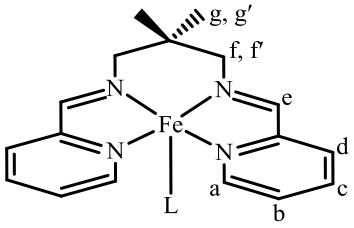

Compound	a	b	c	d	e	f	f’	g	g'
{dmp(PI)$_2$}FeCO	9.28 (d, 5)	6.45 (t, 6)	6.71 (t, 7)	7.02 (d, 8)	7.56	3.71 (d, 13)	3.28 (d, 13)	0.89	0.80
{dmp(PI)$_2$}FePMe$_3$	9.51 (d, 6)	6.75 (t, 7)	6.81 (t, 8)	7.26 (d, 8)	8.31	3.60 (d, 13)	3.31 (d, 13)	1.11	0.73

2.12 Attempts towards the synthesis of {dmp(PI)$_2$}M (M = Mg, Zn, Co, Ti)

Exposure of {dmp(PI)$_2$} to 1.0 equiv Mg^0 in THF at room temperature resulted in formation of a deep magenta solution after 3 d, presumably due to a small amount of {dmp(PI)$_2^{2-}$}Mg^{II}. However, ^{1}H NMR analysis revealed only free {dmp(PI)$_2$} in the reaction mixture and complete consumption of Mg^0 was not observed after 4 wks. A

color change was not observed upon treatment of {dmp(PI)$_2$} with 1.0 equiv Zn^0 in THF, and no consumption of {dmp(PI)$_2$} was observed after 4 wks.

Reaction of {dmp(PI)$_2$} with 1.0 equiv Co(PMe$_3$)$_4$(Me) resulted in immediate precipitation of unidentified, virtually insoluble reaction products, but treatment with Co(PMe$_3$)$_4$ resulted in a color change from brown to blue with concomitant formation of gold solid. The gold solid was virtually insoluble in THF and decomposed in polar solvents such as CD_3CN and CD_2Cl_2, precluding characterization by NMR spectroscopy. ^{1}H NMR spectroscopy on the blue filtrate revealed only free PMe$_3$ in the diamagnetic region (no paramagnetically shifted resonances were observed), and attempts to obtain crystalline material for X-ray analysis are ongoing.

Similar to the reaction with FeX_2 described above, a mixture of {dmp(PI)$_2$} with $TiCl_2(TMEDA)_2$ (TMEDA = tetramethylethylenediamine) triggered release of TMEDA and formation of an insoluble purple-brown precipitate. Treatment of the solid with reducing equivalents in the presence of PMe$_3$ or 3,3-diphenylcyclopropene generated intractable reaction mixtures, and exposure to ^{neo}PeLi or LiHMDS (HMDS = hexamethyldisilazane) in THF or C_6H_6 formed a deep purple product (or mixture of products) that was fully soluble in C_6D_6 but NMR-silent. As such, characterization of the reaction mixture has thus far remained elusive. Fortunately, a quench of the purple-brown solid with H_2O allowed recovery of free {dmp(PI)$_2$}, suggesting the identity of the solid is of the form [{dmp(PI)$_2$}$TiCl_2$]$_n$.

Conclusion

The tetradentate ligand, $dmp(PI)_2$, permitted the synthesis and characterization of a pseudo-square planar nickel complex in five different redox states. The electronic structure of these complexes has been thoroughly investigated through a variety of electrochemical, spectrochemical, magnetic, and computational methods. It was determined that in these complexes the metal center typically remains Ni^{II}, with the possible exception of **Ni**[+], and redox changes are primarily ligand-centered. It is perhaps unsurprising that the oxidation state of Ni in these complexes does not change, as it is well-known that elements will not vary substantially from their stable oxidation states(s), particularly when confined to a stable geometry.[72,85]

The chemistry of $dmp(PI)_2$ was extended to iron, and $\{dmp(PI)_2\}FePMe_3$ (**Fe**[0]) was synthesized and fully characterized. As with **Ni**[0], the electronic structure of **Fe**[0] was determined as a M^{II} center bound to a dianionic ligand framework. **Fe**[0] was capable of two chemical oxidations and two chemical reductions, but because it was expected that **Fe**[0] had similar electronic behavior as **Ni**[0], the thorough electronic structure determination of these redox complexes was not perused. **Fe**[0] was screened for competence in group-transfer reactions, but was unable to cleanly mediate the reactions tested due to the necessity of a strongly-donating PMe_3 ligand to stabilize the $\{dmp(PI)_2\}Fe$ center. Preliminary attempts to metallate $dmp(PI)_2$ with cobalt and titanium are ongoing.

Experimental

General Considerations. All manipulations of air sensitive materials were performed using glove box and high vacuum techniques under an inert atmosphere. Hydrocarbon or ethereal solvents were refluxed over sodium, and vacuum transferred from sodium benzophenone ketyl (with 3–6 mL tetraglyme/L added to hydrocarbons). Benzene-d_6 was heated to reflux over sodium to dry and vacuum transferred from freshly cut sodium. THF-d_8 was dried over NaK and stored over 4 Å sieves. {dmp$(PI)_2$},[56] $Ni(COD)_2$,[63] $Fe(PMe_3)_4$,[76,77] $AgBAr_4^F$ (BAr_4^F = B(3,5-$CF_3(C_6H_3)$)$_4$),[79] and {dmp$(PI)_2^{2-}$}Ni^{II} [56] were prepared according to literature procedures. CO (Matheson) was dried via passage through dry ice traps. All other chemicals were commercially available and used as received. All glassware was oven dried for a minimum of 2 h. NMR tubes for sealed tube experiments and glass bombs were flame dried under dynamic vacuum prior to use.

^1H, $^{13}C\{^1H\}$, ^{13}C and $^{31}P\{^1H\}$ NMR spectra were obtained on Varian INOVA 400, Varian INOVA 500, and Varian Mercury 300 spectrometers and chemical shifts are reported relative to benzene-d_6 (^1H, δ 7.16; $^{13}C\{^1H\}$, δ 128.39) and THF-d_8 (^1H, δ 3.58; $^{13}C\{^1H\}$, δ 67.57) and multidimensional techniques were conducted using INOVA software affiliated with the spectrometers. UV-visible spectra were obtained on a Cary 60 UV/Vis spectrometer. Solution magnetic measurements were conducted via Evans' method.[70,71] Elemental analyses were performed by Complete Analysis Laboratories, Inc., Parsippany, New Jersey, or by the laboratory of Professor Karsten Meyer, University of Erlangen – Nuremberg, Department of Chemistry & Pharmacy, Egerlandstr. 1, D-91058 Erlangen, Germany.

Synthesis. 1. [{dmp(PI)$_2^-$}$_2$Ni^{II}]$^+$(OTf$^-$) (*sol'n*) and [{dmp(PI)$_2$}$_2$Ni^{II}Ni^0]$^{2+}$ (OTf$^-$)$_2$ (Ni[2+]Ni[0]) (*sol. st.*). To a 25 mL flask charged with **Ni**[0] (0.250 g, 0.74 mmol) and AgOTf (0.190 g, 0.74 mmol) cooled to −78 °C was vacuum transferred 10 mL of acetonitrile (10 mL). The solution was stirred at 23 °C for 1 h, and the solution changed from dark green to red-orange. The solution was filtered to remove Ag^0 and yield a solution of the monomer, **Ni**[+]. The acetonitrile was removed *in vacuo*. The red-orange residue was triturated ten times with 10 mL potions of THF, dissolved in 5 mL THF, cooled to −78 °C, filtered, and dried in vacuo to yield 0.252 g (0.48 mmol, 65%) of red-orange, crystalline **Ni**[2+]**Ni**[0]. UV-vis (THF) = 390 nm (ε ~ 2900 M^{-1} cm^{-1}), 440 nm (ε ~ 2800 M^{-1} cm^{-1}), 830 nm (ε ~ 2100 M^{-1} cm^{-1}), 940 nm (ε ~ 1600 M^{-1} cm^{-1}). Anal. calcd for $C_{18}H_{20}F_3N_4NiO_3S$: C, 44.29%; H, 4.13%; N, 11.68%. Found: C, 44.13, 44.20%; H, 4.27, 4.07%; N, 11.04, 11.07%.

2. [{dmp(PI)$_2$}Ni^{II}]$^{2+}$(PF$_6^-$)$_2$ (Ni[2+]). To a 25 mL round bottom flask charged with **Ni**[0] (150. mg, 0.442 mmol) and Cp_2FePF_6 (293 mg, 0.885 mmol) at −78 °C was vacuum transferred 15 mL acetonitrile. The solution was allowed to warm to 23 °C, and turned from forest green to orange-red to pale yellow over 5 min. The reaction was allowed to stir an additional 12 h, and solvent was removed *in vacuo* to yield a pale yellow powder. Crystalline product (210. mg, 0.280 mmol, 63%) was obtained as dark yellow needles from slow diffusion of Et_2O into a saturated CH_3CN solution over two days at room temperature. μ_{eff} (Evans' Method, CD_3CN, 25 °C) = 2.9 μ_β. Anal. calcd for $C_{23}H_{29}F_{12}N_7NiP_2$: C, 36.73%; H, 3.89%; N, 13.04%. Found: C, 36.69%: H, 3.870%; N, 13.01%.

3. [{dmp(PI)$_2^{3-}$}Ni^{II}]$^-$(K(THF)$_2$)$^+$ (Ni[−]). To a 20 mL vial charged with **Ni**[0] (200. mg, 0.590 mmol) and KC_8 (80. mg, 0.59 mmol) at 23 °C was added 10 mL THF. Over 30 min, the forest green color darkened to deep brown. The vial was capped and stirred for 2d. The reaction mixture was filtered through celite and the volatiles were removed *in vacuo*. Crystalline product was obtained as long brown needles from slow diffusion of pentane into a saturated 1 : 1 THF–pentane solution over 24 hours at 23 °C (180. mg, 0.345 mmol, 58%). μ_{eff} (Evans' Method, THF-d_8, 25 °C) = 1.7 μ_B. Anal. calcd for $C_{25}H_{36}KN_4NiO_2$: C, 57.48%; H, 6.95%; N, 10.73%. Found: C, 57.61%; H, 6.89%; N, 10.66%.

4. [{dmp(PI)$_2^{3-}$}Ni^{II}]$^-$(K(crypt-2.2.2))$^+$ (Ni[−]). To a 20 mL vial charged with crystalline [{dmp(PI)$_2^{3-}$}Ni^{II}]$^-$(K(THF)$_2$)$^+$ (**Ni**[−]) (20. mg, 0.038 mmol) and 3 mL THF was dropwise added a 2 mL solution of crypt-222 (14 mg, 0.37 mmol). The resulting solution was quickly filtered, and the filtrate placed in a capped vial at 23 °C for 14 h. Small brown blocks suitable for X-ray diffraction were isolated.

5. [{dmp(PI)$_2^{4-}$}Ni^{II}]$^{2-}$[Cs$^+$(THF)$_n$]$_2$ (Ni[2−]). To a 20 mL vial charged with **Ni**[0] (100. mg, 0.295 mmol) and Cs° (78 mg, 0.59 mmol) at 23 °C was added 10 mL THF. The forest green color darkened to purple-brown over 20 min and stirring was continued for 24 h. Solvent was removed *in vacuo* to yield a deep purple-brown solid (110. mg, 62%). ^{1}H NMR (THF-d_8, 400 MHz, 23 °C): δ 0.81 (s, *g*, 6H), 2.06 (s, *f*, 4H), 4.05 (t, J = 5 Hz, *b*, 2H), 4.11 (s, *e*, 2H), 4.97 (dd, J = 5 Hz, 9 Hz, *c*, 2H), 5.21 (d, J = 9 Hz, *d*, 2H), 6.25 (d, J = 5 Hz, *a*, 2H). ^{13}C NMR (THF-d_8, 100 MHz, 23 °C): δ 25.17 (*g*), 37.90 (*i*), 67.65 (*f*), 91.60 (*b*), 114.33 (*e*), 114.66 (*d*), 118.50 (*c*), 134.81 (*h*), 149.20 (*a*). See below for labeling scheme.

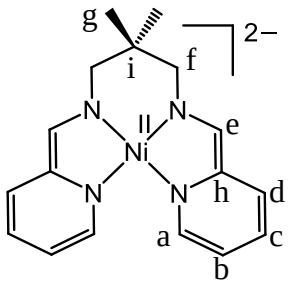

6. [{dmp(PI)$_2$$^{4-}$}Ni^{II}]$^{2-}$[K$^+(THF)_n$]$_2$ (Ni[2−]). To a 25 mL flask charged with Ni[0] (150. mg, 0.442 mmol) and K° (35 mg, 0.90 mmol) at −78 °C was transferred 10 mL THF. The solution warmed to 23 °C, and darkened from green to brown. After stirring for 3 days, no more K° was visible and the solvent was removed to yield a red-brown solid. ^{1}H NMR (THF-d_8, 400 MHz, 25 °C): δ 0.84 (s, *g*, 6H), 2.20 (s, *f*, 4H), 4.02 (t, J = 5 Hz, *b*, 2H), 4.16 (s, *e*, 2H), 4.87 (dd, J = 5 Hz, 9 Hz, *c*, 2H), 5.22 (d, J = 9 Hz, *d*, 2H), 6.15 (d, J = 5 Hz, *a*, 2H). See above for labeling scheme.

7. [{2-py,3-PI,4-Me$_2$-azacyclopent-2-ene^{2-}}$_2$Ni]$^{2-}$ [K$^+$(crypt-2.2.2)]$_2$ (Ni[AcPP]). To a 20 mL vial charged with crude **Ni**[2−](K$^+$(THF)$_2$)$_2$ (20. mg) was added 2 mL THF. A 2 mL solution of crypt-2.2.2 (49 mg, 0.13 mmol) was added dropwise at 23 °C. The deep brown solution was filtered into a 5 mL vial, capped, and allowed to stand at −30 °C. After 3 days, brown needles (~5 mg) suitable for X-ray diffraction were obtained.

8. {dmp(PI)$_2$}FePMe$_3$ (Fe[0]). To a 25 mL flask charged with dmp(PI)$_2$ (0.219 g, 0.78 mmol) and Fe(PMe$_3$)$_4$ (0.281 g, 0.78 mmol) at −78 °C was added 10 mL benzene via vacuum transfer. The solution was allowed to thaw and warm to 23 °C, and the solution turned dark brown. Stirring was maintained 18 h, and the solution was filtered and volatiles removed *in vacuo*. The residual solid was triturated with two 5 mL portion of pentane, redissolved in 10 mL pentane, cooled to −78 °C, and filtered to

yield the brown product as a microcrystalline powder (0.145 g, 0.35 mmol, 45%). ^{1}H NMR (C_6D_6, 400 MHz, 23 °C): δ 0.24 (s, P(C*H*$_3$)$_3$, 9H), 0.73 (s, *g*, 6H), 3.31 (d, J = 13 Hz, *f'*, 2H), 3.60 (d, J = 13 Hz, *f*, 2H), 6.75 (t, J = 7 Hz, *b*, 2H), 6.81 (t, J = 8 Hz, *c*, 2H), 7.26 (d, J = 8 Hz, *d*, 2H), 8.31 (s, *e*, 2H), 9.51 (d, J = 6 Hz, *a*, 2H). ^{31}P NMR (C_6D_6, 162 MHz, 23 °C): δ 15.30 (s, *P*(CH$_3$)$_3$). See below for number scheme. Anal. calcd. for $C_{20}H_{29}FeN_4P$: C, 58.26%; H, 7.09%; N, 13.59%. Found: C, 56.38%; H, 6.86%; N, 13.56%.

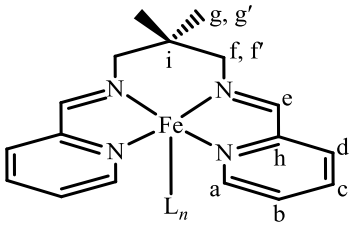

9. [{dmp(PI)$_2$}Fe(PMe$_3$)$_n$][K(THF)$_m$] (Fe[-]). To a 20 mL vial charged with **Fe**[0] (15 mg, 0.036 mmol) and KC_8 (5 mg, 0.04 mmol) at 23 °C was added 2 mL THF. Over 2 h the dark brown color faded to turquoise. The vial was capped and stirred for 2d. The reaction mixture was filtered through celite to remove carbon and the volatiles were removed *in vacuo*. The green powder was redissolved in THF-d_8 for NMR analysis. ^{1}H NMR (THF-d_8, 400 MHz, 23 °C, assignments tentative): δ -59.20 ($\nu_{1/2}$ = 3040 Hz, py-C*H*, 2H), -14.97 ($\nu_{1/2}$ = 370 Hz, P(C*H*$_3$)$_3$, 18H), -7.87 ($\nu_{1/2}$ = 350 Hz, C*H*$_2$, 4H), 1.35 ($\nu_{1/2}$ = 80 Hz, C*H*$_3$, 6H), 30.28 ($\nu_{1/2}$ = 1710 Hz, py-C*H*, 4H), 36.77 ($\nu_{1/2}$ = 3180 Hz, py-C*H*, 2H). Imine C*H* not found. μ_{eff} (Evans' Method, THF-d_8, 25 °C) = 1.4 μ_β.

10. [{dmp(PI)$_2$}Fe(PMe$_3$)][K(THF)$_m$]$_2$ (Fe[2-]). To a 20 mL vial charged with **Fe**[0] (15 mg, 0.036 mmol) and KC_8 (10. mg, 0.072 mmol) at 23 °C was added 2

mL THF. Over 2 h the dark brown color faded to turquoise, then darkened to brown again over 12 h. The capped vial was stirred for 2d, the reaction mixture was filtered through celite to remove carbon, and the volatiles were removed *in vacuo*. The brown powder was redissolved in THF-d_8 for NMR analysis. ^{1}H NMR (THF-d_8, 400 MHz, 23 °C, assignments tentative): δ -115.57 ($\nu_{1/2}$ = 390 Hz, py-C*H*, 2H), -58.63 ($\nu_{1/2}$ = 580 Hz, py-C*H*, 2H), -24.95 ($\nu_{1/2}$ = 460 Hz, py-C*H*, 2H), -9.67 ($\nu_{1/2}$ ~ 540 Hz, Im-C*H*, 2H), -8.58 ($\nu_{1/2}$ = 160 Hz, P(CH_3)$_3$, 9H), 23.08 ($\nu_{1/2}$ = 940 Hz, py-C*H*, 2H). Methylene CH_2 and methyl CH_3 not found.

11. [{dmp(PI)$_2$}Fe(PMe$_3$)](BAr$_4^F$) (Fe[+]). To a 20 mL vial charged with **Fe**[0] (10. mg, 0.024 mmol) was added 2 mL THF. A 2 mL solution of AgBAr$_4^F$ (24 mg, 0.024 mmol) in THF was added dropwise at 23 °C. Over 30 min, the dark brown color deepened to forest green. The vial was capped and stirred for 2d. The reaction mixture was filtered through celite to remove Ag^0 and the volatiles were removed *in vacuo*. The resulting deep green powder was redissolved in THF-d_8 for NMR analysis. ^{1}H NMR (THF-d_8, 400 MHz, 23 °C, assignments tentative): δ -18.62 ($\nu_{1/2}$ = 1130 Hz, im-C*H*, 2H), -12.02 ($\nu_{1/2}$ = 560 Hz, py-C*H*, 2H), -1.49 ($\nu_{1/2}$ = 65 Hz, P(CH_3)$_3$, 9H), 9.75 ($\nu_{1/2}$ = 300 Hz, CH_3, CH_2, 10H), 13.30 ($\nu_{1/2}$ = 170 Hz, py-C*H*, 2H), 18.10 ($\nu_{1/2}$ = 180 Hz, py-C*H*, 2H), 23.38 ($\nu_{1/2}$ = 530 Hz, py-C*H*, 2H). μ_{eff} (Evans' Method, THF-d_8, 25 °C) = 1.5 μ_β.

12. {dmp(PI)$_2$}Fe(PMe$_3$)$_2$](BAr$_4^F$)$_2$ (Fe[2+]). To a 20 mL vial charged with **Fe**[0] (10. mg, 0.024 mmol) was added 2 mL THF. A 2 mL solution of AgBAr$_4^F$ (47 mg, 0.48 mmol) in THF was added dropwise at 23 °C. Over 2 h, the dark brown color faded to purple-magenta. The vial was capped and stirred for 2d. The reaction mixture

was filtered through celite to remove Ag^0 and the volatiles were removed *in vacuo*. The resulting magenta powder was redissolved in THF-d_8 for NMR analysis. ^{1}H NMR (THF-d_8, 400 MHz, 23 °C): δ 0.76 (s, P(CH_3)$_3$, 18H), 1.21 (s, *g*, 6H), 4.01 (s, *f*, 4H), 7.58 (s, B[3,5-CF_3(C_6H_3)]$_4$, 8H), 7.79 (s, B[3,5-CF_3(C_6H_3)]$_4$, 16H), 7.93 (t, J = 7 Hz, *b*, 2H), 8.25 (d, J = 7 Hz, *d*, 2H), 8.35 (t, J = 7 Hz, *c*, 2H), 9.13 (d, J = 5 Hz, *a*, 2H), 9.21 (s, *e*, 2H). See above for number scheme.

13. {dmp(PI)$_2$}FeBr$_2$. To a 20 mL vial charged with $FeBr_2(THF)_2$ (100. mg, 0.278 mmol) was added 8 mL THF. An 8 mL solution of {dmp(PI)$_2$} (78 mg, 0.28 mmol) in THF was added dropwise at 23 °C while stirring vigorously. Over 10 min, a bright yellow virtually insoluble precipitate formed. The solution was filtered and the precipitate was washed with three 10 mL portions of THF to yield bright yellow {dmp(PI)$_2$}$FeBr_2$ (128 mg, 0.258 mmol, 93%).

14. {dmp(PI)$_2$}FeCO. To a J. Young tube charged with {dmp(PI)$_2$}$FePMe_3$ (**Fe**[0], 10. mg, 0.024 mmol) at −78 °C was added C_6D_6 (0.4 mL). Carbon monoxide (1 atm) was admitted to the NMR tube and the solution was allowed to warm to 23 °C. Upon warming, the solution turned from deep brown to forest green. ^{1}H NMR (C_6D_6, 400 MHz, 23 °C): δ 0.80 (s, *g*, 6H), 3.28 (d, J = 13 Hz, *f'*, 2H), 3.71 (d, J = 13 Hz, *f*, 2H), 6.45 (t, J = 6 Hz, *b*, 2H), 6.71 (t, J = 7 Hz, *c*, 2H), 7.02 (d, J = 8 Hz, *d*, 2H), 7.56 (s, *e*, 2H), 9.28 (d, J = 5 Hz, *a*, 2H). See above for labeling scheme. IR (C_6D_6): 1872 cm^{-1}.

15. Oxidative quench of [{dmp(PI)$_2^{4-}$}Ni^{II}]$^{2-}$[Cs$^+$(THF)$_n$]$_2$ (Ni[2−]). To a J. Young tube charged with [{dmp(PI)$_2^{4-}$}Ni^{II}]$^{2-}$[Cs$^+$(THF)$_n$]$_2$ (**Ni**[2−], 30 mg, 0.05 mmol) and Cp_2FePF_6 (16 mg, 0.048 mmol) at −78 °C was added THF-d_8 (0.4 mL).

Upon thawing, solid precipitated, and the ^{1}H NMR spectrum revealed production of Cp_2Fe. A second equiv. of Cp_2FePF_6 (16 mg, 0.048 mmol) was added, resulting in an immediate color change to forest green and formation of more precipitate. ^{1}H NMR analysis revealed formation of **Ni**[0] and a second equiv. of Cp_2Fe. Calibration to an internal TMS standard revealed approximately 75% overall conversion.

16. Comproportionation of $[\{dmp(PI)_2^{3-}\}Ni^{II}]^-(K(THF)_2)^+$ and $[\{dmp(PI)_2\}_2Ni^{II}Ni^0]^{2+}$ $(OTf^-)_2$. To a J. Young tube charged with $[\{dmp(PI)_2^{3-}\}Ni^{II}]^-(K(THF)_2)^+$ (**Ni**[−], 18 mg, 0.034 mmol) and $[\{dmp(PI)_2\}_2Ni^{II}Ni^0]^{2+}$ $(OTf^-)_2$ (**Ni**[2+]**Ni**[0], 15 mg, 0.015 mmol) at −78 °C was added CD_3CN (0.4 mL). Upon thawing, the solution changed to a forest green color and light brown solid precipitated out of solution. ^{1}H NMR analysis revealed formation of **Ni**[0], and calibration to an internal TMS standard revealed approximately 90% conversion.

Calculations. Calculations were performed on geometry-optimized molecules using version 2.8.0 of the ORCA quantum chemistry suite.[86] Geometries were optimized using the BP86[87] density functional with the def2-TZVP(-f) basis set.[87-89] Solvation was modeled by the conductor-like screening model (COSMO)[90] using a dielectric of 7.6 (THF). Electronic energies and properties were calculated at these geometries using the B3LYP functional,[91-93] the scalar-relativistically contracted def2-TZVP(-f) basis set,[94] and the zeroth order regular approximation for relativistic effects (ZORA),[95,96] and COSMO(THF). The integration accuracy was increased for Ni (ORCAGRID14). EPR properties were calculated using coupled perturbation Kohn–Sham (KS) theory for the g-tensor[97] and the spin–orbit coupling (SOC) operator was

treated by the spin–orbit mean-field approximation.[98] Molecular orbital diagrams were constructed following quasi-restricted orbital (QRO) transformations of the unrestricted Kohn–Sham (UKS) solutions.[99] In cases where broken symmetry (BS)[100-102] solutions were generated, molecular orbital energies were taken as the average of UKS spin–orbital pairs. BS solutions are only reported when they are significantly lower in energy than the UKS calculation; only Ni[0] met this criterion. Magnetically interacting non-orthogonal orbitals were identified using the corresponding orbital transformation as previously described.[103]

Spectroscopy-oriented configuration interaction (SORCI) calculations were performed as described previously[104] to calculate excitation energies and the g-matrix for Ni[+].[105]Calculations were performed over a CAS(13,11) complete active space, which includes the Ni ligand field as well as proximal PI π and π* as well as pyridine π* molecular orbitals. The def2-TZVP(-f) basis set was used for all atoms.[94] As described elsewhere, individual selection was used in order to ease the computational burden.[94] The size of the first-order interacting space was reduced with a threshold Tsel = 10−6 Eh. A further approximation involved reduction of the reference space through another selection – all initial references that contribute less than a second threshold (Tpre = 10−5) to the zeroth-order states were rejected from the reference space. The initial orbitals from the first step of the SORCI procedure were taken from QROs[99] generated via standard B3LYP/def2-TZVP-ZORA calculations described herein.

Magnetic susceptibility measurements. Magnetic susceptibility measurements of crystalline powdered samples (10–20 mg) were performed on a

Quantum Design MPMS-5 SQUID magnetometer at 10 kOe (1 T) between 5 and 300 K for all samples. All sample preparations and manipulations were performed under an inert atmosphere due to the air sensitivity of the samples. The samples were measured in gelatin capsules, and the diamagnetic contribution from the sample container was subtracted from the experimental data. Pascal's constants[106] were used to subtract diamagnetic contributions, yielding paramagnetic susceptibilities. The program julX written by E. Bill was used for (elements of) the simulation and analysis of magnetic susceptibility data.[107]

EPR Spectroscopy. Solution and frozen glass EPR spectra were recorded on a JEOL continuous wave spectrometer, JES-FA200 equipped with an X-band Gunn oscillator bridge, a cylindrical mode cavity, and a helium cryostat. For all samples, a modulation frequency of 100 kHz and a time constant of 0.1 s were employed. Frequencies were close to 9.0 GHz and all spectra were obtained on freshly prepared solutions in quartz tubes. Background spectra were obtained on clean solvents at the same measurement conditions. Spectral simulations were performed using the programs W95EPR by Prof. Dr. Frank Neese[108] and ESRSIM by Prof. Dr. Høgni Weihe, University of Copenhagen, Denmark. Collinear *g* and *A* tensors were used, and deviations from isotropic parameters in spectra of frozen glasses were only used when clearly justified.

Single-Crystal X-ray Diffraction Studies. Upon isolation, crystals were covered in polyisobutenes and placed under a 173 K N_2 stream on the goniometer head of a Siemens P4 SMART CCD area detector (graphite-monochomated Mo Kα radiation, $\lambda = 0.71073$ Å). The structures were solved by direct methods (SHELXS).

All non-hydrogen atoms were refined anisotropically unless otherwise stated, and hydrogen atoms were treated as idealized contributions (Riding model).

*Crystal data for **Ni**[2+]**Ni**[0]*: $C_{36}H_{40}N_8O_6F_6S_2Ni$, M = 976.30, triclinic, P-1, a = 10.0760(7), b = 10.6657(7), c = 19.6623(14) Å, α = 90.050(3)°, β = 97.940(3)°, γ = 105.384(3)°, V = 2016.3(2) Å^3, T = 173(2), Z = 2, R_{int} = 0.0235, 33779 reflections, 9861 independent, R_1(all data) = 0.0385, wR_2 = 0.0733, GOF = 1.016.

*Crystal data for **Ni**[2+](PF6)$_2$·NCMe:* $C_{23}H_{29}N_7F_{12}P_2Ni$, M = 752.18, monoclinic, Cc, a = 9.2230(4), b = 23.7522(8), c = 15.2139(6) Å, β = 107.3500(10)°, V = 3181.2(2) Å^3, T = 173(2), Z = 4, R_{int} = 0.0143, 15695 reflections, 7932 independent, R_1(all data) = 0.0303, wR_2 = 0.0796, GOF = 1.051.

*Crystal data for **Ni**[−](K(THF)$_2$)*: $C_{25}H_{36}N_4O_2KNi$, M = 522.39, monoclinic, P2(1)/n, a = 10.5982(8), b = 12.3634(8), c = 19.8165(13) Å, β = 95.155(3)°, V = 2586.0(3) Å^3, T = 173(2), Z = 4, R_{int} = 0.0246, 25673 reflections, 6390 independent, R_1(all data) = 0.0511, wR_2 = 0.0952, GOF = 1.016.

*Crystal data for **Ni**[−](K(crypt-2.2.2))*: $C_{35}H_{56}N_6O_6KNi$, M = 754.67, monoclinic, P21c, a = 12.7277(11), b = 21.000(2), c = 28.837(3) Å, β = 99.126(4)°, V = 7610.2.0(13) Å^3, T = 173(2), Z = 8, R_{int} = 0.0896, 35129 reflections, 8405 (4964 2σ) independent, R_1(2σ) = 0.0695, wR_2 = 0.1682, GOF = 1.012.

*Crystal data for **Ni**[AcPP]:* $C_{70}H_{106}N_{12}O_{12}K_2Ni$, M = 1444.58, monoclinic, C2/c, a = 34.460(7), b = 10.852(5), c = 23.144(4) Å, β = 100.903(4)°, V = 2586.0(3) Å^3, T = 243(2), Z = 4, R_{int} = 0.0455, 24183 reflections, 6091 independent, R_1(all data) = 0.0676, wR_2 = 0.0942, GOF = 0.989.

*Crystal data for **Fe**[0]:* $C_{20}H_{29}FeN_4P$, M = 412.29, monoclinic, P2(1)/n, a =13.2546(5), b =9.6896(3), c = 15.8409(5) Å, β = 91.0510(10)°, V = 2034.13(12) Å^3, T = 193(2), Z = 4, R_{int} = 0.0248, 21768 reflections, 6451 independent, R_1(all data) = 0.0443, wR_2 = 0.0963, GOF = 1.042.

REFERENCES

1. Frazier, B. A.; Wolczanski, P. T.; Lobkovsky, E. B. *Inorg. Chem.* **2009,** *48,* 11576 – 11585.

2. Frazier, B. A.; Wolczanski, P. T.; Lobkovsky, E. B.; Cundari, T. R. *J. Am. Chem. Soc.* **2009,** *131,* 3428 – 3429.

3. Frazier, B. A.; Williams, V. A.; Wolczanski, P. T.; Bart, S. C.; Meyer, K.; Cundari, T. R.; Lobkovsky, E. B. *Inorg. Chem.* **2013,** *52,* 3295 – 3312.

4. Kahn, S. D.; Hehre, W. J.; Pople, J. A. *J. Am. Chem. Soc.* **1987,** *109,* 1871 – 1873.

5. Volpe, E. C.; Wolczanski, P. T.; Lobkovsky, E. B. *Organometallics* **2010,** *29,* 364 – 377.

6. Hulley, E. B.; Wolczanski, P. T.; Lobkovsky, E. B. *J. Am. Chem. Soc.* **2011,** *133,* 18058 – 18061.

7. Lu, C. C.; Bill, E.; Weyhermüller, T.; Bothe, E.; Wieghardt, K. *J. Am.Chem. Soc.* **2008,** *130,* 3181 – 3197.

8. Trifonov, A. A.; Fedorova, E. A.; Borovkov, I. A.; Fukin, G. K.; Baranov, E. V.; Larionova, J.; Druzhkov, N. O. *Organometallics* **2007,** *26,* 2488 – 2491.

9. Mondal, A.; Weyhermüller, T.; Wieghardt, K. *Chem. Commun.* **2009,** 6098 – 6100.

10. Zhu, D.; Budzelaar, P. H. M. *Organometallics* **2010,** *29,* 5759 – 5761.

11. Zhu, D.; Korobkov, I.; Budzelaar, P. H. M. *Organometallics* **2012,** *31,* 3958 – 3971.

12. Knijnenburg, Q.; Hetterscheid, D.; Kooistra, T. M.; Budzelaar, P. H. M. *Eur. J. Inorg. Chem.* **2004,** 1204 – 1211.

13. Zhu, D.; Thapa, I.; Korobkov, I.; Gambarotta, S.; Budzelaar, P. H. M. *Inorg. Chem.* **2011,** *50,* 9879 – 9887.

14. Knijnenburg, Q.; Gambarotta, S.; Budzelaar, P. H. M. *Dalton Trans.* **2006,** 5442 – 5448.

15. Budzelaar, P. H. M. *Eur. J. Inorg. Chem.* **2012,** 530 – 534.

16. Heyduk, A. F.; Zarkesh, R. A.; Nguyen, A. I. *Inorg. Chem.* **2011,** *50,* 9849 – 9863.

17. Ray, K.; Petrenko, T.; Wieghardt, K.; Neese, F. *Dalton Trans.* **2007,** 1552 – 1566.

18. De Bruin, B.; Hetterscheid, D. G. H.; Koekkoek, A. J. J.; Grutzmacher, H. *Prog. Inorg. Chem.* **2007,** *55*, 247 – 354.

19. Blanchard, S.; Derat, E.; Desage-El Murr, M.; Fensterbank, L.; Malacria, M.; Mouries-Mansuy, V. *Eur. J. Inorg. Chem.* **2012,** 376 – 389.

20. Khusniyarov, M. M.; Weyhermüller, T.; Bill, E.; Wieghardt, K. *J. Am.Chem. Soc.* **2009,** *131*, 1208 – 1221.

21. Darmon, J. M.; Stieber, S. C.; Sylvester, K. L.; Fernández, I.; Lobkovsky, E.; Semproni, S. P.; Bill, E.; Wieghardt, K.; DeBeer, S.; Chirik, P. J. *J. Am. Chem. Soc.* **2012,** *134*, 17125 – 17137.

22. Bart, S. C.; Lobkovsky, E.; Bill, E.; Chirik, P. J. *J. Am. Chem. Soc.* **2006,** *128*, 5302 – 5303.

23. Sylvester, K. T.; Chirik, P. J. *J. Am. Chem. Soc.* **2009,** *131*, 8772 – 8773.

24. Bouwkamp, M. W.; Bowman, A. C.; Lobkovsky, E.; Chirik, P. J. *J. Am. Chem. Soc.* **2006,** *128*, 13340 – 13341.

25. Russell, S. K.; Lobkovsky, E.; Chirik, P. J. *J. Am. Chem. Soc.* **2011,** *133*, 8858 – 8861.

26. Russell, S. K.; Lobkovsky, E.; Chirik, P. J. *J. Am. Chem. Soc.* **2009,** *131*, 36 – 37.

27. Monfette, S.; Turner, Z. R.; Semproni, S. P.; Chirik, P. J. *J. Am. Chem. Soc.* **2012,** *134*, 4561 – 4564.

28. Russell, S. K.; Darmon, J. M.; Lobkovsky, E.; Chirik, P. J. *Inorg. Chem.* **2010,** *49*, 2782 – 2792.

29. Yu, R. P.; Darmon, J. M.; Hoyt, H. M.; Margulieux, G. W.; Turner, Z.; Chirik, P. J. *ACS Catal.* **2012,** *2*, 1760 – 1764.

30. Tondreau, A. M.; Darmon, J. D.; Wile, B. M.; Floyd, S. K.; Lobkovsky, E. B.; Chirik, P. J. *Organometallics* **2009,** *28*, 3928 – 3940.

31. Trovitch, R. J.; Lobkovsky, E.; Bill, E.; Chirik, P. J. *Organometallics* **2008,** *27*, 1470 – 1478.

32. Bart, S. C.; Lobkovsky, E.; Chirik, P. J. *J. Am. Chem. Soc.* **2004,** *126*, 13794 – 13807.

33. Archer, A. M.; Bouwkamp, M. W.; Cortez, M. -P.; Lobkovsky, E.; Chirik, P. J. *Organometallics* **2006,** *25,* 4269 – 4278.

34. Tondreau, A. M.; Atienza, C. C. H. A.; Weller, K. J.; Nye, S. A.; Lewis, K. M.; Delis, J. G. P.; Chirik, P. J. *Science* **2012,** *335,* 567 – 570.

35. Tondreau, A. M.; Atienza, C. C. H. A.; Darmon, J. M.; Milsmann, C.; Hoyt, H. M.; Weller, K. J.; Nye, S. A.; Lewis, K. N.; Boyer, J.; Delis, J. G. P.; Lobkovsky, E.; Chirik, P. J. *Organometallics* **2012,** 4886 – 4893.

36. Atienza, C. C. H. A.; Tondreau, A. M.; Weller, K. J.; Lewis, K. M.; Cruse, R.; Nye, S. A.; Boyer, J. L.; Delis, J. P.; Chirik, P. J. *ACS Catal.* **2012,** *2,* 2169 – 2172.

37. Tondreau, A. M.; Lobkovsky, E.; Chirik, P. J. *Org. Lett.* **2008,** *10,* 2789 – 2792.

38. Atienza, C. C. H. A.; Milsmann, C.; Lobkovsky, E.; Chirik, P. J. *Angew. Chem. Int. Ed.* **2011,** *50,* 8143 – 8147.

39. Tondreau, A. M.; Milsmann, C.; Patrick, A. D.; Hoyt, H. M.; Lobkovsky, E.; Wieghardt, K.; Chirik, P. J. *J. Am. Chem. Soc.* **2010,** *132,* 15046 – 15059.

40. Bouwkamp, M. W.; Lobkovsky, E.; Chirik, P. J. *J. Am. Chem Soc.* **2005,** *127,* 9660 – 9661.

41. Atienza, C. C. H. A.; Bowman, A. C.; Lobkovsky, E.; Chirik, P. J. *J. Am. Chem. Soc.* **2010,** *132,* 16343 – 16345.

42. Trovitch, R. J.; Lobkovsky, E.; Bouwkamp, M. W.; Chirik, P. J. *Organometallics* **2008,** *27,* 6264 – 6278.

43. Trovitch, R. J.; Lobkovsky, E.; Chirik, P. J. *J. Am. Chem. Soc.* **2008,** *130,* 11631 – 11640.

44. Bowman, A. C.; Bart, S. C.; Heinemann, F. W.; Meyer, K.; Chirik, P. J. *Inorg. Chem.* **2009,** *48,* 5587 – 5589.

45. Obligacion, J. V.; Chirik, P. J. *J. Am. Chem. Soc.* **2013,** *135,* 19107 – 19110.

46. Obligacion, J. V.; Chirik, P. J. *Org. Lett.* **2013,** 15, 2680 – 2683.

47. Obligacion, J. V.; Semproni, S. P.; Chirik, P. J. *J. Am. Chem. Soc.* **2014,** *136,* 4133 – 4136.

48. Haneline, M. R.; Heyduk, A. F. *J. Am. Chem. Soc.* **2006,** *128,* 8410 – 8411.

49. Blackmore, K. J.; Ziller, J. W.; Heyduk, A. F. *Inorg. Chem.* **2005,** *44,* 5559 – 5561.

50. Zarkesh, R. A.; Ziller, J. W.; Heyduk, A. F. *Angew. Chem. Int. Ed.* **2008,** *47,* 4715 – 4718.

51. Blackmore, K. J.; Lal, N.; Ziller, J. W.; Heyduk, A. F. *J. Am. Chem. Soc.* **2008,** *130,* 2728 – 2729.

52. Nguyen, A. I.; Zarkesh, R. A.; Lacy, D. C.; Thorson, M. K.; Heyduk, A. F. *Chem. Sci.* **2011,** *2,* 166 – 169.

53. Ketterer, N. A.; Fan, H.; Blackmore, K. J.; Yang, X.; Ziller, J. W.; Baik, M. -H.; Heyduk, A. F. *J. Am. Chem. Soc.* **2008,** *130,* 4364 – 4374.

54. Williams, V. A.; Hulley, E. B.; Wolczanski, P. T.; Lancaster, K. M.; Lobkovsky, E. B. *Chem. Sci.* **2013,** *4,* 3636 – 3648.

55. Schunn, R. A. *Inorg. Synth.* 1974, *15,* 5 – 9.

56. Hulley, E. B. Ph.D. Thesis, Cornell University, Ithaca, NY, **2011.**

57. Kanamori, J. *Phys. Chem. Solids* **1959,** *10,* 87 – 88.

58. Goodenough, J. B. *Phys. Chem. Solids* **1958,** *6,* 287 – 297.

59. Girerd, J. -J.; Journaux, Y. "Molecular Magnetism in Bioinorganic Chemistry": in *Physical Methods in Bioinorganic Chemistry: Spectroscopy and Magnetism,* Que, L. Ed; University Science Books, Sausalito, CA, **2000**.

60. Noodleman, L.; Norman, J. G. *J. Chem. Phys.* **1979,** *70,* 4903 – 4906.

61. Noodleman, L. *J. Chem. Phys.* **1980,** *74,* 5737 – 5743.

62. Nesse, F. *J. Phys. Chem. Solids* **2004,** *65,* 781 – 785.

63. Derning, D. E.; Miedaner, A.; Curtis, C. J.; Noll, B. C.; DuBois, M. C. R.; DuBois, D. L. *Organometallics* **2001,** *20,* 1832 – 1839.

64. Derning, D. E.; Noll, B. C.; DuBois, D. L. *J. Am. Chem. Soc.* **1999,** *121,* 11432 – 11447.

65. Redin, K.; Wilson, A. D.; Newell, R.; R. DuBois, M. C.; DuBois, D. L. *Inorg. Chem.* **2007,** *46,* 1268 – 1276.

66. Tereniak, S. J.; Marlier, E. E.; Lu, C. C. *Dalton Trans.* **2012,** *41,* 7862 – 7865.

67. Bontempelli, G.; Magno, F.; Schiavon, G.; Corain, B. *Inorg. Chem.* **1981,** *20,* 2579 – 2586.

68. Bontempelli, G.; Magno, F. *J. Electroanal. Chem.* 1979, **103**, 243 – 350.

69. Daniele, S.; Basato, M.; Corain, B.; Favero, G.; Bontempelli, G. *J. Chem. Soc. Dalton Trans.* **1988,** 1425 – 1428.

70. Evans, D. F. *J. Chem. Soc.* **1959,** 2003 – 2005.

71. Schubert, E. M. *J. Chem. Ed.* **1992,** *69*, 62.

72. Figgis, B. N.; Hitchman, M. A. *Ligand Field Theory and Its Applications*; Wiley-VCH: New York, 2000.

73. Ciszewski, J. T.; Mikhaylov, D. Y.; Holin, K. V.; Kadirov, M. K.; Budnikova, Y. H.; Sinyashin, O.; Vicic, D. A. *Inorg. Chem.* **2011,** *50*, 8630 – 8635.

74. Frazier, B. A.; Williams, V. A.; Wolczanski, P. T.; Bart, S.; Meyer, K.; Cundari, T. R.; Lobkovsky, E. B. *Inorg. Chem.* **2013,** *52,* 3295 – 3312.

75. Carter, S. M.; Sia, A.; Shaw, M. J.; Heyduk, A. F. *J. Am. Chem. Soc.* **2008,** *130*, 5838 – 5839.

76. Karsch, H. H. *Chem. Ber.* **1977**, *110*, 2699 – 2711.

77. Bhattacharya, P.; Krause, J. A.; Guan, H. *Organometallics*, **2011**, *30*, 4720 – 4729.

78. Addison, A. W.; Rao, T. N.; Reedijk, J.; van Rijn, J.; Verschoor, G. C. *J. Chem. Soc., Dalton Trans.* **1984,** 1349 – 1356.

79. Buschmann, W. E.; Miller, J. S. *Inorg. Synth.* **2002,** *33,* 83 – 91.

80. Connelly, N. G.; Geiger, W. E. *Chem. Rev.* **1996,** *96*, 877 – 910.

81. Smith, A. L.; Hardcastle, K. I.; Soper, J. D. *J. Am. Chem. Soc.* **2010,** *132*, 14358 – 14360.

82. Smith, L. I.; Howard, K. L. *Org. Synth.* **1944**, *24*, 53.

83. Gandelman, M.; Rybtchinski, B.; Ashkenazi, N.; Gauvin, R. M.; Milstein, D. *J. Am. Chem. Soc.* **2001,** *123,* 5372 – 5373.

84. Braterman, P. S. *Metal Carbonyl Spectra.* Academic Press: London, 1975.

85. Pauling, L. *J. Chem. Soc.* **1948,** 1461.

86. Neese, F. ; Wennmohs, F.; Becker, U.; Ganyushin, D.; Hansen, A.; Liakos, D. G.; Kollmar, C.; Kossmann, S.; Petrenko, T.; Reimann, C.; Riplinger, C.; Sivalingam, K.; Valeev, E.; Wezisla, B. *Version 2.8.0 Orca Quantum Chemistry Suite* University of Bonn: Bonn, Germany 2010.

87. Perdew, J. P.; Wang, Y. *Phys. Rev. B* **1992,** *45*, 13244 – 13249.

88. Schäfer, A.; Horn, H.; Ahlrichs, R. *J. Chem. Phys.* **1992,** *97*, 2571 – 2577.

89. Weigend, F.; Ahlrichs, R. *Phys. Chem. Chem. Phys.* **2005**, *7*, 3297 – 3305.

90. Klamt, A.; Schuurmann, G. *J. Chem. Soc., Perkin Trans. 2* **1993**, 799.

91. Becke, A. D. *J. Chem. Phys.* **1993,** *98*, 1372 – 1377.

92. Lee, C.; Yang, W.; Parr, R. G. *Phys. Rev. B* **1988,** *37*, 785 – 789.

93. Stephens, P. J.; Devlin, F. J.; Chabalowski, C. F.; Frisch, M. J. *J. Chem. Phys.* **1994,** *98*, 11623 – 11627.

94. Pantazis, D. A.; Chen, X. -Y.; Landis, C. R.; Neese, F. *J. Chem. Theory Comput.* **2008,** *4*, 908 – 919.

95. Van Lenthe, E.; van der Avoird, A.; Wormer, P. E. S. *J. Chem. Phys.* **1998,** *108*, 4783 – 4796.

96. Van Wüllen, C. *J. Chem. Phys.* **1998,** *109*, 392 – 399.

97. Neese, F. *J. Chem. Phys.* **2001,** *115*, 11080 – 11096.

98. Neese, F. *J. Chem. Phys.* **2005,** *122*, 34107.

99. Neese, F. *J. Am. Chem. Soc.* **2006,** *128*, 10213 – 10222.

100. Noodleman, L. *J. Chem. Phys.* **1981,** *74*, 5737 – 5743.

101. Noodleman, L.; Case, D. A.; Aizman, A. *J. Am. Chem. Soc.* **1988,** *110*, 1001 – 1005.

102. Noodleman, L.; Peng, C. Y.; Case, D. A.; Mouesca, J.-M. *Coord. Chem. Rev.* **1995,** *144*, 199 – 244.

103. Neese, F. *J. Chem. Phys. Solids* **2004,** *65*, 781 – 785.

104. Neese, F. *J. Chem. Phys.* **2003,** *119*, 9428 – 9443.

105. Neese, F. *Mag. Reson. Chem.* **2004,** *42*, 187 – 198.

106. Carlin, R. L. *Magnetochemistry*; Springer-Verlag: Berlin, 1986.

107. http://ewww.mpi-muelheim.mpg.de/bac/logins/bill/julX_en

108. Neese, F.; Zumft, W. G.; Antholine, W. E.; Kroneck, P. M. H. *J. Am. Chem. Soc.* **1996,** *118*, 8692 – 8699.

Chapter 3

Iron Complexes Derived from Tetradentate β-Diketiminate Ligands and Stabilization of Fe^{II} via Redox-Non-innocence

Introduction

During investigations into ligand frameworks bearing the 2-azaallyl motif that imparts strong ligand fields on first row transition metal complexes, several unique C-C bond forming reactions were discovered (Schemes 2.2, 2.3).[1-6] These couplings could be considered to occur either via radical couplings or nucleophilic/electrophilic attack. Both mechanisms are illustrated in Scheme 3.1 for the formation of

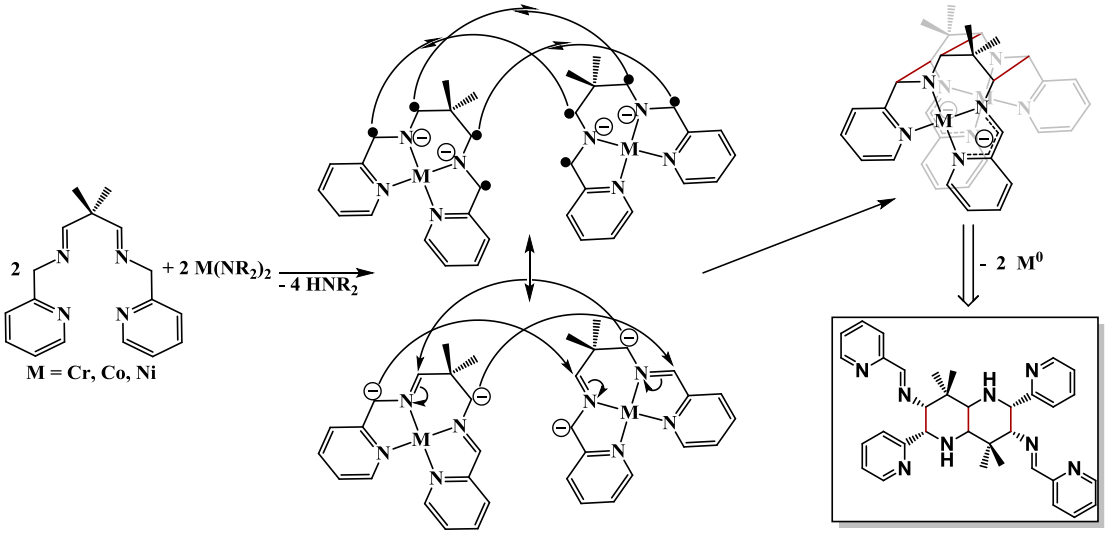

Scheme 3.1. Possible mechanisms for C-C coupling of azaallyl fragments via radical coupling (top) or nucleophilic/electrophilic attack (bottom).

$\{Me_2C(CHNCHpy)_2M\}_2$ (M = Cr, Co, Ni).[4] The reactions were proposed to proceed in part due to the stabilization afforded by redox noninnocent moieties on the ligand frameworks (*cf.* Chapter 2), which could serve as a reservoir for electrons and allow the formation of stable M^{II} centers. As C-C bond formation processes are some of the most important chemical transformations mediated by transition metals, these ligand

couplings showed potential utility in synthesis of cyclic frameworks. In particular, the coupling shown in Scheme 3.1 allowed formation of three C-C bonds with simultaneous generation of six new stereocenters in a single chemical reaction. The organic framework could be quenched from the metal center (M = Ni), resulting in a stereospecific polycyclic molecule (boxed).

Efforts towards extending these C-C bond formation reactions centered on the design of new ligand motifs through removal of the geminal-dimethyl group and incorporation of a β-diketiminate fragment, which could allow for coupling at the mid-carbon of the ligand backbone,[7-72] linked to a pyridine imine fragment that could serve as a redox noninnocent electron reservoir.[73-81] Several possibilities for new ring formations are illustrated in Figure 3.1, and newly formed bonds are highlighted in red. The starting ligand has three acidic positions circled in blue, and deprotonation at a methylene site allows for formation of a pyridine imine moiety.

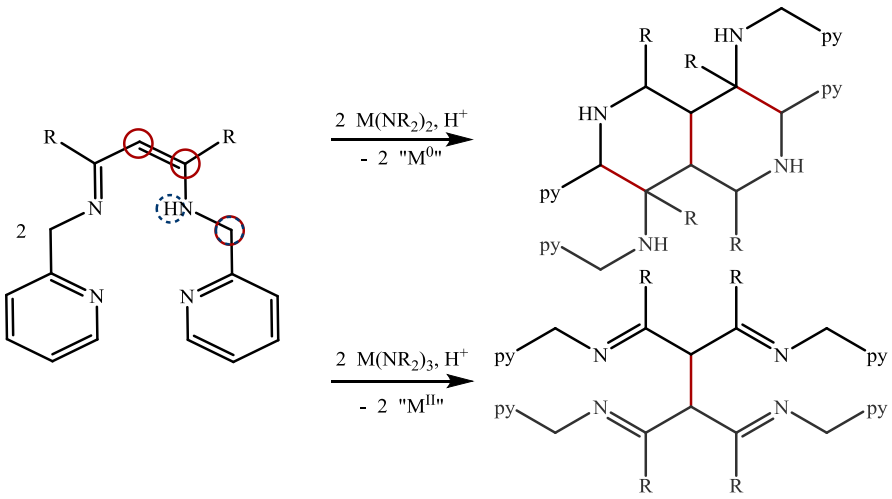

Figure 3.1. Possible C-C bond couplings achievable through deprotonation of a β-diketiminate ligand. Deprotonatable positions are circled in blue (dashed) and coupling sites are circled in red (solid). New C-C bonds are shown in red.

Results and Discussion

3.1. Ligand Synthesis

Initial efforts to synthesize the desired β-diketiminate-based 2,4-bis[(E)-(2-pyridyl)methylideneamino]pentane (H{nn(PM)$_2$}) through direct condensation of 2.0 equiv 2-picolylamine with acetylacetone in the presence of various drying agents and acid catalysts were unsuccessful, even at elevated temperatures and concentrations. Fortunately, H{nn(PM)$_2$} could prepared through sequential condensations over three steps (Scheme 3.2). Reaction of acetylacetone with 1.0 equiv 2-picolylamine in the presence of $MgSO_4$ afforded the mono-condensation product in high yield (93%).[82] Treatment of this compound with 1.0 equiv $(Et_3O)BF_4$ in CH_2Cl_2 at low temperatures resulted in the formation of a tan precipitate, presumably the O-alkylated BF_4 salt, which afforded the salt H_2{nn(PM)$_2$}BF_4 in modest yield (30%) when treated with a second equiv of 2-picolylamine. Deprotonation with KH at elevated temperatures afforded the desired neutral tetradentate ligand H{nn(PM)$_2$} in good yield (83%).

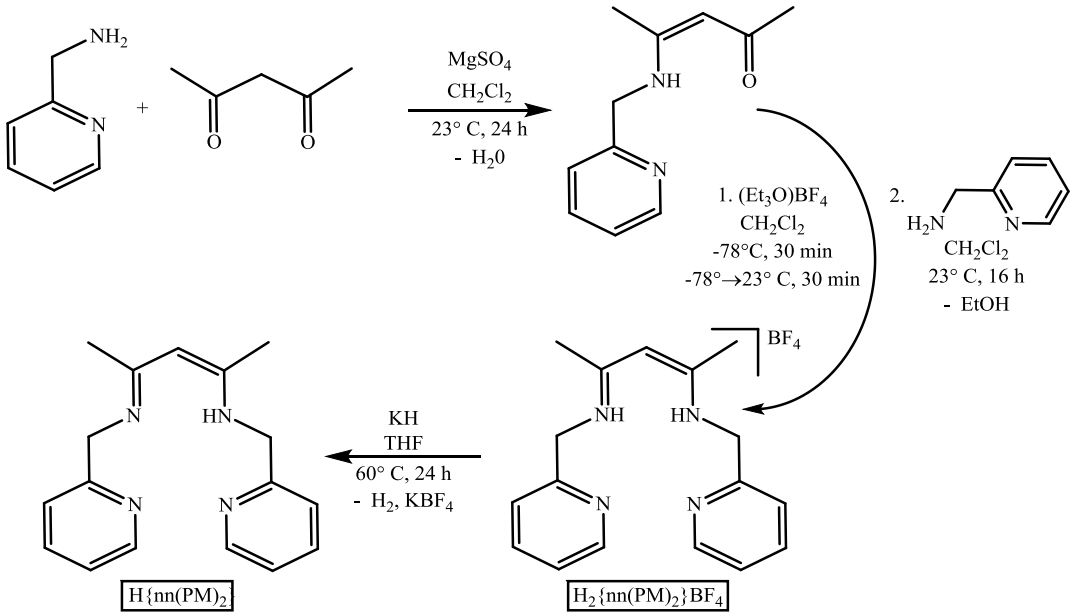

Scheme 3.2. Synthesis of H{nn(PM)$_2$}.

3.2. Synthesis of {nn(PM)$_2$}FeX (X = N(TMS)$_2$, Cl, N$_3$) complexes

3.2.1. {nn(PM)$_2$}FeN(TMS)$_2$

Treatment of H{nn(PM)$_2$} with 1.0 equiv Fe(N(TMS)$_2$)$_2$(THF)[83,84] in C_6H_6 afforded the paramagnetic orange-red amide complex {nn(PM)$_2$}FeN(TMS)$_2$ (**1**-N(TMS)$_2$) in good yield (54 %) (Eq. 3.1). **1**-N(TMS)$_2$ was thermally sensitive and decomposed at room temperature to a brown insoluble material with release of HN(TMS)$_2$, but was stable indefinitely as a solid at -30° C. The complex was highly soluble in organic solvents, and ^{1}H NMR spectroscopy revealed 7 paramagnetically shifted and broadened resonances, indicative of C_s symmetry. Because **1**-N(TMS)$_2$

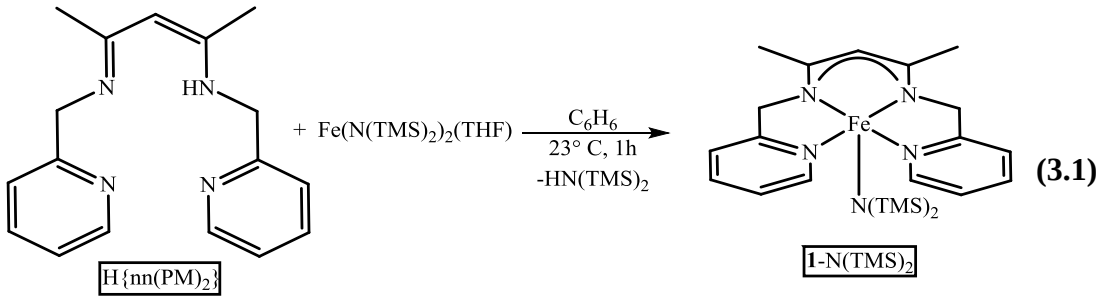

(3.1)

was paramagnetic, Evans Method magnetic measurements were carried out.[85,86] At 23° C, a μ_{eff} of 5.3 μ_β (ave, 2 trials) was determined, indicative of a high-spin, S = 2 metal center with a significant contribution from spin-orbit coupling ($\mu_{spin\text{-}only}$ = 4.90 μ_β).[87,88] Zero-field Mössbauer data were acquired for **1**-N(TMS)$_2$ and are presented in Figure 3.2. Typical isomer shifts (δ) for high-spin Fe^{II} complexes are > 0.8 mms^{-1},[89-91] fully consistent with the observed δ = 0.96(1) mms^{-1} for **1**-N(TMS)$_2$. The quadrupole splitting (ΔE_Q) of 2.84(1) mms^{-1} is quite large and indicates a high degree of electric field asymmetry about the nucleus, as expected of a 5-coordinate complex with three different types of donor ligands in an asymmetric geometric environment.

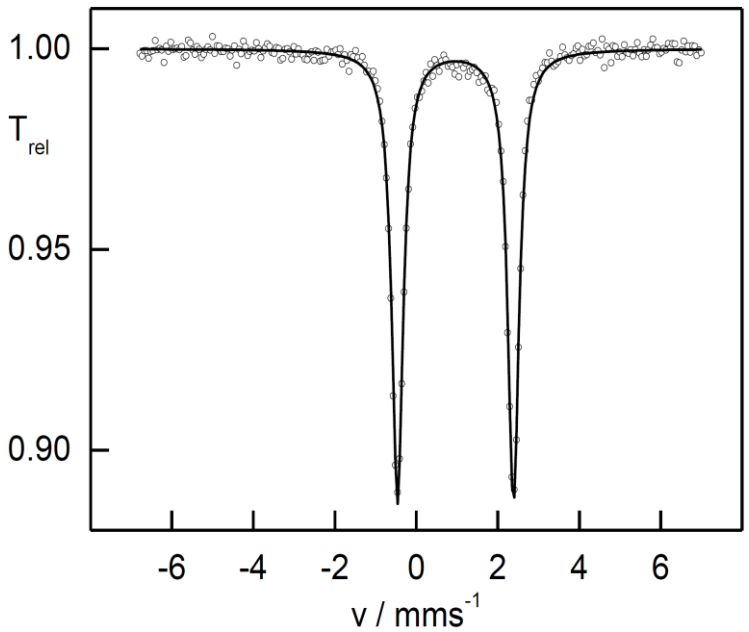

Figure 3.2. Zero field Mössbauer spectrum of {nn(PM)$_2$}Fe(N(TMS)$_2$ (**1**-N(TMS)$_2$). Fit parameters: δ = 0.96(1) mms^{-1}, ΔE_Q = 2.84(1) mms^{-1}, Γ_{FWHM} = 0.34(1) mms^{-1}.

To further probe the structure of **1**-N(TMS)$_2$, a red needle grown from cold pentane was selected and subjected to X-ray analysis. The resulting crystal structure is illustrated in Figure 3.3, and relevant parameters are listed in Table 3.1. There are two molecules in the asymmetric unit related by a mirror plane (dashed line, Figure 3.3). The bond distances and angles of the two molecules identical within 3σ are listed as an average value in Table 3.1. The Fe-N distances, although different between the two molecules, are consistent with a high-spin Fe^{II} center. To describe the geometry about the metal center, it is useful to determine the Addison parameter τ[92] for each iron center. For Fe1 the apical position is N1, with α defined by ∠N3-Fe1-N5 (126.23°) and β defined by ∠N2-Fe1-N4 (149.89°). The resulting value τ = 0.39 is roughly between a trigonal bipyramidal structure (τ = 1) and a square pyramidal structure (τ = 0). For Fe2 the apical position is N6, with α defined by ∠N8-Fe2-N10 (126.02°) and β defined by ∠N9-Fe2-N7 (148.79°). The resulting value τ = 0.38 is very similar to that

of Fe1, again indicative of an intermediate structure between trigonal bipyramidal and square pyramidal.

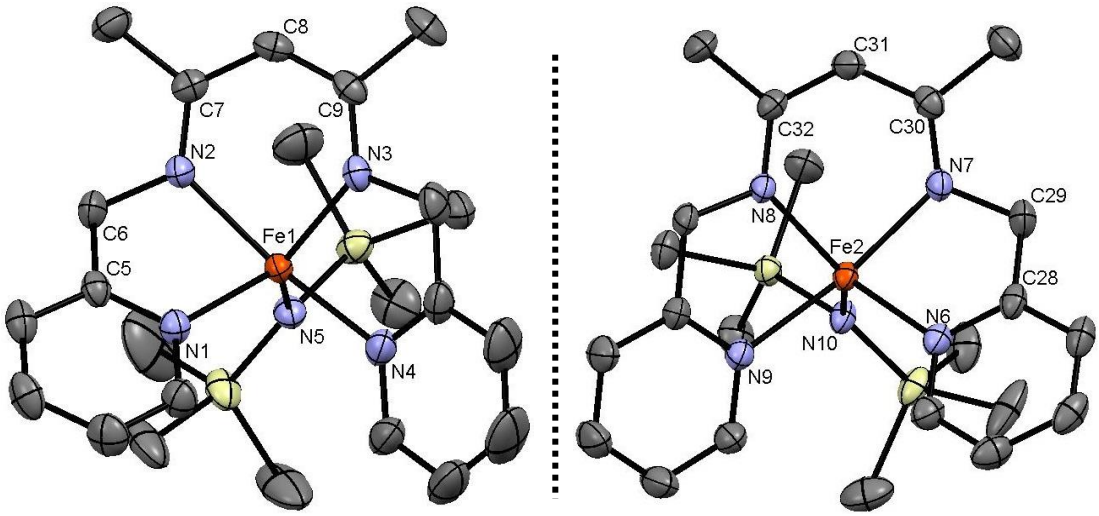

Figure 3.3. Molecular structure of the two independent molecules in the asymmetric unit for **1**-N(TMS)$_2$. Hydrogen atoms have been omitted for clarity.

Table 3.1. Selected interatomic distances and bond angles for **1**-N(TMS)$_2$. Bond distances and angles have been averaged where values for the two independent molecules in the asymmetric unit are identical within 3σ.

Selected Bond Distances (Å)		Selected Bond Angles (°)	
Fe1-N1	2.2342(12)	N1-Fe1-N2	74.69(5)
Fe1-N2	2.1052(12)	N1-Fe1-N3	116.11(5)
Fe1-N3	2.0873(12)	N1-Fe1-N4	91.88(5)
Fe1-N4	2.1974(13)	N1-Fe1-N5	117.64(5)
Fe1-N5	2.0163(12)	N2-Fe1-N3	84.45(5)
N1-C5	1.3442(19)	N2-Fe1-N4	149.34(5)
C5-C6	1.502(2)	N2-Fe1-N5	110.53(5)
C6-N2	1.4553(19)		*114.4(5)*
N2-C7	1.3131(19)	N3-Fe1-N4	98.19(5)
C7-C8	1.408(2)	N3-Fe1-N5	126.13(5)
C8-C9	1.401(2)	N4-Fe1-N5	98.19(5)
C9-N3	1.3265(19)		

3.2.2. {nn(PM)$_2$}FeCl

Exposure of {nn(PM)$_2$}FeN(TMS)$_2$ to 1.0 equiv HCl(g) in C_6H_6 at room

temperature resulted in the gradual precipitation of a yellow solid, formulated as {nn(PM)$_2$}FeCl (**1**-Cl), with concomitant release of HN(TMS)$_2$ (Eq. 3.2). The solid could be recrystallized from hot THF to yield sparingly soluble bright yellow plates of

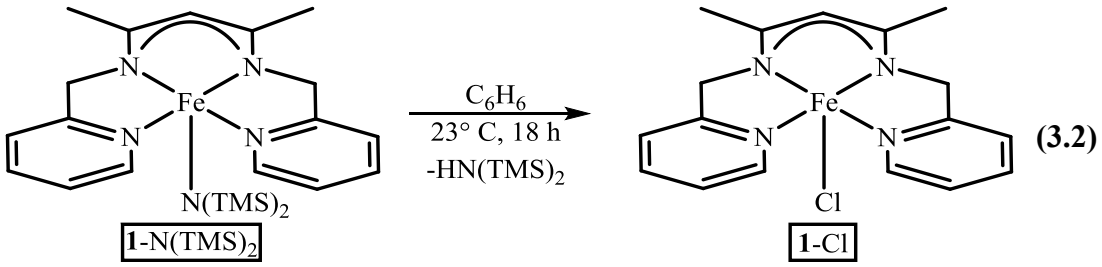

(3.2)

1-Cl (57%). Similar to that observed for **1**-N(TMS)$_2$, ^{1}H NMR spectroscopy revealed 7 paramagnetically shifted and broadened resonances, indicative of C_s symmetry. A comparison of proton chemical shifts is given in Table 3.2, and reveals only minor changes in chemical shift upon substitution of the X-type substituent. In particular, both spectra exhibit a broad upfield resonance attributable to the β-diketiminate backbone proton at δ -80.10 for **1**-N(TMS)$_2$ and δ -74.28 for **1**-Cl, and two relatively sharp resonances at δ 38.38 and 49.17 (**1**-N(TMS)$_2$) and δ 38.26 and 51.87 (**1**-Cl), attributable to two of the pyridine C-H protons. These three resonances are quite characteristic of species of the type {nn(PM)$_2$}FeX.

An Evans Method magnetic susceptibility measurement[85,86] at 23° C revealed a μ_{eff} of 5.3 μ_β, identical to that measured for **1**-N(TMS)$_2$ and indicative of a high-spin, S = 2 iron center with substantial spin-orbit coupling. Zero-field Mössbauer data were acquired for 1-Cl and are presented in Figure 3.4. The isomer shift (δ) of 0.99 mms^{-1} is remarkably similar to that of 1-N(TMS)$_2$ (δ = 0.96(1) mms^{-1}) and suggests a high-spin Fe^{II} center with very similar M-L bonds for the two compounds.[89-91] The quadrupole splitting (ΔE_Q) of 3.42(1) mms^{-1} is larger than that of 1-N(TMS)$_2$ and indicates an

Table 3.2. ^{1}H NMR data (δ, linewidth (*ital.*, $\nu_{1/2}$) in Hz) of **1**-N(TMS)$_2$, **1**-Cl, and **1**-N$_3$ acquired in C_6D_6 (a) or THF-d_8 (b) in a 400 MHz spectrometer. Assignments are tentative.

Compound	C*H*$_3$	nn-C*H*	C*H*$_2$	py-C*H*	py-C*H*	py-C*H*	py-C*H*
1-N(TMS)$_2$[a]	0.42 (*200*)	-80.10 (*450*)	10.75 (*380*)	96.27 (*1380*)	38.38 (*125*)	49.17 (*110*)	-2.45 (*70*)
1-Cl[b]	5.10 (*120*)	-74.28 (*270*)	1.57 (*30*)	146.27 (*770*)	38.26 (*80*)	51.87 (*95*)	-0.05 (*34*)
1-N$_3$[b]	5.93 (*95*)	-82.18 (*278*)	1.29 (*20*)	156.09 (*675*)	40.07 (*105*)	53.45 (*100*)	133.05 (*945*)

even greater degree of electric field asymmetry about the nucleus, as predicted due to the greater difference between a chloride and the nitrogen chelates (**1**-Cl) as compared to the difference between an amide and the four nitrogen chelates (**1**-N(TMS)$_2$).

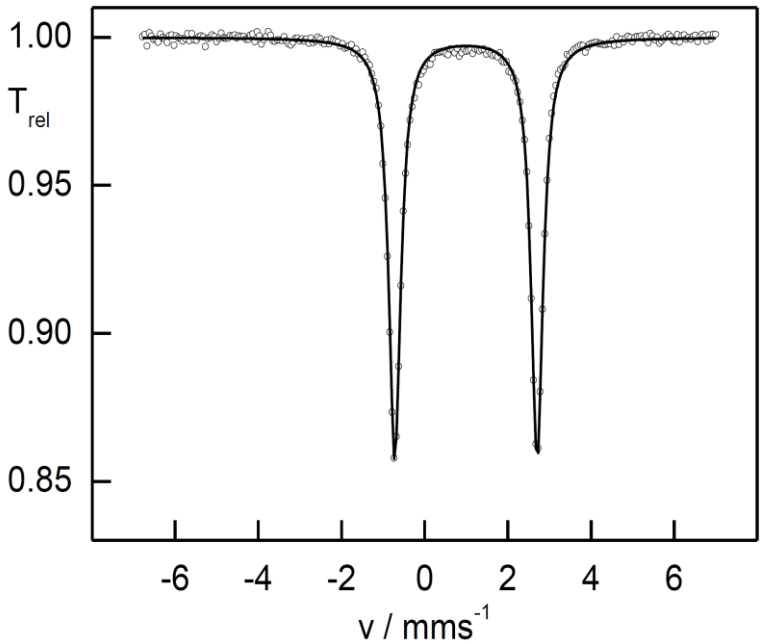

Figure 3.4. Zero field Mössbauer spectrum of {nn(PM)$_2$}FeCl (**1**-Cl). Fit parameters: $\delta = 0.99(1)$ mms^{-1}, $\Delta E_Q = 3.42(1)$ mms^{-1}, $\Gamma_{FWHM} = 0.35(1)$ mms^{-1}.

3.2.3. {nn(PM)$_2$}FeN$_3$

Treatment of {nn(PM)$_2$}FeCl with 1.0 equiv NaN$_3$ at room temperature afforded {nn(PM)$_2$}FeN$_3$ (**1**-N$_3$) as a sparingly soluble orange-yellow material after 4

days (Eq. 3.3). Recrystallization from THF/pentane allowed isolation of orange-yellow plates in 53% yield, and ^{1}H NMR analysis revealed a spectrum consistent with the expected C_s symmetry of **1**-N_3. Proton chemical shifts are listed in Table 3.2 and show the three resonances (δ -82.18, β-diketiminate C*H*; δ 40.07, py- C*H*;

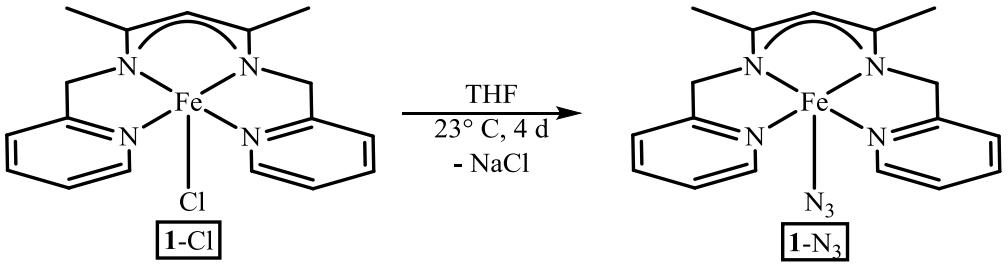

(3.3)

δ 53.45, py-C*H*) characteristic of {nn(PM)$_2$}FeX complexes. IR spectroscopy revealed a ν_{NNN} of 2062 cm^{-1}, further supporting the formation of **1**-N_3.

The synthesis of an iron azide from **1**-N_3 was attempted, but photolysis or thermolysis of **1**-N_3 with or without Lewis acid additives generated only tan insoluble material. One could imagine that photolysis of **1**-N_3 would form the desired Fe^{IV} nitride transiently, which could then undergo inter- or intramolecular H-atom abstraction from the methylene position of the ligand backbone to achieve a more stable Fe^{II} configuration (Scheme 3.3). However, the insolubility of the resulting tan material precluded spectroscopic characterization. Attempts to obtain single crystals for X-ray analysis are currently ongoing. Initial attempts at photolysis and thermolysis

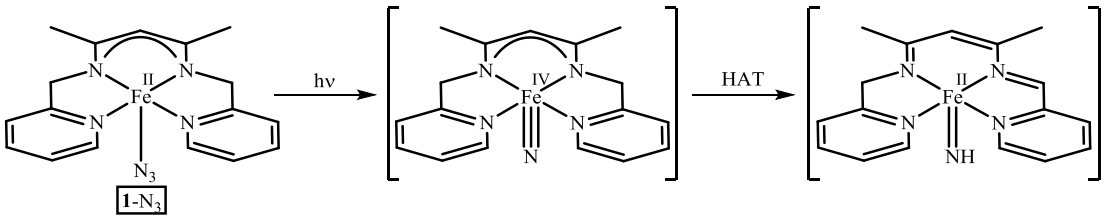

Scheme 3.3. Possible reaction cascade for the photolysis of **1**-N_3. Here, for simplicity H-atom transfer (HAT) is shown as an intramolecular event.

of **1**-N_3 in the presence of H-atom sources such as 9,10-dihydroanthracene and 1,3-cyclohexadiene have revealed no H-atom transfer, implying that if H-atom transfer is occurring, abstraction from the ligand framework is faster than from the organic additive.

3.3. Synthesis of {nn(PM)(PI)}FeLL'^{m} (L = L' = PMe_3, *m* = 0, 1+, 2+; L = PMe_3, L' = CO, *m* = 0) complexes

3.3.1. {nn(PM)(PI)}Fe(PMe_3)$_2$

Because {nn$(PM)_2$}Fe$N(TMS)_2$ (**1**-$N(TMS)_2$) was prone to thermal degradation with concomitant loss of $HN(TMS)_2$, it was conceivable that dehydroamination could be triggered in a controlled fashion. Exposure of **1**-$N(TMS)_2$ to an excess of PMe_3 in C_6H_6 resulted in a color change from orange-red to deep purple-red and release of $HN(TMS)_2$, and new diamagnetic species was observed by ^{1}H NMR spectroscopy. Thirteen resonances were seen in the ^{1}H NMR spectrum, indicating a desymmetrization of the nn$(PM)_2$ ligand backbone via deprotonation of a methylene C*H* to generate {nn(PM)(PI)}Fe$(PMe_3)_2$ (**2**-$(PMe_3)_2$) (Eq. 3.4). Chemical

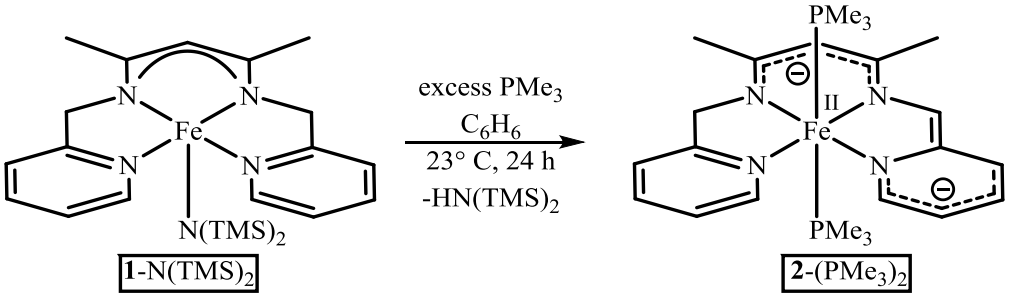

(3.4)

shifts of **2**-$(PMe_3)_2$ are listed in Table 3.7. Of note are the chemical shifts of the imine proton (e, δ 6.47) and the β-diketiminate proton (f, δ 4.99), both of which are shifted upfield, indicating a significant degree of electron density on the ligand backbone. The

doubly deprotonated ligand is in the -2 oxidation state, consistent with observed ^{1}H NMR resonances, and the 18 e^{-} Fe^{II} metal center is electronically saturated.

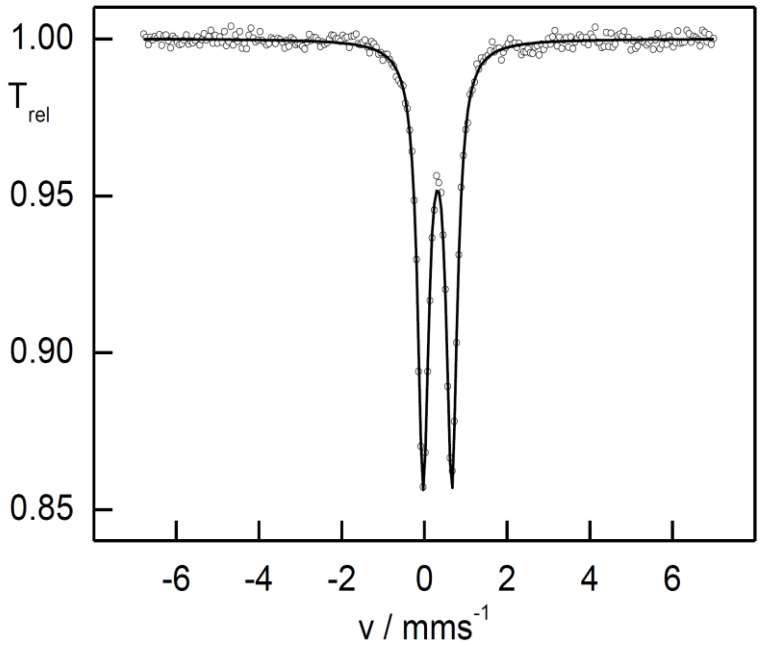

Figure 3.5. Zero field Mössbauer spectrum of {nn(PM)(PI)}$Fe(PMe_3)_2$ (**2**-$(PMe_3)_2$). Fit parameters: δ = 0.32(1) mms^{-1}, ΔE_Q = 0.69(1) mms^{-1}, Γ_{FWHM} = 0.32(1) mms^{-1}.

Zero-field Mössbauer data were acquired for **2**-$(PMe_3)_2$ and are presented in Figure 3.5. The quadrupolar splitting (ΔE_Q) of 0.69(1) mms^{-1} is quite low compared to that of **1**-$N(TMS)_2$ and **1**-Cl (2.84(1) and 3.42(1), respectively) suggesting a much more symmetric electric field about the nucleus, as expected for a complex with pseudo-octahedral geometry about the metal center. Unfortunately an isomer shift of 0.32(1) mms^{-1} is not characteristic of any one iron oxidation and spin state, but *is* outside the range expected for high-spin Fe^{II} complexes.[89-91] Therefore, δ = 0.32 mms^{-1} could correspond to low- or intermediate-spin Fe^{0}, Fe^{I}, or Fe^{II} and exact determination is largely dependent on coordination environment.

X-ray analysis was carried out (Figure 3.6) and confirmed the formulation of **2**-$(PMe_3)_2$. The molecule is pseudo octahedral, with angles of 96.7° (ave) and 176.8°

(ave) (Table 3.3). Bond distances support the dianionic nature of the ligand backbone, as the *d*(C10-C11) of 1.381 Å is within the range expected of a double bond[93] and significantly contracted relative to a standard C(sp^2)-C(sp^2) single bond. The *d*(N4-C11) in the pyridine ring is slightly elongated (1.3972 Å), implicating additional electron density in the backbone. In addition, the β-diketiminate portion of the backbone is roughly symmetric, with *d*(N2-C7) = 1.3453 Å and *d*(N3-C9) = 1.3303 Å, and *d*(C7-C8) = 1.393 Å and *d*(C8-C9) = 1.416 Å, lending credence to the representation of **2**-$(PMe_3)_2$ illustrated in Eq. 3.4. The Fe-N core distances are normal and within the range expected for low-spin octahedral complexes. It is important to note that the well-established metric parameters of related pyridine-imine ligand[94-96] (Figure 2.2) are not applicable here, as charge delocalization into the β-diketiminate framework attenuates the metric differences between each oxidation state.[97-101]

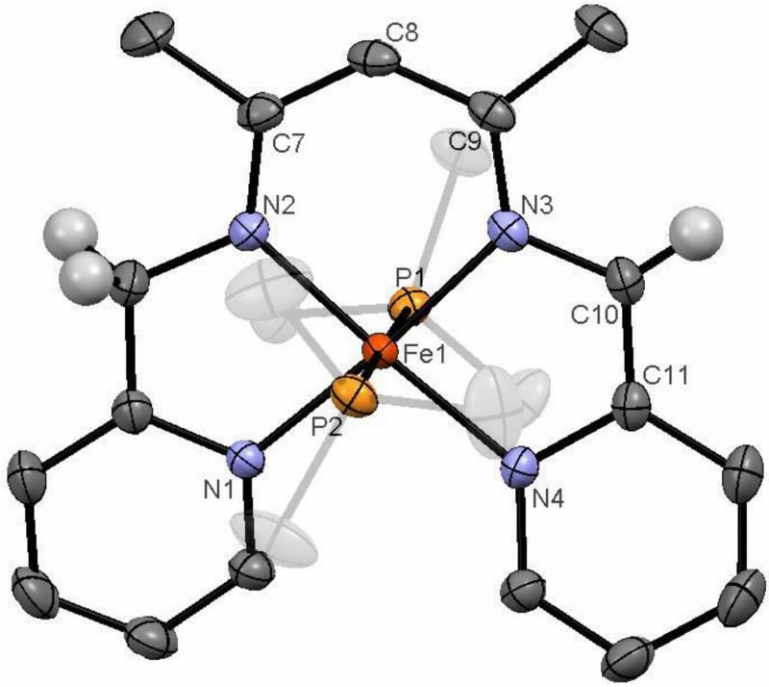

Figure 3.6. Molecular structure of **2**-$(PMe_3)_2$. Phosphine methyl groups and selected hydrogen atoms are omitted for clarity.

Table 3.3. Selected interatomic distances and bond angles for **2**-$(PMe_3)_2$. Distances in bold refer to computed values.

Selected Bond Distances (Å)			Selected Bond Angles (°)	
Fe1-N1	1.9749(11)	**2.010**	N1-Fe1-N2	82.81(4)
Fe1-N2	1.9487(11)	**1.973**	N2-Fe1-N3	93.58(4)
Fe1-N3	1.9648(11)	**1.979**	N3-Fe1-N4	83.05(4)
Fe1-N4	1.9913(11)	**2.025**	N4-Fe1-N1	100.91(4)
Fe1-P1	2.2737(4)	**2.362**	N1-Fe1-P1	87.39(3)
Fe1-P2	2.2629(4)	**2.344**	N1-Fe1-P2	93.18(3)
N4-C11	1.3972(17)	**1.404**	N2-Fe1-P1	91.04(4)
C11-C10	1.3810(19)	**1.384**	N2-Fe1-P2	89.85(4)
C10-N3	1.3931(17)	**1.388**	N3-Fe1-P1	87.22(3)
N3-C9	1.3303(17)	**1.329**	N3-Fe1-P2	92.26(3)
C9-C8	1.416(2)	**1.427**	N4-Fe1-P1	92.64(3)
C8-C7	1.393(2)	**1.394**	N4-Fe1-P2	86.45(3)
C7-N2	1.3453(17)	**1.349**	N1-Fe1-N3	173.45(4)
			N2-Fe1-N4	174.88(5)
			P1-Fe1-P2	178.996(15)

To further probe the electronic structure of **2**-$(PMe_3)_2$, calculations were carried out on the molecule. Calculated bond distances are listed in bold in Table 3.3 and match up well with experiment, and a truncated molecular orbital diagram is given in Figure 3.7. The ligand and metal d-orbitals are quite similar in energy, and a weak interaction between the Fe d_{xz} and a {nn(PM)(PI)} π^b orbital results in bonding and antibonding orbitals that are ~50% metal-based and ~50% ligand-based. Along with the filled d_{xy} and d_{yz} orbitals, these two orbitals comprise a filled "t_{2g}" set corresponding to a d^6 Fe^{II} metal center. The HOMO is a doubly occupied {nn(PM)(PI)} π^* orbital, confirming the dianionic nature of the ligand, and is well below the empty d_{z^2} and $d_{x^2-y^2}$ orbitals in energy.

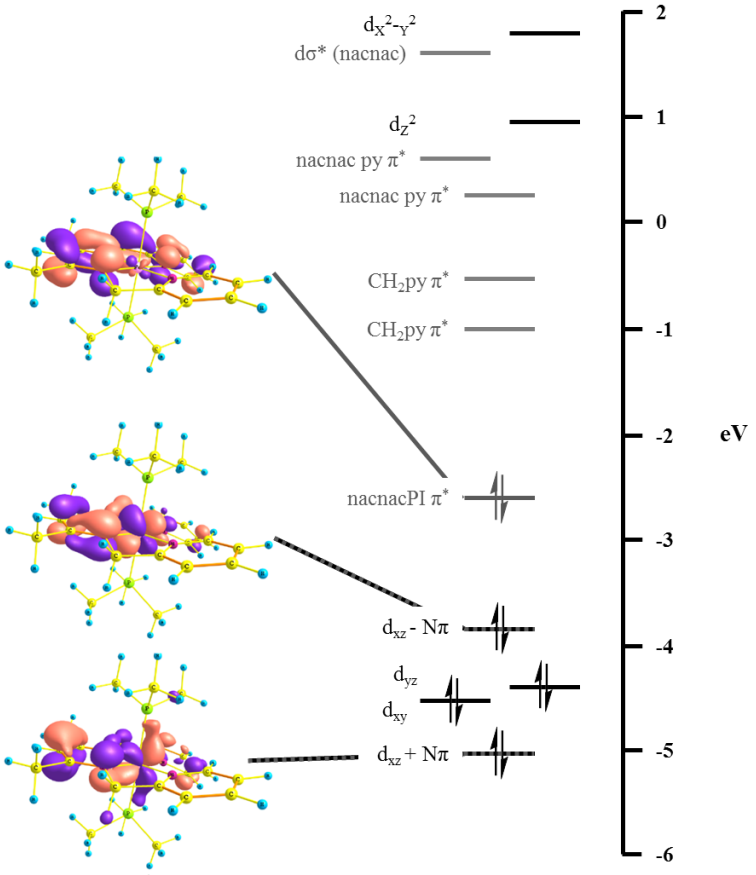

Figure 3.7. Truncated molecular orbital diagram of {nn(PM)(PI)}Fe(PMe_3)$_2$ (**2**-(PMe_3)$_2$) showing a ligand π*-localized HOMO and two molecular orbitals comprised of ~50% Fe d_{xz} and ~50% {nn(PM)(PI)} π^b.

3.3.2. [{nn(PM)(PI)}Fe(PMe_3)$_2$](PF$_6$)

To probe the redox capabilities of {nn(PM)(PI)}, **2**-(PMe_3)$_2$ was treated with 1.0 equiv Cp_2FePF_6 in THF to yield thermally-unstable brown crystals of [{nn(PM)(PI)}Fe(PMe_3)$_2$](PF$_6$) (**2**$^+$-(PMe_3)$_2$) (Eq. 3.5). Evans Method magnetic measurements[85,86] revealed a μ_{eff} of 1.6 ($\mu_{spin\text{-}only}$ = 1.73 μ_β), fully consistent with the expected S = ½ spin state.

Zero-field Mössbauer data for **2**$^+$-(PMe_3)$_2$ are given in Figure 3.8. The spectrum consists of two sets of Kramer's doublets, one corresponding to **2**$^+$-(PMe_3)$_2$

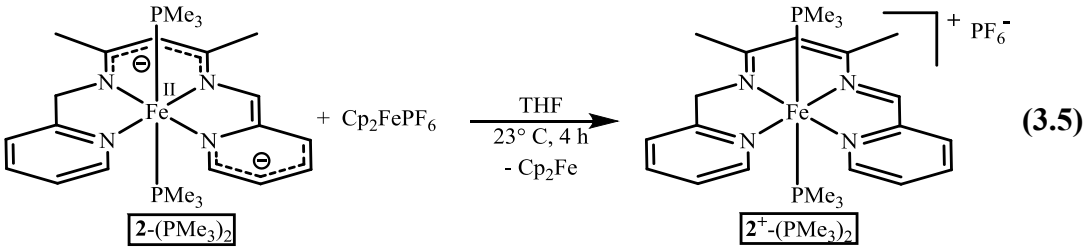

(3.5)

and one corresponding to a compound arising from thermal degradation of $\mathbf{2}^{+}$-$(PMe_3)_2$. The high isomer shift (δ = 1.05 mms^{-1}) and large quadrupole splitting (ΔE_Q = 3.29 mms^{-1}) of the degradation product (Figure 3.8, blue trace) are quite similar to the parameters obtained for **1**-$N(TMS)_2$ (δ = 0.96(1) mms^{-1}, ΔE_Q = 2.84(1) mms^{-1}) and **1**-Cl (δ = 0.99(1) mms^{-1}, ΔE_Q = 3.42(1) mms^{-1}) and are clearly indicative of a high-spin Fe^{II} metal center with significant asymmetry. The isomer shift δ = 0.35(1) mms^{-1} and quadrupole splitting ΔE_Q = 0.52(1) mms^{-1} of $\mathbf{2}^{+}$-$(PMe_3)_2$ are very similar to **2**-$(PMe_3)_2$ (δ = 0.32(1) mms^{-1}, ΔE_Q = 0.69(1) mms^{-1}), demonstrating substantial similarity at the metal center for the two complexes. The Mössbauer data support the formulation of $\mathbf{2}^{+}$-$(PMe_3)_2$ as an Fe^{II} metal center with a singly reduced ligand backbone, $[\{nn(PM)(PI)\}^{-}Fe^{II}(PMe_3)_2]^{+}$, suggesting the one electron oxidation shown in Eq. 3.5 is a ligand-based redox event.[89-91]

Although clearly a decomposition product is present in samples of $\mathbf{2}^{+}$-$(PMe_3)_2$ (Figure 3.8), the observed impurity is a high-spin Fe^{II} complex and is unlikely to exhibit an X-band EPR spectrum. Therefore, clean EPR data were acquired for $\mathbf{2}^{+}$-$(PMe_3)_2$ and are presented in Figure 3.9. A fit of the data revealed a rhombic field with g_1 = 2.014, g_2 = 2.036, and g_3 = 2.125. The average g_{iso} = 2.058 is somewhat similar to that of a free electron and can be interpreted as a ligand-based radical with substantial metal character. However, a metal-based SOMO with a sizeable amount of

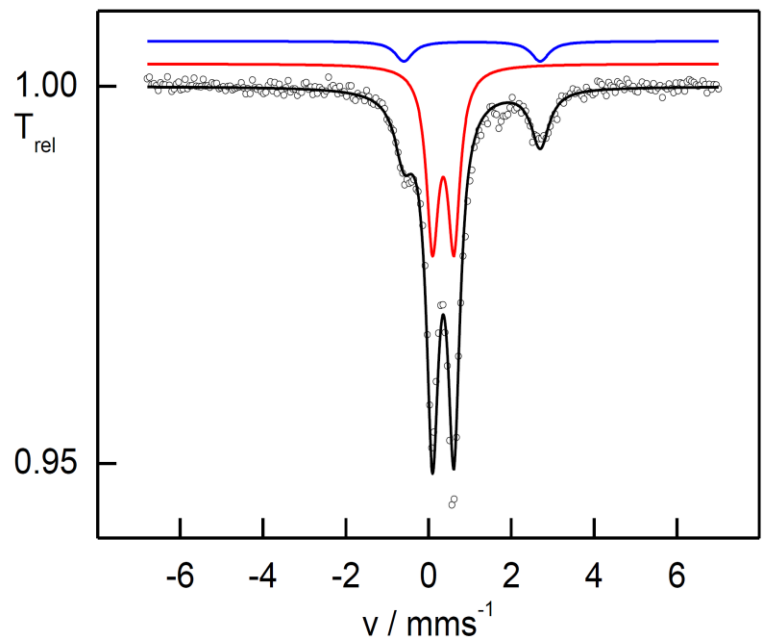

Figure 3.8. Zero field Mössbauer spectrum of [{nn(PM)(PI)}Fe(PMe_3)$_2$](PF_6) (**2**$^+$-(PMe_3)$_2$) with ~20% degradation product. Fit parameters: δ = 0.35(1) mms^{-1}, ΔE_Q = 0.52(1) mms^{-1}, Γ_{FWHM} = 0.36(1) mms^{-1} (**2**$^+$-(PMe_3)$_2$, red trace, ~80%); δ = 1.05(1) mms^{-1}, ΔE_Q = 3.29(1) mms^{-1}, Γ_{FWHM} = 0.35(1) mms^{-1} (Degradation product, blue trace, ~20%).

ligand character cannot be ruled out, and in either depiction, the SOMO is clearly highly covalent.[102-106] Hyperfine coupling is observed for g_3 to the two phosphorus nuclei (A_3 = 256 MHz), as expected for two PMe_3 ligands in a pseudo-octahedral

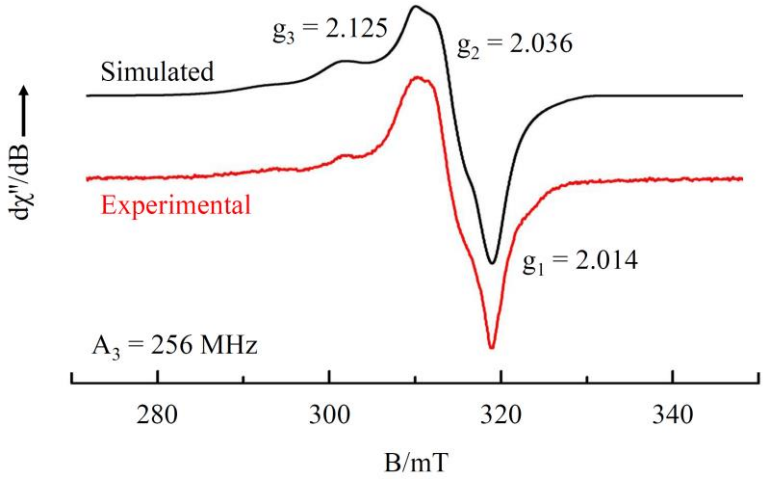

Figure 3.9. X-band EPR spectrum of [{nn(PM)(PI)}Fe(PMe_3)$_2$](PF_6) (**2**$^+$-(PMe_3)$_2$) in DME glass (0.5 mM, 8.954 GHz). Hyperfine coupling is observed with two equivalent ^{31}P nuclei (A_3 = 256 MHz).

environment.

X-ray analysis was carried out on a single crystal of $\mathbf{2}^{+}$-$(PMe_3)_2$, and the resulting crystal structure is illustrated in Figure 3.10. Two independent molecules were found in the asymmetric unit, with bond distances and angles equivalent within 3σ. Selected average parameters are presented in Tables 3.4 and 3.5. Unfortunately

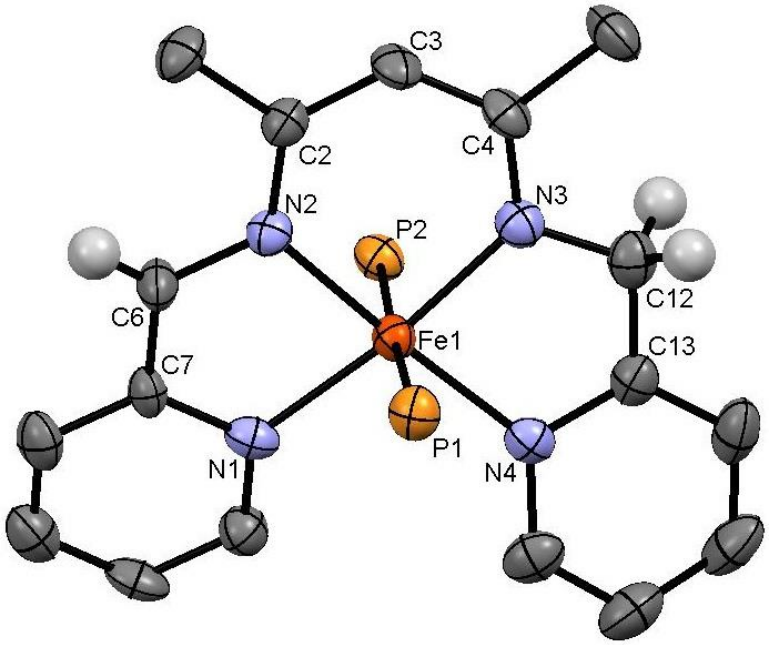

Figure 3.10. Molecular structure of one of the identical molecules in the asymmetric unit of $\mathbf{2}^{+}$-$(PMe_3)_2$. One PF_6 counterion, phosphine methyl groups, and selected hydrogen atoms are omitted for clarity.

Table 3.4. Selected interatomic distances for $\mathbf{2}^{+}$-$(PMe_3)_2$. Distances are average values of the two independent molecules in the asymmetric unit (identical within 3σ).

Selected Bond Distances (Å)		Selected Bond Distances (Å)	
Fe1-N1	2.006(4)	Fe1-N4	1.998(4)
Fe1-N2	1.944(4)	Fe1-N3	1.939(4)
Fe1-P1	2.280(2)	Fe1-P2	2.271(2)
C3-C2	1.391(7)	C3-C4	1.388(7)
C2- N2	1.340(6)	C4-N3	1.333(6)
N2- C6	1.396(6)	N3- C12	1.404(6)
C6- C7	1.445(7)	C12- C13	1.453(7)
C7- N1	1.363(6)	C13- N4	1.359(6)

Table 3.5. Selected bond angles for $\mathbf{2}^{+}$-$(PMe_3)_2$. Angles are average values of the two independent molecules in the asymmetric unit (identical within 3σ).

Selected Bond Angles (°)		Selected Bond Angles (°)	
N1-C7-C6	115.7(4)	N4-C13-C12	115.8(4)
C7-C6-N2	113.0(4)	C13-C12-N3	113.3(5)
C6-N2-C2	119.3(4)	C12-N3-C4	118.6(4)
N2-C2-C3	122.2(4)	N3-C4-C3	122.3(5)

disorder renders bond distance analysis difficult: bond distances and angles for the methylene and imine sides of the molecule are identical within error. Assuming the observed distances arise from a 1:1 average of methylene and imine sides of the {dmp(PM)(PI)} ligand and that methylene distances remain constant between **2**-$(PMe_3)_2$ and $\mathbf{2}^{+}$-$(PMe_3)_2$, the pyridine imine bond distances of $\mathbf{2}^{+}$-$(PMe_3)_2$ can be estimated (Table 3.6). Comparison of metric parameters with the imine half of **2**-$(PMe_3)_2$ (Table 3.3) suggests that the {nn(PM)(PI)} ligand is *not* bis-reduced.

Due to the difficulty in interpretation of metric parameters of $\mathbf{2}^{+}$-$(PMe_3)_2$, DFT calculations on the molecule were carried out. Calculated bond distances for the imine half of the molecule are presented in Table 3.6 (*ital.*) and agree quite well with those estimated from the disordered structure in Figure 3.10. The molecule is a low-spin Fe^{II} complex with a SOMO that is ~95% ligand in character. A partial MO diagram is given in Figure 3.11 (center) with correlation to the orbitals of **2**-$(PMe_3)_2$ shown. The orbital energies decrease upon increasing oxidation, but the relative orbital ordering remains unchanged and an electron has clearly been removed from a ligand π^* orbital to afford an Fe^{II} metal center bound to a mono-reduced {nn(PM)(PI)} ligand. The proximity of the ligand-based SOMO to metal d-orbitals of the same symmetry allow for a slight degree of mixing, accounting for the metal character implicated by EPR

Table 3.6. Determination of metric parameters for imine fragment of $\mathbf{2}^{+}$-$(PMe_3)_2$ from known parameters of **2**-$(PMe_3)_2$ (Table 3.3). Values in *italics* were determined from DFT calculations of $\mathbf{2}^{+}$-$(PMe_3)_2$.

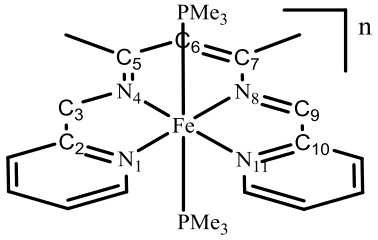

Methylene/Imine	**2**-$(PMe_3)_2$ (Methylene) (Å)	$\mathbf{2}^{+}$-$(PMe_3)_2$ (Average) (Å)	$\mathbf{2}^{+}$-$(PMe_3)_2$ (Imine, calculated) (Å)
C_6-C_5/C_6-C_7	1.393	1.390	1.387 *(1.39)*
C_5-N_4/C_7-N_8	1.345	1.337	1.329 *(1.35)*
N_4-C_3/N_8-C_9	1.435	1.400	1.365 *(1.34)*
C_3-C_2/C_9-C_{10}	1.483	1.449	1.415 *(1.41)*
C_2-N_1/C_{10}-N_{11}	1.359	1.361	1.363 *(1.37)*

studies. However, the π-type interaction with the two equivalent PMe_3 groups does not account for the high phosphorous hyperfine coupling value of 256 Hz, suggesting either coupling derived from spin polarization and other effects or error in the computed SOMO composition.[107-109]

3.3.3. [{nn(PM)(PI)}Fe(PMe$_3$)$_2$](BAr$_4^F$)$_2$

A second oxidation of {nn(PM)(PI)}Fe$(PMe_3)_2$ (**2**-$(PMe_3)_2$) was achieved through treatment of **2**-$(PMe_3)_2$ with 2.0 equiv $AgBAr_4^F$ (BAr_4^F = B[3,5-$CF_3(C_6H_3)]_4$)[110] to yield the lime green [{nn(PM)(PI)}Fe$(PMe_3)_2$]$(BAr_4^F)_2$ in high yield (70%) (Eq. 3.6). The diamagnetic dication exhibited 14 resonances in the ^{1}H NMR spectrum, listed in Table 3.7. Protons bound to carbons within the β-diketiminate and pyridine-imine framework are shifted significantly downfield relative to **2**-$(PMe_3)_2$. In particular, the imine C*H* (δ = 8.95) and β-diketiminate C*H* (δ = 6.47) protons are shifted 1.5 – 2.5 ppm downfield (δ = 6.47 and 4.99, respectively, for

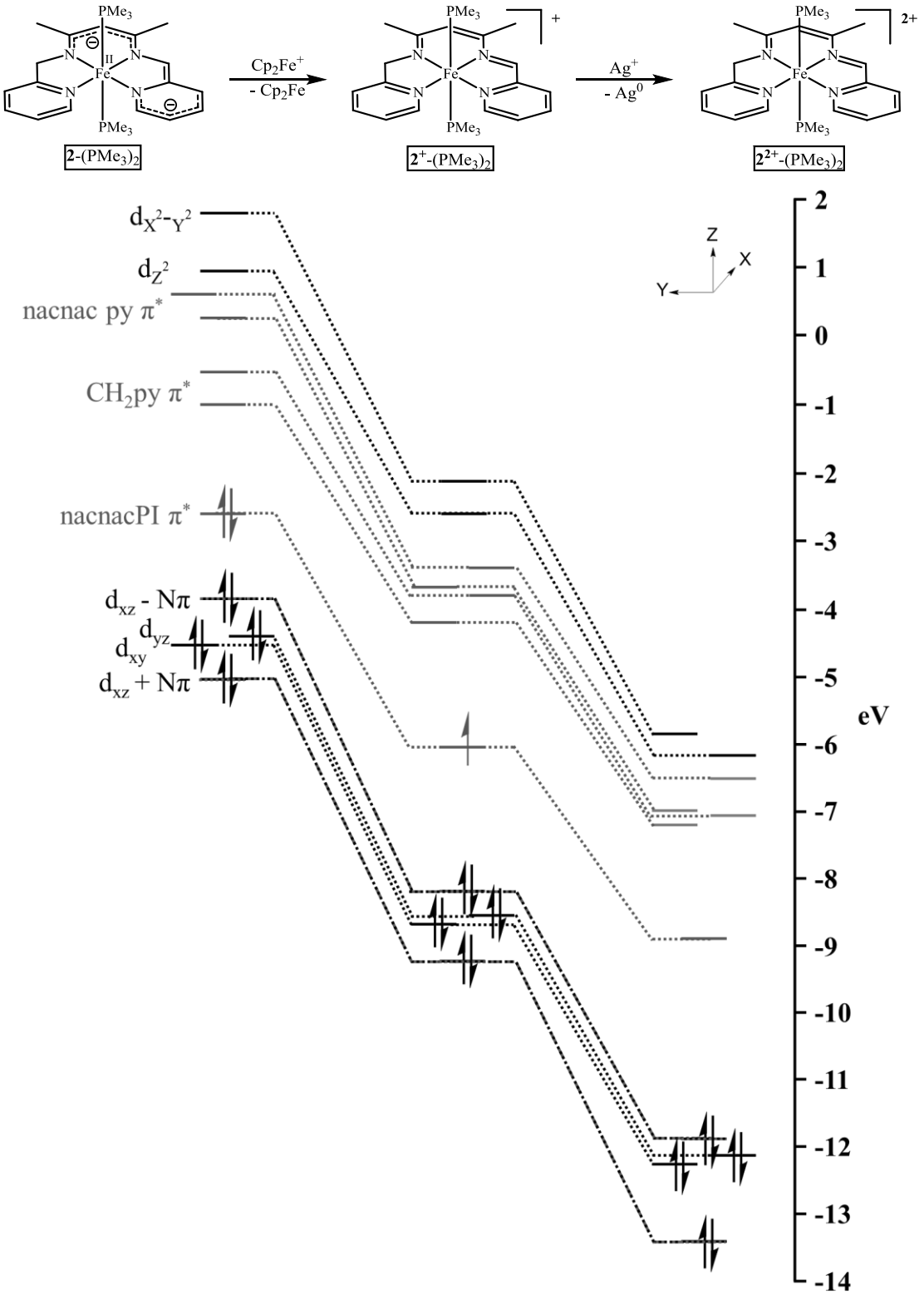

Figure 3.11. Partial molecular orbital diagrams for **2**-$(PMe_3)_2$, $\mathbf{2}^{+}$-$(PMe_3)_2$, and $\mathbf{2}^{2+}$-$(PMe_3)_2$. Broken symmetry calculations were carried out on $\mathbf{2}^{+}$-$(PMe_3)_2$; orbital energies given are an average of α and β magnetic orbitals.

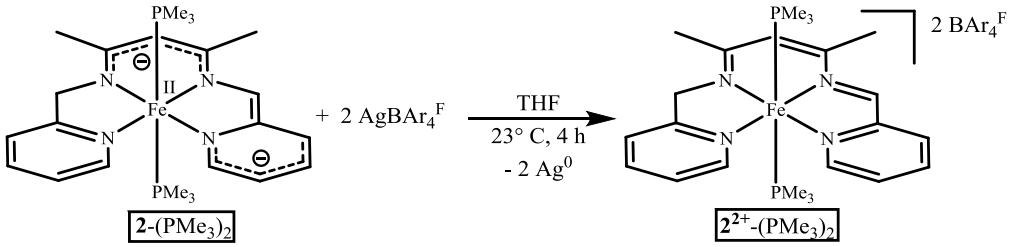

2-$(PMe_3)_2$), indicative of a significant decrease in ligand-localized electron density for $\mathbf{2}^{2+}$-$(PMe_3)_2$. Thus, NMR data are consistent with a neutral ligand framework bound to a Fe^{II} metal center.

Zero-field Mössbauer data were acquired for $\mathbf{2}^{2+}$-$(PMe_3)_2$ and are presented in Figure 3.12. The isomer shift of $\delta = 0.33(1)$ mms^{-1} and quadrupole splitting $\Delta E_Q = 0.25(1)$ mms^{-1} are very similar to the Mössbauer parameters of **2**-$(PMe_3)_2$ and $\mathbf{2}^{+}$-$(PMe_3)_2$ ($\delta = 0.32(1)$ mms^{-1}, $\Delta E_Q = 0.69(1)$ mms^{-1}, **2**-$(PMe_3)_2$; $\delta = 0.35(1)$ mms^{-1}, $\Delta E_Q = 0.52(1)$ mms^{-1}, $\mathbf{2}^{+}$-$(PMe_3)_2$) and offer strong evidence of very similar iron environments among the three redox species. Because the metals in **2**-$(PMe_3)_2$ and $\mathbf{2}^{+}$-$(PMe_3)_2$ are low-spin Fe^{II} centers, $\mathbf{2}^{2+}$-$(PMe_3)_2$ is also presumably low-spin Fe^{II}. Thus, Mössbauer data offer evidence for redox events that are solely ligand-based.[89-91]

$\mathbf{2}^{2+}$-$(PMe_3)_2$ was highly crystalline and large single crystals were easily obtained from THF/pentane for X-ray analysis. Unfortunately although a decent set of data were obtained, refinement proved difficult due to a large degree of disorder. The current model is illustrated in Figure 3.13. Disorder is observed for the CF_3 groups in the two BAr_4^F counterions as well as cocrystalized solvent, and a full-molecule disorder is observed for the dication, rendering bond distance and angle determination inaccessible. As it is unlikely that future models would solve these issues, refinement of the data set was abandoned.

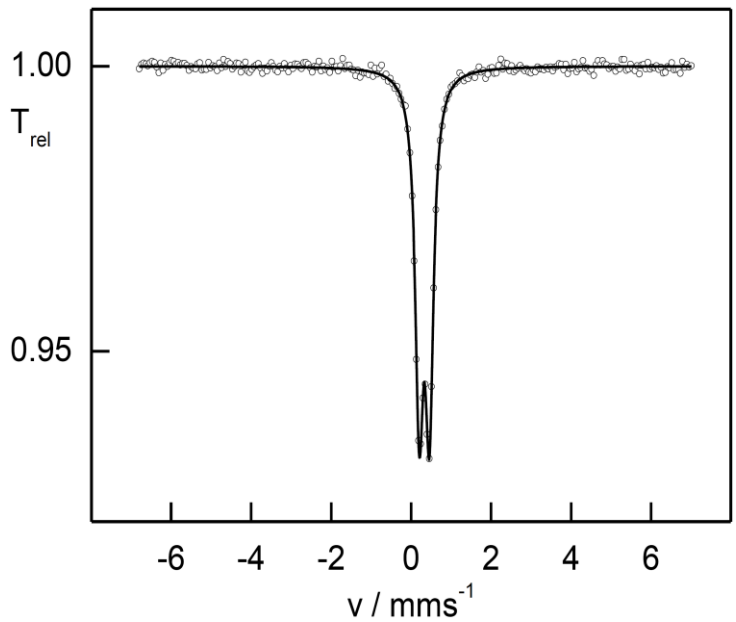

Figure 3.12. Zero field Mössbauer spectrum of [{nn(PM)(PI)}Fe(PMe_3)$_2$](BAr_4^F)$_2$ (**2**$^{2+}$-(PMe_3)$_2$. Fit parameters: δ = 0.33(1) mms^{-1}, ΔE_Q = 0.25(1) mms^{-1}, Γ_{FWHM} = 0.24(1) mms^{-1}.

In the absence of meaningful structural data, calculations were carried out on **2**$^{2+}$-(PMe_3)$_2$ and resulting geometry-optimized structural parameters are presented in Figure 3.14 alongside calculated parameters for **2**-(PMe_3)$_2$ and **2**$^{+}$-(PMe_3)$_2$. The calculated distances for the β-diketiminate/pyridine imine fragment of **2**$^{2+}$-(PMe_3)$_2$ are indicative of a neutral ligand, as the distances within the pyridine-imine portion approach those of previously tabulated pyridine imine ligands with *d*(N_{im}-C_{im}) = 1.30 Å, *d*(C_{im}-C_{py}) = 1.44 Å, *d*(C_{py}-N_{py}) = 1.36 Å for **2**$^{2+}$-(PMe_3)$_2$ *vs.* *d*(N_{im}-C_{im}) = 1.28 Å, *d*(C_{im}-C_{py}) = 1.47 Å, *d*(C_{py}-N_{py}) = 1.35 Å for (pyridine-Imine)^0 (Figure 2.2).[94-96] Metal-ligand bond distances elongate slightly upon oxidation due to a decreased electrostatic interaction from diminished charge on the ligand framework.[111,112] As expected, bond distances within the methylene-pyridine portion of the ligand remain unchanged upon sequential oxidation.

A partial MO diagram for **2**$^{2+}$-(PMe_3)$_2$ is presented in Figure 3.11 (right). Consistent with NMR and Mössbauer data, oxidation of **2**$^{+}$-(PMe_3)$_2$ results in removal of

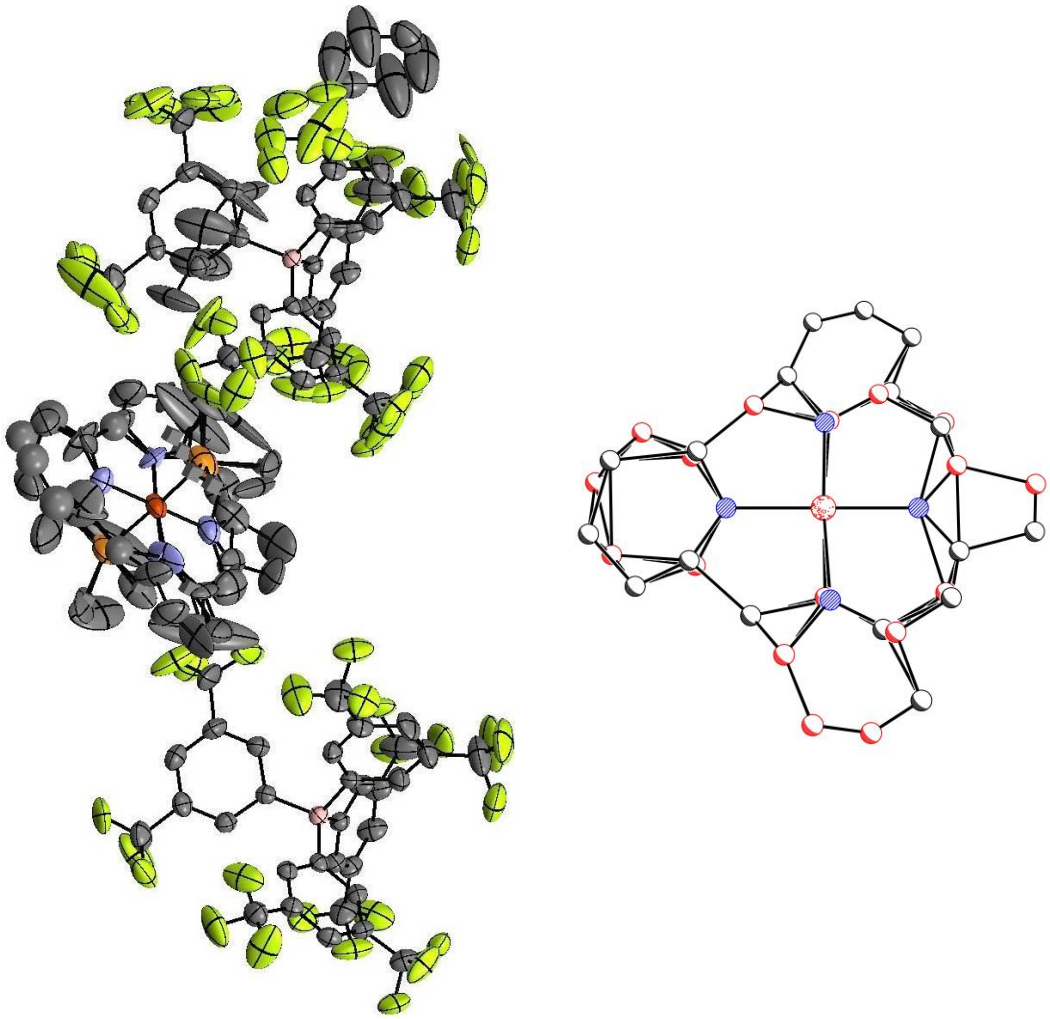

Figure 3.13. View of the incomplete model of [{nn(PM)PI}Fe(PMe_3)$_2$](BAr_4^F)$_2$ (**2**$^{2+}$-(PMe_3)$_2$ (left) and overlay showing the full molecule (dication) disorder (right).

an electron from the ligand-localized SOMO, corresponding to a {nn(PM)(PI)}^{0}/low-spin Fe^{II} configuration. Sequential oxidations of **2**-(PMe_3)$_2$ are ligand-based and the iron metal center remains throughout in the +2 oxidation state.

3.3.4. {nn(PM)(PI)}Fe(PMe_3)CO

One phosphine group of **2**-(PMe_3)$_2$ was quite labile, and exposure of a solution of **2**-(PMe_3)$_2$ to 1 atm CO resulted in ligand exchange to quantitatively form {nn(PM)(PI)}Fe(PMe_3)CO (**2**-(PMe_3)CO), with a characteristic carbonyl stretching frequency of ν_{CO} = 1912 cm^{-1} (Eq. 3.7). Exposure of **2**-(PMe_3)CO to excess PMe_3

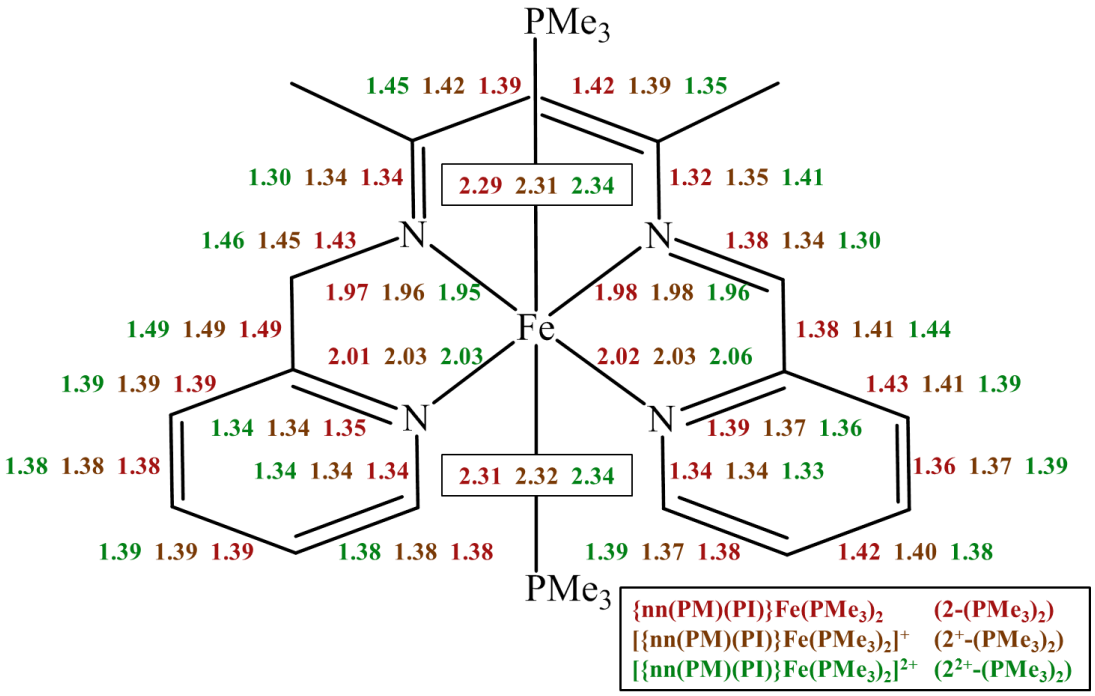

Figure 3.14. Calculated bond distances for {nn(PM)(PI)}Fe(PMe_3)$_2$ (**2**-(PMe_3)$_2$) (red), [{nn(PM)(PI)}Fe(PMe_3)$_2$]$^+$ (**2**$^+$-(PMe_3)$_2$) (brown), and [{nn(PM)(PI)}Fe(PMe_3)$_2$]$^{2+}$ (**2**$^{2+}$-(PMe_3)$_2$) (green).

under vacuum allowed for regeneration of **2**-(PMe_3)$_2$, demonstrating the reversibility of Eq. 3.7. ^{1}H NMR spectroscopy revealed 14 resonances in the diamagnetic region, consistent with the expected C_s-symmetric **2**-(PMe_3)CO, and chemical shifts are listed

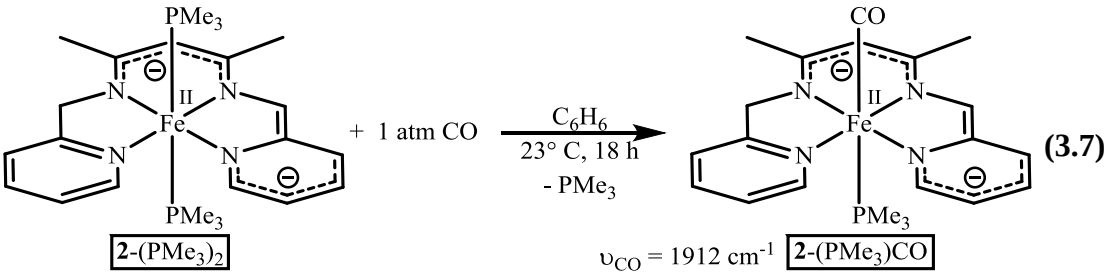

(3.7)

in Table 3.7. The NMR shifts of **2**-(PMe_3)CO are remarkably similar to those of the related **2**-(PMe_3)$_2$, indicating a very similar ligand environment for the two compounds. Indeed, the six-coordinate **2**-(PMe_3)CO must necessarily consist of a dianionic ligand chelated to Fe^{II} to maintain an 18 e$^-$ count at the metal center.

Mössbauer data were acquired for **2**-(PMe_3)CO (Figure 3.15) and reveal a very low isomer shift of $\delta = 0.08$ mms^{-1} ($\delta = 0.32$ mms^{-1} for **2**-(PMe_3)$_2$). Because π-withdrawing species such as carbonyl ligands tend to reduce isomer shifts due to a contraction of the metal-ligand bonds, the low $\delta = 0.08$ mms^{-1} of **2**-(PMe_3)CO is still fully consistent with an Fe^{II} metal center bound to a carbonyl ligand with non-negligible π- backbonding.[89-91,113-116] The quadrupole splitting of $\Delta E_Q = 0.37$ mms^{-1} is suggestive of highly symmetric electric field about the metal center, consistent with octahedral geometry.

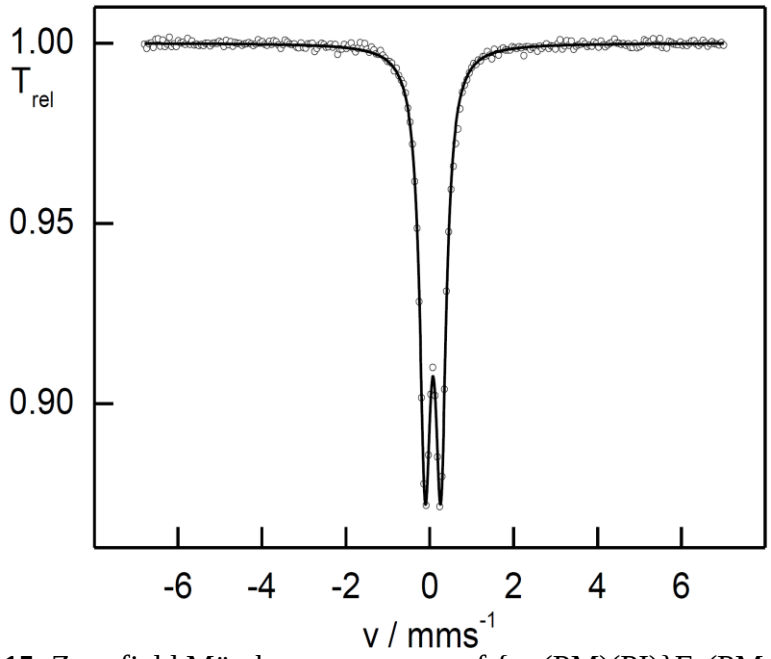

Figure 3.15. Zero field Mössbauer spectrum of {nn(PM)(PI)}Fe(PMe_3)CO (**2**-(PMe_3)CO. Fit parameters: $\delta = 0.08(1)$ mms^{-1}, $\Delta E_Q = 0.37(1)$ mms^{-1}, $\Gamma_{FWHM} = 0.31(1)$ mms^{-1}.

3.4. Synthesis of {nn(PM)(PI)}FeL (L = PMe_3, CO) complexes

3.4.1. {nn(PM)(PI)}Fe(PMe_3)

In addition to facile ligand substitution, **2**-(PMe_3)$_2$ could easily undergo dissociation of the labile phosphine in the absence of an additional donor ligand.

Table 3.7. ^{1}H NMR data (δ, coupling (mult, *J*) in Hz) of **2**-$(PMe_3)_2$, **2**$^{2+}$-$(PMe_3)_2$, **2**-$(PMe_3)CO$, and **2**-$(PMe_2Ph)_2$ acquired in C_6D_6 (a) or THF-d_8 (b) in a 400 MHz spectrometer.

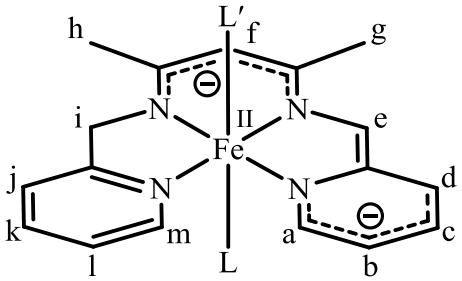

Compound	a / m	b / l	c / k	d /j	e	f	g	h	i
2-$(PMe_3)_2$[a]	7.51 (d, 6)	5.77 (t, 6)	6.60 (t, 7)	6.39 (d, 7)	6.47	4.99	2.09	2.28	4.14
	8.80 (d, 6)	6.17 (t, 6)	6.61 (t, 6)	6.39 (d, 8)					
2^{2+}-$(PMe_3)_2$[b]	8.67 (d, 6)	7.82 (t, 6)	8.12 (t, 7)	7.68 (d, 7)	8.95	6.47	2.40	2.39	5.21
	8.71 (d, 6)	7.63 (t, 6)	8.10 (t, 7)	7.93 (d, 7)					
2-$(PMe_3)CO$[a]	7.79 (d, 6)	5.54 (t, 7)	6.13 (t, 7)	6.24 (d, 7)	6.41	4.98	2.13	2.08	4.68
	8.01 (d, 7)	6.15 (t, 7)	6.52 (t, 7)	6.55 (d, 7)					
2-$(PMe_2Ph)_2$[a]	7.59 (d, 6)	5.91 (t, 6)	6.68 (t, 6)	6.81 (d, 8)	6.93	5.47	2.46	2.11	3.54
	8.52 (d, 6)	6.12 (t, 6)	6.09 (t, 6)	6.48 (d, 8)					

Repeated exposure of a C_6D_6 solution of **2**-$(PMe_3)_2$ to vacuum resulted in a color change from purple to red-brown as a new set of resonances in the diamagnetic region appeared by ^{1}H NMR, consistent with loss of 1 equiv PMe_3 to form {nn(PM)(PI)}Fe(PMe_3) (**3**-PMe_3). **3**-PMe_3 could be prepared independently through treatment of **1**-$N(TMS)_2$ with 1.0 equiv PMe_3 (Scheme 3.4). The ^{1}H NMR resonances of **3**-PMe_3 are given in Table 3.10. The complex is pseudo-C_S symmetric and rapidly

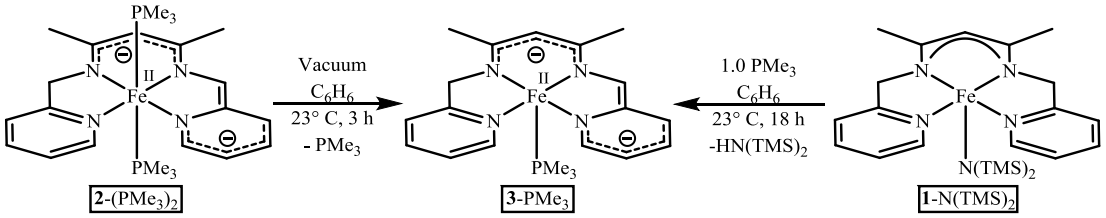

Scheme 3.4. Synthesis of **3**-PMe_3.

exchanges PMe_3 in solution, as the two methylene protons appear chemically equivalent. Due to this rapid exchange, addition of small amounts of additional phosphine to **3**-PMe_3 led to immediate formation of **2**-$(PMe_3)_2$ with a ^{1}H NMR spectrum that was a weighted average of **3**-PMe_3 and **2**-$(PMe_3)_2$. This phenomenon is clearly illustrated in Figure 3.17, in which increasing amounts of phosphine shift the resonances characteristic of **3**-PMe_3 towards those of **2**-$(PMe_3)_2$. Unsurprisingly, treatment of **3**-PMe_3 with 1 atm CO resulted in the quantitative formation of **2**-$(PMe_3)CO$. **3**-PMe_3 was fairly sensitive, and decomposed in solution at 23 °C over ~ 1 d to a virtually insoluble brown powder with release of PMe_3.

One could imagine three different electronic configurations available to **3**-PMe_3, illustrated in Figure 3.16. The ligand may remain dianionic upon PMe_3 loss and bind a Fe^{II} metal center (right), or the ligand could reduce iron by one or two electrons and bind to a Fe^{I} or Fe^{0}center, respectively (Figure 3.16 center, left). Several of the ^{1}H NMR resonances observed for **2**-$(PMe_3)_2$ shift significantly downfield upon loss of phosphine to form **3**-PMe_3, suggestive of reduced electron density on the

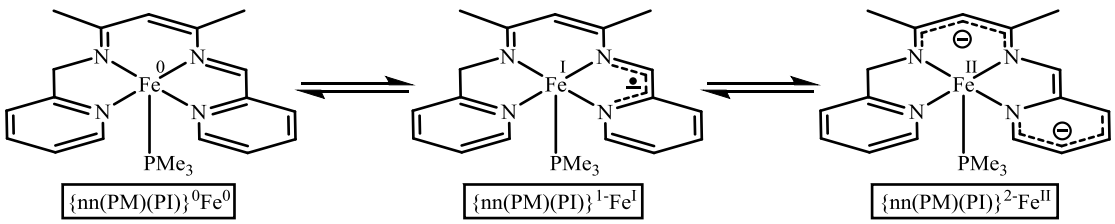

Figure 3.16. Possible electronic configurations for **3**-PMe_3.

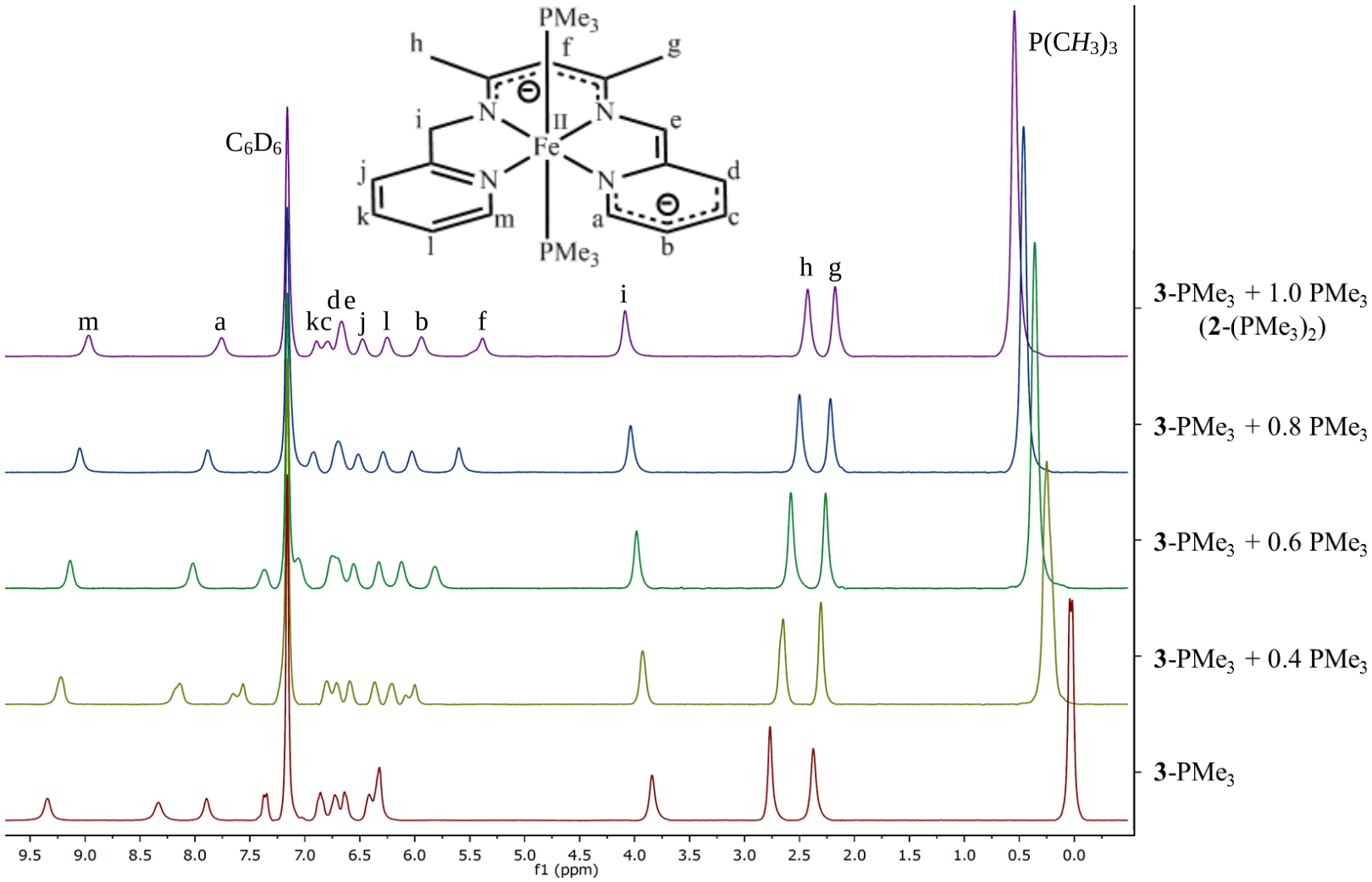

Figure 3.17. Transition from **3**-PMe_3 to **2**-$(PMe_3)_2$ upon addition of excess PMe_3.

ligand framework in **3**-PMe_3 and a more reduced iron center. In particular, the imine-C*H* shifts from δ 6.47 in **2**-$(PMe_3)_2$ to δ 7.24 in **3**-PMe_3 and the β-diketiminate-C*H* shifts from δ 4.99 in **2**-$(PMe_3)_2$ to δ 5.82 in **3**-PMe_3, However, variation of the coordination environment via conversion from a 6-coordinate to a 5-coordinate species could also alter the observed chemical shifts of **3**-PMe_3.

Mössbauer data for **3**-PMe_3 (Figure 3.18) reveal a fairly large ΔE_Q of 1.62 mms^{-1}, consistent with a 5-coordinate species with a moderate degree of asymmetry in the electric field about the iron center. The isomer shift of $\delta = 0.17$ mms^{-1} is low relative to **2**-$(PMe_3)_2$ ($\delta = 0.32$ mms^{-1}) and could be indicative of shorter metal-ligand bond lengths, corresponding to a more oxidized metal center in **3**-PMe_3. However, as with the NMR data discussed previously, Mössbauer spectroscopy is highly sensitive to minor changes in coordination environment[90] and the small difference in isomer shift between the two compounds could simply be a reflection of differing coordination geometries about the metal center, thus, it is difficult to make a definitive argument for one particular electron configuration.

3.4.1. {nn(PM)(PI)}FeCO

Analogous to the reaction shown in Scheme 3.4, repeated exposure of a solution of **2**-(PMe_3)CO to vacuum resulted in selective loss of PMe_3 to generate {nn(PM)(PI}FeCO (**3**-CO) as shown in Scheme 3.5. Unfortunately, complete conversion to **3**-CO was never observed, and an alternate synthesis was sought out. Gratifyingly, the internal deprotonation of **1**-N(TMS) did not require strong σ-donors to initiate, and deprotonation was elicited through treatment with 1 atm CO to generate **3**-CO in high yield (79%).

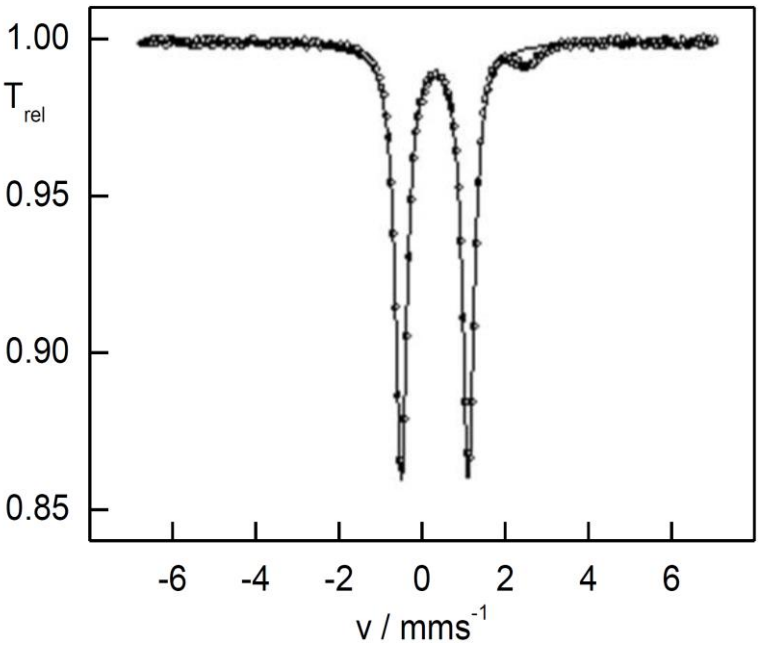

Figure 3.18. Zero field Mössbauer spectrum of {nn(PM)(PI)}Fe(PMe_3) (**3**-PMe_3). Fit parameters: $\delta = 0.17(1)$ mms^{-1}, $\Delta E_Q = 1.62(1)$ mms^{-1}, $\Gamma_{FWHM} = 0.34(1)$ mms^{-1}.

The ^{1}H NMR spectrum of **3**-CO was quite similar to that of **3**-PMe_3, and chemical shifts are listed in Table 3.10. In contrast to **3**-PMe_3, ligand exchange of **3**-CO was slow and two resonances corresponding to the diastereotopic methylene protons were observed. As with **3**-PMe_3, resonances corresponding to the imine-C*H* and β-diketiminate-C*H* protons ($\delta = 7.73$ and 6.31, respectively) were shifted

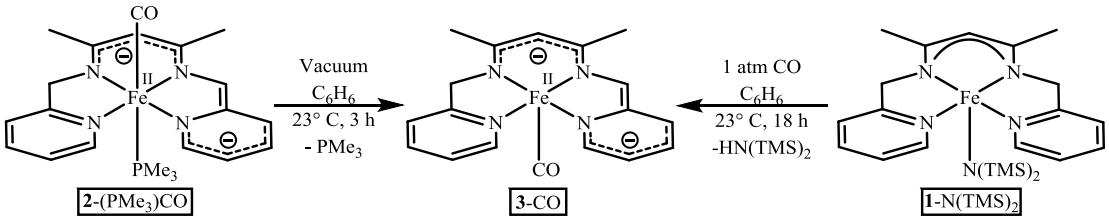

Scheme 3.5. Synthesis of **3**-CO.

~1 – 2 ppm downfield relative to the 6-coordinate complexes **2**-$(PMe_3)_2$ and **2**-(PMe_3)CO (Table 3.7) suggesting a similar electronic configuration for both **3**-PMe_3 and **3**-CO.

To further probe the electronic structure of **3**-CO, Mössbauer data were acquired and are presented in Figure 3.19. Fit parameters are comparable to **3**-PMe_3, suggestive of a similar oxidation state and coordination environment for both compounds. The quadrupole splitting of $\Delta E_Q = 1.13$ mms^{-1} is consistent with a 5-coordinate species and is slightly lowered relative to **3**-PMe_3 ($\Delta E_Q = 1.62$) due to the increased similarity between the nitrogen-based chelate and CO relative to PMe_3. The isomer shift of $\delta = 0.14$ mms^{-1} is again slightly lower than that of **3**-PMe_3, presumably due to presence of a π-withdrawing ligand (*vide supra*). Isomer shifts of ~ 0.0 – 0.3 mms^{-1} have been observed for a variety of iron carbonyl compounds in both the +2 and +0 oxidation states,[89-91,117-120] so again definitive assignment of the iron oxidation state in **3**-CO is difficult.

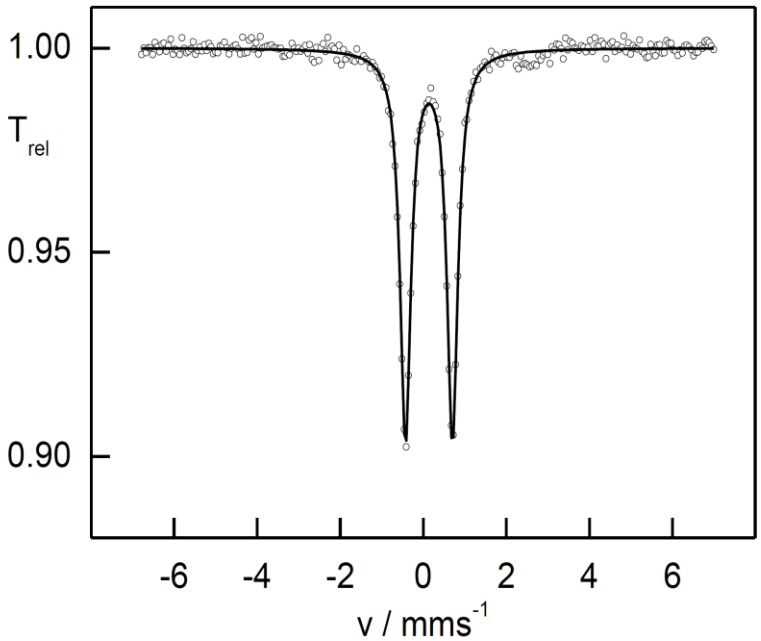

Figure 3.19. Zero field Mössbauer spectrum of {nn(PM)(PI)}FeCO (**3**-CO). Fit parameters: $\delta = 0.14(1)$ mms^{-1}, $\Delta E_Q = 1.13(1)$ mms^{-1}, $\Gamma_{FWHM} = 0.31(1)$ mms^{-1}.

IR spectroscopy of **3**-CO revealed a $\nu_{CO} = 1879$ cm^{-1}, significantly lowered relative to free CO ($\nu_{CO} = 2143$ cm^{-1}). Surprisingly, the CO stretching frequency of

3-CO is lower than that of **2**-(PMe_3)CO (ν_{CO} = 1912 cm^{-1}). One might expect that the 6-coordinate **2**-(PMe_3)CO would produce a lower ν_{CO} due to a greater degree of electron density at the metal center, which would permit a greater degree of π-backdonation into the carbonyl ligand. Presumably, the presence of a strong *trans* ligand in **2**-(PMe_3)CO elongates the Fe-CO bond relative to **3**-CO and decreases overlap, reducing the amount of π-backbonding available to **2**-(PMe_3)CO and increasing the ν_{CO}. This proposal was borne out computationally: the *d*(Fe-C) in

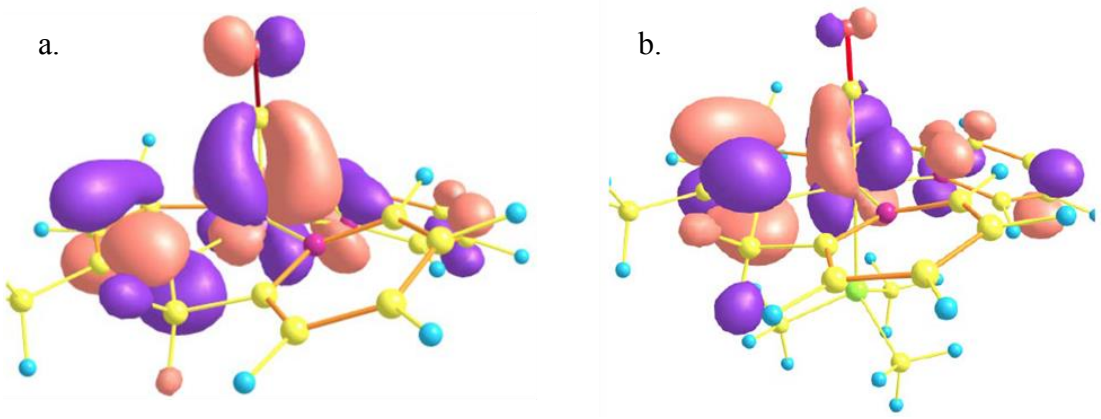

Figure 3.20. Principle π-backbonding orbitals of **3**-CO (a) and **2**-(PMe_3)CO (b).

2-(PMe_3)CO was computed as 0.08 Å longer than that of **3**-CO. The HOMO-1 orbitals, which constitute the principle π-backbonding orbitals of **3**-CO and **2**-(PMe_3)CO, are illustrated in Figure 3.20. A greater degree of Fe-CO π-overlap is clearly seen for **3**-CO (left), leading to the lower ν_{CO} observed experimentally.

3.5. Alternate synthesis of {nn(PM)(PI)}FeL_n (L = PMe_2Ph, *n* = 2; L = $PMePh_2$, PPh_3, *n* = 1) complexes

3.5.1. {nn(PM)(PI)}Fe(PMe_2Ph)$_2$

An alternative synthetic route to preparation of {nn(PM)(PI)}FeL_n complexes allowed study of the tendency to adopt either 5-coordinate or 6-coordinate geometries.

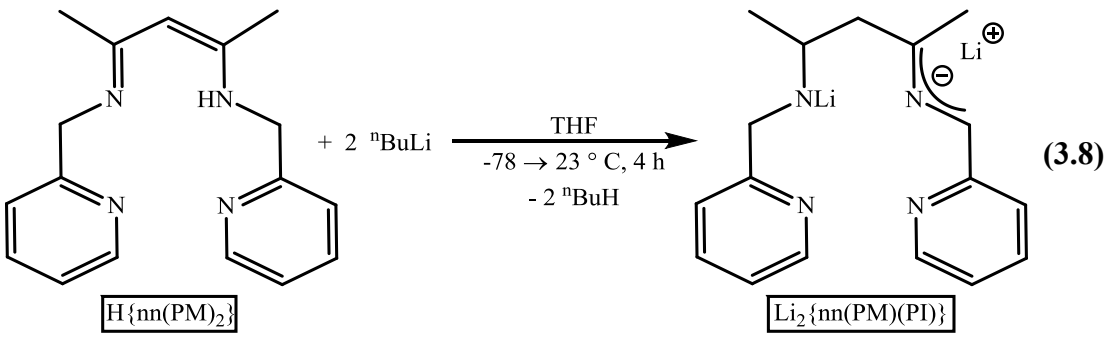

(3.8)

The purple Li_2{nn(PM)(PI)} salt could be prepared through treatment of H{nn$(PM)_2$} with 2.0 equiv ^{n}BuLi at low temperatures (Eq. 3.8). Li_2{nn(PM)(PI)} was quite thermally sensitive and decomposed to a brown solid at 23° C, but was indefinitely stable at -30° C in the solid state.

Addition of Li_2{nn(PM)(PI)} to a slurry of $FeBr_2(THF)_2$ in the presence of excess PMe_2Ph in THF resulted in formation of a new C_s-symmetric product, formulated as {nn(PM)(PI)}Fe$(PMe_2Ph)_2$ (**2**-$(PMe_2Ph)_2$) (Eq. 3.9). ^{1}H NMR chemical shifts are listed in Table 3.7, and are quite similar to the other 6-coordinate complexes **2**-$(PMe_3)_2$ and **2**-(PMe_3)CO. Because **2**-$(PMe_2Ph)_2$ was likely similar electronically to the 6-coordinate **2**-$(PMe_3)_2$ and **2**-(PMe_3)CO, further study was not pursued.

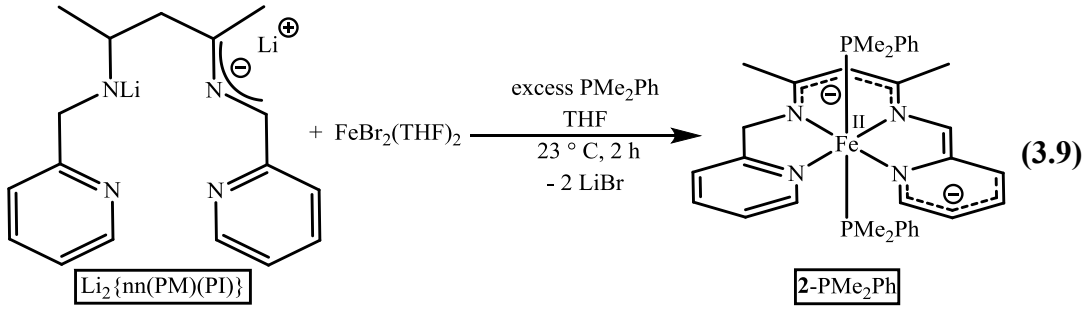

(3.9)

3.5.2. {nn(PM)(PI)}Fe$(PMePh_2)$

The synthetic method illustrated in Eq. 3.9 could be expanded to installation of a variety of different phosphines as supporting ligands. Unexpectedly, treatment of

$FeBr_2(THF)_2$ with Li_2{nn(PM)(PI)} in the presence of the slightly less σ-donating $PMePh_2$ resulted in the formation of 5-coordinate {nn(PM)(PI)}Fe($PMePh_2$) (**3**-$PMePh_2$), even with a vast excess of phosphine (Eq. 3.10). This is an intriguing result, as it clearly demonstrates the effect of minor electronic changes in the peripheral ligands on the electronics at the metal center. Strong σ-donors such as PMe_3

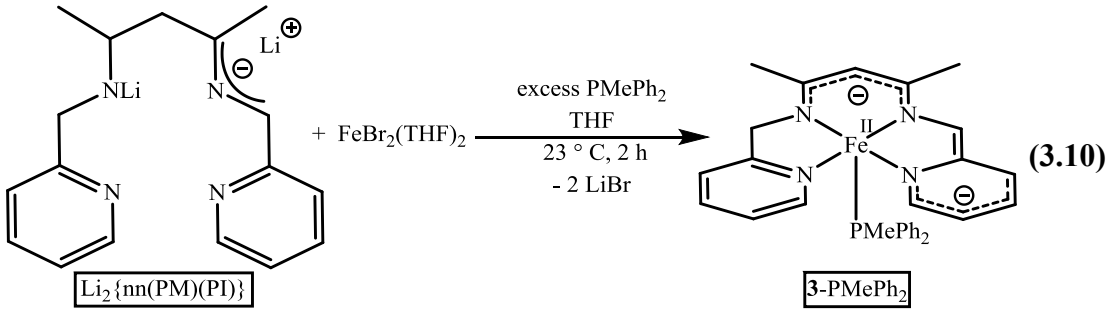

(3.10)

and PMe_3Ph were capable of six-coordination, but replacement of a single methyl group with phenyl to weaken the σ-donating ability of the phosphine and improve π-backbonding ability rendered **3**-$PMePh_2$ unable to adopt the same six-coordination.

The ^{1}H NMR resonances corresponding to **3**-$PMePh_2$ are listed in Table 3.10, and bear a striking similarity to the other 5-coordinate compounds described above. Despite the inability of **3**-$PMePh_2$ to bind a 6th ligand, the complex must undergo rapid phosphine exchange in solution as the methylene-C*H* protons appeared equivalent by ^{1}H NMR. **3**-$PMePh_2$ exhibited the characteristic downfield-shifted imine-C*H* (δ = 8.03) and β-diketiminate-C*H* (δ = 6.45), again suggestive of increased ligand-based electron density for **3**-$PMePh_2$ relative to the 6-coordinate species (Table 3.7).

3-$PMePh_2$ was prone to phosphine loss, and in solution at 23°C in the absence of added phosphine, formed an insoluble material over several days. In the solid state, at 23°C **3**-$PMePh_2$ reacted over weeks to generate a new sparingly soluble

paramagnetic complex that appeared C_S-symmetric by ^{1}H NMR, tentatively formulated as a {nn(PM)$_2$}FeX species due to similarity in solubility and NMR spectral signatures with **1**-Cl and **1**-N_3. Presumably, during degradation of **3**-$PMePh_2$, an equivalent of phosphine dissociated and the pyridine-imine arm of the ligand

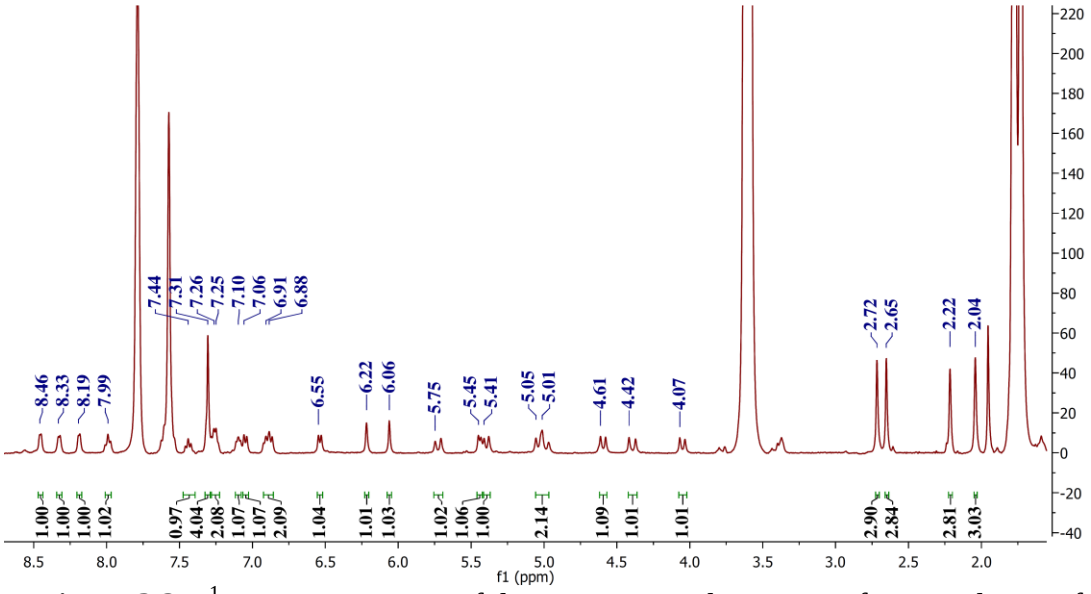

Figure 3.21. ^{1}H NMR spectrum of diamagnetic product arising from oxidation of material formed upon gradual degradation of **3**-$PMePh_2$.

backbone underwent H-atom abstraction to regenerate the symmetric {nn(PM)$_2$} framework. Treatment of this paramagnetic material with one equiv $AgBAr_4^F$ afforded a sparingly soluble diamagnetic complex featuring 4 inequivalent methyl groups and 4 inequivalent pyridine rings. The ^{1}H NMR spectrum of this new complex in THF-d_8 is given in Figure 3.21. The new species forms quite cleanly, and from other oxidatively-induced C-C coupling events observed in these laboratories,[1-6] is tentatively formulated as a dimer generated through C-C coupling at the ligand backbone. Unfortunately, application of 2-dimensional NMR correlation methods was unsuccessful in determination of the complete molecular structure of the new species

and, because the compound could not be synthesized rationally from **1**-L and oxidant, further study of the complex was not pursued.

Zero-field Mössbauer data were acquired to aid in the electronic structure determination of **3**-$PMePh_2$ and are displayed in Figure 3.22. The degradation product is clearly evident as a small percentage of the total sample (11%, blue trace). Mössbauer parameters of the degradation product (δ = 1.12(1) mms^{-1}, ΔE_Q = 3.12(1) mms^{-1}) are consistent with a 5-coordinate high-spin Fe^{II} complex, as expected for a species of the type {nn$(PM)_2$}FeX. The quadrupole splitting of **3**-$PMePh_2$ (ΔE_Q = 1.67(1) mms^{-1}) is on par with that expected of a 5-coordinate pseudo-square pyramidal complex. The isomer shift (δ = 0.39(1) mms^{-1}) is higher than that of **3**-CO (δ = 0.14), as predicted upon removal of the strongly π-withdrawing CO ligand, but is also significantly higher than that of **3**-PMe_3 (δ = 0.17(1) mms^{-1}). This difference can be

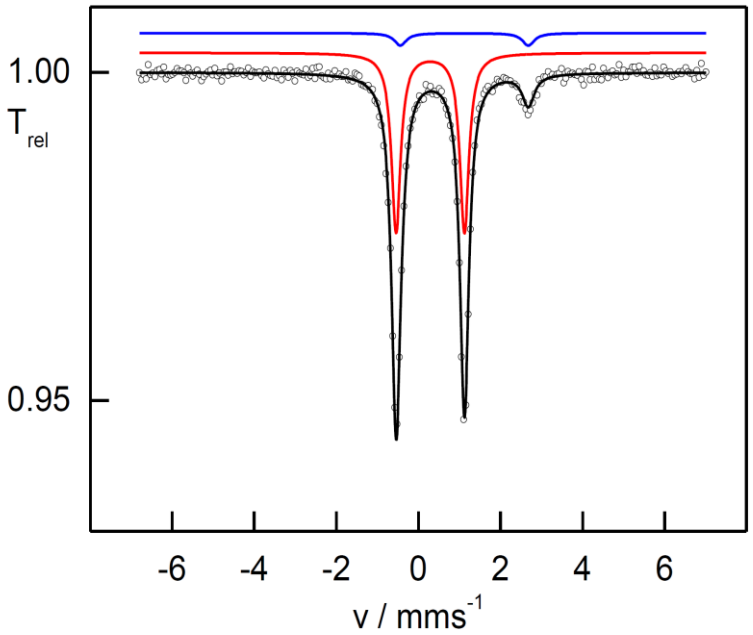

Figure 3.22. Zero field Mössbauer spectrum of {nn(PM)(PI)}Fe($PMePh_2$) (**3**-$PMePh_2$) with ~11% degradation product. Fit parameters: δ = 0.39(1) mms^{-1}, ΔE_Q = 1.67(1) mms^{-1}, Γ_{FWHM} = 0.27(1) mms^{-1} (**3**-$PMePh_2$, red trace, ~89%); δ = 1.12(1) mms^{-1}, ΔE_Q = 3.12(1) mms^{-1}, Γ_{FWHM} = 0.36(1) mms^{-1} (Degradation product, blue trace, ~11%).

rationalized through consideration of steric strain: the $PMePh_2$ ligand of **3**-$PMePh_2$ is slightly larger than the PMe_3 of **3**-PMe_3 ($\Theta(PMe_3) = 118°$ *vs.* $\Theta(PMePh_2) = 136°$).[121] Thus, the *d*(Fe-P) distance would be elongated in **3**-$PMePh_2$ and, because larger Fe-L distances result in higher isomer shifts,[90] δ should be greater for **3**-$PMePh_2$. Although the isomer shift of **3**-$PMePh_3$ falls in a region that could correspond to a variety of oxidation and spin states (*vide supra*), $\delta = 0.39(1)$ mms^{-1} is fully consistent with a low-spin Fe^{II} metal center.

Due to its inability to bind a 6th ligand, **3**-$PMePh_2$ was significantly easier to synthesize cleanly than the related **3**-PMe_3 and crystalline material suitable for X-ray analysis could be obtained. The resulting structure is presented in Figure 3.23, and relevant parameters are given in Table 3.8. The geometry about the metal center is pseudo-square pyramidal, with an Addison parameter[92] of $\tau = 0.37$. The *d*(Fe-N_{im}) distances are 1.8847(11) and 1.9197(11) Å and the *d*(Fe-N_{py}) distances are 1.9389(10) and 1.9746(10) Å, contracted 0.02 – 0.06 Å relative to **2**-$(PMe_3)_2$. This core distance contraction is likely due to the lower coordination number of **3**-$PMePh_2$, which allows for less steric hindrance about the metal center.

The bond distances in the ligand framework listed in Table 3.8 are quite similar to the corresponding distances in **2**-$(PMe_3)_2$ (Table 3.3) and indeed, many of the distances are identical within 3σ. Additionally, the experimentally determined metric parameters of **3**-$PMePh_2$ match up well to those calculated for $\{nn(PM)(PI)\}^{2-}$ shown in Figure 3.14. These data are clearly indicative of a doubly reduced ligand bound to a 16 e^- Fe^{II} metal center. Thus, the downfield chemical shifts of the 5-coordinate 3-L species are most likely reflective of a general decrease in

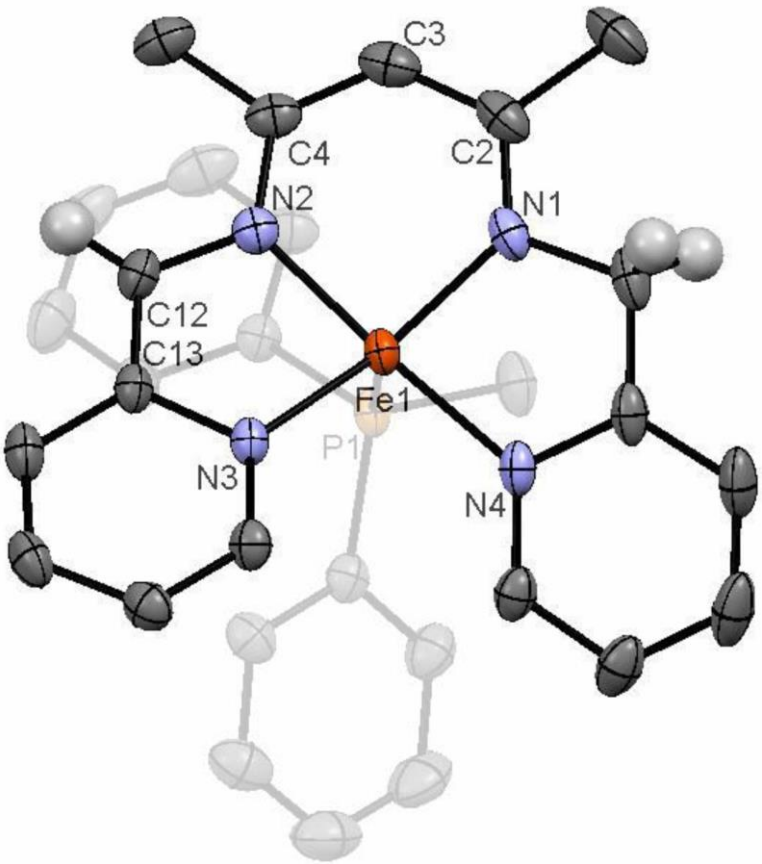

Figure 3.23. Molecular structure of **3**-$PMePh_2$. Selected hydrogen atoms are omitted for clarity.

Table 3.8. Selected interatomic distances and bond angles for **3**-$PMePh_2$.

Selected Bond Distances (Å)		Selected Bond Angles (°)	
Fe1-N1	1.8847(11)	N1-Fe1-N2	93.26(5)
Fe1-N2	1.9197(11)	N2-Fe1-N3	82.35(5)
Fe1-N3	1.9379(10)	N3-Fe1-N4	98.94(4)
Fe1-N4	1.9746(10)	N4-Fe1-N1	83.77(5)
Fe1-P1	2.1630(3)	N1-Fe1-P1	103.00(3)
N3-C13	1.4075(14)	N2-Fe1-P1	93.32(3)
C13-C12	1.382(2)	N3-Fe1-P1	103.39(3)
C12-N2	1.3705(16)	N4-Fe1-P1	90.35(3)
N2-C4	1.3591(17)	N1-Fe1-N3	153.45(4)
C4-C3	1.385(2)	N2-Fe1-N4	175.72(4)
C3-C2	1.409(2)		
C2-N1	1.336(2)		

Table 3.9. Structural comparison of **1**-$N(TMS)_2$, **2**-$(PMe_3)_2$, $\mathbf{2}^{+}$-$(PMe_3)_2$, $\mathbf{2}^{2+}$-$(PMe_3)_2$,[b] and **3**-$PMePh_2$. [a] Empirical formula. [b] Structural refinement is incomplete.

Crystal Data					
Formula	$C_{23}H_{37}FeN_5Si_2$	$C_{23}H_{36}FeN_4P_2$	$C_{23}H_{36}F_6FeN_4P_3$	$C_{53.75}H_{44.75}BF_{23.50}Fe_{0.50}N_2P$[a]	$C_{30}H_{31}FeN_4P$
Formula Weight	495.61	486.35	631.32	1234.87	534.41
Crystal System	Monoclinic	Monoclinic	Orthorhombic	Monoclinic	Monoclinic
Space Group	P2(1)/n	P2(1)/c	P2(1)2(1)2	C2/c	C2
Z	8	4	8	8	4
a, Å	22.344(4)	10.1579(8)	17.6532(14)	28.799(2)	17.4724(6)
b, Å	9.5554(14)	16.4764(12)	35.819(3)	18.8777(11)	10.0996(3)
c, Å	25.374(4)	15.0780(11)	8.8940(7)	24.191(3)	14.5690(5)
α, deg	90	90	90	90	90
β, deg	98.763(5)	103.175(3)	90	125.079(2)	101.8790(10)
γ, deg	90	90	90	90	90
Volume, $Å^3$	5354.4(15)	2457.1(3)	5623.9(8)	10762.5(17)	2515.85(14)
D (calc.), g/cm^3	1.230	1.315	1.491	1.524	1.411
Absorption coeff., mm^{-1}	0.672	0.761	0.767	0.302	0.690
F(000)	2112	1032	2616	5006	1120
Crystal Size, mm	0.45 x 0.30 x 0.15	0.40 x 0.30 x 0.25	0.20 x 0.15 x 0.03	0.40 x 0.40 x 0.04	0.60 x 0.40 x 0.30
Data Collection and Refinement					
Temp, K	173(2)	173(2)	183(2)	203(2)	193(2)
Wavelength (λ), Å	0.71073	0.71073	0.71073	0.71073	0.71073
θ limits, deg	1.84 to 31.00	1.86 to 28.28	1.29 to 23.53	1.40 to 23.58	2.86 to 34.40
Index Ranges	-32<=h<=32, -10<=k<=13, -36<=l<=31	-13<=h<=13, -21<=k<=19, -16<=l<=20	-19<=h<=19, -38<=k<=40, -9<=l<=9	-32<=h<=32, -21<=k<=20, -27<=l<=27	-25<=h<=25, -15<=k<=10, -22<=l<=22
Reflections Collected	55921	23781	50336	33715	15608
Absorption Correction	Semi-empirical from equivalents	Semi-empirical from equivalents	Semi-empirical from equivalents	Semi-empirical from equivalents	Semi-empirical from equivalents
Max. and Min. Transmission	0.9060 and 0.7520	0.8325 and 0.7505	0.9811 and 0.8617	0.9880 and 0.8889	0.8196 and 0.6821
Refinement Method	Full-matrix least-squares on F2	Full-matrix least-squares on F2	Full-matrix least-squares on F2	Full-matrix least-squares on F2	Full-matrix least-squares on F2
Data/Restraints/Params.	17064 / 0 / 679	6086 / 0 / 327	8329 / 0 / 694	8011 / 2 / 1153	7723 / 1 / 438
Goodness-of-Fit on F^2	1.026	1.02	1.012	1.331	1.006
Final R Indeces [I>2σ(I)]	R1 = 0.0355, wR2 = 0.0840	R1 = 0.0266, wR2 = 0.0685	R1 = 0.0437, wR2 = 0.0956	R1 = 0.0773, wR2 = 0.1968	R1 = 0.0233, wR2 = 0.0580
R Indices (all data)	R1 = 0.0573, wR2 = 0.0937	R1 = 0.0324, wR2 = 0.0719	R1 = 0.0613, wR2 = 0.10	R1 = 0.1371, wR2 = 0.2260	R1 = 0.0256, wR2 = 0.0591
Largest Diffraction Peak and Hole (e^- Å)	0.382 and -0.312	.358 and -0.237	0.525 and -0.412	0.620 and -0.452	0.381 and -0.231

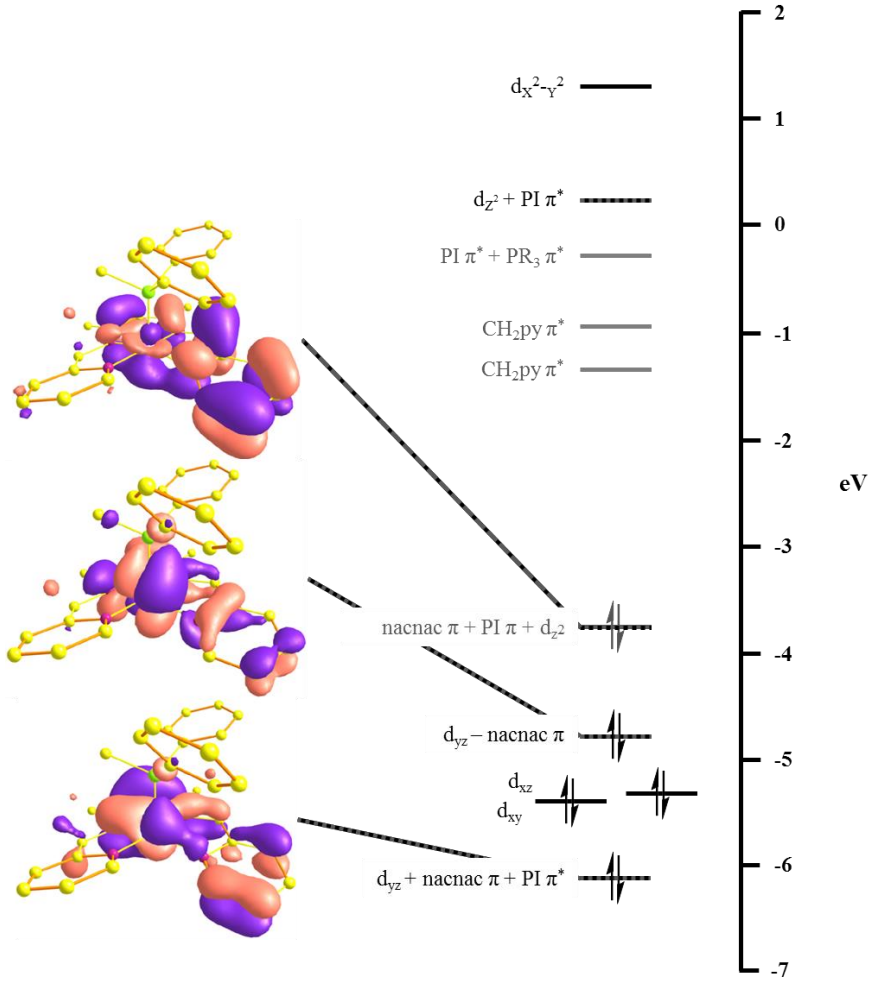

Figure 3.24. Truncated molecular orbital diagram of {nn(PM)(PI)}Fe($PMePh_2$ (**3**-$PMePh_2$ showing a primarily ligand π-localized HOMO with ~20% d_{z^2} contribution and two highly mixed molecular orbitals comprised of Fe d_{yz} and {nn(PM)(PI)}.

electron density at the metal center rather than a formal oxidation state change of the ligand. The changes in Mössbauer isomer shift between five-coordination and six-coordination are most likely a consequence of changing coordination environment rather than formal iron oxidation state change.

Calculations were carried out on **3**-$PMePh_2$, and the resulting truncated molecular orbital diagram is presented in Figure 3.24. The calculated orbitals are more covalent than those of **2**-$(PMe_3)_2$ (Figure 3.7), and many of the frontier orbitals show

highly mixed compositions. The HOMO is primary (~80%) ligand based, with a minor (~20%) metal d_{z^2} contribution. The remainder of d_{z^2} is in a high-energy σ^* orbital with slight ligand character. There are two filled orbitals of pure metal character and two filled mixed orbitals arising from a combination of d_{yz} and ligand for a total of six metal-based electrons. **3**-$PMePh_2$ is best construed as a 16 e^-, Fe^{II} metal center with a dianionic chelate, similar to the configuration of **2**-$(PMe_3)_2$. The remainder of the truncated molecular orbital diagram is comparable to that of **2**-$(PMe_3)_2$, reflective of the similar electronic behavior of the two complexes.

3.5.3. {nn(PM)(PI)}Fe(PPh_3)

To determine the scope of {nn(PM)(PI)}FeL complexes possible, Li_2{nn(PI)(PM)} was treated with $FeBr_2(THF)_2$ in the presence of excess PPh_3. Unsurprisingly, at 23°C a new diamagnetic complex was observed by ^{1}H NMR, consistent with the formation of {nn(PM)(PI)}FePPh_3 (**3**-PPh_3) (Eq. 3.11). ^{1}H NMR chemical shifts are listed in Table 3.10, and match up very well to the previously described 5-coordinate complexes.

3-PPh_3 was quite prone to degradation and, in polar solvents such as THF without excess phosphine present, decomposed within minutes with concomitant phosphine loss. In nonpolar solvents such as C_6H_6, degradation was decelerated, but

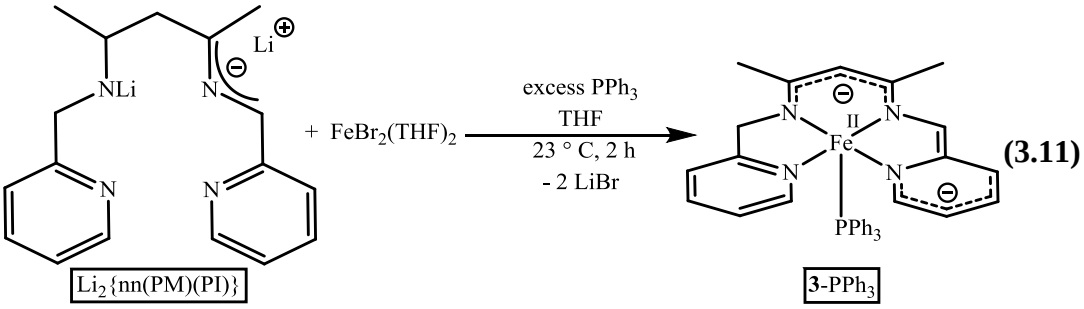

(3.11)

Table 3.10. ^{1}H NMR data (δ, coupling (mult, *J*) in Hz) of **3**-PMe_3, **3**-CO, **3**-$PMePh_2$, and **3**-PPh_3 acquired in C_6D_6 (a) or THF-d_8 (b) in a 400 MHz spectrometer.

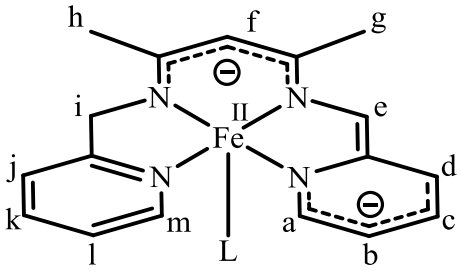

Compound	a / m	b / l	c / k	d /j	e	f	g	h	i
3-PMe_3[b]	7.89 (d, 6)	5.74 (t, 6)	6.34 (t, 7)	6.71 (d, 8)	7.24	5.82	2.45	2.48	4.48
	7.43 (d, 8)	7.42 (t, 7)	7.13 (t, 6)	9.35 (d, 6)					
3-CO[b]	8.43 (d, 6)	6.34 (t, 6)	6.65 (t, 6)	6.36 (d, 6)	7.73	6.31	2.64	2.11	3.60 (d, 21)
	8.95 (d, 6)	6.28 (t, 6)	6.90 (t, 6)	7.34 (d, 7)					4.21 (d, 21)
3-$PMePh_2$[a]	8.46 (d, 6)	6.59 (t, 6)	6.91 (t, 6)	7.45 (d, 6)	8.03	6.45	2.70	2.27	3.20
	9.26 (d, 6)	6.17 (t, 6)	6.58 (t, 6)	6.90 (d, 8)					
3-PPh_3[a]	8.78 (d, 7)	6.07 (t, 7)	6.63 (t, 7)	6.97 (d, 8)	7.20	6.23	2.35	2.29	3.96
	9.47 (d, 7)	6.82 (t, 7)	6.83 (t, 7)	7.41 (d, 8)					

nonetheless complete decomposition was observed over 6 h. As a result, **3**-PPh_3 could not be separated completely from excess PPh_3 for isolation.

The relative instability of **3**-PPh_3 perhaps hints at the necessity of strong σ-donors to stabilize the {nn(PM)(PI)}Fe core. Indeed, attempts at the same salt metathesis of Li_2{nn(PM)(PI)} with $FeBr_2(THF)_2$ in the presence of different L-type donors such as olefins, alkynes, and cyanides resulted in intractable reaction mixtures,

typically with concomitant production of copious amounts of insoluble precipitate.

3.6. Reactivity of {nn(PM)$_2$}FeX, {nn(PM)(PI)}FeLL', and {nn(PM)(PI)}FeL complexes

3.6.1. {nn(PM)$_2$}FeX

Attempts at triggering the internal deprotonation of {nn(PM)$_2$}FeN(TMS)$_2$ (**1**-N(TMS)$_2$) with non-phosphine L-type donors was carried out to minimal success. **1**-N(TMS)$_2$ was unreactive with respect to olefins such as ethylene and reacted nonspecifically with alkynes such as 2-butyne to generate intractable reaction mixtures with copious amounts of insoluble precipitate. Unsurprisingly, the gradual heating of **1**-N(TMS)$_2$ in the presence of N_2 resulted in thermal degradation rather than formation of a dinitrogen complex. Reaction with 3,3-diphenylcyclopropene to generate an iron alkylidene complex through deprotonation and cyclopropene ring-opening resulted only in recovery of starting materials after 2 d at 23°C. Attempts at alkylation or oxidative addition were similarly unsuccessful. Reaction with HBr and HBAr$_4^F$·2 Et$_2$O (BAr$_4^F$ = B(3,5-(CF$_3$)$_2$C$_6$H$_3$)$_4$)[122] allowed for the synthesis of the corresponding {nn(PM)$_2$}FeX (X = Br, BAr$_4^F$) complexes, but these reactions were not as clean as the corresponding synthesis of {nn(PM)$_2$}FeCl (**1**-Cl) from **1**-N(TMS)$_2$ and HCl(g), so further isolation and study was not pursued.

Because reaction of **1**-N(TMS)$_2$ with 1 equiv PMe$_3$ cleanly generated **3**-PMe$_3$, and **3**-CO was easily synthesized under analogous conditions, attempts to generate different 5-coordinate phosphines via the same route were carried out. Unfortunately, treatment of **1**-N(TMS)$_2$ with 1.0 equiv PMe$_2$Ph resulted in consumption of only 0.5 equiv **1**-N(TMS)$_2$ and formation of the bis-phosphine {nn(PM)(PI)}Fe(PMe$_2$Ph)$_2$

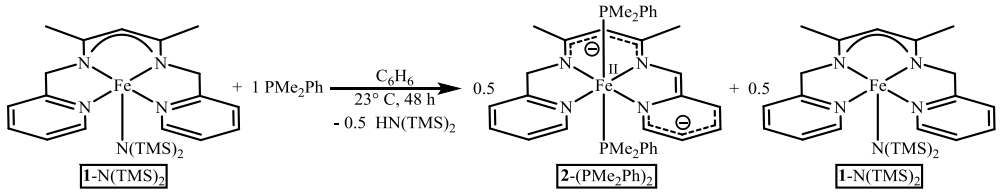

(3.12)

(**2**-$(PMe_2Ph)_2$) (Eq. 3.12). Comproportionation to generate the mono-phosphine complex {nn(PM)(PI)}$FePMe_2Ph$ was *not* observed after 3 days at 23 °C. Because both stronger *and* weaker σ-donors/π-acceptors could successfully stabilize the {nn(PM)(PI)}$FePR_2R'$ framework (**3**-PMe_3 and **3**-$PMePh_2$), one would conclude that the proposed{nn(PM)(PI)}$FePMe_2Ph$ is a stable, isolable compound as well. Presumably, the mono-phosphine is not observed because comproportionation of **2**-$(PMe_2Ph)_2$ and **1**-$(N(TMS)_2$ occurs more slowly than thermal decomposition of **1**-$N(TMS)_2$. Slightly weaker σ-donors such as PPh_3 were unable to trigger internal deprotonation, as was the strong donor P^tBu_3, presumably due to a prohibitively high steric barrier (Tolman's electronic parameter (ν) = 2056.1 cm^{-1}, Tolman's cone angle (Θ) = 182° for P^tBu_3 *vs.* ν = 2064.1 cm^{-1}, Θ = 118° for PMe_3).[121]

Treatment of **1**-$N(TMS)_2$ with excess 2,6-dimethylphenylisocyanide *did* induce internal deprotonation and resulted in the formation of {nn(PM)(PI)}Fe(2,6-$(Me)_2C_6H_3NC)_2$. As separation of excess isocyanide from the reaction mixture proved difficult, and chemical reactivity was expected to be similar to that of related **2**-LL' complexes, further investigations were not carried out. Treatment of **1**-$N(TMS)_2$ with nitriles (CH_3CN, ^tBuCN) resulted in rapid decomposition of the iron amide starting material with release of $HN(TMS)_2$ and formation of copious amounts of insoluble precipitate.

Attempts to synthesize an iron alkyl species of the form {nn(PM)$_2$}Fe(alk) from {nn(PM)$_2$}FeCl (**1**-Cl) were met with limited success: treatment of **1**-Cl with 1.0 equiv MeLi at -78°C followed by gradual warming afforded a deep blue complex at -50°C that, unfortunately, darkened to brown and precipitated out of THF solution at temperatures above -30°C (Scheme 3.6). The thermal sensitivity of the putative

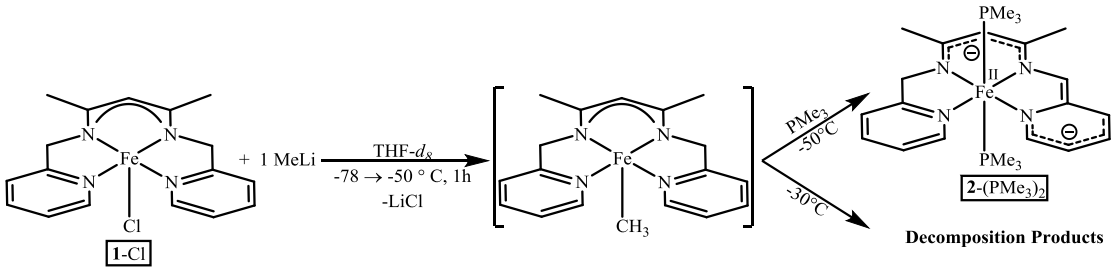

Scheme 3.6. Reaction of 1-Cl with MeLi to form **2**-(PMe$_3$)$_2$.

{nn(PM)$_2$}FeMe precluded isolation and characterization, but addition of PMe$_3$ to the blue solution at -50°C allowed for the generation of **2**-(PMe$_3$)$_2$ with release of CH$_4$. While this result supports the transient formation of {nn(PM)$_2$}FeMe, it is important to note that the possibility of a bimolecular deprotonation with MeLi is not excluded. Indeed, treatment of **1**-Cl with 1.0 equiv LiN(TMS)$_2$ did *not* result in the formation of **1**-N(TMS)$_2$, but treatment of **1**-Cl with Li(N(TMS)$_2$ in the presence of PMe$_3$ allowed the generation of **2**-(PMe$_3$)$_2$ in low yield.

3.6.2. {nn(PM)$_2$}FeLL'

One could imagine that {nn(PM)(PI)}FeLL' species could stabilize "Fe^{IV}" complexes *via* redox noninnocence of the {nn(PM)(PI)} fragment as shown in Scheme 3.7. It has been hypothesized that a metal alkylidene complex with a *d*-count of 4 or less (*i.e.*, Fe^{IV}) is necessary for olefin metathesis,[123] so the synthesis of a "masked Fe^{IV}" alkylidene was targeted. Unfortunately, treatment of **2**-(PMe$_3$)$_2$ with carbene

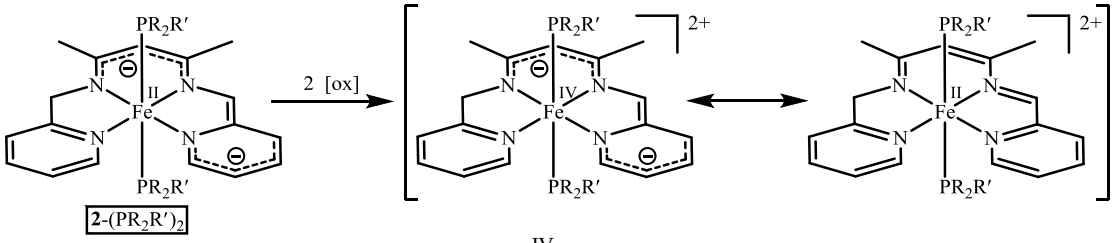

Scheme 3.7. Possible stabilization of "Fe^{IV}" *via* redox noninnocence of {nn(PM)(PI)}.

transfer reagents such as $TMS(H)CN_2$, Ph_2CN_2,[124] and 3,3-diphenylcyclopropene[125,126] resulted in decomposition of starting materials. Similar attempts at alkylation with MeI or oxidative addition with I_2 and Br_2 resulted in formation of intractable reaction mixtures and precipitation of unidentified solids. A mixed strategy of oxidation with Ph_3CCl followed by alkylation with neopentyllithium was similarly unsuccessful.

In lieu of clean chemistry at the iron metal center, reactivity at the ligand backbone was explored. Treatment of **2**-$(PMe_3)_2$ with base in an attempt to deprotonate the pyridine-methylene fragment of {nn(PM)(PI)} resulted in generation of copious amounts of unidentified insoluble precipitate. Similarly, treatment with H-atom transfer reagents to transform the pyridine-imine fragment to a pyridine-methylene group resulted only in recovery of starting materials.

3.6.3. {nn(PM)$_2$}FeL

One explanation for the lack of clean reactivity for **2**-$(PMe_3)_2$ was coordinative saturation: for chemical transformations to occur at the metal center, a bound phosphine would first have to dissociate. Given that phosphines are very good ligands,[127] dissociation of PMe_3 followed by substrate coordination and reaction was unlikely. Indeed, **2**-$(PMe_3)_2$ was entirely unreactive with respect to H_2, olefins, and alkynes. However, although {nn(PM)PI)}$FePMe_3$ (**3**-PMe_3) was similarly unreactive with respect to H_2 (only decomposition to **2**-$(PMe_3)_2$ and unidentified insoluble

byproducts was observed after 3 d), reaction of **3**-PMe_3 with excess ethylene resulted in partial conversion to a new diamagnetic product, consistent with formation of {nn(PM)(PI)}Fe(C_2H_4). Ethylene binding was quite weak, and any attempt to isolate the putative 5-coordinate species resulted in ligand loss and reformation of **3**-PMe_3. With evidence of ethylene binding, {nn(PM)(PI)}Fe(C_2H_4) could be considered as a potential olefin hydrogenation catalyst, but treatment of **3**-PMe_3 with excess ethylene under a hydrogen atmosphere resulted only in formation of the adduct {nn(PM)(PI)}Fe(C_2H_4) and **2**-$(PMe_3)_2$.

The addition of 3,3-diphenylcyclopropene to **3**-PMe_3 was conducted with the hope of generating a vinyl alkylidene iron species, but decomposition of starting materials was noted. Attempts at synthesizing an iron imido species *via* reaction of **3**-$PMePh_2$ with adamantly azide also failed. Treatment of **3**-PMe_3 with alkylating agents resulted in formation of intractable mixtures similar to those observed during alkylation attempts of **2**-$(PMe_3)_2$.

Because **2**-$(PMe_3)_2$ was shown to undergo clean oxidative chemistry, attempts towards the oxidation of **3**-PMe_3 and **3**-$PMePh_2$ were carried out. However, treatment of either starting material with Ag^+ or Cp_2Fe^+ reagents resulted in formation of green or brown insoluble precipitates and isolation of a clean oxidation product was unsuccessful.

Fortunately, treatment of **3**-CO with 1.0 equiv 3,3-diphenylcyclopropene did result in the clean generation of a new *C_1*-symmetric diamagnetic species as observed by ^1H and ^{13}C NMR. Surprisingly, the cyclopropene reagent did not react at the metal center to form an iron alkylidene complex, but rather, reaction likely occurred at the

{nn(PM)(PI)} ligand backbone. The observed ν_{CO} of 1869 cm^{-1} is quite similar to that of **3**-CO (ν_{CO} = 1879 cm^{-1}) suggestive of a 5-coordinate species. Unfortunately the high solubility of the reaction product in organic solvents precluded study *via* X-ray crystallography, and precise connectivity in the complete molecular structure could not be determined from $^{1}H/^{13}C$ correlation techniques.

Because clean reaction with 3,3-diphenylcyclopropene was observed for **3**-CO, further attempts to elicit clean chemistry from **3**-CO were carried out. Treatment of **3**-CO with 1.0 equiv MeI in THF resulted in the precipitation of a highly insoluble bright yellow powder with a single ν_{CO} = 1942 cm^{-1} (Eq. 3.13). One could imagine alkylation at two positions, either at the iron metal center or the electrophilic imine carbon as illustrated in Eq. 3.13. The IR stretching frequency was somewhat similar to that of **2**-(PMe_3)CO (ν_{CO} = 1912 cm^{-1}) and suggests six-coordination, but cannot distinguish between a methyl or iodide group in the position *trans* to the carbonyl. Unfortunately, the insolubility of the alkylated product prevented study *via* NMR analysis, and suitable crystals for X–ray analysis proved elusive. Attempts to generate

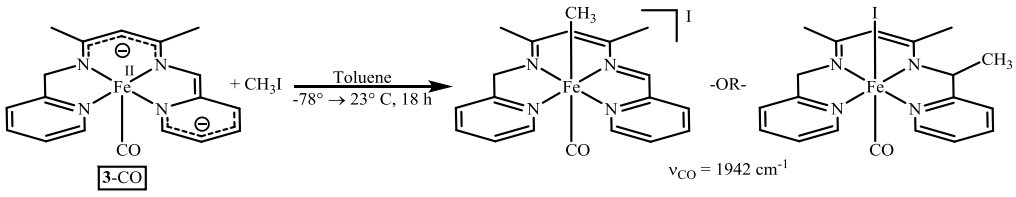

(3.13)

a more soluble product through reaction with larger linear alkyl halides or attempts at metathesis to replace the iodide ligand with a bulkier counterion resulted only in the same yellow precipitate. Without proper characterization, formulation of the alkylated product shown in Eq. 3.13 is only tentative.

Similar to the reactivity observed for **2**-LL' and other **3**-L species, treatment with group transfer reagents such as Ph_2CN_2 or $TMSN_3$ failed to produce the desired alkylidene or imido complexes. H-atom transfer was not observed with dihydroanthracene, and attempts at deprotonation of the pyridine-methylene fragment of **3**-CO resulted in production of intractable reaction mixtures and copious amounts of insoluble precipitate.

3.7. The role of redox-noninnocence in chemical reactivity

Many attempts towards utilizing the redox noninnocence of {nn(PM)(PI)} through extraction of the ligand-based electrons were carried out, with minimal success. The {nn(PM)(PI)} chelate remained dianionic in most complexes, and oxidative chemical transformations resulted in degradation. The only complex prepared with {nn(PM)(PI)} in the neutral oxidation state was the dication $[\{nn(PM)(PI)\}Fe(PMe_3)_2](BAr_4^F)_2$, which was presumably stabilized with respect to degradation via its electronic saturation and relative insolubility in organic solvents. Thus, one could imagine that the electrons stored in $\{nn(PM)(PI)\}^{2-}$ were inaccessible due to the relative instability of $\{nn(PM)(PI)\}^0$.

To rationalize the lack of redox-noninnocent behavior of {nn(PM)(PI)}, it is useful to consider several examples of how redox-noninnocence potentially enables unique reactivity. Heyduk *et al.* have shown that use of a redox-noninnocent trianionic trisamide (NNN) chelated to Zr^{IV} or Ta^{V} has allowed for mediation of group transfer reactions to organic substrates.[128-133] Figure 3.25a illustrates the transfer of a nitrene fragment from an organic azide to ^{t}BuNC with a (NNN)ZrCl(CN^{t}Bu) catalyst (**A**). Formation of the metal imido intermediate (**B**) occurs through ligand oxidation, while

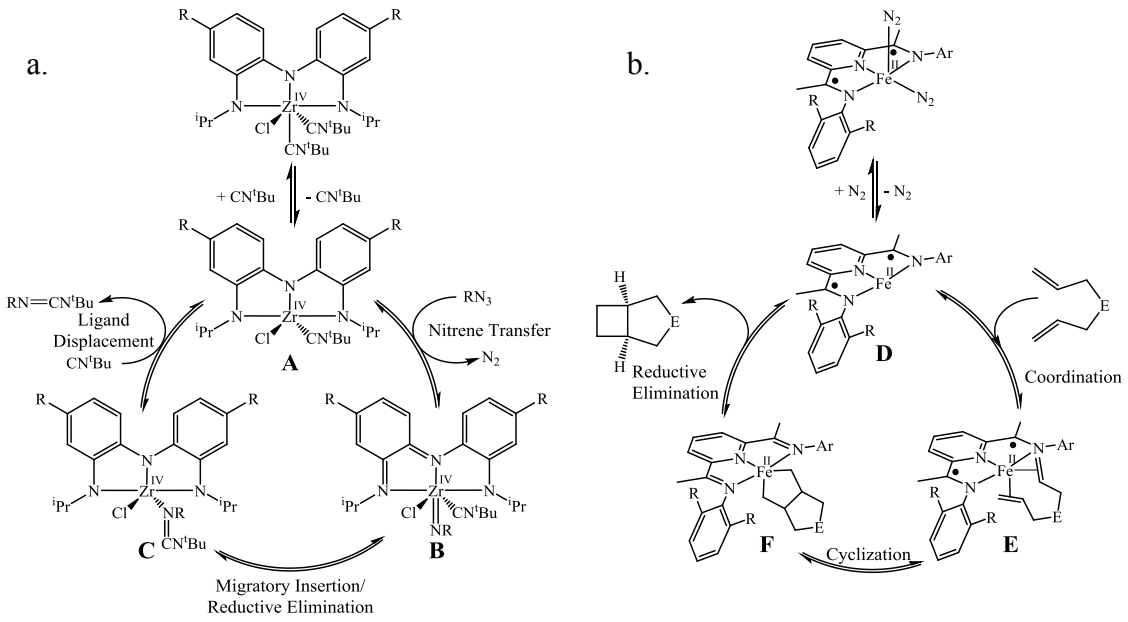

Figure 3.25. Proposed mechanisms for nitrene transfer from organic azides to isonitriles (a)[128-133] and intramolecular [2 π +2 π] cycloaddition of dienes (b).[147]

zirconium remains in the Zr^{IV} state. Insertion into the pendant isonitrile is followed by reductive elimination, which again occurs via ligand reduction and allows zirconium to remain in the Zr^{IV} oxidation state (**C**). External isocyanide then displaces the newly formed carbodiimide product to regenerate the catalyst (**A**). In its reduced state (**A, C)**, the NNN ligand exists as an 18 e^-, 4*n*+2 π system.[134] In its oxidized form (**B**) the NNN ligand is intrinsically unstable as a 4*n* π system,[134] but is stabile with respect to reduction by the chelated zirconium because Zr^{IV} is a d^0 metal center and, hence, has no *d*-electrons with which to reduce the ligand.

The 2,6-pyridinediimine (PDI) system developed by Chirik *et al.* provides another set of examples in which the PDI ligand allows mediation of chemistry that may not be accessible by more conventional methods,[135-146] and the intramolecular [2 π +2 π] cycloaddition of dienes is illustrated in Figure 3.25b.[147] Again, the redox-noninnocence of the PDI ligand is invoked, albeit in a different manner than the

example in Figure 3.25a. The diene substrate coordinates to the active catalytic species (**D**) to form an Fe^{II} intermediate (**E**). In these intermediates, the dianionic PDI is an unstable 12-e^- 4*n* π system, but is conferred electrostatic stabilization through coordination to an Fe^{II} metal center. The reductive cyclization event occurs, in which ligand oxidation affords a stable $(PDI)^0$ 10 e^- 4*n*+2 π system (**F**). Elimination of the cyclized product regenerates the catalyst (**D**). Although the redox processes in the catalytic cycle cannot be definitively proven in this case, ample physical and computational characterization for these complexes certainly support the redox-noninnocence of PDI.

It is probable that {nn(PM)(PI)} cannot assist in mediation of the redox processes described above because, although certainly capable of redox-noninnocence, {nn(PM)(PI)} is too stable in its dianionic form as a 4*n*+2 π system with electrostatic stabilization through coordination to an Fe^{II} center. The neutral form of {nn(PM)(PI)} is relatively unstable with a 12 e^- 4*n* π system chelated to a reducing Fe^0 metal center

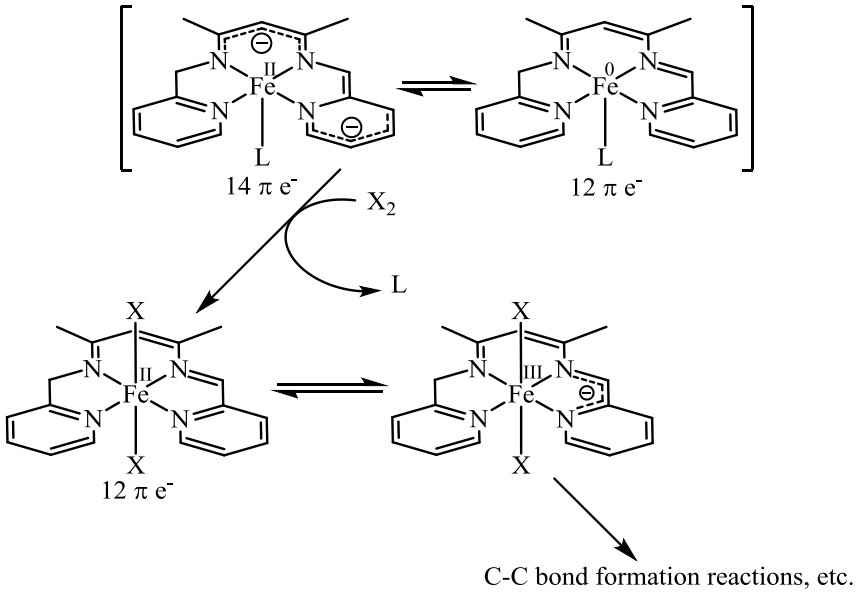

.

Scheme 3.8. Hypothetical X_2 oxidative addition to **3**-L.

(Scheme 3.8 top). As shown in Scheme 3.8, the hypothetical oxidative addition of X_2 to {nn(PM)(PI)}FeL_n results in formation of an unstable 4*n* π ligand framework. The electrostatic stabilization afforded by coordination to an Fe^{II} center must not be capable of stabilizing the oxidized product to the extent necessary for productive chemistry. In addition, the oxidized product {nn(PM)(PI)}FeX_2 may access the {nn(PM)(PI)}$^{\cdot}$/Fe^{III} electronic configuration, allowing for other degradative pathways such as C-C bond forming reactions observed in related systems.[1-6]

The (NNN) system developed by Heyduk *et al.* is quite similar to the {nn(PM)(PI)} system developed here in that both ligands are most stable in their reduced state and electrostatically stabilized through coordination to a charged metal center. The success of (NNN) in mediating oxidative processes can be rationalized through two considerations: because the Heyduk system operates with early transition metals, the energetic tradeoff of a trisamide donor for two nitrogen lone-pair donors, an amide group, and an imido group at the d^0 metal center is minimal. In contrast, for {nn(PM)(PI}FeL_n the formation of an iron imido at a d^6 metal center cannot compensate energetically for loss of the dianionic chelate. In addition, the neutral ligand in the oxidation product {nn(PM)(PI)}FeX_2 is *not* stable with respect to redox chemistry. Because the {nn(PM)(PI)}$^{\cdot}$/Fe^{III} configuration is accessible (*cf.* intermediate **B**, Figure 3.25a), additional degradative pathways may account for the lack of clean reactivity observed for {nn(PM)(PI)}FeL_n.

Conclusion

A tetradentate β-diketiminate-based ligand incorporating two pyridine-methylene units was successfully synthesized and metallated with $Fe(N(TMS)_2)_2(THF)$ to generate $\{nn(PM)_2\}FeN(TMS)_2$ (**1**-$N(TMS)_2$). **1**-$N(TMS)_2$ could be further derivatized to form $\{nn(PM)_2\}FeX$ (X = Cl, N_3). One of the methylene fragments of the ligand backbone was prone to facile deprotonation and allowed synthesis of $\{nn(PM)(PI)\}FeLL'$ (LL' = $(PMe_3)_2$, $(PMe_2Ph)_2$, $(PMe_3)CO$; **2**-LL') and $\{nn(PM)(PI)\}FeL$ (L = PMe_3, $PMePh_2$, PPh_3, CO; **3**-L). Structural, spectroscopic, and computational methods suggest these species exist as Fe^{II} metal centers bound to $\{nn(PM)(PI)\}^{2-}$, with a strong degree of metal-ligand covalency. Oxidation studies on **2**-$(PMe_3)_2$ showed two successive ligand-based $1e^-$ oxidations, a result supported by computational studies. The complexes **2**-LL' and **3**-L were unsuccessful at productively mediating the chemical transformations screened here, but offer insight into the role of redox noninnocence in chemical transformations.

Experimental

General Considerations. All manipulations were performed using either glovebox or high vacuum line techniques under an inert atmosphere. All glassware was oven dried. THF and ether were distilled under nitrogen from purple sodium benzophenone ketyl and vacuum transferred from the same prior to use. Hydrocarbon solvents were treated in the same manner with the addition of 1-2 mL/L tetraglyme. Benzene-d_6 was heated to reflux over sodium to dry and vacuum transferred from freshly cut sodium prior to use. THF-d_8 was dried over sodium and vacuum transferred from sodium benzophenone ketyl prior to use. $Fe\{N(TMS)_2\}_2(THF)$,[51] $HBAr_4^F \cdot 2\ Et_2O$,[148] $AgBAr_4^F$ ($BAr_4^F = B[3,5\text{-}CF_3(C_6H_3)]_4$),[149] Ph_2CN_2,[150] and 3,3-diphenylcyclopropene[151,152] were prepared according to literature procedures. Lithium bis(trimethylsilyl)amide was purchased from Aldrich and recrystallized from hexanes prior to use. CO (Matheson) was dried via passage through dry ice traps. All other chemicals were commercially available and used as received.

All NMR spectra were obtained on Varian INOVA 400, Varian INOVA 500, Varian INOVA 600, and Varian Mercury 300 spectrometers. Chemical shifts are reported relative to benzene-d_6 (^1H, δ 7.16; $^{13}C\{^1H\}$, δ 128.39) THF-d_8 (^1H, δ 3.58; $^{13}C\{^1H\}$, δ 67.57) and multidimensional techniques were conducted using INOVA software affiliated with the spectrometers. Solution magnetic measurements were conducted via Evans' method.[52] Elemental analyses were performed by Complete Analysis Laboratories, Inc. (E & R Microanalytical Division), Parsippany, New Jersey, and at the University of Erlangen-Nuremberg, Germany.

Synthesis. 1. H{nn(PM)$_2$}. *a. pyCH_2(NHCMeCHCOMe).* A 100 mL flask was charged with 2,4-pentane-dione (4.00 g, 39.9 mmol), $MgSO_4$ (2.40 g, 20 mmol) and 20 mL CH_2Cl_2. A solution of 2-picolylamine (4.32 g, 39.9 mmol) in 20 mL CH_2Cl_2 was added dropwise over 5 minutes at 23°C. The mixture was allowed to stir an additional 2 h at 23°C, then filtered and concentrated to a golden oil *in vacuo* to yield 7.10 g (37.3 mmol, 93 %) of pure ketoenamine, pyCH_2(NHCMeCHCOMe). ^{1}H NMR ($CDCl_3$, 400 MHz): δ1.82 (s, C*H*$_3$, 3 H), 1.92 (s, C*H*$_3$, 3H), 4.47 (d, J = 6 Hz, C*H*$_2$, 2H), 4.96 (s, nacnac-C*H*, 1 H), 7.07 (dd, J = 5, 8 Hz, py-C*H*, 1 H), 7.15 (d, J = 8 Hz, py-C*H*, 1 H), 7.55 (t, J = 8 Hz, py-C*H*, 1 H), 8.44 (d, J = 5 Hz, py-C*H*, 1 H), 11.16 (br s, N*H*, 1 H). *b. H$_2${nn(PM)$_2$}BF_4.* A 100 mL flask with dropping funnel and 180° needle valve were flame-dried under vacuum. The apparatus was backfilled with Ar and pyCH_2(NHCMeCHCOMe) (7.00 g, 36.8 mmol) was added under Ar. The apparatus was evacuated and 25 mL dry CH_2Cl_2 was added via vacuum transfer. The addition funnel was charged with Et_3OBF_4 (6.99 g, 36.8 mmol) in 20 mL dry CH_2Cl_2 under an Ar counterflow and the reaction flask was cooled to -78°C. The Et_3OBF_4 solution was added dropwise over 15 minutes and allowed to stir an additional 30 minutes at -78°C. The reaction flask was then allowed to warm to 23°C while stirring another 30 minutes, during which time a thick tan precipitate formed. The addition funnel was then charged with 2-picolylamine (3.98 g, 36.8 mmol) in 15 mL dry CH_2Cl_2, and the solution was added to the reaction mixture dropwise at 23°C over 30 minutes. During this addition, the solution turned briefly dark red and the precipitate slowly dissolved. The reaction mixture was allowed to stir at 23°C for 16 hours, over which time the solution turned brown and a bright yellow powder precipitated out of

solution. The precipitate was collected via filtration to yield pure $H_2\{nn(PM)_2\}BF_4$ (4.08 g, 11.1 mmol, 30 %). ^{1}H NMR (DMSO-d_6, 400 MHz): δ2.43 (s, CH_3, 6 H), 4.51 (s, CH_2, 4H), 5.23 (s, nacnac-C*H*, 1 H), 7.25 (d, J= 8 Hz, py-C*H*, 1 H), 7.30 (dd, J = 5 Hz, 8 Hz, py-C*H*, 1 H), 7.73 (t, J = 8 Hz, py-C*H*, 1 H), 8.48 (d, J = 5 Hz, py-C*H*, 1 H), 9.52 (br s, N*H*, 1 H). *c. H{nn(PM)$_2$}.* A 100 mL glass bomb reactor was charged with $H_2\{nn(PM)_2\}BF_4$ (4.00g, 10.8 mmol), KH (0.434g, 10.8 mmol), and 30 mL THF. The vessel was evacuated, sealed, and heated to 60°C for 24 hours, over which time H_2 was evolved and the solution turned pale orange. THF was removed *in vacuo* and the crude reaction mixture was taken up in dry C_6D_6, filtered, and concentrated to dryness to yield 2.53g (9.0 mmol, 83%) of $H\{nn(PM)_2\}$ as a pale orange solid. ^{1}H NMR (C_6D_6, 400 MHz): δ2.26 (s, CH_3, 6 H), 4.34 (s, CH_2, 4H), 5.07 (s, nacnac-C*H*, 1 H), 7.08 (d, J = 8 Hz, py-C*H*, 1 H), 7.12 (dd, J = 5, 8 Hz, py-C*H*, 1 H), 7.55 (t, J = 8 Hz, py-C*H*, 1 H), 8.31 (d, J = 5 Hz, py-C*H*, 1 H), 9.34 (br s, N*H*, 1 H).

2. {nn(PM)$_2$}FeN(TMS)$_2$ (1-N(TMS)$_2$). In an N_2 dry-box, a 100 mL flask was charged with $Fe(N(TMS)_2)_2(THF)$ (800. mg, 1.78 mmol) and benzene (15 mL). A solution of $H\{nn(PM)_2\}$ (500. mg, 1.78 mmol) in 10 mL C_6H_6 was added dropwise while stirring over 3 min at 23°C, over which time the solution changed from pale green to an intense cherry red. The solution was stirred 1 h at 23°C, and solvent was removed *in vacuo*. Pentane (25 mL) was added via vacuum transfer and the red mixture was filtered. The filter cake was washed with (8 x 20 mL) pentane. The solution was concentrated to 10 mL, cooled to -78°C, filtered, and dried *in vacuo* to yield 480. mg (0.969 mmol, 54%) of thermally-sensitive red crystalline **1**-$N(TMS)_2$. ^{1}H NMR (C_6D_6, 400 MHz): δ -80.10 ($\nu_{1/2} \approx 450$ Hz, nacnac-C*H*, 1H), -2.45 ($\nu_{1/2} \approx 70$ Hz, py-

C*H*, 2H), 0.42 ($\nu_{1/2} \approx 200$ Hz, CH_3, 6H), 10.75 ($\nu_{1/2} \approx 380$ Hz, CH_2, N(Si(CH_3)$_3$)$_2$, 22 H), 33.38 ($\nu_{1/2} \approx 125$ Hz, py-C*H*, 2H), 49.17 ($\nu_{1/2} \approx 110$ Hz, py-C*H*, 2H), 96.27 ($\nu_{1/2} \approx 1380$ Hz, py-C*H*, 2H). Anal. Calc'd for $C_{23}H_{37}N_5Si_2Fe$: C, 55.74%; H, 7.53%; N, 14.13%. Found: C, 55.58%, H, 7.38%, N, 14.33%. μ_{eff} (Evans' Method, C_6D_6, 293 K) = 5.3 μ_B.

3. {nn(PM)$_2$}FeCl (1-Cl). A 25 mL flask charged with **1**-N(TMS)$_2$ (150. mg, 0.303 mmol) and equipped with a calibrated 110 mL gas bulb was evacuated and 5 mL C_6H_6 was added via vacuum transfer. The gas bulb was charged with 50 torr of HCl (0.30 mmol) and opened to the reaction flask at 23°C. Upon exposure to HCl, a small amount of orange-yellow precipitate formed from the red benzene solution. The reaction was allowed to stir an additional 18 h, and the solvent was removed *in vacuo*. The crude reaction mixture was slurried in 5 mL Et_2O, filtered, and washed with cold Et_2O (3 x 1 mL) to remove unreacted **1**-N(TMS)$_2$. **1**-Cl was obtained as a yellow powder (62 mg, 0.17 mmol, 57%). ^{1}H NMR (THF-d_8, 400 MHz): δ -84.28 ($\nu_{1/2} \approx 270$ Hz, nacnac-C*H*, 1H), -0.05 ($\nu_{1/2} \approx 34$ Hz, py-C*H*, 2H), 1.57 ($\nu_{1/2} \approx 30$ Hz, CH_2, 4 H), 5.10 ($\nu_{1/2} \approx 120$ Hz, CH_3, 6H), 38.26 ($\nu_{1/2} \approx 80$ Hz, py-C*H*, 2H), 51.87 ($\nu_{1/2} \approx 95$ Hz, py-C*H*, 2H), 146.27 ($\nu_{1/2} \approx 770$ Hz, py-C*H*, 2H). Anal. Calc'd for $C_{17}H_{19}N_4ClFe$: C, 55.09%; H, 5.17%; N, 15.12%. Found: C, 54.09%, H, 5.12 %, N, 14.18%. μ_{eff} (Evans' Method, THE-d_8, 293 K) = 5.3 μ_B.

4. {nn(PM)$_2$}FeN$_3$ (1-N$_3$). A 4 dram vial was charged with **1**-Cl (44 mg, 0.12 mmol), NaN_3 (8 mg, 0.1 mmol), and 10 mL THF. The vial was capped and the solution was stirred for 4 d, turning from yellow to orange-yellow over time. The reaction mixture was filtered, concentrated to dryness, and orange crystalline **1**-N_3 was obtained from a saturated THF solution layered with pentane (24 mg, 0.064 mmol,

53%). ^{1}H NMR (THF-d_8, 400 MHz): δ -82.18 ($\nu_{1/2} \approx 278$ Hz, nacnac-C*H*, 1H), 1.29 ($\nu_{1/2} \approx 20$ Hz, CH_2, 4 H), 5.93 ($\nu_{1/2} \approx 95$ Hz, CH_3, 6H), 40.07 ($\nu_{1/2} \approx 105$ Hz, py-C*H*, 2H), 53.45 ($\nu_{1/2} \approx 100$ Hz, py-C*H*, 2H), 133.05 ($\nu_{1/2} \approx 945$ Hz, py-C*H*, 2H), 156.09 ($\nu_{1/2} \approx 675$ Hz, py-C*H*, 2H). Anal. Calc'd for $C_{17}H_{19}FeN_7$: C, 54.13%; H, 5.08%; N, 25.99%. Found: C, 52.79%, H, 4.89 %, N, 23.74%. μ_{eff} (Evans' Method, THF-d_8, 295 K, 1 trial) = 5.3 μ_B. IR (nujol): 2062 cm^{-1} (ν_{NNN}).

5. {nn(PM)(CHPy)}Fe(PMe$_3$)$_2$ (2-(PMe$_3$)$_2$). A 50 mL flask was charged with **1**-N(TMS)$_2$ (400. mg, 0.807 mmol) and 20 mL benzene, and PMe$_3$ (0.5 mL, 5 equiv) was added via vacuum transfer. The reaction was stirred at 23°C for 24 h, and the cherry-red solution darkened to a deeper magenta-red. The reaction mixture was concentrated to dryness, and 15 mL pentane and 0.5 mL PMe$_3$ were added via vacuum transfer. The solution was filtered, and the filter cake was washed with five 10 mL portions of pentane. The solution was concentrated to 8 mL, cooled to -78°C, and filtered to afford 280. mg (0.576 mmol, 71%) of deep purple **2**-(PMe$_3$)$_2$ upon drying *in vacuo*. ^{1}H NMR (C_6D_6, 400 MHz): δ 0.66 (d, J = 6 Hz, **s**, 18 H), 2.09 (s, **g**, 3 H), 2.28 (s, **h**, 3H), 4.14 (s, **i**, 2H), 4.99 (s, **f**, 1 H), 5.77 (t, J = 6 Hz, **b**, 1 H), 6.17 (t, J = 6 Hz, **l**, 1 H), 6.39 (d, J = 8 Hz, **j**, 1 H), 6.47 (s, **e**, 1 H), 6.53 (d, 6 Hz, **d**, 1H), 6.60 (t, 6 Hz, **c**, 1H), 6.61 (t, 6 Hz, **k**, 1H), 7.51 (d, J = 6 Hz, **a**, 1 H), 8.80 (d, J = 6 Hz, **m**, 1 H). ^{13}C NMR (C_6D_6, 100 MHz): δ 13.33 (**s**), 22.10 (**g**), 22.26 (**h**), 62.70 (**i**), 96.28 (**f**), 100.87 (**b**), 108.78 (**e**), 112.80 (**d**), 117.81 (**j**), 120.83 (**l**), 125.06 (**c**), 129.41 (**k**), 136.56 (**p**), 149.43 (**q**), 150.61 (**a**), 153.90 (**n**), 155.41 (**m**), 169.92 (**o**). ^{31}P NMR (C_6D_6, 162 MHz): δ19.6 (s, $\nu_{1/2} \approx 60$ Hz). Anal. Calc'd for $C_{23}H_{36}N_4P_2Fe$: C, 56.80%; H, 7.46%; N, 11.52%. Found: C, 56.95%, H, 7.31%, N, 11.47%.

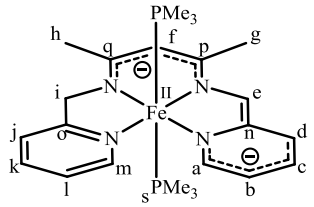

6. [{nn(PM)(PI)}Fe(PMe$_3$)$_2$][PF$_6$] (2^+-(PMe$_3$)$_2$). In an N_2 dry-box, a 4-dram vial was charged with **2**-(PMe$_3$)$_2$ (30. mg, 0.062 mmol) and 2 mL THF. A 3 mL THF solution of Cp_2FePF_6 (20. mg, 0.060 mmol) was added dropwise at 23°C while stirring. The solution slowly darkened to brown over 15 minutes. The mixture was stirred for 12 h, and solvent was removed *in vacuo*. The crude material was washed with 1 mL cold THF, redissolved in THF, and layered with pentane. Brown crystalline $\mathbf{2}^+$-(PMe$_3$)$_2$ was obtained after 12 h. Anal. Calc'd for $C_{23}H_{36}FeN_4P_3F_6$: C, 43.76%; H, 5.75%; N, 8.87%. Found: C, 42.74%, H, 5.11%, N, 7.34%. μ_{eff} (Evans' Method, THF-d_8, 295 K, 1 trial) = 1.6 μ_B.

7. [{nn(PM)(PI)}Fe(PMe$_3$)$_2$][B(3,5-(CF$_3$)$_2$C$_6$H$_3$)$_4$]$_2$ (2^{2+}-(PMe$_3$)$_2$). In an N_2 dry-box, a 4-dram vial was charged with {nn(PM)(PI)}Fe(PMe$_3$)$_2$ (50. mg, 0.10 mmol) and 2 mL THF. To this, a 3 mL THF solution of Ag[B(3,5-(CF$_3$)$_2$C$_6$H$_3$)$_4$] (200. mg, 0.206 mmol) was added dropwise at room temperature while stirring. Upon addition, the solution turned initially brown (indicative of {nn(PM)(PI)}Fe(PMe$_3$)$_2$(BAr$^F{}_4$)), then deep green with the precipitation of dark brown Ag^0. The mixture was allowed to stir an additional 4 hours then filtered through Celite to remove Ag^0. The THF solution was layered with pentane and left overnight to yield deep green crystalline material (160. mg, 0.0723 mmol, 70 %). ^{1}H NMR (THF-d_8, 400 MHz): δ 0.93 (dd, J = 4, 5 Hz, **s**, 18 H), 2.39 (s, **h**, 3 H), 2.40 (s, **g**, 3H), 5.21 (s, **i**, 2H), 6.47 (s, **f**, 1 H), 7.58 (s, **t**, 8 H), 7.63 (t, J = 6 Hz, **l**, 1 H), 7.68 (d, J = 7

Hz, **d**, 1 H), 7.79 (s, **u**, 16 H) , 7.82 (t, J = 6 Hz, **b**, 1 H), 7.93 (d, 7 Hz, **j**, 1H), 8.10 (t, 7 Hz, **k**, 1H), 8.12 (t, 7 Hz, **c**, 1H), 8.67 (d, J = 6 Hz, **a**, 1 H), 8.71 (d, J = 6 Hz, **m**, 1 H), 8.95 (s, **e**, 1 H). ^{13}C NMR (THF-d_8, 100 MHz): δ 10.84 (**s**), 21.36 (**g**), 26.39 (**h**), 67.52 (**i**), 98.94 (**b**), 119.50 (**t**), 128.28 (**f**), 128.63 (**l**), 129.97 (**j**), 135.75 (**e**), 136.69 (**u**), 140.77 (**p**), 141.92 (**k**), 141.50 (**c**), 144.35 (**d**), 156.14 (**a**), 159.34 (**m**), 159.45 (**q**), 163.53 (**n**), 176.75 (**o**). ^{31}P NMR (THF-d_8, 162 MHz): δ 13.8 (s, $\nu_{1/2} \approx 10$ Hz). Anal. Calc'd for $C_{87}H_{60}FeN_4P_2B_2F_{48}$: C, 47.22%; H, 2.73%; N, 2.53%. Found: C, 49.28%, H, 3.40%, N, 2.29%.

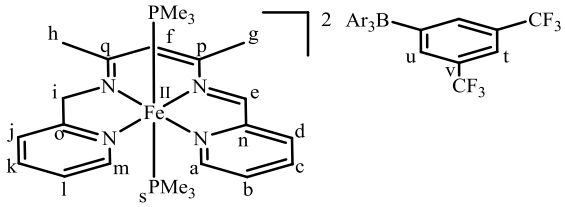

8. {nn(PM)(PI)}Fe(PMe$_3$)CO (2-(PMe$_3$)CO). *a.* A 50 mL flask was charged with {nn(PM)(PI)}Fe(PMe$_3$)$_2$ (150. mg, 0.308 mmol) and equipped with a 180° needle valve. The apparatus was evacuated and 15 mL C_6H_6 was added via vacuum transfer. The system was charged with 1 atm CO at 23°C and allowed to stir for 18 hours, over which time the magenta-red solution lightened slightly to a deep orange-red. Solvent was removed *in vacuo*, and the resulting solid was washed with cold pentane to yield {nn(PM)(PI)}Fe(PMe$_3$)CO as a red-brown solid (112 mg, 0.256 mmol, 85%). ^{1}H NMR (C_6D_6, 400 MHz): δ 0.83 (d, J = 10 Hz, **s**, 9 H), 2.08 (s, **h**, 3 H), 2.13 (s, **g**, 3 H), 4.68 (br s, $\nu_{1/2} \approx 25$, **i**, 2 H), 4.98 (s, **f**, 1 H), 5.54 (t, J = 7 Hz, **b**, 1 H), 6.13 (t, J = 7 Hz, **c**, 1 H), 6.15 (t, J = 7 Hz, **l**, 1 H), 6.24 (d, J = 7 Hz, **d**, 1 H), 6.41 (s, **e**, 1 H), 6.52 (t, J = 7 Hz, **k**, 1 H), 6.55 (d, J = 7 Hz, **j**, 1 H), 7.79 (d, J = 6 Hz, **a**, 1 H), 8.01 (d, J = 7 Hz, **m**, 1 H). ^{13}C NMR (C_6D_6, 100 MHz): δ 15.19 (**s**), 22.31 (**g**), 22.42 (**h**), 64.98 (**i**),

100.42 (**f**), 102.03 (**b**), 118.00 (**d**), 121.87 (**l**), 121.92 (**c**), 124.42 (**e**), 130.43 (**j**), 134.88 (**k**), 138.73 (**a**), 139.58 (**p**), 150.25 (**m**), 152.73 (**n**), 153.29 (**q**), 174.38 (**o**). ^{31}P NMR (C_6D_6, 162 MHz): δ41.2 (s, $\nu_{1/2} \approx 880$ Hz). Anal. Calc'd for $C_{21}H_{27}N_4FeOP$: C, 57.55 %; H, 6.21%; N, 12.78%. Found: C, 56.49%, H, 7.09%, N, 10.78%. *b.* A J. Young tube was charged with {nn(PM)(PI)}Fe(PMe_3) (**3**-PMe_3, 10. mg, 0.024 mmol) and 0.4 mL C_6D_6. The tube was evacuated via three freeze-pump-thaw cycles, and charged with 1 atm CO. The red-brown solution lightened slightly to an orange red. The formation of {nn(PM)(PI)}Fe(PMe_3)CO (**2**-(PMe_3)CO) was confirmed by ^{1}H NMR spectroscopy.

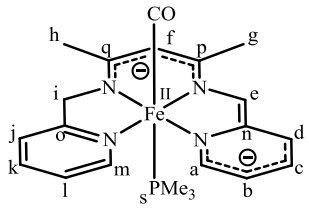

9. {nn(PM)(PI)}Fe(PMe_3) (3-PMe_3). A 50 mL flask was charged with {nn(PM)(PI)}Fe(PMe_3)$_2$ (**2**-(PMe_3)$_2$, 100. mg, 0.206 mmol), and 20 mL hexanes was added via vacuum transfer. The solution was stirred for 30 min at 23°C. The solvent was removed *in vacuo*, and the residual solid was triturated 8 times with 15 mL portions of hexanes. With each successive trituration, the hexanes solution gradually changed from magenta-red to red-brown. The crude red-brown solid was collected and identified as **3**-PMe_3 (70. mg, 0.17 mmol, 81 %). ^{1}H NMR (THF-d_8, 400 MHz): δ 0.24 (d, J = 8 Hz, **s**, 9 H), 2.45 (s, **g**, 3 H), 2.48 (s, **h**, 3H), 4.48 (s, **i**, 2H), 5.82 (s, **f**, 1 H), 5.74 (t, J = 6 Hz, **b**, 1 H), 6.34 (t, J = 7 Hz, **c**, 1 H), 6.71 (d, J = 8 Hz, **d**, 1 H), 7.13 (t, J = 6 Hz, **l**, 1 H), 7.24 (s, **e**, 1 H), 7.42 (t, J = 7 Hz, **k**, 1 H), 7.43 (d, J = 8 Hz, **j**, 1 H), 7.89 (d, J = 6 Hz, **a**, 1 H), 9.35 (d, J = 6 Hz, **m**, 1 H). ^{13}C NMR (THF-d_8, 100 MHz): δ

11.99 (**s**), 21.77 (**g**), 22.48 (**h**), 65.58 (**i**), 102.91 (**b**), 103.48 (**f**), 112.13 (**e**), 114.59 (**d**), 117.93 (**j**), 121.69 (**l**), 123.14 (**c**), 130.04 (**k**), 137.37 (**p**), 149.36 (**q**), 151.41 (**a**), 154.22 (**n**), 157.67 (**m**), 170.90 (**o**). ^{31}P NMR (C_6D_6, 162 MHz): δ45.0 (s, $\nu_{1/2} \approx 220$ Hz). Anal. Calc'd for $C_{20}H_{27}N_4FeP$: C, 58.55 %; H, 6.63%; N, 13.66%. Found: C, 56.49%, H, 6.30%, N, 13.09%.

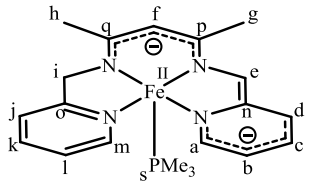

10. {nn(PM)(PI)}FeCO (3-CO). A 50 mL flask was charged with **1**-N(TMS)$_2$ (75 mg, 0.15 mmol) and 15 mL C_6H_6 was added via vacuum transfer. CO (1 atm) was placed over the solution, which was stirred for 18 h at 23°C. Over time, the cherry red solution turned to a lighter brick red color. Solvent was removed *in vacuo*, and the residual solid was washed with pentane to yield 40. mg (0.11 mmol, 79 %) of **3**-CO. ^{1}H NMR (THF-d_8, 400 MHz): δ 2.11 (s, **h**, 3 H), 2.64 (s, **g**, 3H), 3.60 (d, J = 21 Hz, **i**, 1H), 4.21 (d, J = 21 Hz, **i'**, 1 H), 6.28 (t, J = 6 Hz, **l**, 1 H), 6.31 (s, **f**, 1 H), 6.34 (t, J = 6 Hz, **b**, 1 H), 6.36 (d, J = 6 Hz, **d**, 1 H), 6.65 (t, J = 6 Hz, **c**, 1 H), 6.90 (t, J = 6 Hz, **k**, 1 H), 7.34 (d, J = 7 Hz, **j**, 1 H), 7.73 (s, **e**, 1 H), 8.43 (d, J = 6 Hz, **a**, 1 H), 8.95 (d, J = 6 Hz, **m**, 1 H). ^{13}C NMR (THF-d_8, 100 MHz): δ 21.71 (**h**), 21.83 (**g**), 64.88 (**i**), 106.10 (**b**), 109.11 (**f**), 117.33 (**e**), 118.68 (**d**), 119.98 (**j**), 122.85 (**l**), 125.42 (**c**), 134.78 (**k**), 143.30 (**p**), 148.28 (**a**), 152.62 (**q**), 153.42 (**n**), 155.67 (**m**), 166.81 (**o**). Anal. Calc'd for $C_{18}H_{18}N_4OFe$: C, 59.69 %; H, 5.01%; N, 15.47%. Found: C, 57.25%, H, 4.84%, N, 14.64%; successive attempts were similarly low in all elements.

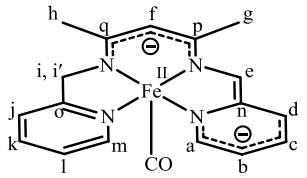

11. Li_2{nn(PM)(PI)}. A 100 mL flask was charged with H{nn$(PM)_2$} (500. mg, 1.78 mmol) and 20 mL THF, and cooled to -78°C. Under an Ar purge, 1.6 M ^{n}BuLi in hexanes (2.23 mL, 3.57 mmol) was added dropwise over 10 min. Upon addition of the first equivalent of ^{n}BuLi the solution darkened from orange-yellow to red-orange, and addition of the second equiv resulted in a color change to dark purple and precipitation of a dark solid. The reaction was allowed to warm to 23°C and stirred an additional 4 h. Solvent was removed *in vacuo*, and the resulting purple solid was triturated once with 20 mL C_6H_6 and filtered in 20 mL C_6D_6 to yield Li_2{nn(PM)(PI)} as a purple powder (310. mg, 1.06 mmol, 60%); this material was used without further purification. ^{1}H NMR (THF-d_8, 400 MHz): δ 1.62 (s, **h**, 3 H), 1.91 (s, **g**, 3H), 4.05 (s, **f**, 1H), 4.61 (t, J = 7, **b**, 1 H), 4.78 (s, **i**, 2 H), 5.37 (s, **e**, 1H), 5.50 (d, J = 8, **d**, 1 H), 5.86 (t, J = 7 Hz, **c**, 1 H), 6.46 (d, J = 6 Hz, **a**, 1 H), 7.16 (t, J = 7 Hz, **l**, 1 H), 7.22 (d, J = 7 Hz, **j**, 1 H), 7.64 (t, J = 8 Hz, **k**, 1 H), 8.47 (d, J = 6 Hz, **m**, 1 H). ^{13}C NMR (THF-d_8, 100 MHz): δ 19.05 (**h**), 22.93 (**g**), 56.78 (**i**), 95.48 (**f**), 97.90 (**b**), 99.24 (**e**), 115.62 (**d**), 121.73 (**l**), 122.60 (**j**), 130.86 (**c**), 137.15 (**k**), 142.46 (**p**), 149.63 (**m**), 150.63 (**a**), 153.32 (**n**), 158.13 (**q**), 166.29 (**o**).

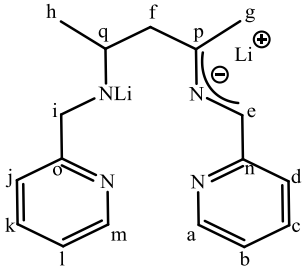

12. {nn(PM)(PI)}Fe(PMe_2Ph)$_2$ (2-(PMe_2Ph)$_2$). In an N_2 dry-box, a 4-dram vial was charged with $FeBr_2(THF)_2$ (25 mg, 0.069 mmol), PMe_2Ph (19 mg, 0.14 mmol), and 3 mL THF. A 1 mL THF solution of Li_2{nn(PM)(PI)} (20. mg, 0.068 mmol) was added to the solution dropwise at room temperature while stirring. Upon addition, the solution turned purple-brown and a fine light precipitate was formed. The mixture was allowed to stir an additional 2 hours, and solvent was removed *in vacuo*. The crude mixture was dissolved in C_6H_6, filtered, and concentrated to dryness to yield **2**-(PMe_2Ph)$_2$ as a purple-brown solid. ^{1}H NMR (C_6D_6, 400 MHz): δ 0.85 (s, **s**, 3 H) 0.88 (s, **t**, 3 H), 2.11 (s, **h**, 3 H), 2.46 (s, **g**, 3 H), 3.54 (s, **i**, 2H), 5.47 (s, **f**, 1 H), 5.91 (t, J = 6 Hz, **b**, 1 H), 6.09 (t, J = 6 Hz, **k**, 1 H), 6.12 (t, J = 6 Hz, **l**, 1 H), 6.48 (d, J = 8 Hz, **j**, 1 H), 6.68 (t, 6 Hz, **c**, 1H), 6.81 (d, 6 Hz, **h**, 1H), 6.89 (m, **u**, 8 H), 6.93 (s, **e**, 1 H), 7.00 (m, **v**, 2 H), 7.59 (d, J = 6 Hz, **a**, 1 H), 8.52 (d, J = 6 Hz, **m**, 1 H). ^{13}C NMR (C_6D_6, 100 MHz): δ 11.86 (**s**), 14.65 (**t**), 22.57 (**h**), 22.70 (**g**), 63.29 (**i**), 99.34 (**f**), 101.99 (**b**), 110.93 (**u**), 110.93 (**e**), 113.86 (**d**), 117.46 (**l**),120.75 (**k**), 124.98 (**c**), 127.76 (**u**), 129.52 (**j**), 130.13 (**v**), 137.33 (**p**), 149.55 (**q**), 151.59 (**a**), 154.07 (**n**), 155.42 (**a**), 169.48 (**o**). ^{31}P NMR (C_6D_6, 162 MHz): δ 16.6 (s, $\nu_{1/2} \approx 130$ Hz). The preparation of **2**-(PMe_2Ph) was conducted only on a small scale, precluding attempts at EA.

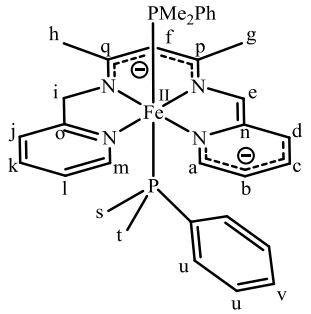

13. {nn(PM)(PI)}Fe($PMePh_2$) (3-$PMePh_2$). A 4-dram vial was charged with $FeBr_2(THF)_2$ (25 mg, 0.070 mmol), $PMePh_2$ (28 mg, 0.14 mmol), and 3 mL THF. A 1 mL THF solution of Li_2{nn(PM)(PI)} (20. mg, 0.068 mmol) was added dropwise at 23°C while stirring. Upon addition, the solution turned brown and a brown solid precipitated. The mixture was allowed to stir an additional 2 h, and solvent was removed *in vacuo*. The crude mixture was washed with C_6H_6 and filtered through Celite in THF. Crystalline **3**-$PMePh_2$ was obtained from a THF solution layered with pentane over 2 days (21 mg, 0.039 mmol, 56%). ^{1}H NMR (C_6D_6, 400 MHz): δ 0.38 (s, **s**, 3 H), 2.27 (s, **h**, 3 H), 2.70 (s, **g**, 3 H), 3.20 (s, **i**, 2H), 6.17 (t, J = 6 Hz, **l**, 1 H), 6.45 (s, **f**, 1 H), 6.58 (t, J = 6 Hz, **k**, 1 H), 6.59 (t, 6 Hz, **b**, 1H), 6.71 (m, **u**, 4 H), 6.90 (d, J = 8 Hz, **j**, 1 H), 6.91 (t, 6 Hz, **c**, 1H), 6.93 (m, **t**, **v**, 6 H), 7.45 (d, J = 6 Hz, **d**, 1 H), 8.03 (s, **e**, 1 H), 8.46 (d, J = 6 Hz, **a**, 1 H), 9.26 (d, J = 6 Hz, **m**, 1 H). ^{13}C NMR (C_6D_6, 100 MHz): δ 21.46 (**h**), 21.57 (**s**), 22.00 (**g**), 64.86 (**i**), 105.96 (**b**), 106.93 (**f**), 116.10 (**d**), 116.44 (**e**), 120.52 (**l**), 123.40 (**j**), 123.45 (**c**), 127.71 (**t**),128.38 (**3**), 130.85 (**u**), 131.55 (**p**), 131.57 (**v**), 151.28 (**a**), 151.96 (**q**), 155.08 (**n**), 156.90 (**m**), 169.63 (**o**). ^{31}P NMR (C_6D_6, 162 MHz): δ 68.8 (s, $\nu_{1/2} \approx 650$ Hz). Anal. Calc'd for $C_{30}H_{31}FeN_4P$: C, 67.42 %; H, 5.85%; N, 10.48%. Found: C, 62.49%, H, 5.54%, N, 8.98%.

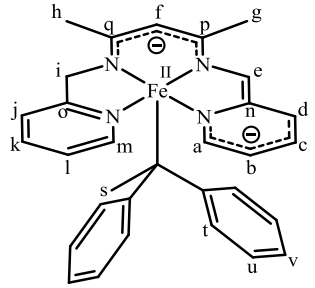

14. {nn(PM)(PI)}Fe(PPh_3) (3-PPh_3). A 4-dram vial was charged with $FeBr_2(THF)_2$ (20. mg, 0.056 mmol), PPh_3 (44 mg, 0.17 mmol), and 3 mL THF. Solid Li_2{nn(PM)(PI)} (16 mg, 0.055 mmol) was added to the solution in small portions at

23°C while stirring. Upon complete addition, the solution turned purple-brown and a fine light precipitate was formed. The mixture was allowed to stir an additional 2 h, and solvent was removed *in vacuo*. The crude mixture was dissolved in C_6H_6, filtered, and concentrated to dryness to yield **3**-PPh_3 as a purple solid. ^{1}H NMR (C_6D_6, 400 MHz): δ 2.29 (s, **h**, 3 H), 2.35 (s, **g**, 3H), 3.96 (s, **i**, 2H), 6.07 (t, J = 7 Hz, **b**, 1 H), 6.23 (s, **f**, 1 H), 6.63 (t, J = 7 Hz, **c**, 1 H), 6.82 (t, J = 7 Hz, **l**, 1 H), 6.83 (t, J = 7 Hz, **c**, 1 H), 6.97 (d, J = 7 Hz, **d**, 1 H), 7.02 (m, **t**, 3 H), 7.20 (s, **e**, 1 H), 7.28 (m, **s**, 2 H), 7.41 (d, J = 8 Hz, **j**, 1 H), 8.78 (d, J = 7 Hz, **a**, 1 H), 9.47 (d, J = 7 Hz, **m**, 1 H). ^{13}C NMR (C_6D_6, 100 MHz): δ 23.05 (**g**), 24.41 (**h**), 67.96 (**i**), 100.76 (**b**), 108.61 (**f**), 120.54 (**c**), 121.27 (**l**), 121.76 (**d**), 125.25 (**k**), 128.43 (**t**), 128.24 (**e**), 128.51 (**j**), 134.24 (**s**), 137.69 (**p**), 147.64 (**q**), 147.68 (**n**), 154.78 (**o**), 155.38 (a), 158.21 (**m**). ^{31}P NMR (THF-d_8, 162 MHz): δ 30.5 (s, $\nu_{1/2} \approx 1600$ Hz). The preparation of **3**-PPh_3 was conducted only on a small scale for the sake of preparing a derivative, precluding attempts at EA.

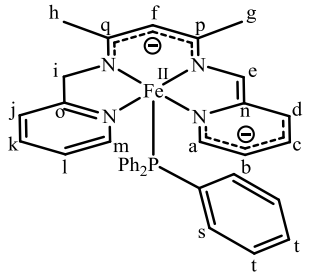

15. Oxidation of {nn(PM)(PI)}Fe(PMePh$_2$) decay product. A vial of solid {nn(PM)(PI)}Fe(PMePh$_2$) was stored uncapped in an N_2 drybox for 20 d to allow formation of the putative ligand-free {nn(PM)(PI)}Fe decay product (see text). A 4-dram vial was charged with this material (3 mg, ~0.009 mmol), $AgBAr_4^F$ (9 mg, 0.009 mmol) and THF-d_8 (0.04 mL). The resulting solution turned red immediately, and then turned brown over 2 min with concomitant formation of a small amount of brown precipitate (Ag^0). The solution was filtered to remove Ag^0 and transferred to a J.

Young tube for NMR analysis. Although definitive structural determination was elusive, chemical shifts of the product as determined by standard 2-dimensional techniques are given below in Figure 3.26.

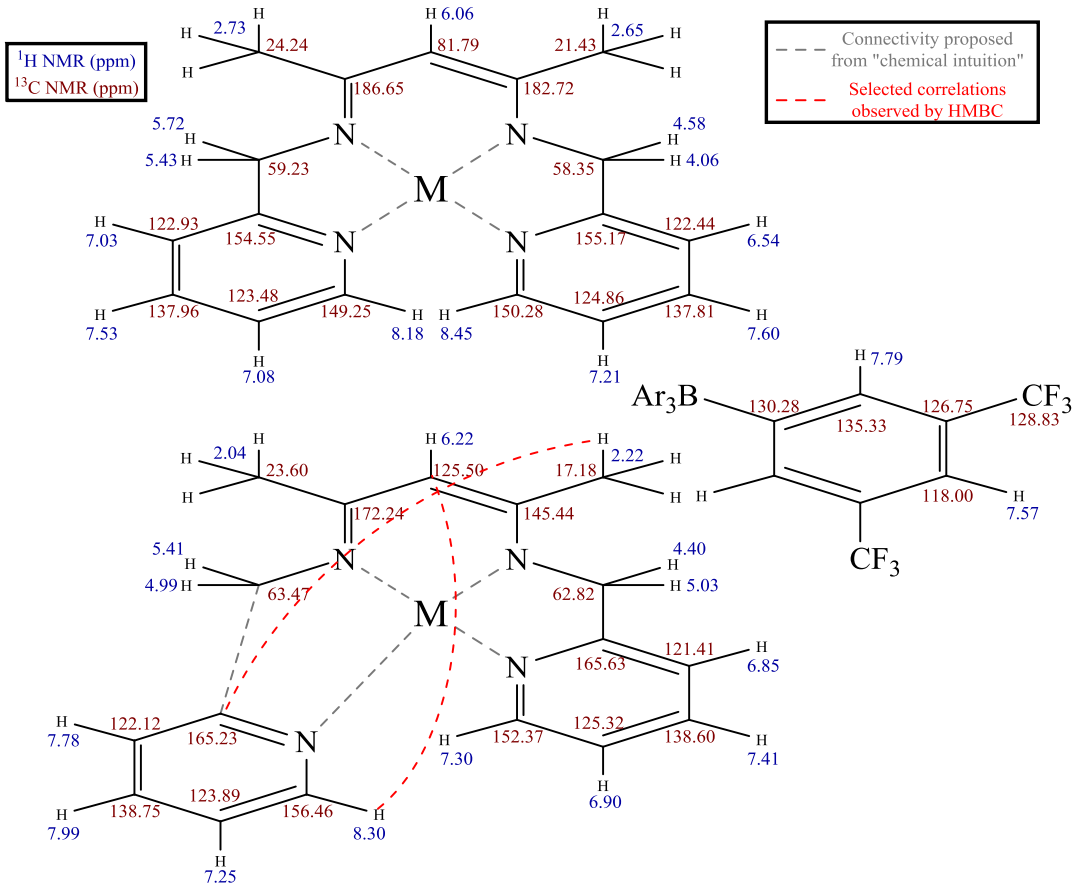

Figure 3.26. Chemical shifts of oxidation product as determined by ^{1}H, ^{13}C, (HH) gCOSY, (HC) HSQCAD, and (HC) gHMBSAD. Two independent ligand frameworks were determined, and no long-range correlations between the two frameworks were observed. No standard HMBC correlations between the main β-diketiminate framework and a pyridine fragment (bottom left) were observed, but long range-correlations to the β-diketiminate backbone were seen (dashed red curves).

16. {nn(PM)$_2$}FeBr. A 10 mL flask was charged with {nn(PM)$_2$}FeN(TMS)$_2$ (**1**-N(TMS)$_2$, 20. mg, 0.040 mmol) and benzene (2 mL). A solution of HBr in HOAc (5.7 M, 7 μL, 0.04 mmol) was added slowly at 23 °C under Ar purge while stirring vigorously. Upon acid addition, the cherry red solution lightened to orange red and an

orange precipitate formed. The reaction was stirred 10 min at 23 °C and solvent was removed *in vacuo*. The resulting orange solid was washed with two 2 mL portions of benzene and two 1 mL portions of pentane, and dissolved in THF-d_8 for NMR analysis. ^{1}H NMR (THF-d_8, 400 MHz): δ -86.71 ($\nu_{1/2} \approx 150$ Hz, nacnac-C*H*, 1H), 5.27 ($\nu_{1/2} \approx 60$ Hz, py-C*H*, 2H), 4.67 ($\nu_{1/2} \approx 90$ Hz, CH_3, 6H), 6.58 ($\nu_{1/2} \approx 130$ Hz, CH_2, 4 H), 41.38 ($\nu_{1/2} \approx 90$ Hz, py-C*H*, 2H), 53.49 ($\nu_{1/2} \approx 90$ Hz, py-C*H*, 2H), 128.75 ($\nu_{1/2} \approx$ 700 Hz, py-C*H*, 2H).

17. [{nn(PM)$_2$}Fe](BAr$_4^F$)(THF)$_n$. A 4-dram vial was charged with {nn(PM)$_2$}FeN(TMS)$_2$ (**1**-N(TMS)$_2$, 15 mg, 0.030 mmol) and THF (2 mL). A 2 mL THF solution of HBAr$_4^F$·2 Et$_2$O was added dropwise at 23 °C while stirring vigorously. Upon complete addition, the cherry red solution turned yellow-brown and a small amount of yellow precipitate formed. The reaction mixture was allowed to stir 2 h and solvent was removed *in vacuo*. The crude solid was washed with two 2 mL portions of pentane and dissolved in C_6D_6 for NMR analysis. ^{1}H NMR (C_6D_6, 400 MHz): δ -57.56 ($\nu_{1/2} \approx 200$ Hz, nacnac-C*H*, 1H), 1.11 ($\nu_{1/2} \approx 30$ Hz, THF),1.11 ($\nu_{1/2} \approx$ 30 Hz, CH_3, 6H), 3.26 ($\nu_{1/2} \approx 30$ Hz, THF), 7.36 ($\nu_{1/2} \approx 80$ Hz, CH_2, 4 H), 7.92 ($\nu_{1/2} \approx$ 40 Hz, BAr$_4^F$, 4 H), 8.71 ($\nu_{1/2} \approx 30$ Hz, BAr$_4^F$, 8 H), 27.31 ($\nu_{1/2} \approx 90$ Hz, py-C*H*, 2H), 37.76 ($\nu_{1/2} \approx 80$ Hz, py-C*H*, 2H), 105.13 ($\nu_{1/2} \approx 420$ Hz, py-C*H*, 2H), 133.91 ($\nu_{1/2} \approx$ 450 Hz, py-C*H*, 2H).

18. Attempt at synthesis of {nn(PM)(PI)}FePMe$_2$Ph. A 4-dram vial was charged with PMe$_2$Ph (5 mg, 0.04 mmol) and C_6D_6 (0.4 mL). Solid {nn(PM)$_2$}FeN(TMS)$_2$ (**1**-N(TMS)$_2$, 18 mg, 0.36 mmol) was added in portions at 23 °C while stirring, and over 1 min the cherry red solution darkened to brown. The

reaction mixture was transferred to a J. Young tube and the presence of a 1:1 mixture of **2**-$(PMe_2Ph)_2$ and **1**-$N(TMS)_2$ and release of $HN(TMS)_2$ was confirmed by ^1H NMR. Storage of the reaction mixture at 23 °C resulted only in thermal decomposition of **1**-$N(TMS)_2$ over 3 d.

19. {nn(PM)(PI)}Fe(3,6-$(CH_3)_2C_6H_3NC)_2$. A J. Young tube was charged with {nn(PM)(PI)}$FeN(TMS)_2$ (**1**-$N(TMS)_2$, 10. mg, 0.020 mmol) and C_6D_6 (0.4 mL). Solid 2,6-dimethylphenyl isocyanide (5 mg, 0.4 mmol) was added and the cherry red solution turned red-brown. ^1H NMR analysis revealed the formation of {nn(PM)(PI)}Fe(3,6-$(CH_3)_2C_6H_3NC)_2$. ^1H NMR (C_6D_6, 400 MHz): δ 2.12 (s, **s**, 12 H), 2.29 (s, **g**, 3 H), 2.31 (s, **h**, 3H), 4.86 (s, **i**, 2H), 5.18 (s, **f**, 1 H), 5.55 (t, J = 6 Hz, **b**, 1 H), 6.32 (t, J = 6 Hz, **l**, 1 H), 6.44 (d, J = 6 Hz, **j**, 1 H), 6.53 (s, **c**, 1 H), 6.63 (mult, **u**, **t**, 6H), 6.64 (d, 6 Hz, **d**, 1H), 6.70 (t, 6 Hz, **c**, 1H), 6.71 (t, 6 Hz, **k**, 1H), 7.94 (d, J = 5 Hz, **a**, 1 H), 8.52 (d, J = 5 Hz, **m**, 1 H). IR (Nujol): 2036 cm^{-1} (ν_{NC}).

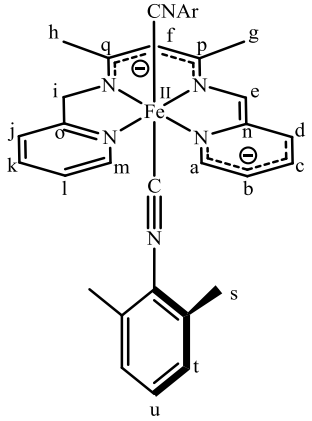

20. Alkylation of {nn$(PM)_2$}FeCl. A J. Young tube was charged with {nn$(PM)_2$}FeCl (**1**-Cl, 20. mg, 0.054 mmol) and THF-d_8 (0.4 mL). A solution of MeLi in Et_2O (1.6 M, 34 μL, 0.054 mmol) was added at -78 °C under Ar counterflow. Upon complete addition, the yellow solid **1**-Cl dissolved and the solution turned deep blue. The tube was gradually warmed to 23 °C over 10 min. At approximately -50 °C, the

blue solution turned brown and a brown precipitate formed. ^{1}H NMR analysis revealed evolution of CH_4, but the insolubility of the brown precipitate precluded further NMR analysis.

21. {nn(PM)(PI)}Fe(C_2H_4). A J. Young tube was charged with {nn(PM)(PI}FePMe$_3$ (**3**-PMe$_3$, 10. mg, 0.024 mmol) and C_6D_6 (0.4 mL). Ethylene (1 atm) was admitted to the tube at 23 °C. No physical changes were observed, but ^{1}H NMR analysis revealed formation of a new diamagnetic species consistent with {nn(PM)(PI)}Fe(C_2H_4). ^{1}H NMR (C_6D_6, 400 MHz): 2.54 (s, **h**, 3 H), 2.72 (s, **g**, 3 H), 4.47 (s, **i**, 2H), 6.19 (t, J = 6 Hz, **l**, 1 H), 6.34 (s, **f**, 1 H), 6.46 (t, J = 6 Hz, **k**, 1 H), 6.79 (t, 6 Hz, **b**, 1H), 6.81 (d, J = 6 Hz, **j**, 1 H), 6.84 (t, 6 Hz, **c**, 1H), 7.37 (d, J = 6 Hz, **d**, 1 H), 7.91 (s, **e**, 1 H), 8.37 (d, J = 6 Hz, **a**, 1 H), 9.42 (d, J = 6 Hz, **m**, 1 H).

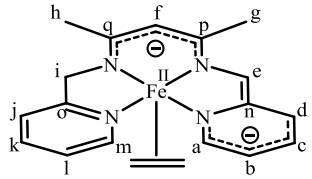

22. Reaction of {nn(PM)(PI)}FeCO with 3,3-diphenylcyclopropene. A 10 mL flask was charged with {nn(PM)(PI)}FeCO (**3**-CO, 35 mg, 0.10 mmol) and benzene (2 mL). 3,3-diphenylcyclopropene was added at -78 °C under an Ar purge. The reaction mixture was warmed to 23 °C and the red solution gradually turned brown. Stirring was maintained 1 h, and solvent was removed *in vacuo*. The resulting brown oil was triturated once with 8 mL pentane to yield a thick solid, and the solid was washed with pentane until the washes ran clear (~ 15 mL). NMR analysis of the resulting brown filter cake was carried out and resulting chemical shift assignments are presented in Figure 3.27.

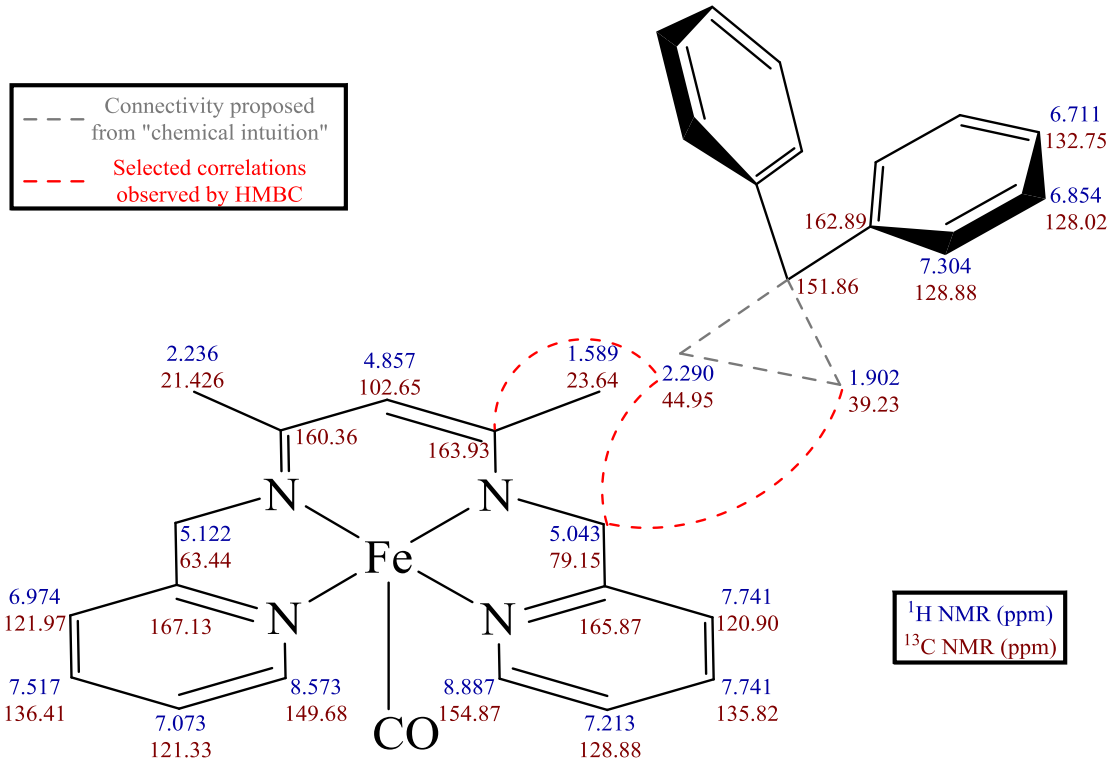

Figure 3.27. Chemical shifts of reaction product of **3**-CO and 3,3-diphenylcyclopropene as determined by ^{1}H, ^{13}C, (HH) gCOSY, (HC) HSQCAD, and (HC) gHMBSAD with ^{1}H (red) and ^{13}C (blue) NMR chemical shifts listed (spectra acquired in THF-d_8).

23. Alkylation of {nn(PM)(PI)}FeCO. A 25 mL flask was charged with {nn(PM)(PI)}FeCO (**3**-CO, 40. mg, 0.11 mmol) and 5 mL toluene, and cooled to -78°C. Under an Ar purge, a toluene solution of CH_3I (6.9 µL in 5 mL, 0.11 mmol) was added dropwise over 3 min. Upon addition, the solution darkened from cherry red to dark red-brown. The reaction was allowed to warm to 23°C and stirred an additional 30 min. Solvent was removed *in vacuo*, and the resulting brown solid was slurried in C_6H_6 and filtered. The filter cake was washed with two 2 mL portions of Et_2O to yield a sparingly soluble bright yellow powder (25 mg). IR (Nujol) ν_{CO} = 1942 cm^{-1}.

Mössbauer Spectroscopy. ^{57}Fe Mössbauer spectra were recorded on a WissEl Mössbauer spectrometer (MRG-500) at 77 K in constant acceleration mode. ^{57}Co/Rh was used as the radiation source. WinNormos for Igor Pro software has been used for the quantitative evaluation of the spectral parameters (least-squares fitting to Lorentzian peaks). The minimum experimental line widths were 0.20 mms^{-1}. The temperature of the samples was controlled by an MBBC-HE0106 MÖSSBAUER He/N_2 cryostat within an accuracy of ±0.3 K. Isomer shifts were determined relative to α-iron at 298 K.

EPR Spectroscopy. Solution and frozen glass EPR spectra were recorded on a JEOL continuous wave spectrometer, JES-FA200 equipped with an X-band Gunn oscillator bridge, a cylindrical mode cavity, and a helium cryostat. For all samples, a modulation frequency of 100 kHz and a time constant of 0.1 s were employed. Frequencies were close to 9.0 GHz and all spectra were obtained on freshly prepared solutions in quartz tubes. Background spectra were obtained on clean solvents at the same measurement conditions. Spectral simulations were performed using the programs W95EPR by Prof. Dr. Frank Neese[153] and ESRSIM by Prof. Dr. Høgni Weihe, University of Copenhagen, Denmark. Collinear *g* and *A* tensors were used, and deviations from isotropic parameters in spectra of frozen glasses were only used when clearly justified.

Calculations. Calculations were carried out at the M06/6-311+G(d)[154,155] level of theory. An ultrafine grid was used for integration in all calculations. Simulations were performed with the Gaussian 09 program.[156] All structures were optimized with restraint of neither symmetry nor geometry. Open-shell complexes

were modeled within the framework of the unrestricted Kohn-Sham formalism; spin contamination was deemed to be minimal via calculation of the $<\hat{S}^2>_{UDFT}$ expectation value. Systems were judged to be minima via calculation of the energy Hessian. Energetics are free energies (kcal/mol) and were determined with unscaled vibrational frequencies assuming standard temperature and pressure.

Single-Crystal X-ray Diffraction Studies. Upon isolation, crystals were covered in polyisobutenes and placed under a 173 K N_2 stream on the goniometer head of a Siemens P4 SMART CCD area detector (graphite-monochomated Mo Kα radiation, λ = 0.71073 Å). The structures were solved by direct methods (SHELXS). All non-hydrogen atoms were refined anisotropically unless otherwise stated, and hydrogen atoms were treated as idealized contributions (Riding model).

*Crystal data for {nn(PM)$_2$}FeN(TMS)$_2$ (**1**-N(TMS)$_2$).* A blocky red needle (0.45 x 0.30 x 0.15 mm^3) of **1**-N(TMS)$_2$ was obtained from pentane at 23°C. $C_{23}H_{37}FeN_5Si_2$, M = 495.61, monoclinic, P2(1)/n, a = 22.344(4), b = 9.5554(14), c = 25.374(4) Å, α = 90°, β = 98.763(5)°, γ = 90°, V = 5354.4(15) Å^3, T = 173(2) , Z = 8, R_{int} = 0.0271, 55921 reflections, 17064 independent, R_1(all data) = 0.0573, wR_2 = 0.0937, GOF = 1.026.

*Crystal data for {nn(PM)(PI)}Fe(PMe$_3$)$_2$ (**2**-(PMe$_3$)$_2$).* A purple block (0.40 x 0.30 x 0.25 mm^3) of **2**-(PMe$_3$)$_2$ was obtained from pentane at 23°C. $C_{23}H_{36}FeN_4P_2$, M = 486.35, monoclinic, P2(1)/c, a = 10.1579(8), b = 16.4764(12), c = 15.0780(11) Å, α = 90°, β = 103.175(3)°, γ = 90°, V = 2457.1(3) Å^3, T = 173(2) , Z = 4, R_{int} = 0.0217, 23781 reflections, 6086 independent, R_1(all data) = 0.0324, wR_2 = 0.0719, GOF = 1.023.

*Crystal data for [{nn(PM)(PI)}Fe(PMe$_3$)$_2$][PF$_6$] (**2**$^+$-(PMe$_3$)$_2$).* A dark brown plate (0.40 x 0.40 x 0.04 mm^3) of **2**$^+$-(PMe$_3$)$_2$ was obtained from THF/pentane at 23°C. $C_{23}H_{36}F_6FeN_4P_3$, M = 631.32, Orthorhombic, P2(1)2(1)2, a = 17.6532(14), b = 35.819(3), c = 8.8940(7) Å, α = 90°, β = 90°, γ = 90°, V = 5623.9(8) Å^3, T = 183(2), Z = 8, R_{int} = 0.0583, 50336 reflections, 8329 independent, R_1(all data) = 0.0613, wR_2 = 0.1039, GOF = 1.012.

*Crystal data for [{nn(PM)(PI)}Fe(PMe$_3$)$_2$][BAr$_4^F$]$_2$ (**2**$^{2+}$-(PMe$_3$)$_2$).* A dark green plate (0.20 x 0.15 x 0.03 mm^3) of **2**$^{2+}$-(PMe$_3$)$_2$ was obtained from THF/pentane at 23°C. As shown in Figure 3.13 and described in the text, data were collected on **2**$^{2+}$-(PMe$_3$)$_2$ but a high degree of disorder precluded structure refinement. $C_{53.75}H_{44.75}BF_{23.50}Fe_{0.50}N_2$ P (empirical), M = 1234.87, Monoclinic, C2/c, a = 28.799(2), b = 18.8777(11), c = 24.191(3) Å, α = 90°, β = 125.079(2)°, γ = 90°, V = 10762.5(17) Å^3, T = 203(2), Z = 8, R_{int} = 0.0587, 33715 reflections, 8011 independent, R_1(all data) = 0.1371, wR_2 = 0.2260, GOF = 1.331.

*Crystal data for {nn(PM)(PI)}Fe(PMePh$_2$) (**3**-PMePh$_2$).* A black block (0.60 x 0.40 x 0.30 mm) of **3**-PMePh$_2$ was obtained from THF/pentane at 23°C. $C_{30}H_{31}FeN_4P$, M = 534.41, Monoclinic, C2, a = 17.4724(6), b = 10.0996(3), c = 14.5690(5) Å, α = 90°, β = 101.8790(10)°, γ = 90°, V = 2515.85(14) Å^3, T = 193(2), Z = 4, R_{int} = 0.0149, 15608 reflections, 7723 independent, R_1(all data) = 0.0256, wR_2 = 0.0591, GOF = 1.006.

REFERENCES

1. Frazier, B. A.; Wolczanski, P. T.; Lobkovsky, E. B. *Inorg. Chem.* **2009,** *48,* 11576 − 11585.

2. Frazier, B. A.; Bartholomew, E. R.; Wolczanski, P. T.; DeBeer, S.; Santiago-Berrios, M.; Abruña, H. D.; Lobkovsky, E. B.; Bart, S. C.; Mossin, S.; Meyer, K.; Cundari, T. R. *Inorg. Chem.* **2011,** *50,* 12414 − 12436.

3. Frazier, B. A.; Wolczanski, P. T.; Lobkovsky, E. B.; Cundari, T. R. *J. Am. Chem. Soc.* **2009,** *131,* 3428 − 3429.

4. Hulley, E. B.; Wolczanski, P. T.; Lobkovsky, E. B. *J. Am. Chem. Soc.* **2011,** *133,* 18058 − 18061.

5. Frazier, B. A.; Wolczanski, P. T.; Keresztes, I.; DeBeer, S.; Lobkovsky, E. B.; Pierpont, A. W.; Cundari, T. R. *Inorg. Chem.* **2012,** *51,* 8177 − 8186.

6. Frazier, B. A.; Williams, V. A.; Wolczanski, P. T.; Bart, S.; Meyer, K.; Cundari, T. R.; Lobkovsky, E. B. *Inorg. Chem.* **2013,** *52,* 3295 − 3312.

7. Jiao, R.; Shen, X. D.; Xue, M. Q.; Zhang, Y.; Yao, Y. M.; Shen, Q. *Chem. Commun.* **2010,** *46,* 4118 − 4120.

8. Holland, P. L. *Acc. Chem. Res.* **2008,** *41,* 905 − 914.

9. Smith, J. M.; Sadique, A. R.; Cundari, T. R.; Rodgers, K. R.; Lakat-Rodgers, G.; Lachicotte, R. J.; Flaschenriem, C. J.; Vela, J.; Holland, P. L. *J. Am. Chem. Soc.* **2006,** *128,* 756 − 769.

10. Smith, J. M.; Lachicotte, R. J.; Pittard, K. A.; Cundari, T. R.; Lukat-Rodgers, G.; Rodgers, K. R.; Holland, P. L. *J. Am. Chem. Soc.* **2001,** *123,* 9222 − 9223.

11. Holland, P. L.; Cundari, T. R.; Perez, L. L.; Eckert, N. A.; Lachicotte, R. J. *J. Am. Chem. Soc.* **2002,** *124,* 14416 − 14424.

12. Andres, H.; Bominaar, E. L.; Smith, J. M.; Eckert, N. A.; Holland, P. L.; Munck, E. *J. Am. Chem. Soc.* **2002,** *124,* 3012 − 3025.

13. Cowley, R. E.; Eckert, N. A.; Vaddadi, S.; Figg, T. M.; Cundari, T. R.; Holland, P. L. *J. Am. Chem. Soc.* **2011,** *133,* 9796 − 9811.

14. Eckert, N. A.; Vaddadi, S.; Stoian, S.; Lachicotte, R. J.; Cundari, T. R.; Holland, P. L. *Angew. Chem., Int. Ed.* **2006,** *45,* 6868 − 6871.

15. Cowley, R. E.; Holland, P. L. *Inorg. Chem.* **2012,** *51,* 8352 − 8361.

16. Yu, Y.; Sadique, A. R.; Smith, J. M.; Dugan, T. R.; Cowley, R. E.; Brennessel, W. W.; Flaschenriem, C. J.; Bill, E.; Cundari, T. R.; Holland, P. L. *J. Am. Chem. Soc.* **2008,** *130,* 6624 − 6638.

17. Vela, J.; Smith, J. M.; Yu, Y.; Ketterer, N. A.; Flaschenriem, C. J.; Lachicotte, R. J.; Holland, P. L. *J. Am. Chem. Soc.* **2005,** *127,* 7857 − 7870.

18. Dugan, T. R.; Goldberg, J. M.; Brennessel, W. W.; Holland, P. L. *Organometallics* **2012,** *31,* 1349 − 1360.

19. Dugan, T. R.; Bill, E.; MacLeod, K. C.; Christian, G. J.; Cowley, R. E.; Brennessel, W. W.; Ye, S. F.; Neese, F.; Holland, P. L. *J. Am. Chem. Soc.* **2012,** *134,* 20352 − 20364.

20. Cowley, R. E.; Golder, M. R.; Eckert, N. A.; Al-Afyouni, M. H.; Holland, P. L. *Organometallics* **2013,** *32,* 5289 − 5298.

21. Rodriguez, M. M.; Bill, E.; Brennessel, W. W.; Holland, P. L. *Science* **2011,** *334,* 780 − 783.

22. Chiang, K. P.; Bellows, S. M.; Brennessel, W. W.; Holland, P. L. *Chem. Sci.* **2014,** *5,* 267 − 274.

23. Wiese, S.; McAfee, J. L.; Pahls, D. R.; McMullin, C. L.; Cundari, T. R.; Warren, T. H. *J. Am. Chem. Soc.* **2012,** *134,* 10114 − 10121.

24. Kogut, E.; Wiencko, H. L.; Zhang, L. B.; Cordeau, D. E.; Warren, T. J. *J. Am. Chem. Soc.* **2005,** *127,* 11248 − 11249.

25. Kogut, E.; Zeller, A.; Warren, T. H.; Strassner, T. *J. Am. Chem. Soc.* **2004,** *126,* 11984 − 11994.

26. Gephart, R. T.; Huang, D. L.; Aguila, M. J. B.; Schmidt, G.; Shahu, A.; Warren, T. H. *Angew. Chem., Int. Ed.* **2012,** *51,* 6488 − 6492.

27. Badei, Y. M.; Krishnaswamy, A.; Melzer, M. M.; Warren, T. H. *J. Am. Chem. Soc.* **2006,** *128,* 15056 − 15057.

28. Dai, X. L.; Warren, T. H. *J. Am. Chem. Soc.* **2004,** *126,* 10085 − 10094.

29. Gephart, R. T.; McMullin, C. L.; Sapiezynski, N. G.; Jang, E. S.; Aguila, M. J. B.; Cundari, T. R.; Warren, T. H. *J. Am. Chem. Soc.* **2012,** *134,* 17350 − 17353.

30. Dai, X. L.; Kapoor, P.; Warren, T. H. *J. Am. Chem. Soc.* **2004,** *126,* 4798 − 4799.

31. Mindiola, D. J. *Acc. Chem. Res.* **2006,** *39,* 813 − 821.

32. Mindiola, D. J. *Angew. Chem., Int. Ed.* **2009,** *48,* 6198 − 6200.

33. Tran, B. L.; Washington, M. P.; Henckel, D. A.; Gao, X. F.; Park, H.; Pink, M.; Mindiola, D. J. *Chem. Commun.* **2012,** 1529−1531.

34. Bailey, B. C.; Basuli, F.; Huffman, J. C.; Mindiola, D. J. *Organometallics* **2006,** *25,* 3963 − 3968.

35. Kilgore, U. J.; Basuli, F.; Huffman, J. C.; Mindiola, D. J. *Inorg. Chem.* **2006,** *45,* 487 − 489.

36. Basuli, F.; Aneetha, H.; Huffman, J. C.; Mindiola, D. J. *J. Am. Chem. Soc.* **2005,** *127,* 17992 − 17993.

37. Zhao, G. Y.; Basuli, F.; Kilgore, U. J.; Fan, H. J.; Aneetha, H.; Huffman, J. C.; Wu, G.; Mindiola, D. J. *J. Am. Chem. Soc.* **2006,** *128,* 13575 − 13585.

38. Adhikari, D.; Basuli, F.; Orlando, J. H.; Gao, X. F.; Huffman, J. C.; Pink, M.; Mindiola, D. J. *Organometallics* **2009,** *28,* 4115 − 4125.

39. Tran, B. L.; Singhal, M.; Park, H.; Lam, O. P.; Pink, M.; Krzystek, J.; Ozarowski, A.; Telser, J.; Meyer, K.; Mindiola, D. J. *Angew. Chem., Int. Ed.* **2010,** *49,* 9871 − 9875.

40. Tran, B. L.; Pinter, B.; Nichols, A. J.; Konopka, F. T.; Thompson, R.; Chen, C. H.; Krzystek, J.; Ozarowski, A.; Telser, J.; Baik, M. H.; Meyer, K.; Mindiola, D. J. *J. Am. Chem. Soc.* **2012,** *134,* 13035 − 13045.

41. Fan, H. J.; Adhikari, D.; Saleh, A. A.; Clark, R. L.; Zuno-Cruz, F. J.; Cabrera, G. S.; Huffman, J. C.; Pink, M.; Mindiola, D. J.; Baik, M. H. *J. Am. Chem. Soc.* **2008,** *130,* 17351 − 17361.

42. MacAdams, L. A.; Kim, W. K.; Liable-Sands, L. M.; Guzei, I. A.; Rheingold, A. L.; Theopold, K. H. *Organometallics* **2002,** *21,* 952 − 960.

43. Kim, W. K.; Fevola, M. J.; Liable-Sands, L. M.; Rheingold, A. L.; Theopold, K. H. *Organometallics* **1998,** *17,* 4541 − 4543.

44. MacAdams, L. A.; Buffone, G. P.; Incarvito, C. D.; Rheingold, A. L. *J. Am. Chem. Soc.* **2005,** *127,* 1082 − 1083.

45. Monillas, W. H.; Young, J. F.; Yap, G. P. A.; Theopold, K. H. *Dalton Trans.* **2013,** *42,* 9198 − 9210.

46. Monillas, W. H.; Yap, G. P. A.; MacAdams, L. A.; Theopold, K. H. *J. Am. Chem. Soc.* **2007,** *129,* 8090 − 8091.

47. Dai, F.; Yap, G. P. A.; Theopold, K. H. *J. Am. Chem. Soc.* **2013,** *135,* 16774 − 16776.

48. Monillas, W. H.; Yap, G. P. A.; Theopold, K. H. *Inorg. Chim. Acta* **2011,** *369,* 103 − 119.

49. Whitehorne, T. J. J.; Schaper, F. *Inorg. Chem.* **2013,** *52,* 13612 − 13622.

50. Gupta, A. K.; Tolman, W. B. *Inorg. Chem.* **2012,** *51,* 1881 − 1888.

51. Chang, K. C.; Lu, C. F.; Wang, P. Y.; Lu, D. Y.; Chen, H. Z.; Kuo, T. S.; Tsai, Y. C. Dalton Trans. 2011, 40, 2324−2331. (b) Lin, K. M.; Wang, P. Y.; Shieh, Y. J.; Chen, H. Z.; Kuo, T. S.; Tsai, Y. C. *New J. Chem.* **2010,** *34,* 1737 − 1745.

52. Tonzetich, Z. J.; Heroquel, F.; Do, L. H.; Lippard, S. J. *Inorg. Chem.* **2011,** *50,* 1570 − 1579.

53. Zhou, W.; Tang, L. M.; Patrick, B. O.; Smith, K. M. *Organometallics* **2011,** *30,* 603 − 610.

54. Chapouret, Y.; MacLeod, K. C.; Baisch, U.; Patrick, B. O.; Smith, K. M.; Poli, R. *Organometallics* **2010,** *29,* 167 − 176.

55. El-Zoghbi, I.; Kebdani, M.; Whitehorne, T. J. J.; Schaper, F. *Organometallics* **2013,** *32,* 6986 − 6995.

56. Gianetti, T. L.; Nocton, G.; Minasian, S. G.; Tomson, N. C.; Kilcoyne, A. L. D.; Kozimor, S. A.; Shuh, D. K.; Tyliszczak, T.; Bergman, R. G.; Arnold, J. *J. Am. Chem. Soc.* **2013,** *135,* 3224 − 3236.

57. Gianetti, T. L.; Bergman, R. G.; Arnold, J. *J. Am. Chem. Soc.* **2013,** *135,* 8145 − 8148.

58. Gianetti, T. L.; Tomson, N. C.; Arnold, J.; Bergman, R. G. *J. Am. Chem. Soc.* **2011,** *133,* 14904 − 14907.

59. Tomson, N. C.; Arnold, J.; Bergman, R. G. *Organometallics* **2010,** *29,* 5010 − 5025.

60. Tomson, N. C.; Arnold, J.; Bergman, R. G. *Organometallics* **2010,** *29,* 2926 − 2942.

61. Tomson, N. C.; Arnold, J.; Bergman, R. G. *Dalton Trans.* **2011,** *40,* 7718 − 7729.

62. Hadzovic, A.; Song, D. T. *Inorg. Chem.* **2008,** *47,* 12010 − 12017.

63. Annibale, V. T.; Tan, R. Y.; Janetzko, J.; Lund, L. M.; Song, D. T. *Inorg. Chim. Acta* **2012,** *380,* 308 − 321.

64. Phillips, A. D.; Thommes, K.; Scopelliti, R.; Gandolfi, C.; Albrecht, M.; Severin, K.; Schreiber, D. F.; Dyson, P. J. *Organometallics* **2011,** *30,* 6119 − 6132.

65. Phillips, A. D.; Zava, O.; Scopelitti, R.; Nazarov, A. A.; Dyson, P. J. *Organometallics* **2010,** *29,* 417 − 427.

66. Tsai, Y. C. *Coord. Chem. Rev.* **2012,** *256,* 722 − 758.

67. Yao, S. L.; Driess, M. *Acc. Chem. Res.* **2012,** *45,* 276 − 287.

68. Marshak, M. P.; Chambers, M. B.; Nocera, D. G. *Inorg. Chem.* **2012,** *51,* 11190 − 11197.

69. Khusniyarov, M. M.; Bill, E.; Weyhermüller, T.; Bothe, E.; Wieghardt, K. *Angew. Chem., Int. Ed.* **2011,** *50,* 1652 − 1655.

70. Hope, J. M.; Wilson, J. J.; Lippard, S. J. *Dalton Trans.* **2013,** *42,* 3176 − 3180.

71. Marlier, E. E.; Sadowsky, D.; Cramer, C. J.; McNeill, K. *Inorg. Chim. Acta* **2011,** *369,* 173 − 179.

72. Marlier, E. E.; Ulrich, B. A.; McNeill, K. *Inorg. Chem.* **2012,** *51,* 2079 − 2085.

73. Jørgensen, C. K. *Helv. Chim. Acta* **1967,** *50 (Supp. 1),* 131 − 146.

74. Pierpont, C. G. *Coord. Chem. Rev.* **2001,** *216,* 99 − 125.

75. Evangelio, E.; Ruiz-Molina, D. *Eur. J. Inorg. Chem.* **2005,** 2957 − 2971.

76. Ray, K.; Petrenko, T.; Wieghardt, K.; Neese, F. *Dalton Trans.* **2007,** 1552 − 1566.

77. De Bruin, B.; Hetterscheid, D. G. H.; Koekkoek, A. J. J.; Grutzmacher, H. *Prog. Inorg. Chem.* **2007,** *55,* 247 − 354.

78. Dzik, W. I.; van der Vlugt, J. I.; Reek, J. N. H.; de Bruin, B. *Angew. Chem., Int. Ed.* **2011,** *50,* 3356 − 3358.

79. Blanchard, S.; Derat, E.; Desage-El Murr, M.; Fensterbank, L.; Malacria, M.; Mouries-Mansuy, V. *Eur. J. Inorg. Chem.* **2012,** 376 − 389.

80. Budzelaar, P. H. M. *Eur. J. Inorg. Chem.* **2012,** 530 − 534.

81. Caulton, K. G. *Eur. J. Inorg. Chem.* **2012,** 435 − 443.

82. Williams, V. A.; Wolczanski, P. T.; Sutter, J.; Meyer, K.; Lobkovsky, E.; Cundari, T. R. *Inorg. Chem.* **2014,** *53,* 4459 − 4474.

83. Olmstead, M. M.; Power, P. P.; Shoner, S. C. *Inorg. Chem.* **1991,** *30,* 2547 − 2551.

84. Andersen, R. A.; Faegri, K.; Green, J. C.; Haaland, A.; Lappert, M. F.; Leung, W. P.; Rypdal, K. *Inorg. Chem.* **1988,** *27,* 1782 − 1786.

85. Evans, D. F. *J. Chem. Soc.* **1959,** 2003 − 2005.

86. Schubert, E. M. *J. Chem. Ed.* **1992,** *69,* 62.

87. Carlin, R. L. *Magnetochemistry;* Springer-Verlag: Berlin, 1986.

88. Figgis, B. N.; Hitchman, M. A. *Ligand Field Theory and Its Applications;* Wiley-VCH: New York, 2000.

89. Parish, R. V. *NMR, NQR, EPR, and Mössbauer Spectroscopy in Inorganic Chemistry;* Ellis Horwood: West Sussex, England, 1990.

90. Gütlich, P.; Bill, E.; Trautwein, A. X. *Mössbauer Spectroscopy and Transition Metal Chemistry;* Springer: New York, 2011.

91. Fultz, B. *Mössbauer Spectrometry. In Characterization of Materials;* Kaufmann, E., Ed.; John Wiley: New York, 2011.

92. Addison, A. W.; Rao, T. N.; Reedijk, J.; van Rijn, J.; Verschoor, G. C. *J. Chem. Soc., Dalton Trans.* **1984,** 1349 − 1356.

93. Allen, F. H.; Kennard, O.; Watson, D. G.; Brammer, L.; Orpen, A. G.; Taylor, R. *J. Chem. Soc., Perkin Trans. 2* **1987,** S1 − S19.

94. Lu, C. C.; Bill, E.; Weyhermüller, T.; Bothe, E.; Wieghardt, K. *J. Am. Chem. Soc.* **2008,** *130,* 3181 − 3197.

95. Lu, C. C.; Weyhermüller, T.; Bill, E.; Wieghardt, K. *Inorg. Chem.* **2009,** *48,* 6055 − 6064.

96. Williams, V. A.; Hulley, E. B.; Wolczanski, P. T.; Lancaster, K. M.; Lobkovsky, E. B. *Chem. Sci.* **2013,** *4,* 3636 − 3648.

97. Stieber, S. C. E.; Milsmann, C.; Hoyt, J. M.; Turner, Z. R.; Finkelstein, K. D.; Wieghardt, K.; DeBeer, S.; Chirik, P. J. *Inorg. Chem.* **2012,** *51,* 3770 − 3785.

98. Russell, S. K.; Bowman, A. C.; Lobkovsky, E.; Wieghardt, K.; Chirik, P. J. *Eur. J. Inorg. Chem.* **2012,** 535 − 545.

99. Bowman, A. C.; Milsmann, C.; Bill, E.; Lobkovsky, E.; Weyhermüller, T.; Wieghardt, K.; Chirik, P. J. *Inorg. Chem.* **2010,** *49,* 6110 − 6123.

100. Bowman, A. C.; Milsmann, C.; Atienza, C. C. H.; Lobkovsky, E.; Wieghardt, K.; Chirik, P. J. *J. Am. Chem. Soc.* **2010,** *132,* 1676 − 1684.

101. Wile, B. M.; Trovitch, R. J.; Bart, S. C.; Tondreau, A. M.; Lobkovsky, E. B.; Milsmann, C.; Bill, E.; Wieghardt, K.; Chirik, P. J. *Inorg. Chem.* **2009,** *48,* 4190 − 4200.

102. Therien, M. J.; Trogler, W. C. *J. Am. Chem. Soc.* **1986,** *108,* 3697 − 3702.

103. MacNeil, J. H.; Chiverton, A. C.; Fortier, S.; Baird, M. C.; Hynes, R. C.; Williams, A. J.; Preston, K. F.; Ziegler, T. *J. Am. Chem. Soc.* **1991,** *113,* 9834 − 9842.

104. Baird, M. C. *Chem. Rev.* **1988,** *88,* 1217 − 1227.

105. Mankad, N. P.; Whited, M. T.; Peters, J. C. *Angew. Chem., Int. Ed.* **2007,** *46,* 5768 − 5771.

106. Lee, Y.; Kinney, R. A.; Hoffman, B. M.; Peters, J. C. *J. Am. Chem. Soc.* **2011,** *133,* 16366 − 16369.

107. Sinnecker, S.; Neese, F. *J. Phys. Chem. A* **2006,** *110,* 12267 − 12275.

108. Orio, M.; Pantazis, D. A.; Petrenko, T.; Neese, F. *Inorg. Chem.* **2009,** *48,* 7251 − 7260.

109. Neese, F. *J. Phys. Chem. A* **2001,** *105,* 4290 − 4299.

110. Buschmann, W. E.; Miller, J. S. *Inorg. Synth.* **2002,** *33,* 83 − 91.

111. Volpe, E. C.; Wolczanski, P. T.; Lobkovsky, E. B. *Organometallics* **2010,** *29,* 364 − 377.

112. Bartholomew, E. R.; Volpe, E. C.; Wolczanski, P. T.; Lobkovsky, E. B.; Cundari, T. R. *J. Am. Chem. Soc.* **2013,** *135,* 3511 − 3527.

113. Volpe, E. C.; Wolczanski, P. T.; Darmon, J. M.; Lobkovsky, E. B. *Polyhedron* **2013,** *52,* 406 − 415.

114. Lee, Y.; Mankad, N. P.; Peters, J. C. *Nat. Chem.* **2010,** *2,* 558 − 565.

115. Heinrich, M. P.; Gunderson, W.; Behan, R. K.; Green, M. T.; Mehn, M. P.; Betley, T. A.; Lu, C. C.; Peters, J. C. *Proc. Natl. Acad. Sci. U.S.A.* **2006,** *46,* 17107 − 17112.

116. Chlopek, K.; Bill, E.; Weyhermüller, T.; Wieghardt, K. *Inorg. Chem.* **2005,** *44,* 7087 − 7089.

117. Vasudev, P.; Jones, C. H. W. *Can. J. Chem.* **1973,** *51,* 405 − 410.

118. Collins, R. L.; Pettit, R. *J. Chem. Phys.* **1963,** *39,* 3433 − 3436.

119. Dias, G. H. M.; Morigaki, M. K. *Polyhedron* **1992,** *11,* 1629 − 1636.

120. Thammavongsy, Z.; Seda, T.; Zakharov, L. N.; Kaminsky, W.; Gilbertson, J. D. *Inorg. Chem.* **2012,** *51,* 9168 − 9170.

121. Tolman, C. A. *Chem. Rev*, **1977,** 77, 313 − 348.

122. Brookhart, M.; Grant, B.; Volpe, A. F. *Organometallics,* **1992,** *11,* 3920 − 3922.

123. Eisenstein, O.; Hoffmann, R.; Rossi, A. R. *J. Am. Chem. Soc.* **1981,** *103,* 5582 − 5584.

124. Javed, M. I.; Brewer, M. *Org. Lett.* **2007,** *9,* 1789 − 1792.

125. Hughes, D. L.; Leigh, G. J; Mc Mahon, C. N. *J. Chem. Soc., Dalton Trans.* **1997,** 1301 − 1307.

126. Krämer, K.; Leong, P.; Lautens, M. *Org. Lett.* **2011,** *13,* 819 − 821.

127. Miessler, G. L.; Tarr, D. A. *Inorganic Chemistry;* Pearson Prentice Hall: New Jersey, 2004.

128. Heyduk, A. F.; Zarkesh, R. A.; Nguyen, A. I. *Inorg. Chem.* **2011,** *50,* 9849 − 9863.

129. Blackmore, K. J.; Lal, N.; Ziller, J. W.; Heyduk, A. F. *J. Am. Chem. Soc.* **2008,** *130,* 2728 − 2729.

130. Nguyen, A. I.; Zarkesh, R. A.; Lacy, D. C.; Thorson, M. K.; Heyduk, A. F. *Chem. Sci.* **2011,** *2,* 166 − 169.

131. Blackmore, K. J.; Ziller, J. W.; Heyduk, A. F. *Inorg. Chem.* **2005,** *44,* 5559 − 5561.

132. Zarkesh, R. A.; Ziller, J. W.; Heyduk, A. F. *Angew. Chem., Int. Ed.* **2008,** *47,* 4715 − 4718.

133. Haneline, M. R.; Heyduk, A. F. *J. Am. Chem. Soc.* **2006,** *128,* 8410 − 8411.

134. Goldstein, M.; Hoffmann, R. *J. Am. Chem. Soc.* **1971,** *93,* 6193 − 6204.

135. Hoyt, J. M.; Sylvester, K. T.; Semproni, S. P.; Chirik, P. J. *J. Am. Chem. Soc.* **2013,** *135,* 4862 − 4877.

136. Russell, S. K.; Lobkovsky, E.; Chirik, P. J. *J. Am. Chem. Soc.* **2011,** *133,* 8858 − 8861.

137. Darmon, J. M.; Stieber, S. C.; Sylvester, K. L.; Fernańdez, I.; Lobkovsky, E.; Semproni, S. P.; Bill, E.; Wieghardt, K.; DeBeer, S.; Chirik, P. J. *J. Am. Chem. Soc.* **2012,** *134,* 17125 − 17137.

138. Monfette, S.; Turner, Z. R.; Semproni, S. P.; Chirik, P. J. *J. Am. Chem. Soc.* **2012,** *134,* 4561 − 4564.

139. Yu, R. P.; Darmon, J. M.; Hoyt, H. M.; Margulieux, G. W.; Turner, Z.; Chirik, P. J. *ACS Catal.* **2012,** *2,* 1760 − 1764.

140. Trovitch, R. J.; Lobkovsky, E.; Bill, E.; Chirik, P. J. *Organometallics* **2008,** *27,* 1470 − 1478.

141. Bart, S. C.; Lobkovsky, E.; Chirik, P. J. *J. Am. Chem. Soc.* **2004,** *126,* 13794 − 13807.

142. Tondreau, A. M.; Atienza, C. C. H. A.; Weller, K. J.; Nye, S. A.; Lewis, K. M.; Delis, J. G. P.; Chirik, P. J. *Science* **2012,** *335,* 567 − 570.

143. Tondreau, A. M.; Atienza, C. C. H. A.; Darmon, J. M.; Milsmann, C.; Hoyt, H. M.; Weller, K. J.; Nye, S. A.; Lewis, K. N.; Boyer, J.; Delis, J. G. P.; Lobkovsky, E.; Chirik, P. J. *Organometallics* **2012,** 4886 − 4893.

144. Atienza, C. C. H. A.; Tondreau, A. M.; Weller, K. J.; Lewis, K. M.; Cruse, R.; Nye, S. A.; Boyer, J. L.; Delis, J. P.; Chirik, P. J. *ACS Catal.* **2012,** *2,* 2169 − 2172.

145. Tondreau, A. M.; Lobkovsky, E.; Chirik, P. J. *Org. Lett.* **2008,** *10,* 2789 − 2792.

146. Tondreau, A. M.; Darmon, J. D.; Wile, B. M.; Floyd, S. K.; Lobkovsky, E. B.; Chirik, P. J. *Organometallics* **2009,** *28,* 3928 − 3940.

147. Chirik, P. J.; Wieghardt, K. W. *Science* **2010,** *327,* 794 − 795.

148. Neese, F.; Zumft, W. G.; Antholine, W. E.; Kroneck, P. M. H. J. Am. Chem. Soc. 1996, 118, 8692 − 8699.

149. Zhao, Y.; Truhlar, D. G. *Acc. Chem. Res*. **2008,** *41,* 157 − 167.

150. Krishnan, R.; Binkley, J. S.; Seeger, R.; Pople, J. A. *J. Chem. Phys.* **1980,** *72,* 650 − 654.

151. Frisch, M. J.; Trucks, G. W.; Schlegel, H. B.; Scuseria, G. E.; Robb, M. A.; Cheeseman, J. R.; Scalmani, G.; Barone, V.; Mennucci, B.; Petersson, G. A.; Nakatsuji, H.; Caricato, M.; Li, X.; Hratchian, H. P.; Izmaylov, A. F.; Bloino, J.; Zheng, G.; Sonnenberg, J. L.; Hada, M.; Ehara, M.; Toyota, K.; Fukuda, R.; Hasegawa, J.; Ishida, M.; Nakajima, T.; Honda, Y.; Kitao, O.; Nakai, H.; Vreven, T.; Montgomery, J. A., Jr.; Peralta, J. E.; Ogliaro, F.; Bearpark, M.; Heyd, J. J.; Brothers, E.; Kudin, K. N.; Staroverov, V. N.; Kobayashi, R.; Normand, J.; Raghavachari, K.; Rendell, A.; Burant, J. C.; Iyengar, S. S.; Tomasi, J.; Cossi, M.; Rega, N.; Millam, J. M.; Klene, M.; Knox, J. E.; Cross, J. B.; Bakken, V.; Adamo, C.; Jaramillo, J.; Gomperts, R.; Stratmann, R. E.; Yazyev, O.; Austin, A. J.; Cammi, R.; Pomelli, C.; Ochterski, J. W.; Martin, R. L.; Morokuma, K.; Zakrzewski, V. G.; Voth, G. A.; Salvador, P.; Dannenberg, J. J.; Dapprich, S.; Daniels, A. D.; Farkas, Ö .; Foresman, J. B.; Ortiz, J. V.; Cioslowski, J.; Fox, D. J. Gaussian 09, revision A.1; Gaussian, Inc.: Wallingford, CT, 2009.

Chapter 4

Synthesis, Characterization, and Reactivity of First-Row Transition Metal Complexes supported by a Tetradentate β-diketiminate-based Ligand

Introduction

β-diketiminate ligands have been ubiquitous in transition metal-based coordination chemistry, and complexes featuring β-diketiminate moieties have been used to support low-coordinate metal centers,[1-10] metal-ligand multiple bonds,[11-19] and a variety of different catalytic processes.[20-31] The β-diketiminate-based 2,4-bis[(E)-(2-pyridyl)methylideneamino]pentane (H{nn(PM)$_2$}) ligand was shown to be highly effective in supporting various iron complexes as both high-spin Fe^{II} ({nn(PM)$_2$}FeX) and low-spin Fe^{II} ({nn(PM)(PI)}FeL_n) (Figure 4.1).

Coupling at the mid carbon of a β-diketiminate backbone has been observed

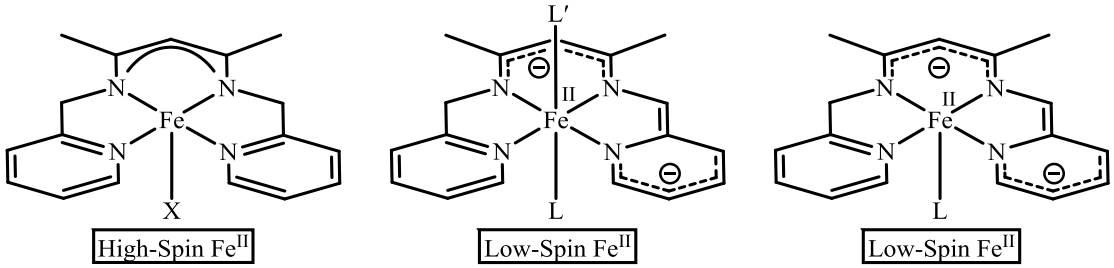

Figure 4.1. Fe^{II} complexes supported by a β-diketiminate-based ligand featuring pyridine-methylene and pyridine-imine moieties.

previously,[2] so the incorporation of an azaallyl fragment into the β-diketiminate framework was an attractive target for discovery of carbon-carbon bond forming reactions.[32-34] Because research in this laboratory has focused on the discovery of unique carbon-carbon bond forming reactions in organometallic systems, application of the H{nn(PM)$_2$} ligand to other transition metals of the first row was carried out.

Results and Discussion

4.1. Synthesis of {nn(PM)$_2$}MX$_n$ (M = V, X = Cl$_2$; M = Co)

4.1.1. {nn(PM)$_2$}VCl$_2$

Treatment of V(N(TMS)$_2$)$_2$Cl(THF)[35,36] with 1.0 equiv H{nn(PM)$_2$} in THF resulted in the immediate formation of a deep red solution and release of HN(TMS)$_2$, with precipitation of a dark red solid that was virtually insoluble in organic solvents (Eq. 4.1). Highly crystalline material was obtained in 36% yield through slow diffusion of a THF solution of H{nn(PM)$_2$} into a solution of V(N(TMS)$_2$)$_2$Cl(THF)

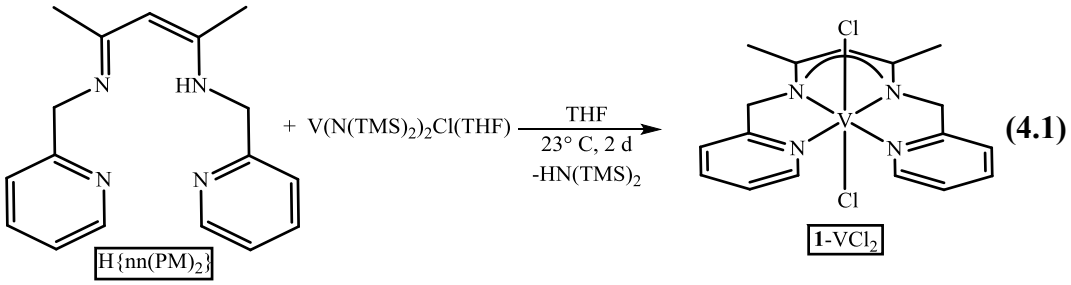

(4.1)

and was subjected to X-ray analysis. The resulting structure is shown in Figure 4.2 with relevant parameters displayed in Table 4.1. Rather than the predicted singly or doubly deprotonated products,{nn(PM)$_2$}V(Cl)(N(TMS)$_2$) and {nn(PM)(PI)}VCl, respectively, X-ray analysis revealed {nn(PM)$_2$}VCl$_2$ (**1**-VCl$_2$). The molecule has distorted octahedral geometry, with average angles of 90.5° (*cis*) and 165.3° (*trans*). The two chloride ligands are bent away from the β-diketiminate moiety (∠Cl1-V1-Cl2 = 158.741°) and the {nn(PM)$_2$} ligand has a slight twist (∠N1-N2-N3-N4 (dihedral) = 10.5°) from planarity. A ligand exchange event necessarily occurred to provide the dichloride **1**-VCl$_2$ because the V(N(TMS)$_2$)$_2$Cl(THF) starting material contained only one chloride per metal center. A possible mechanism for this reaction, consistent with the <50% observed yield of **1**-VCl$_2$, is an initial metallation/deprotonation event to

generate the {nn(PM)$_2$}V(Cl)(N(TMS)$_2$) intermediate, followed by either ligand exchange to form {nn(PM)$_2$}V(N(TMS)$_2$)$_2$ and {nn(PM)$_2$}VCl$_2$ in a 1:1 ratio, or exchange with the V(N(TMS)$_2$)$_2$Cl(THF) starting material to generate **1**-VCl$_2$ and

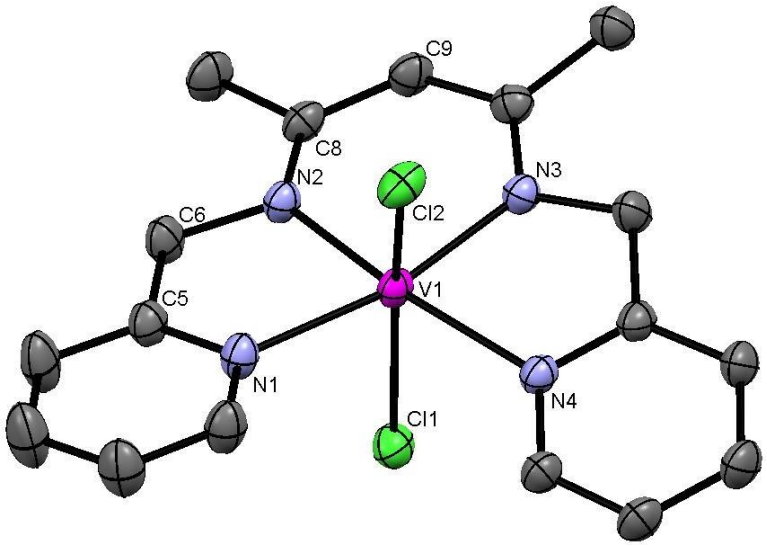

Figure 4.2. Molecular structure of **1**-VCl$_2$. Hydrogen atoms are omitted for clarity.

Table 4.1. Selected interatomic distances and bond angles for **1**-VCl$_2$.

Selected Bond Distances (Å)		Selected Bond Angles (°)	
V1-N1	2.1615(11)	N1-V1-N2	79.52(4)
V1-N2	2.0025(10)	N2-V1-N3	91.05(4)
V1-N3	1.9989(11)	N3-V1-N4	79.77(4)
V1-N4	2.1641(10)	N4-V1-N1	110.28(4)
V1-Cl1	2.3728(4)	N1-V1-Cl1	85.57(3)
V1-Cl2	2.3763(4)	N2-V1-Cl1	93.29(3)
N1-C5	1.3367(16)	N3-V1-Cl1	102.33(3)
C5-C6	1.5024(19)	N4-V1-Cl1	83.20(3)
C6-N2	1.4577(17)	N1-V1-Cl2	84.49(3)
N2-C8	1.3392(17)	N2-V1-Cl2	103.30(3)
C8-C9	1.3942(19)	N3-V1-Cl2	90.72(3)
		N4-V1-Cl2	82.70(3)
		N1-V1-N3	168.11(4)
		N2-V1-N4	169.18(5)
		Cl1-V1-Cl2	158.741(15)

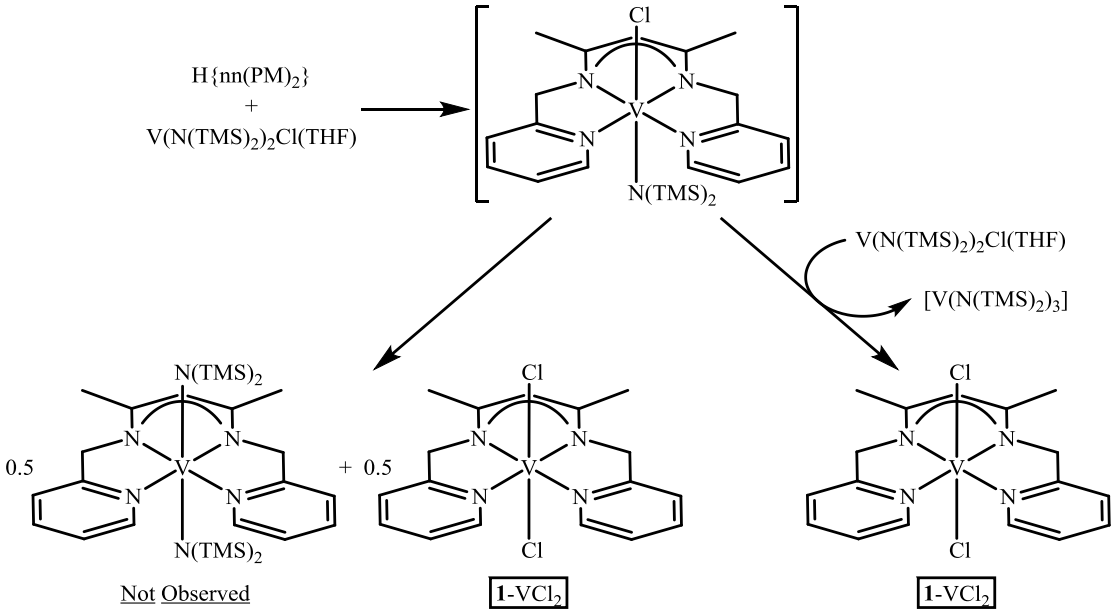

Scheme 4.1. Proposed mechanism for the formation of **1**-VCl_2.

$V(N(TMS)_2)_3(THF)_n$[37,38] (Scheme 4.1).Although the possible paramagnetism and large quadrupolar broadening intrinsic to vanadium nuclei[39] precluded direct NMR analysis of the reaction shown in Eq. 4.1, filtration of the reaction mixture to remove **1**-V and thermolysis of the resulting NMR-silent mother liquor resulted in the gradual production of $HN(TMS)_2$ and virtually insoluble precipitate, suggesting the gradual decomposition of a $N(TMS)_2$-containing vanadium complex. **1**-VCl_2 could be synthesized rationally through the reaction of $VCl_3(THF)$ with 1.0 equiv $Na\{nn(PM)_2\}$ in THF, but due to the poor solubility of **1**-VCl_2 in organic solvents, the NaCl byproduct could not easily be separated from the desired product.

The negligible solubility of **1**-VCl_2 in organic solvents greatly limited its utility in chemical transformations, so to increase solubility the installation bulky alkyl groups was targeted. Treatment of a THF slurry of **1**-VCl_2 with 2.0 equiv ^{neo}PeLi at -78°C and subsequent warming to 23°C formed a dark brown-black solution, which, gratifyingly, was fully soluble in THF (Eq. 4.2). However, the reaction mixture was

NMR-silent, as one might predict for a V^{III} complex. Removal of solvent resulted in a thick black film, and repeated trituration with organic solvents did not yield a solid material. As such, growth of high-quality crystals for X-ray analysis remained elusive and proper characterization was abandoned.

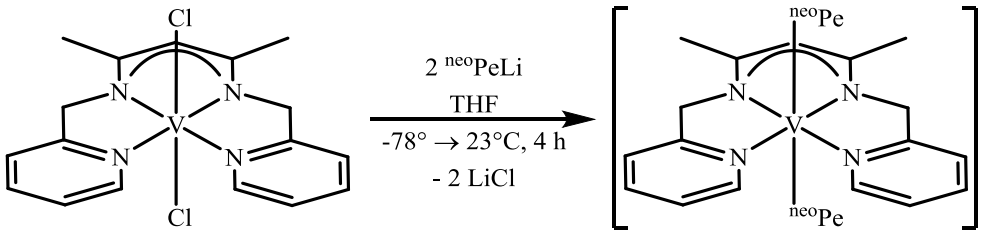

1-VCl_2 **(4.2)**

Attempts towards dehydrohalogenation to generate $\{nn(PM)(PI)\}^{2-}V^{III}Cl$ with the hope of accessing chemistry analogous to the iron system seen previously was carried out. However, exposure of **1**-VCl_2 to 1.0 equiv $LiN(TMS)_2$ resulted in decomposition of starting material, and reaction with $LiN(TMS)_2$ in the presence of pyridine-N-oxide to generate $\{nn(PM)(PI)\}^{2-}V^{V}$=O(Cl) resulted also only in decomposition of starting material.

4.1.2. {nn(PM)$_2$}Co

Treatment of $Co(N(TMS)_2)_2(THF)$[40,41] with 1.0 equiv H{nn$(PM)_2$} to synthesize {nn(PM)(PI)}Co produced a deep indigo-blue solution with concomitant release of $HN(TMS)_2$. ^{1}H NMR analysis revealed a diamagnetic species with C_2 symmetry, inconsistent with the expected $\{nn(PM)(PI)\}^{2-}Co^{II}$ product, but suggestive of the reduced complex {nn$(PM)_2$}Co (**1**-Co) (Eq. 4.3). Bright gold crystals were grown from THF/pentane at -35 °C, and single-crystal X-ray analysis confirmed the formulation of **1**-Co as a low-spin Co^{I} metal center in a pseudo-square planar geometry. Presumably, $Co(N(TMS)_2)_2(THF)$ reacts with H{nn$(PM)_2$} to transiently

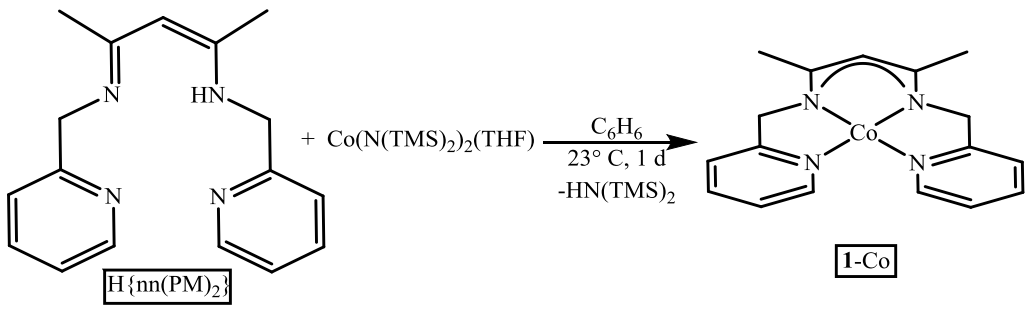

(4.3)

form {nn(PM)$_2$}CoN(TMS)$_2$, which then undergoes disproportion to afford the reduced {nn(PM)$_2$}Co^{I} product and a [N(TMS)$_2$]$_n$ byproduct. Unfortunately, [N(TMS)$_2$]$_n$ could not be quantified by ^{1}H NMR due to chemical shift overlap with HN(TMS)$_2$.

The structure of **1**-Co is shown in Figure 4.3 with relevant parameters displayed in Table 4.2. The molecule has a crystallographic C_2 axis of symmetry through the C9-Co1 axis, and as expected, the bond distances of the chelate are quite similar to that of **1**-VCl$_2$. The *d*(M-N) are quite contracted relative to **1**-VCl$_2$

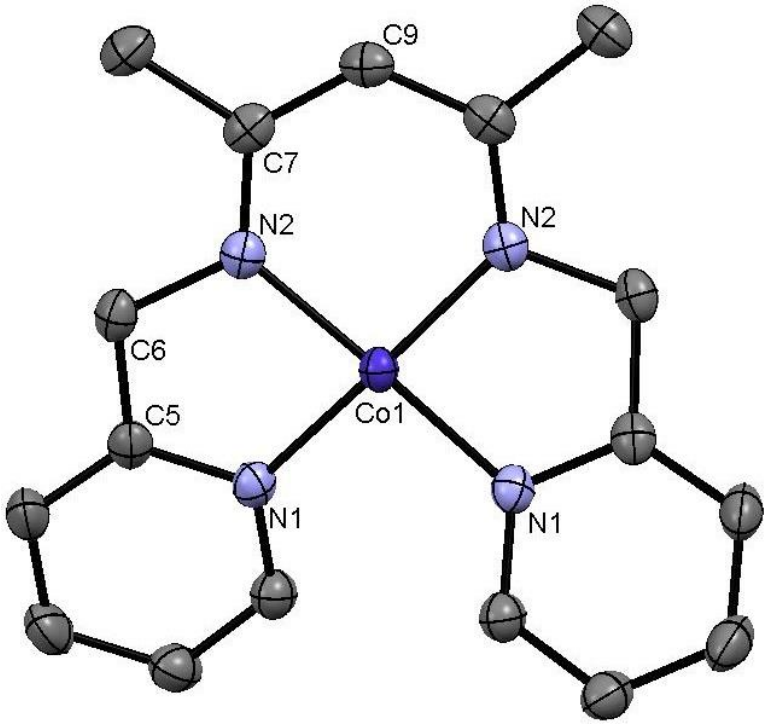

Figure 4.3. Molecular structure of **1**-Co. Hydrogen atoms are omitted for clarity.

Table 4.2. Selected interatomic distances and bond angles for **1**-Co.

Selected Bond Distances (Å)		Selected Bond Angles (°)	
Co1-N1	1.8869(11)	N1-Co1-N2	84.85(5)
Co1-N2	1.8588(11)	N1'-Co1-N2'	84.85(5)
Co1-N1'	1.8870(11)	N1-Co1-N1'	98.00(6)
Co1-N2'	1.8587(11)	N2-Co1-N2'	94.98(7)
N1-C5	1.3602(17)	N1'-Co1-N2	167.51(5)
C5-C6	1.4934(19)	N2'-Co1-N1	167.51(5)
C6-N2	1.4639(16)	N1-N2-N2'-N1'	18.58 (6)
N2-C7	1.3394(16)	(dihedral)	
C7-C9	1.3985(16)		

(Δ *d*(M- N) ~ 0.1 – 0.3 Å), which is attributable to the smaller covalent radius of cobalt relative to vanadium. **1**-Co displays a slight chelate twist of 15.58°, allowing for reduced overlap with the torus of the filled d_{z^2} orbital and attenuation of its σ^* character.

The UV-visible spectrum of **1**-Co acquired in C_6H_6 is presented in Figure 4.4 and extinction coefficients are listed in Table 4.3. The spectrum is dominated by charge transfer bands, masking any weak d-d transitions that would otherwise be observed. Due to the insolubility of the singly deprotonated ligand, Na{nn(PM))$_2$}, in organic solvents, a UV-visible spectrum of the transition metal-free ligand could not be obtained for comparison. However, as Na{nn(PM)$_2$} is nearly colorless, the observed bands are unlikely due to intraligand charge transfer and instead arise from metal-to-ligand or ligand-to metal charge transfer.

Attempts to convert the {nn(PM)$_2$} ligand to the redox-active {nn(PM)(PI)} focused initially on direct H-atom abstraction from the methylene position of the ligand backbone. However, treatment of **1**-Co with H-atom abstraction agents such as

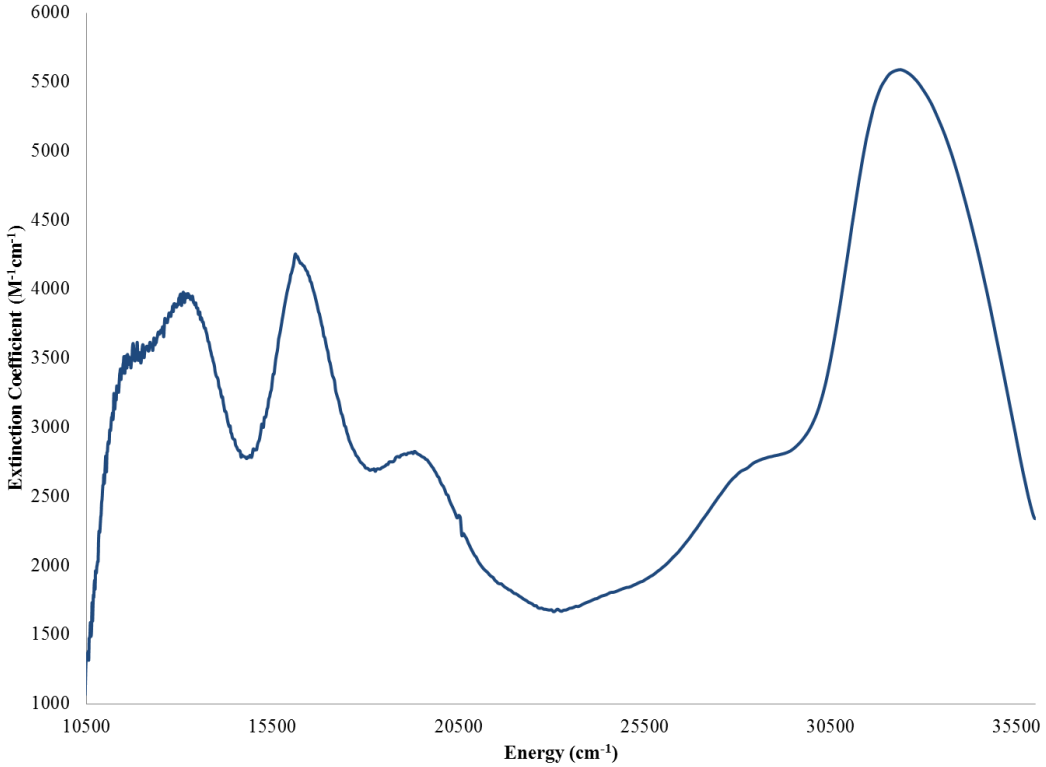

Figure 4.4. UV-visible spectrum of {nn(PM_2)}Co (**1**-Co).

Table 4.3. Extinction coefficient values (ε) for {nn(PM_2)}Co (**1**-Co).

ν (cm^{-1})	ε ($M^{-1}cm^{-1}$)	ν (cm^{-1})	ε ($M^{-1}cm^{-1}$)
11600	3440	24500	1800
13100	3970	28800	2750
16300	4190	32300	5590
19300	2820		

TEMPO, benzoquinone, or organic peroxides resulted in decomposition, and exposure of **1**-Co to 9,10-dihydroanthracene or 1,3-cyclohexadiene resulted only in recovery of starting materials.

Because the direct H-atom abstraction from **1**-Co was unsuccessful, oxidation followed by deprotonation was attempted. Treatment of **1**-Co with X_2 (X = Br, I) in the presence of base resulted in rapid decomposition of starting materials. Gratifyingly, treatment of **1**-Co with 1.0 equiv Cp_2FePF_6 afforded a dark blue solid

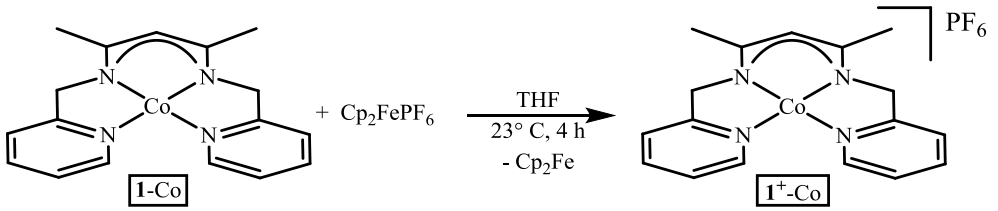

(4.4)

that was sparingly soluble in organic solvents, consistent with [{nn(PM)$_2$}Co](PF$_6$) (**1**$^+$-Co), with release of 1.0 equiv Cp_2Fe (Eq. 4.4). NMR analysis of saturated THF-d_8 solutions of **1**$^+$-Co did not reveal any characteristic spectral signatures, presumably because the concentration of the paramagnetic cation was too low for detection. However, the presence of a PF_6 counterion in the complex was confirmed by ^{19}F NMR.

Treatment of **1**$^+$-Co with KH resulted in the evolution of H_2 with formation of copious solids and regeneration of **1**-Co. Reaction with other strong bases such as LDA similarly afforded the one-electron reduction of **1**$^+$-Co to **1**-Co, and **1**$^+$-Co was unreactive with respect to weaker bases such as DBU. Attempts to alkylate or protonate **1**-Co to generate the cobalt(III) {nn(PM)$_2$}Co^{III}(CH$_3$)(I) or [{nn(PM)$_2$}Co^{III}H]$^+$complexes, respectively, resulted in decomposition of starting materials.

As the synthesis of cobalt carbene and imido complexes supported by porphyrin ligands is known,[42-46] attempts to prepare analogous complexes from **1**-Co were carried out. Addition of 1-adamantyl azide to **1**-Co in C_6D_6 resulted in a color change from blue to red-brown, consumption of both starting materials, and precipitation of a sparingly soluble solid (Scheme 4.2). ^{1}H NMR analysis revealed a new diamagnetic species with five resonances that integrated in a 1:1:1:1:1 ratio and a complex chemical shift pattern between 1.5 – 2 ppm corresponding to adamantyl

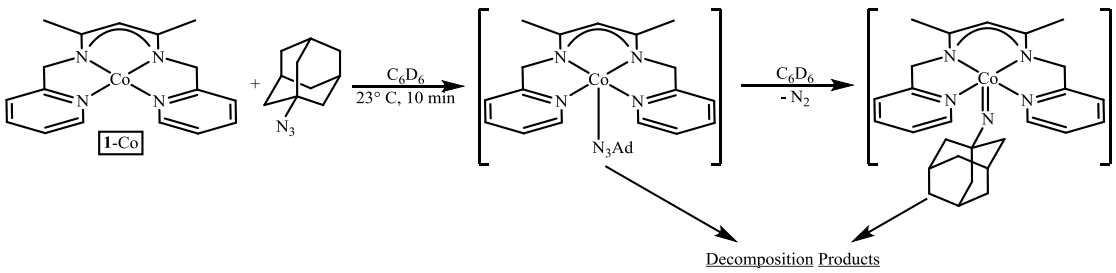

Scheme 4.2. Reaction of **1**-Co with 1-adamantyl azide.

protons. Unfortunately the resonances corresponding to the methylene CH_2 and the β-diketiminate backbone C*H* protons were not observed, suggesting that if either the {nn(PM)$_2$}Co(N$_3$Ad) or {nn(PM)$_2$}CoNAd products were formed, they rapidly decomposed to the sparingly soluble precipitate observed in the reaction mixture.

Reaction of **1**-Co with carbene transfer reagents fared no better. Treatment of **1**-Co with 3,3-diphenylcyclopropene[47,48] formed a red solution and insoluble precipitate, with ^{1}H NMR analysis of the solution revealing two major diamagnetic products in a 1:1 ratio and at least three minor products. Reaction with diphenyldiazomethane[49] similarly degraded nonspecifically to a virtually insoluble precipitate.

Due to its electronic and coordinative unsaturation, **1**-Co was capable of binding L-type donor ligands such as PMe$_3$ to form stable complexes. Treatment of

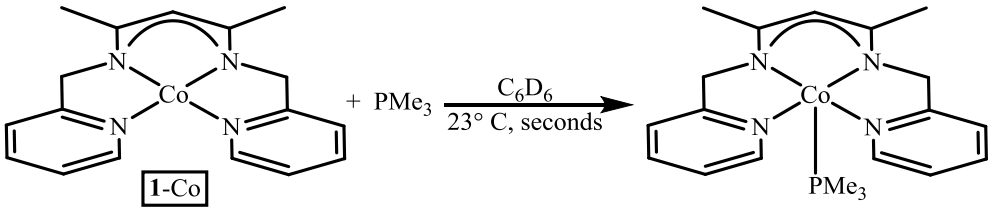

(4.5)

1-Co with excess PMe$_3$ formed a deep red highly soluble complex identified by ^{1}H NMR spectroscopy as the electronically saturated {nn(PM)$_2$}CoPMe$_3$ (Eq. 4.5). PMe$_3$ binding was seemingly irreversible, as repeated exposure of {nn(PM)$_2$}CoPMe$_3$

solutions to vacuum did not result in regeneration of **1**-Co. As **1**-Co was unable to afford clean and productive chemistry in the reactions screened, further study was not pursued.

4.2. Synthesis of {nn(PM)(PI) }M (M = Cr, Ni)

4.2.1. {nn(PM)(PI)}Cr

Exposure of $Cr(N(TMS)_2)_2(THF)_2$[50,51] to 1.0 equiv $H\{nn(PM)_2\}$ in C_6D_6 resulted in an immediate color change from purple to dark brown and release of $HN(TMS)_2$ and THF in a 1:1 ratio. Dark green needles precipitated over 4 d at 23 °C, and X-ray analysis revealed double deprotonation to generate {nn(PM)(PI)}Cr, **4**-Cr

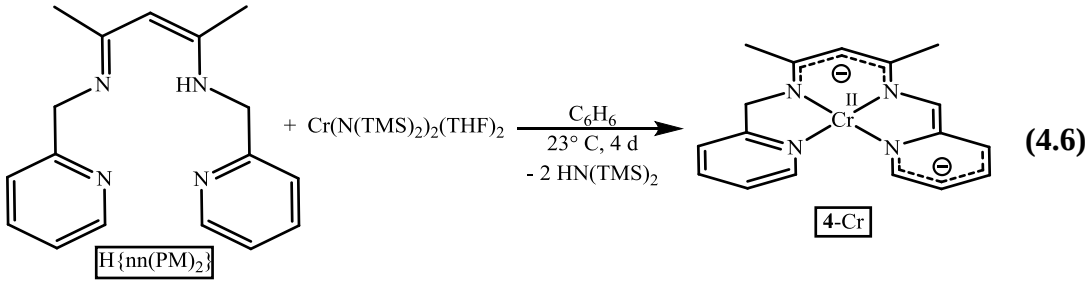

(4.6)

(Eq. 4.6).The resulting structure is presented in Figure 4.5 and relevant parameters are given in Table 4.4. There are two independent molecules in the asymmetric unit, with similar bond angles and bond distances that are identical within error. **4**-Cr is nearly planar, with only a slight chelate twist of 2.5° for one molecule and 4.2° for the other. A clear differentiation between the pyridine-methylene and pyridine-imine halves of the molecule is evident from bond distances. The N2-C6 bond length of 1.391 Å is contracted nearly 0.5 Å relative to the N3-C10 bond (1.451 Å), suggestive of substantially more double bond character in the former. Similarly, the *d*(C6-C5) of 1.371 Å and the *d*(C5-N1) of 1.405 Å are elongated and contracted, respectively,

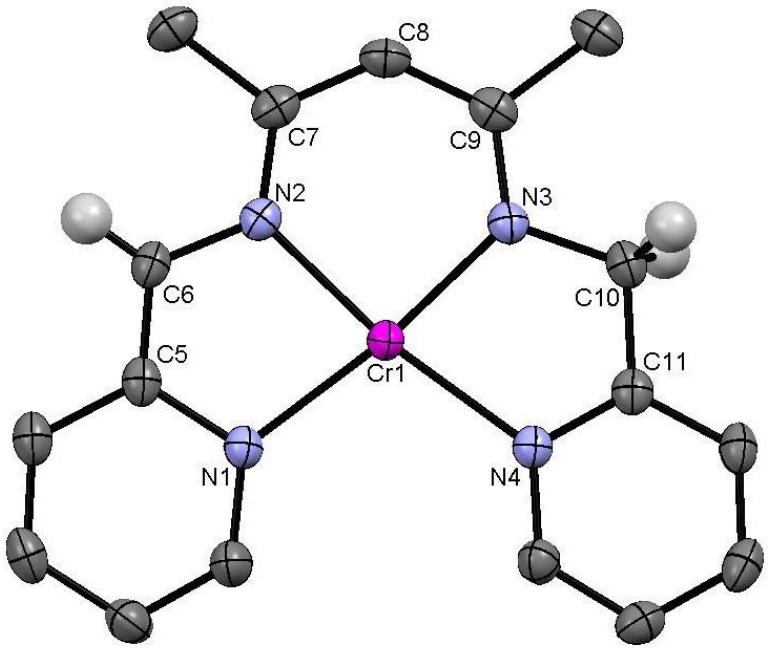

Figure 4.5. Molecular structure of **4**-Cr. Selected hydrogen atoms are omitted for clarity.

Table 4.4. Selected interatomic distances and bond angles for **4**-Cr. Parameters listed are an average of the two independent molecules in the asymmetric unit when equivalent to within 3 σ. Both values are given in *italics* when outside 3 σ.

Selected Bond Distances (Å)		Selected Bond Angles (°)	
Cr1-N1	2.0686(15)	N1-Cr1-N2	81.57(6)
Cr1-N2	2.0254(15)	N2-Cr1-N3	91.01(6)
Cr1-N3	1.9999(15)	N3-Cr1-N4	80.75(6)
Cr1-N4	2.1138(15)	N4-Cr1-N1	106.44(6)
N1-C5	1.405(2)	N1-Cr1-N3	*171.05(6)*
C5-C6	1.371(3)		*171.72(6)*
C6-N2	1.391(2)	N2-Cr1-N4	*171.90(6)*
N2-C7	1.341(2)		*169.38(6)*
C7-C8	1.402(3)	N2-C6-C5	117.88(17)
C8-C9	1.397(3)	N3-C10-C11	111.94(15)
C9-N3	1.345(2)	N1-N2-N3-N4	*4.2 (1)*
N3-C10	1.451(2)	(dihedral)	*2.5 (1)*
C10-C11	1.499(3)		
C11-N4	1.346(2)		

Table 4.5. Structural comparison of **1**-VCl_2, **1**-Co, and **4**-Cr.

Crystal Data			
Formula	$C_{17}H_{19}Cl_2N_4V$	$C_{17}H_{19}CoN_4$	$C_{17}H_{18}CrN_4$
Formula Weight	401.20	338.29	330.35
Crystal System	Monoclinic	Orthorhombic	Triclinic
Space Group	C2/c	Pccn	P-1
Z	8	4	4
a, Å	20.4128(16)	5.3435(7)	7.4675(4)
b, Å	12.9424(11)	14.9830(19)	11.0204(6)
c, Å	16.2616(13)	18.744(3)	19.4260(10)
α, deg	90	90	73.613(2)
β, deg	113.009(4)	90	79.583(2)
γ, deg	90	90	74.918(2)
Volume, $Å^3$	3954.4(6)	1500.7(3)	1470.90(14)
D (calc.), g/cm^3	1.348	1.497	1.492
Absorption coeff., mm^{-1}	0.777	1.145	0.779
F(000)	1648	704	688
Crystal Size, mm	0.22 x 0.15 x 0.03	0.40 x 0.20 x 0.15	0.35 x 0.10 x 0.08
Data Collection and Refinement			
Temp, K	173(2)	173(2) K	173(2)
Wavelength (λ), Å	0.71073	0.71073 Å	0.71073
θ limits, deg	1.91 to 30.51	2.56 to 28.28	1.10 to 28.28
Index Ranges	$-26 \le h \le 29$, $-13 \le k \le 18$, $-23 \le l \le 21$	$-6 \le h \le 7$, $-18 \le k \le 19$, $-24 \le l \le 24$	$-9 \le h \le 9$, $-14 \le k \le 14$, $-25 \le l \le 25$
Reflections Collected	48211	7788	26414
Absorption Correction	Semi-empirical from equivalents	Semi-empirical from equivalents	Semi-empirical from equivalents
Max. and Min. Transmission	0.9771 and 0.8476	0.8470 and 0.6573	0.9439 and 0.7721
Refinement Method	Full-matrix least-squares on F^2	Full-matrix least-squares on F^2	Full-matrix least-squares on F^2
Data/Restraints/Params.	6034 / 0 / 293	1855 / 0 / 139	7236 / 0 / 541
Goodness-of-Fit on F^2	1.045	1.011	1.041
Final R Indeces [$I>2\sigma(I)$]	R1 = 0.0299, wR2 = 0.0892	R1 = 0.0236, wR2 = 0.0641	R1 = 0.0349, wR2 = 0.0843
R Indices (all data)	R1 = 0.0362, wR2 = 0.0925	R1 = 0.0283, wR2 = 0.0676	R1 = 0.0502, wR2 = 0.0913
Largest Diffraction Peak and Hole (e^- Å)	0.385 and -0.240	0.306 and -0.215	0.337 and -0.306

relative to *d*(C10-C11) and *d*(C11-N4) (1.499 Å and 1.346Å). The bond distances of the pyridine-imine half of the molecule are identical within error to those of {nn(PM)(PI)}Fe(PMe_3)$_2$ (Table 3.3), suggesting a similar ligand oxidation state for both complexes. Furthermore, the ligand metrics of **4**-Cr match up better to those calculated for $\{nn(PM)(PI)\}^{2-}Fe^{II}$ than those for $[\{nn(PM)(PI)\}^{-}Fe^{II}]^{+}$ and $[\{nn(PM)(PI)\}^{0}Fe^{II}]^{2+}$ (Figure 3.14). Thus, the electronic structure of **4**-Cr is most likely $[\{nn(PM)(PI)\}^{2-}Cr^{II}]$. Multiple reasonable configurations exist for a monomeric d^4 metal center and doubly reduced ligand, several of which are illustrated in Figure 4.6. However, the poor solubility of **4**-Cr precluded solution state magnetic measurements, and acquisition of solid state SQUID data to differentiate between the possible configurations is underway.

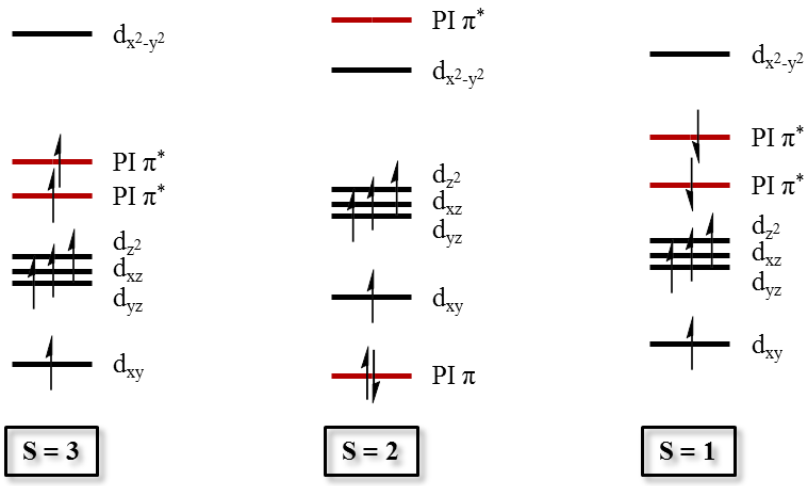

Figure 4.6. Several possible electronic configurations for monomeric **4**-Cr.

Due to the electronic unsaturation of the d^4 metal center, interactions of individual molecules of **4**-Cr in the crystal structure were further examined for evidence of metal-metal bonding. Figure 4.7 illustrates the packing of **4**-Cr, in which the nearly planar molecules stack in 1-dimensional columns. The *d*(Cr-Cr) in each

column alternate between 3.329(3) Å and 4.284(3) Å. The shorter distance of 3.329 Å is longer than the sum of covalent radii for the two chromium centers and longer than a standard single bond, but within the range of some unusually long Cr-Cr single bonds reported in the literature.[52-57] To the best of our knowledge, the longest unsupported Cr-Cr single bond reported is that of $[Cr(\eta^5\text{-}C_5H_4PMePh_2)(CO)_3]_2[B(C_6F_5)_4]_2$ at 3.3509(7) Å.[52] However, although a bonding interaction between adjacent molecules of **4**-Cr is certainly possible, the long *d*(Cr-Cr) suggests that if metal-metal interactions exist, they are quite weak.

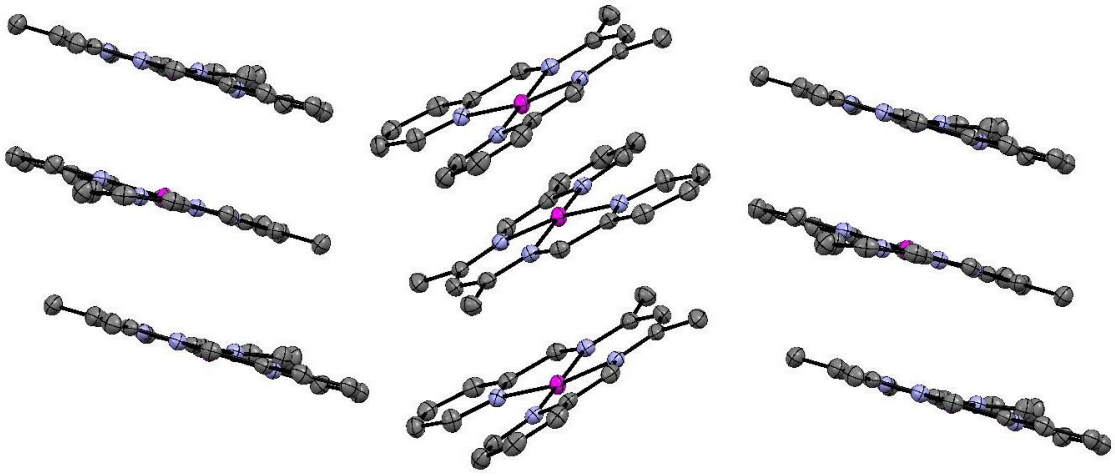

Figure 4.7. Illustration of solid-state packing in **4**-Cr.

4-Cr was sparingly soluble in THF, and although the limited solubility and probable paramagnetism prevented analysis via NMR spectroscopy, the species colored THF solutions enough to acquire UV-Visible data (Figure 4.8). Due to the electronic unsaturation of **4**-Cr it is highly probable that in solution, **4**-Cr coordinates one or two molecules of THF to achieve a higher electron count at the metal center. Thus, it is important to note that the spectrum shown in Figure 4.8 may be that of a THF adduct of **4**-Cr.

The UV-visible spectrum displays numerous charge transfer bands, listed in

Table 4.6, which mask any low-intensity d-d transitions that would otherwise be observed. For comparison, the UV-visible spectrum of Li_2{nn(PM)(PI)} is presented in Figure 4.8 and clearly exhibits intraligand charge transfer bands that match up well to the major absorptions of **4**-Cr but are red-shifted by ~ 400 cm^{-1}. The low-energy features exhibited by **4**-Cr between 14,000 and 18,000 cm^{-1} do not match up to any red-shifted bands of Li_2{nn(PM)(PI)} and likely arise from ligand-to-metal or metal-to-ligand charge transfers. A possible vibronic progression is exhibited in the spectrum of Li_2{nn(PM)(PI)} between 14000 and 18500, where the features centered at 14200, 15500, 16830, and 18215 cm^{-1} could correspond to the $\nu_{GS} = 0$ to $\nu_{ES} = 0$, 1, 2, and 3 vibrational components. The IR spectrum of Li_2{nn(PM)(PI)} exhibits numerous

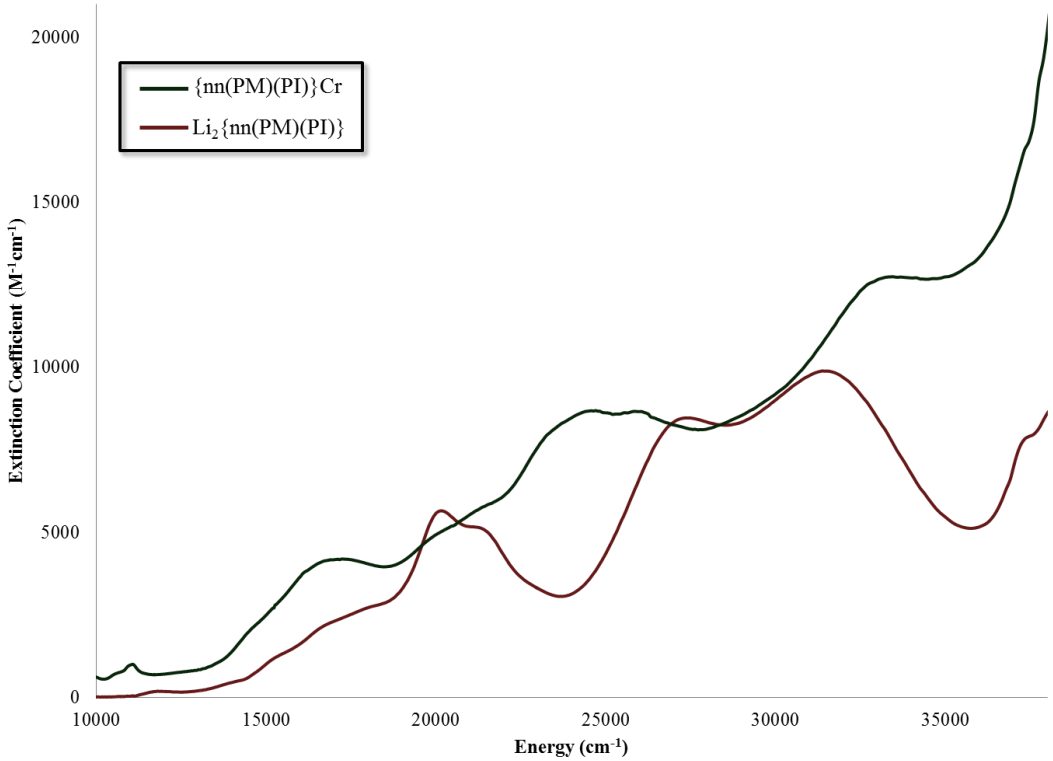

Figure 4.8. UV-visible spectra of {nn(PM)(PI)}Cr(THF)$_n$ (green) and Li_2{nn(PM)(PI} (purple). The small features at 11000 cm^{-1} are an artifact arising from a source change in the spectrometer.

Table 4.6. Extinction coefficient (ε) values for **4**-Cr and Li_2{nn(PM)(PI}.

4-Cr		Li_2{nn(PM)(PI}	
ν (cm^{-1})	ε ($M^{-1}cm^{-1}$)	ν (cm^{-1})	ε ($M^{-1}cm^{-1}$)
14600	2100	11800	190
17000	4190	14200	500
20120	5000	15500	1350
21350	5770	16830	2250
23450	8090	18215	2790
24500	8680	20120	5640
26100	8630	21050	5100
29600	8900	27400	8460
33000	12700	31450	9880

stretches in the region between 1,300 and 1,400 cm^{-1}, which match up well to the difference of ~1,350 cm^{-1}.

Because any useful reactivity of **4**-Cr would likely be hindered by its poor solubility, the synthesis of a {nn(PM)(PI)}CrL_n complex with bulky L groups was targeted. Surprisingly, treatment of **4**-Cr with excess PMe_3 did not result in a soluble material. As the dissolution of **4**-Cr could have been prohibitively kinetically hindered, the reaction shown in Eq. 4.6 was run in the presence of excess PMe_3 to generate the proposed {nn(PM)(PI)}$Cr(PMe_3)_n$ species prior to crystallization of **4**-Cr. Unfortunately, isolation of a soluble material was unsuccessful, suggesting that if the desired complex was synthesized, the solubility was not significantly different from that of **4**-Cr. Exposure of a slurry of **4**-Cr to a CO atmosphere did not result in material that exhibited a ν_{CO}, possibly due to prohibitively slow dissolution of **4**-Cr in organic solvents. It is unusual that **4**-Cr does not form monomeric ligand adducts given that the complex is both electronically and coordinatively unsaturated, and binding of donor ligands would be expected to be facile, but presumably the stability afforded by π-

stacking and/or the weak metal-metal interaction in the solid state of **4**-PMe_3 dominates.

Because a more soluble analogue of **4**-Cr remained elusive, the direct reactivity of **4**-Cr was explored. Initial efforts centered on oxidative chemistry with the intent of utilizing the two electrons stored in the redox-noninnocent ligand framework of **4**-Cr. Unfortunately, attempts to access oxidative chemistry through treatment with CH_3I, I_2, Br_2, or N-bromosuccinimide under various reaction conditions resulted in nonspecific degradation of starting materials.

Treatment with group-transfer reagents were met with limited success. Exposure of **4**-Cr to 1.0 equiv diazodiphenylmethane[49] resulted in immediate dissolution of insoluble **4**-Cr and formation of an orange-brown solution. One could envision either the simple binding of the N_2 unit in the diphenyldiazomethane reagent or loss of N_2 to form the Cr^{II} alkylidene, where the ligand backbone was oxidized by two electrons (Scheme 4.3). Unfortunately, the putative chromium product was

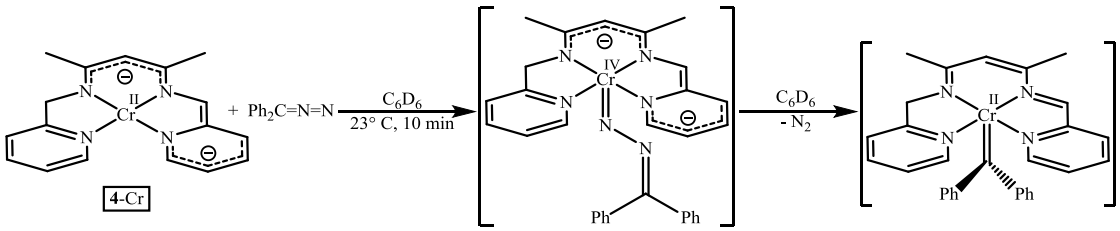

Scheme 4.3. Reaction of **4**-Cr with diphenyldiazomethane and proposed reaction products.

paramagnetically broadened and NMR analysis of the highly soluble reaction mixture did not reveal any resonances from -300 – 300 ppm. Exhaustive attempts to generate crystalline material for X-ray analysis under a variety of conditions were carried out, but high-quality crystals remained elusive. Treatment of **4**-Cr with 3,3-

diphenylcyclopropene[47,48] to synthesize the corresponding vinyl alkylidene species resulted only in consumption of starting materials and formation of a thick brown precipitate, presumably the result of nonspecific degradation processes.

Reaction of **4**-Cr with 1.0 equiv $TMSN_3$ to synthesize a chromium imido complex was met with similar results. Upon mixture, complete consumption of **4**-Cr was observed and a dark green solution was produced. One could envision the organic azide binding to the Cr^{II} metal center, or loss of N_2 to generate the desired Cr^{II} imido species with oxidation of the ligand backbone as illustrated in Scheme 4.4. As with the

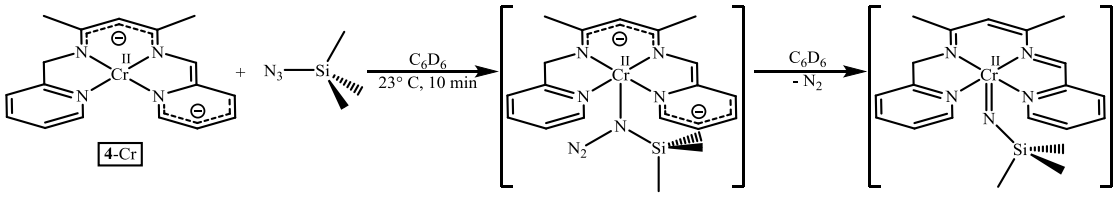

Scheme 4.4. Reaction of **4**-Cr with $TMSN_3$ and proposed reaction products.

reaction illustrated in Scheme 4.3, the chromium product formed in Scheme 4.4 did not exhibit any characteristic NMR resonances from -300 – 300 ppm. Similarly, crystalline material could not be obtained from the reaction mixture for analysis and further study was not pursued.

4.2.2. {nn(PM)(PI)}Ni

Reaction of H{nn$(PM)_2$} with 0.5 equiv $\{Ni(NPh_2)_2\}_2$[58] in C_6H_6 produced a deep red solution and full consumption of starting materials. ^{1}H NMR analysis revealed release of 2.0 equiv $HNPh_2$ and formation of a new diamagnetic species with C_S symmetry, consistent with generation of {nn(PM)(PI)}Ni, **4**-Ni (Eq. 4.7). Unfortunately attempts to obtain crystalline material for X–ray analysis were unsuccessful, but **4**-Ni could be fully characterized via 2-dimentional NMR correlation

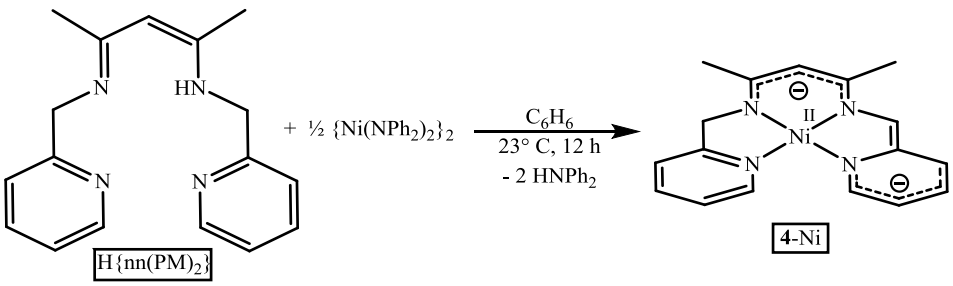

(4.7)

spectroscopy and the ^{1}H NMR spectrum of **4**-Ni is illustrated in Figure 4.9. Although in the absence of crystallographic data the electronic structure of **4**-Ni cannot be easily confirmed, the species is likely a square planar Ni^{II} metal center bound to a dianionic

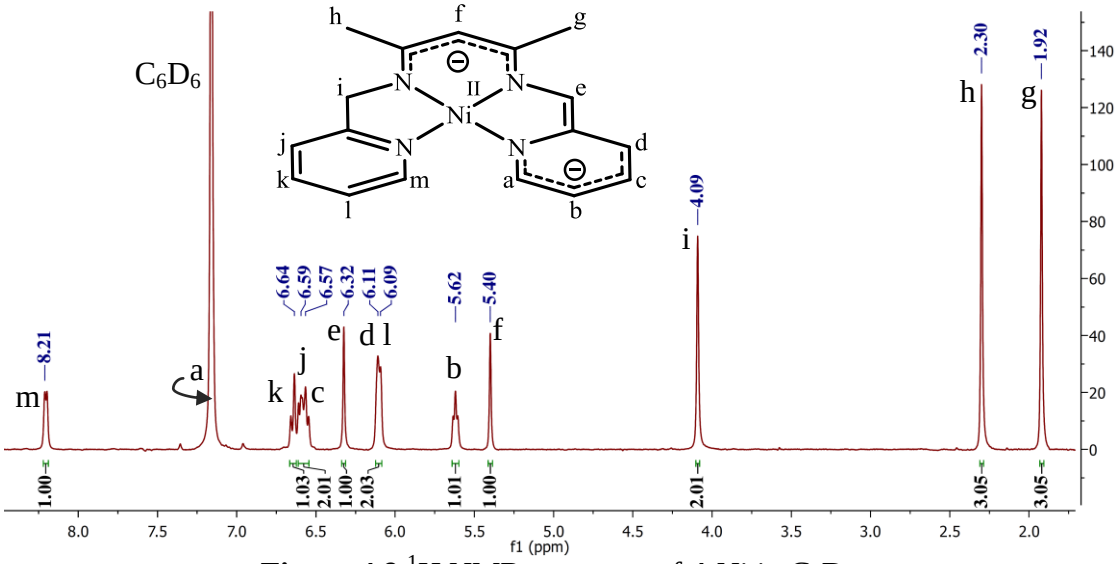

Figure 4.9. ^{1}H NMR spectrum of **4**-Ni in C_6D_6.

ligand, as recent work in this laboratory has demonstrated the extreme stability of Ni^{II} in a square planar geometry (*cf.* Ch. 2). In addition, the ^{1}H NMR spectrum of **4**-Ni features several upfield resonances corresponding to the imine C*H* (e, δ 6.32) and β-diketiminate backbone C*H* (f, δ 5.40), on par with the chemical shifts observed for {nn(PM)(PI)}FeLL' and {nn(PM)(PI)}FeL complexes (e, δ 6.9–6.4; f, δ 5.5–5.0 and e, δ 8.0–7.2; f, δ 6.5–5.8, respectively), indicative of increased electron density on the ligand backbone.

Initial reactivity studies focused on the use of **4**-Ni as a catalyst for olefin hydrogenation. Unfortunately, exposure of solutions of **4**-Ni to excess hydrogen and ethylene offered no evidence of reaction with either reagent. Dishearteningly, exposure of unpurified samples of **4**-Ni to H_2 and C_2H_4 *did* result in rapid production of ethane, suggesting that colloidal nickel, byproducts, etc. were responsible for the observed hydrogenation and were, in fact, far better hydrogenation catalysts than the isolated **4**-Ni.

It is possible the stored electrons in the {nn(PM)(PI)} backbone of **4**-Ni could serve as reducing equivalents to allow for the formation of a nickel alkylidene species stabilized in the Ni^{II} oxidation state, so **4**-Ni was treated with 1.0 equiv 3,3-diphenylcyclopropene (Eq. 4.8). However, 3,3-diphenylcyclopropene was entirely

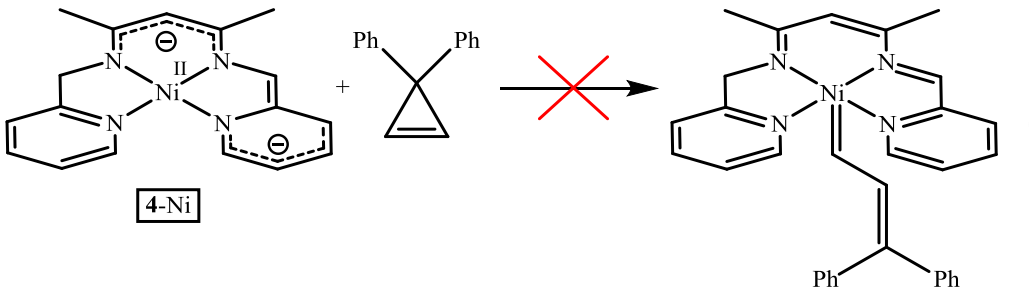

(4.8)

unreactive with **4**-Ni, even at temperatures up to 110 °C (the thermal instability of the cyclopropene reagent precluded prolonged heating at higher temperatures). Because initial reactivity studies of **4**-Ni were not encouraging, further investigation was not pursued.

4.3. Synthesis of {nn(PM)$_2$}MR (M = Mn, R = N(TMS)$_2$; M = Zn, R = Et)

As the design of the {nn(PM)$_2$} ligand allowed for the synthesis of well-behaved coordination complexes of V, Cr, Fe, Co, and Ni, the synthesis of the analogous Ti and Mn species was targeted. The slow addition of a THF solution of

H{nn(PM)$_2$} to Ti(NMe$_2$)$_4$[59] afforded an orange-brown solution and thick dark brown precipitate, and ^{1}H NMR analysis revealed release of HNMe$_2$ and formation of a complex mixture of diamagnetic byproducts. Treatment of TiCl$_2$(TMEDA)$_2$[60] with H{nn(PM)$_2$} to induce dehydrohalogenation with TMEDA and generate the Ti^{II} species {nn(PM)(PI}$^{2-}$Ti^{II} similarly produced a red-brown solution with a thick dark brown precipitate. By ^{1}H NMR spectroscopy a large amount of TMEDA and H{nn(PM)$_2$}was observed, implying that the insoluble precipitate was derived from decomposition of the TiCl$_2$(TMEDA)$_2$ starting material rather than clean formation of {nn(PM)$_2$}Ti and TMEDA·HCl, both of which would be expected to be insoluble. Accordingly, crystalline material could not be isolated from the reaction mixture.

In an attempt to synthesize the analogous manganese complex, H{nn(PM)$_2$} was treated with 1.0 equiv Mn(N(TMS)$_2$)$_2$(THF)[61] in C_6D_6. Immediately upon mixing, the reaction mixture darkened to orange and slowly turned brown over 5 min. ^{1}H NMR analysis indicated formation of HN(TMS)$_2$ and release of THF in a 1:1 ratio,

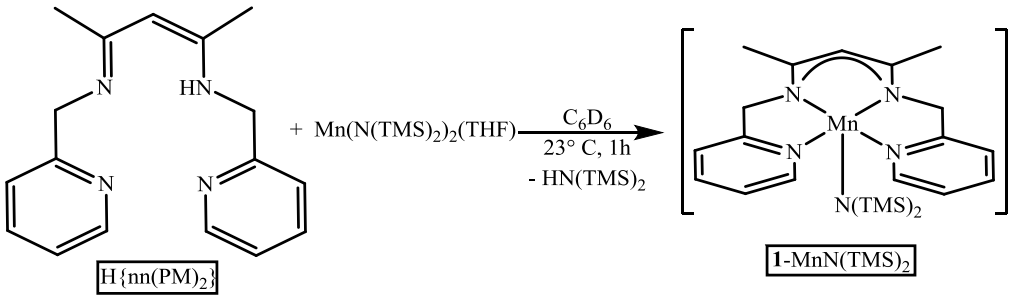

H{nn(PM)$_2$} **1**-MnN(TMS)$_2$ **(4.9)**

suggesting only single deprotonation of the {nn(PM)$_2$} ligand to generate {nn(PM)$_2$}MnN(TMS)$_2$ (Eq. 4.9). Unfortunately, no characteristic resonances were observed from -300 to 300 ppm. Thus far, crystals suitable for X-ray analysis have remained elusive, so the formulation of **1**-MnN(TMS)$_2$ is only tentative.

Reaction of H{nn(PM)$_2$} with Et_2Zn in C_6D_6 resulted in release of 1 equiv ethane and generation of a dark red solution. By ^{1}H NMR, single deprotonation and formation of {nn(PM)$_2$}ZnEt was confirmed (Eq. 4.10, Figure 4.10). Thermolysis of

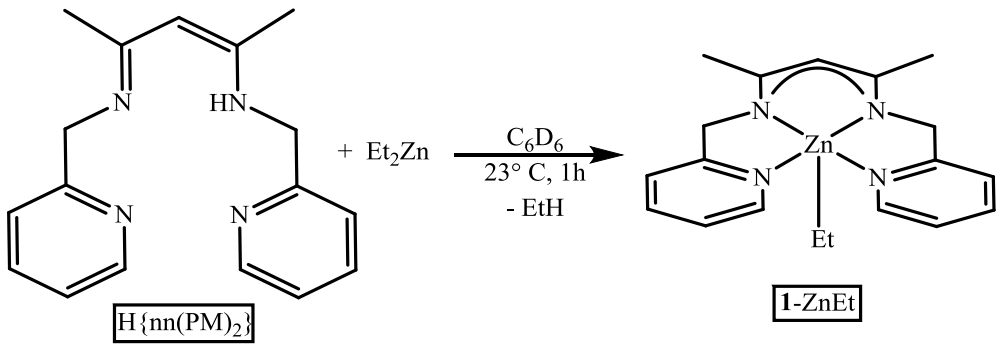

1-ZnEt at 60 °C to induce a second internal deprotonation at the methylene position of the ligand to generate {nn(PM)(PI}Zn resulted only in gradual decomposition to form Zn^0, H{nn(PM)$_2$}, ethane, and several unidentified diamagnetic byproducts.

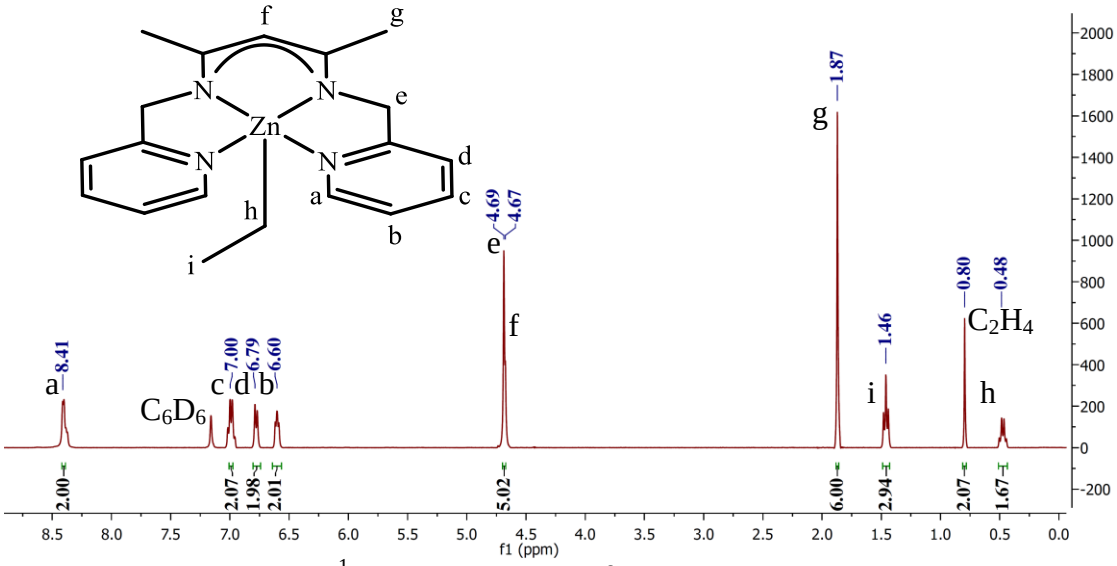

Figure 4.10. ^{1}H NMR spectrum of {nn(PM)$_2$}ZnEt (**1**-ZnEt).

Similarly, the reaction of H{nn(PM)$_2$} with $Zn(N(TMS)_2)_2$[62] in C_6D_6 resulted in immediate color change to dark red-brown and formation of a new C_S-symmetric diamagnetic species, consistent with {nn(PM)$_2$}ZnN(TMS)$_2$. As with **1**-ZnEt,

thermolysis to generate {nn(PM)(PI)}Zn only afforded decomposition products and further study was not pursued.

Experimental

General Considerations. All manipulations of air sensitive materials were performed using glove box and high vacuum techniques under an inert atmosphere. Hydrocarbon or ethereal solvents were refluxed over sodium, and vacuum transferred from sodium benzophenone ketyl (with 3–6 mL tetraglyme/L added to hydrocarbons). Benzene-d_6 was heated to reflux over sodium to dry and vacuum transferred from freshly cut sodium. THF-d_8 was dried over sodium and stored over 4 Å sieves. Diazodiphenylmethane,[49] 3,3-diphenylcyclopropene,[47,48] $V(N(TMS)_2)_2Cl(THF)$,[35,36] $Co(N(TMS)_2)_2(THF)$,[40,41] $Cr(N(TMS)_2)_2(THF)_2$,[50,51] $\{Ni(NPh_2)_2\}_2$,[58] $Ti(NMe_2)_4$,[59] $TiCl_2(TMEDA)_2$,[60] and $Mn(N(TMS)_2)_2(THF)$[61] were prepared according to literature procedures. All other chemicals were commercially available and used as received. All glassware was oven dried for a minimum of 2 h. NMR tubes for sealed tube experiments were flame dried under dynamic vacuum prior to use.

^1H, $^{13}C\{^1H\}$, ^{13}C and $^{31}P\{^1H\}$ NMR spectra were obtained on Varian INOVA 400, Varian INOVA 500, Varian INOVA 600, Varian Mercury 300, and Bruker ARX 300 spectrometers, and chemical shifts are reported relative to benzene-d_6 (^1H, δ 7.16; $^{13}C\{^1H\}$, δ 128.39) and THF-d_8 (^1H, δ 3.58; $^{13}C\{^1H\}$, δ 67.57). Infrared spectra were recorded on a Nicolet Avatar 370 DTGX spectrophotometer interfaced to an IBM PC (OMNIC software). UV-Vis spectra were obtained on a Cary 60 UV/Vis spectrometer. Elemental analyses were performed by Complete Analysis Laboratories, Inc., Parsippany, New Jersey, or by the laboratory of Professor Karsten Meyer, University of Erlangen – Nuremberg, Department of Chemistry & Pharmacy, Egerlandstr. 1, D-91058 Erlangen, Germany.

Synthesis. 1. {nn(PM)$_2$}VCl$_2$ (1-VCl$_2$). *a.* To a 25 mL flask charged with V(N(TMS)$_2$)$_2$Cl(THF) (100. mg, 0.209 mmol) and THF (8 mL) was added a solution of H{nn(PM)$_2$} (59 mg, 0.21 mmol) in 8 mL THF dropwise at 23 °C. The solution turned deep red-brown, a red precipitate was observed, and the solution was allowed to stand at 23 °C for 48 h without stirring. The solvent was decanted, and the resulting red crystals were washed with three 2 mL portions of THF and three 2 mL portions of pentane to yield 30. mg (0.075 mmol, 36%) of red crystalline **1**-VCl$_2$. Anal. Calc'd for C$_{17}$H$_{19}$Cl$_2$N$_4$V: C, 50.98%; H, 4.77%; N, 13.96%. Found: C, 51.87%, H, 5.21%, N, 12.31%; analysis is consistent with 0.5 THF per **1**-VCl$_2$ (C, 52.19%; H, 5.30%; N, 12.81%). *b.* To a 20 mL vial charged with VCl$_3$(THF)$_3$ (309 mg, 0.827 mmol) and Na{nn(PM)$_2$} (250. mg, 0.827 mmol) was added THF (10 mL) at 23 °C. The solution darkened to red-purple over 2 h and stirring was continued 4 d. Solvent was removed *in vacuo* to yield crude **1**-VCl$_2$ as a mixture with NaCl.

2. {nn(PM)$_2$}Co (1-Co). To a 50 mL flask charged with Co(N(TMS)$_2$)$_2$(THF) (150. mg, 0.332 mmol) was added THF (10 mL). A solution of H{nn(PM)$_2$} (93 mg, 0.33 mmol) in 10 mL THF was added dropwise while stirring over 3 min at 23 °C, and the solution turned dark blue-grey with precipitation of a dark blue solid. The solution was stirred 12 h at 23 °C and solvent was removed *in vacuo*. Benzene (25 mL) was added via vacuum transfer and the blue mixture was filtered. The filter cake was washed with benzene until washes ran colorless (~ 20 x 15 mL). The solution was concentrated to 5 mL, pentane (20 mL) was added vacuum transfer, and the mixture was filtered to yield crude **1**-Co. Gold needles were obtained through recrystallization of **1**-Co in THF/pentane at -35 °C (45 mg, 0.13 mmol, 40%). ^{1}H NMR (C$_6$D$_6$, 400

MHz): δ 1.76 (s, **g**, 6H), 3.87 (s, **e**, 4H), 5.35 (s, **f**, 1 H), 6.01 (t, J = 6 Hz, **b**, 2 H), 6.18 (d, J = 7 Hz, **d**, 2 H), 7.10 (t, 6 Hz, **c**, 2H), 9.01 (d, J = 6 Hz, **a**, 2 H). ^{13}C NMR (C_6D_6, 100 MHz): δ 21.45 (**g**), 61.96 (**e**), 125.43 (**f**), 123.09 (**b**), 118.42 (**d**), 122.12 (**c**), 146.77 (**a**). Anal. Calc'd for $C_{17}H_{19}N_4Co$: C, 60.36%; H, 5.66%; N, 16.56%. Found: C, 59.08%, H, 5.63%, N, 14.10%.

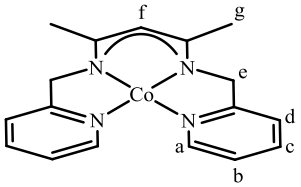

3. {nn(PM)$_2$}CoPMe$_3$. To a J. Young tube charged with {nn(PM)$_2$}Co (**1**-Co, 10. mg, 0.030 mmol) and C_6D_6 (0.4 mL) at 77 K was added PMe_3 (19 torr, 0.15 mmol). The tube was allowed to warm to 23 °C and the solution turned deep red. ^{1}H NMR analysis confirmed formation of {nn(PM)$_2$}CoPMe$_3$. ^{1}H NMR (C_6D_6, 400 MHz): δ 0.10 (s, P(CH_3)$_3$, 9H), 2.82 (s, **g**, 6H), 3.88 (s, **e**, 4H), 6.58 (s, **f**, 1 H), 6.95 (t, J = 6 Hz, **b**, 2 H), 7.10 (d, J = 7 Hz, **d**, 2 H), 7.76 (t, 6 Hz, **c**, 2H), 8.51 (d, J = 6 Hz, **a**, 2 H). ^{13}C NMR (C_6D_6, 100 MHz): δ 1.16 (P(CH_3)$_3$), 19.91 (**g**), 66.65 (**e**), 106.37 (**f**), 125.50 (**b**), 117.28 (**d**), 117.88 (**c**), 149.31 (**a**). ^{31}P NMR (C_6D_6, 162 MHz): δ 48.12 (br s, $\nu_{1/2}$ ~ 700 Hz). See above for numbering scheme.

4. {nn(PM)(PI)}Cr (4-Cr). To a 20 mL scintillation vial charged with Cr(N(TMS)$_2$)$_2$(THF)$_2$ (200. mg, 0.387 mmol) and C_6H_6 (5 mL) was added a solution of H{nn(PM)$_2$} (108 mg, 0.385 mmol) in C_6H_6 (5 mL) at 23 °C while swirling. The solution rapidly turned from light purple to brown. The vial was capped and left unstirred for 4 days and brown crystalline needles formed at the bottom of the vial. The supernatant was decanted and the crystals were washed with three 5 mL portions of C_6H_6 and three 5 mL portions of pentane. Volatiles were removed *in vacuo* to yield

4-Cr as a virtually insoluble brown material (62 mg, 0.19 mmol, 48%). Anal. Calc'd for $C_{17}H_{18}N_4Cr$: C, 61.81%; H, 5.49%; N, 16.96%. Found: C, 62.14%, H, 5.55%, N, 16.12%.

5. {nn(PM)(PI)}Ni (4-Ni). *a.* To a 100 mL flask charged with $\{Ni(NPh_2)_2\}_2$ (282 mg, 0.357 mmol) was added C_6H_6 (15 mL). A solution of H{nn(PM)$_2$} (200. mg, 0.713 mmol) in C_6H_6 (20 mL) was added dropwise while stirring over 3 min at 23 °C, and the solution turned dark red. The solution was stirred 12 h at 23 °C and solvent was removed *in vacuo*. Diethyl ether (40 mL) was added via vacuum transfer and the red solution was filtered. The filter cake was washed with six 20 mL portions of Et_2O, and the filtrate was concentrated to 15 mL, cooled to -78 °C, and filtered to yield red microcrystalline {nn(PM)(PI)}Ni (136 mg, 0.403 mmol, 57%). ^{1}H NMR (THF-d_8, 400 MHz): δ 2.16 (s, **g**, 3H), 3.27 (s, **h**, 3H), 3.44 (s, **i**, 2H), 5.10 (s, **f**, 1H), 5.20 (t, J = 6 Hz, **b**, 1H), 5.80 (s, **e**, 1H), 6.16 (d, J = 6 Hz, **d**, 1H), 6.18 (t, J = 6 Hz, **c**, 1H), 6.92 (d, 5 Hz, **a**, 1H), 7.30 (t, 6 Hz, **l**, 1H), 7.43 (d, 5 Hz, **j**, 1H), 7.80 (t, J = 6 Hz, **k**, 1H), 8.50 (d, J = 6 Hz, **m**, 1H). ^{13}C NMR (THF-d_8, 100 MHz): δ 20.96 (**g**), 59.04 (**h**), 72.53 (**i**), 100.34 (**f**), 101.14 (**b**), 105.53 (**e**), 114.09 (**c**), 123.10 (**l**), 126.50 (**d**), 128.68 (**j**), 136.48 (**k**), 145.55 (**a**), 149.92 (**m**). Anal. Calc'd for $C_{17}H_{18}N_4Ni$: C, 60.58%; H, 5.38%; N, 16.62%. Found: C, 48.42%, H, 4.68%, N, 11.63%; consistent with ~20% residual LiCl and 0.5 THF per molecule of **4**-Ni (C, 48.93%, H, 4.75%, N, 12.01%). *b.* To a 20 mL scintillation vial charged with Li_2{nn(PM)(PI)} (20. mg, 0.067 mmol) and $NiCl_2$(DME) (15 mg, 0.068 mmol) was added THF (2 mL) at 23 °C. Upon addition, the solution turned from dark purple to red with precipitation of a small amount of tan solid. The mixture was allowed to stir for 1 h, filtered through celite, and concentrated

to dryness *in vacuo*. ^{1}H NMR analysis confirmed clean conversion to **4**-Ni.

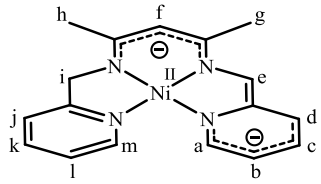

6. {nn(PM)$_2$}ZnEt (1-ZnEt). To a J. Young tube charged with H{nn(PM)$_2$} (20. mg, 0.071 mmol) and C_6D_6 (0.4 mL) was added Et_2Zn (7.3 μL, 0.071 mmol) at 23 °C. The reaction mixture turned from orange to dark red over 20 min, and formation of **1**-ZnEt was observed by ^{1}H NMR. ^{1}H NMR (C_6D_6, 400 MHz): δ 0.47 (q, J = 8 Hz, **h**, 2H), 1.46 (t, J = 8 Hz, **i**, 3H), 1.87 (s, **g**, 6H), 4.69 (s, **e**, 4H), 4.67 (s, **f**, 1 H), 6.60 (t, J = 6 Hz, **b**, 2 H), 6.78 (d, J = 7 Hz, **d**, 2 H), 6.99 (t, 7 Hz, **c**, 2H), 8.41 (d, J = 5 Hz, **a**, 2 H).

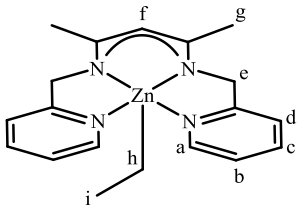

7. {nn(PM)$_2$}MnN(TMS)$_2$ (1-MnN(TMS)$_2$). To a J. Young tube charged with Mn(N(TMS)$_2$)$_2$(THF) (20. mg, 0.045 mmol) and H{nn(PM)$_2$} (13 mg, 0.046 mmol) was added C_6D_6 at 23 °C. Upon mixture, the reaction darkened to orange-brown. ^{1}H NMR analysis revealed release of HN(TMS)$_2$ and THF in a 1:1 ratio, but no resonances attributable to **1**-MnN(TMS)$_2$ were observed from -300 to 300 ppm.

8. Alkylation of 1-VCl$_2$. To a 50 mL flask charged with {nn(PM)$_2$}VCl$_2$ (**1**-VCl$_2$, 40. mg, 0.10 mmol) at -78 °C was transferred 10 mL THF. Under an Ar purge, a solution of ^{neo}PeLi (8 mg, 0.1 mmol) in THF (5 mL) was added dropwise over 5 min. The solution turned dark purple-black immediately upon addition. The reaction was allowed to warm to 23 °C and stirred an additional 12 h. Solvent was removed *in*

vacuo, and the resulting solid was triturated once with 10 mL pentane and washed with 10 mL pentane to yield the putative {nn(PM)$_2$}V(^{neo}Pe)$_2$. The highly soluble material did not exhibit any characteristic ^{1}H NMR resonances and further characterization was not pursued.

9. [{nn(PM)$_2$}Co]PF$_6$ (1$^+$-Co). To a 25 mL flask was added {nn(PM)$_2$}Co (**1**-Co, 50. mg, 0.15 mmol), Cp_2FePF_6 (49 mg, 0.15 mmol) and THF (5 mL) at 23 °C. The blue reaction mixture was allowed to stir at 23 °C 24 h and then filtered to remove Cp_2Fe. The filter cake was washed with three 10 mL portions of THF and dried *in vacuo* to yield crude [{nn(PM)$_2$}Co]PF$_6$ as a dark blue solid.

10. Reaction of {nn(PM)(PI)}Cr with Ph$_2$CN$_2$. To a 5 mL scintillation vial charged with {nn(PM)(PI)}Cr (**4**-Cr, 10. mg, 0.030 mmol) suspended in C_6D_6 (0.2 mL) was added a solution of Ph_2CN_2 (6 mg, 0.03 mmol) in C_6D_6 at 23 °C. Upon addition, the solution darkened to orange-brown and complete dissolution of **4**-Cr was observed. The mixture was allowed to react for 10 min at 23 °C and transferred to a J. Young tube. ^{1}H NMR did not reveal any resonances not attributable to solvents from -300 to 300 ppm.

11. Reaction of {nn(PM)(PI)}Cr with N$_3$TMS. To a 5 mL scintillation vial charged with {nn(PM)(PI)}Cr (**4**-Cr, 10. mg, 0.030 mmol) suspended in C_6D_6 (0.2 mL) was added a solution of N_3TMS (3 mg, 0.03 mmol) in C_6D_6 at 23 °C. Upon addition, the solution darkened to deep green and complete dissolution of **4**-Cr was observed. The mixture was allowed to react for 10 min at 23 °C and transferred to a J. Young tube. ^{1}H NMR did not reveal any resonances not attributable to solvents from -300 to 300 ppm.

Single-Crystal X-ray Diffraction Studies. Upon isolation, crystals were covered in polyisobutenes and placed under a 173 K N_2 stream on the goniometer head of a Siemens P4 SMART CCD area detector (graphite-monochomated Mo Kα radiation, $\lambda = 0.71073$ Å). The structures were solved by direct methods (SHELXS). All non-hydrogen atoms were refined anisotropically unless otherwise stated, and hydrogen atoms were treated as idealized contributions (Riding model).

REFERENCES

1. Holland, P. L. *Acc. Chem. Res.* **2008,** *41,* 905 – 914.

2. Jiao, R.; Shen, X. D.; Xue, M. Q.; Zhang, Y.; Yao, Y. M.; Shen, Q. *Chem. Commun.* **2010,** *46,* 4118 – 4120.

3. Cowley, R. E.; Eckert, N. A.; Vaddadi, S.; Figg, T. M.; Cundari, T. R.; Holland, P. L. *J. Am. Chem. Soc.* **2011,** *133,* 9796 – 9811.

4. Cowley, R. E.; Holland, P. L. *Inorg. Chem.* **2012,** *51,* 8352 – 8361.

5. Chiang, K. P.; Bellows, S. M.; Brennessel, W. W.; Holland, P. L. *Chem. Sci.* **2014,** *5,* 267 – 274.

6. Kogut, E.; Zeller, A.; Warren, T. H.; Strassner, T. *J. Am. Chem. Soc.* **2004,** *126,* 11984 – 11994.

7. Mindiola, D. J. *Angew. Chem., Int. Ed.* **2009,** *48,* 6198 – 6200.

8. Tomson, N. C.; Arnold, J.; Bergman, R. G. *Organometallics* **2010,** *29,* 5010 – 5025.

9. Tsai, Y. C. *Coord. Chem. Rev.* **2012,** *256,* 722 – 758.

10. Marlier, E. E.; Ulrich, B. A.; McNeill, K. *Inorg. Chem.* **2012,** *51,* 2079 – 2085.

11. Badei, Y. M.; Krishnaswamy, A.; Melzer, M. M.; Warren, T. H. *J. Am. Chem. Soc.* **2006,** *128,* 15056 – 15057.

12. Dai, X. L.; Warren, T. H. *J. Am. Chem. Soc.* **2004,** *126,* 10085 – 10094.

13. Dai, X. L.; Kapoor, P.; Warren, T. H. *J. Am. Chem. Soc.* **2004,** *126,* 4798 – 4799.

14. Mindiola, D. J. *Acc. Chem. Res.* **2006,** *39,* 813 – 821.

15. Tran, B. L.; Washington, M. P.; Henckel, D. A.; Gao, X. F.; Park, H.; Pink, M.; Mindiola, D. J. *Chem. Commun.* **2012,** 1529 – 1531.

16. Kilgore, U. J.; Basuli, F.; Huffman, J. C.; Mindiola, D. J. *Inorg. Chem.* **2006,** *45,* 487 – 489.

17. Zhao, G. Y.; Basuli, F.; Kilgore, U. J.; Fan, H. J.; Aneetha, H.; Huffman, J. C.; Wu, G.; Mindiola, D. J. *J. Am. Chem. Soc.* **2006,** *128,* 13575 – 13585.

18. Adhikari, D.; Basuli, F.; Orlando, J. H.; Gao, X. F.; Huffman, J. C.; Pink, M.; Mindiola, D. J. *Organometallics* **2009,** *28,* 4115 – 4125.

19. Tran, B. L.; Pinter, B.; Nichols, A. J.; Konopka, F. T.; Thompson, R.; Chen, C. H.; Krzystek, J.; Ozarowski, A.; Telser, J.; Baik, M. H.; Meyer, K.; Mindiola, D. J. *J. Am. Chem. Soc*. **2012,** *134,* 13035 – 13045.

20. Yu, Y.; Sadique, A. R.; Smith, J. M.; Dugan, T. R.; Cowley, R. E.; Brennessel, W. W.; Flaschenriem, C. J.; Bill, E.; Cundari, T. R.; Holland, P. L. *J. Am. Chem. Soc.* **2008,** *130,* 6624 – 6638.

21. Vela, J.; Smith, J. M.; Yu, Y.; Ketterer, N. A.; Flaschenriem, C. J.; Lachicotte, R. J.; Holland, P. L. *J. Am. Chem. Soc.* **2005,** *127,* 7857 – 7870.

22. Cowley, R. E.; Golder, M. R.; Eckert, N. A.; Al-Afyouni, M. H.; Holland, P. L. *Organometallics* **2013,** *32,* 5289 – 5298.

23. Rodriguez, M. M.; Bill, E.; Brennessel, W. W.; Holland, P. L. *Science* **2011,** *334,* 780 – 783.

24. Gephart, R. T.; Huang, D. L.; Aguila, M. J. B.; Schmidt, G.; Shahu, A.; Warren, T. H. *Angew. Chem., Int. Ed.* **2012,** *51,* 6488 – 6492.

25. Basuli, F.; Aneetha, H.; Huffman, J. C.; Mindiola, D. J. *J. Am. Chem. Soc.* **2005,** *127,* 17992 – 17993.

26. Kim, W. K.; Fevola, M. J.; Liable-Sands, L. M.; Rheingold, A. L.; Theopold, K. H. *Organometallics* **1998,** *17,* 4541 – 4543.

27. MacAdams, L. A.; Buffone, G. P.; Incarvito, C. D.; Rheingold, A. L. *J. Am. Chem. Soc.* **2005,** *127,* 1082 – 1083.

28. Whitehorne, T. J. J.; Schaper, F. *Inorg. Chem.* **2013,** *52,* 13612 – 13622.

29. El-Zoghbi, I.; Kebdani, M.; Whitehorne, T. J. J.; Schaper, F. *Organometallics* **2013,** *32,* 6986 – 6995.

30. Gianetti, T. L.; Tomson, N. C.; Arnold, J.; Bergman, R. G. *J. Am. Chem. Soc.* **2011,** *133,* 14904 – 14907.

31. Yao, S. L.; Driess, M. *Acc. Chem. Res.* **2012,** *45,* 276 – 287.

32. Frazier, B. A.; Williams, V. A.; Wolczanski, P. T.; Bart, S.; Meyer, K.; Cundari, T. R.; Lobkovsky, E. B. *Inorg. Chem.* **2013,** *52,* 3295 – 3312.

33. Frazier, B. A.; Wolczanski, P. T.; Keresztes, I.; DeBeer, S.; Lobkovsky, E. B.; Pierpont, A. W.; Cundari, T. R. *Inorg. Chem.* **2012,** *51,* 8177 – 8186.

34. Hulley, E. B.; Wolczanski, P. T.; Lobkovsky, E. B. *J. Am. Chem. Soc.* **2011,** *133,* 18058 – 18061.

35. Berno, P.; Moore, M.; Minhas, R.; Gambarotta, S. *Can. J. Chem.* **1996,** *74,* 1930 – 1935.

36. Berno, P.; Minhas, R.; Hao, S.; Gambarotta, S. *Organometallics* **1994,** *13,* 1052 – 1054.

37. Berno, P; Gambarotta, S. *J. Chem. Soc., Chem. Commun.* **1994,** 2419 – 2421.

38. Moore, M.; Gambarotta, S.; Bensimon, C. *Organometallics* **1997**, *16,* 1086 – 1088.

39. Günther, H. *NMR Spectroscopy: Basic Principles, Concepts, and Applications in Chemistry*. John Wiley & Sons: New York, 2013.

40. Bürger, H.; Wannagat, U. *Monatsh. Chem.* **1963,** *94,* 1007 – 1012.

41. Andersen, R. A.; Faegri, K.; Green, J. C.; Haaland, A.; Lappert, M. F.; Leung, W. P.; Rypdal, K. *Inorg. Chem.* **1988,** *27,* 1782 – 1786.

42. Guilard , R.; Kadish, K. M. *Chem. Rev.* **1988,** *88,* 1121 – 1146.

43. Pellissier, H.; Clavier, H. *Chem. Rev.* **2014,** *114,* 2775 – 2823.

44. Chen, Y.; Zhang, Z. P. *J. Org. Chem.* **2007,** *72,* 5931 – 5934.

45. Chen, Y.; Fields, K. B.; Zhang, X. P. *J. Am. Chem. Soc.* **2004,** *126,* 14718 – 14719.

46. Xu, X.; Zhu, S.; Cui, X.; Wojtas, L.; Zhang, X. P. *Angew. Chem. Int. Ed.* **2013,** *52,* 11857 – 11861.

47. Hughes, D. L.; Leigh, G. J; Mc Mahon, C. N. *J. Chem. Soc., Dalton Trans.* **1997,** 1301 – 1307.

48. Krämer, K.; Leong, P.; Lautens, M. *Org. Lett.* **2011,** *13,* 819 – 821.

49. Javed, M. I.; Brewer, M. *Org. Lett.* **2007,** *9,* 1789 – 1792.

50. Kern, R. J. J. *Inorg. Nucl. Chem.* **1962,** *24,* 1105 – 1109.

51. Bradley, D. C.; Hursthouse, M. B.; Newing, C. W.; Welch, A. J. *J. Chem. Soc., Chem. Commun.* **1972,** 567 – 568.

52. Brownie, J. H.; Baird, M. C. *Organometallics* **2007,** *26,* 5890 – 5901.

53. Adams, R. D.; Collins, D. E.; Cotton, F. A. *J. Am. Chem. Soc.* **1974,** *96,* 749 – 754.

54. Edelmann, F.; Töfke, S.; Behrens, U. *J. Organomet. Chem.* **1986,** *308,* 27 – 34.

55. Wang, H.; Sun, Z.; Xie, Y.; King, R. B.; Schaefer III, H. F. *Eur. J. Inorg. Chem.* **2010,** 5161 – 5173.

56. McGovern, P. A.; Vollhardt, K. P. C. *Chem. Commun.* **1996**, 1593.

57. Vollhardt, K. P. C; Cammack, J. K.; Matzger, A. J.; Bauer, A.; Capps, K. B.; Hoff, C. D. *Inorg. Chem.* **1999,** *38,* 2624 – 2631.

58. Hope, H.; Olmstead, M.; Murray, B. D.; Power, P. P. *J. Am. Chem. Soc.* **1985,** *107,* 712 – 713.

59. Bradley, D. C.; Thomas, I. M. *J. Chem. Soc.* **1960**, 3857 – 3861.

60. Edema, J. J. H.; Duchateau, R.; Hynes, R.; Gabe, E.; Gambarotta, S. *Inorg. Chem.* **1991,** *30,* 154 – 156.

61. Bürger, H.; Wannagat, U, *Monatsh. Chem.* **1964,** *95,* 1099 – 1102.

62. Darensbourg, D. J.; Holtcamp, M. W.; Struck, G. E.; Zimmer, M. S.; Niezgoda, S. A.; Rainey, P.; Robertson, J. B.; Draper, J. D.; Reibenspies, J. H. *J. Am. Chem. Soc.* **1999,** *121,* 107 – 116.

APPENDIX

A.1. Cyclopropanes for the Reversible Storage of Singlet Diradicals

In recent years, it was discovered in these laboratories that reaction of $Me_2C(CH{=}NCH_2py)_2$ with 1.0 equiv $TiCl_2(TMEDA)_2$ afforded the diamagnetic C-C coupled $[Me_2{}^{cy}Pro(NCH_2py)_2]TiCl_2$ (Eq. A.1).[1] It was thought that the reaction to form the new cyclopropane ring in the ligand backbone arose from reductive coupling

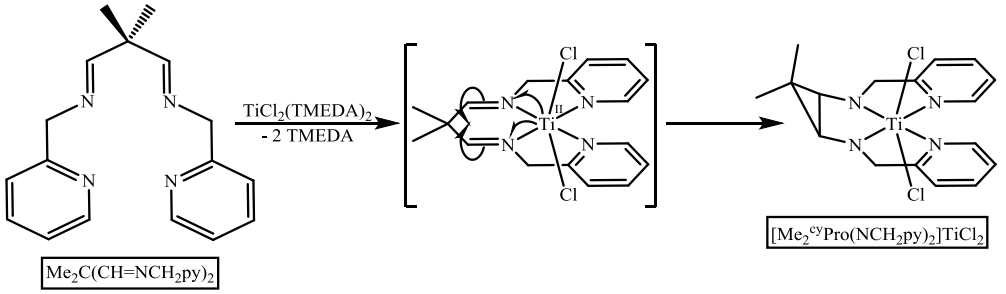

(A.1)

of the two imines, and brought forth the question of whether this coupling was reversible. With the intent to study whether diradical character could be reversibly stored in cyclopropane rings within this ligand system, the rational synthesis of a cyclopropane-based tetradentate ligand was perused. As the cyclopropane ring in $[Me_2{}^{cy}Pro(NCH_2py)_2]TiCl_2$ contained a *cis* linkage within the ligand framework, the synthesis of *cis*-1,2-cyclopropane diamine was initially targeted.

As shown in Scheme A.1, 1,2-cyclopropanedicarboxylic acid could be readily synthesized from ethyl acrylate and chloroacetate in two steps as a mixture of *cis* and *trans* isomers, typically in a 2:1 to 3:1 ratio. Reaction of the mixture with acetic anhydride converted the *cis* isomer exclusively to the corresponding anhydride, which could be separated from the mixture via sublimation and hydrolyzed back to the diacid with H_2O. Further reaction to *cis*-1,2-cyclopropane diisocyanate was accomplished in

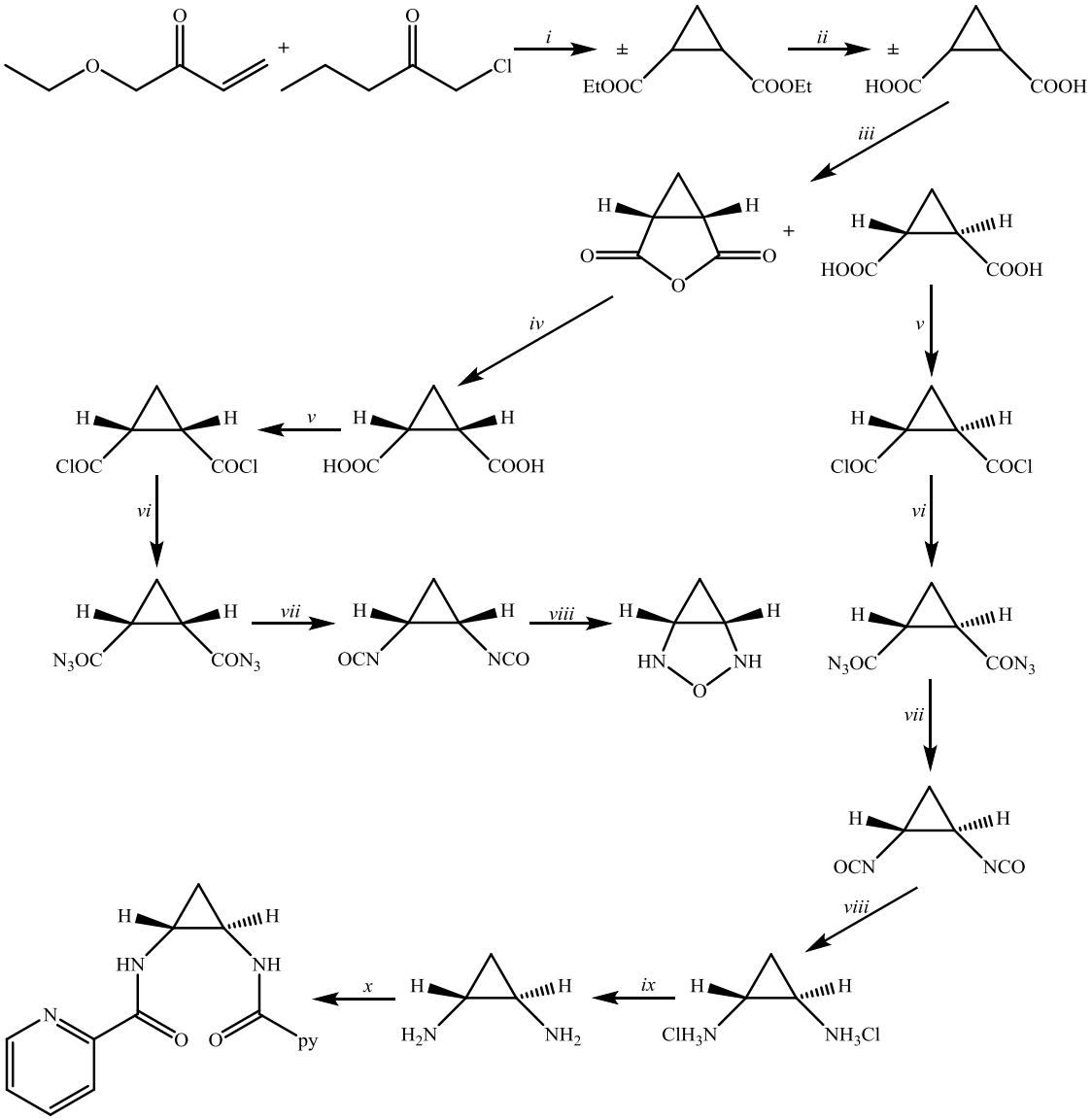

Scheme A.1.[23] Synthesis of various cyclopropane derivatives. Conditions: *i.* NaOMe, neat, 0 °C, 2 h; *ii.* NaOH, H_2O, 100 °C, 4h; *iii.* Ac_2O, neat, 100 °C, 30 min, *cis* and *trans* isomers separated via sublimation; *iv.* H_2O, 100 °C, 10 min; *v.* PCl_5, neat, 100 °C, 5 hr; *vi*, NaN_3, H_2O/acetone, 0 °C, 2 h; *vii.* Toluene, 100 °C, 3 h; *viii.* HCl, H_2O, 23 °C, 30 min; *ix.* NaOMe, MeOH, 23 °C, 20 min; *x.* 2-pyridinecarboxylic acid, triphenylphosphite, pyridine, 100 °C, 4 h.

three steps (Scheme A.1 *v* – *vii*), but conversion to the *cis*-1,2-cyclpropane diamine was unsuccessful. Due to the difficulty of synthesizing the *cis*-cyclopropane reagent, and because a cyclopropane ring with *trans* stereochemistry would likely ring-open

upon binding to a metal center, thus "releasing the diradical stored in the C-C bond", the analogous *trans*-cyclopropane reagents were next targeted.

Trans-1,2-cyclopropane diisocyanate could be readily prepared as illustrated in Scheme A.1 under conditions analogous to those of the corresponding *cis* isomer. Interestingly, the Curtius rearrangement in which the acyl azide moieties were converted to isocyanate fragments seemed to pass through the same intermediate regardless of initial stereochemistry. Illustrated in Figure A.1 is the conversion of 1,2-cyclopropanedicarbonyl diazide to the corresponding diisocyanate as a function of time. At t = 60 min (Figure A.1, top), a set of resonances ($CDCl_3$; δ 1.21, t, J = 7 Hz, 2H; 3.47, q, J = 7 Hz, 2H) appeared. This same set of resonances appeared when the *trans* acyl azide was used instead, and when a mixture of *cis*- and *trans*-1,2-cyclopropanedicarbonyl diazide (Figure A.1, bottom) was heated the sets of resonances corresponding to *cis* and *trans* isomers coalesced to the same triplet and quartet set (t = 120 min) before again separating to the *cis* and *trans*-1,2-cyclopropane diisocyanate products at long reaction times. However, because stereochemistry was clearly conserved in this reaction to yield the desired products, this seemingly common intermediate remained a curiosity as further study was not perused.

Conversion of *trans*-1,2-cyclopropane diisocyanate to the diamine was facile (Scheme A.1, steps *viii – ix*), but due to poor solubility in organic solvents, the complex could not be separated from the NaCl byproduct. Nonetheless, the diamine was used as a 1:1 salt mixture in subsequent reactions.

Unfortunately, condensation of *trans*-1,2-cyclopropane diamine with 2-pyridine carboxyaldehyde (Eq. A.2) was unsuccessful under a variety of reaction

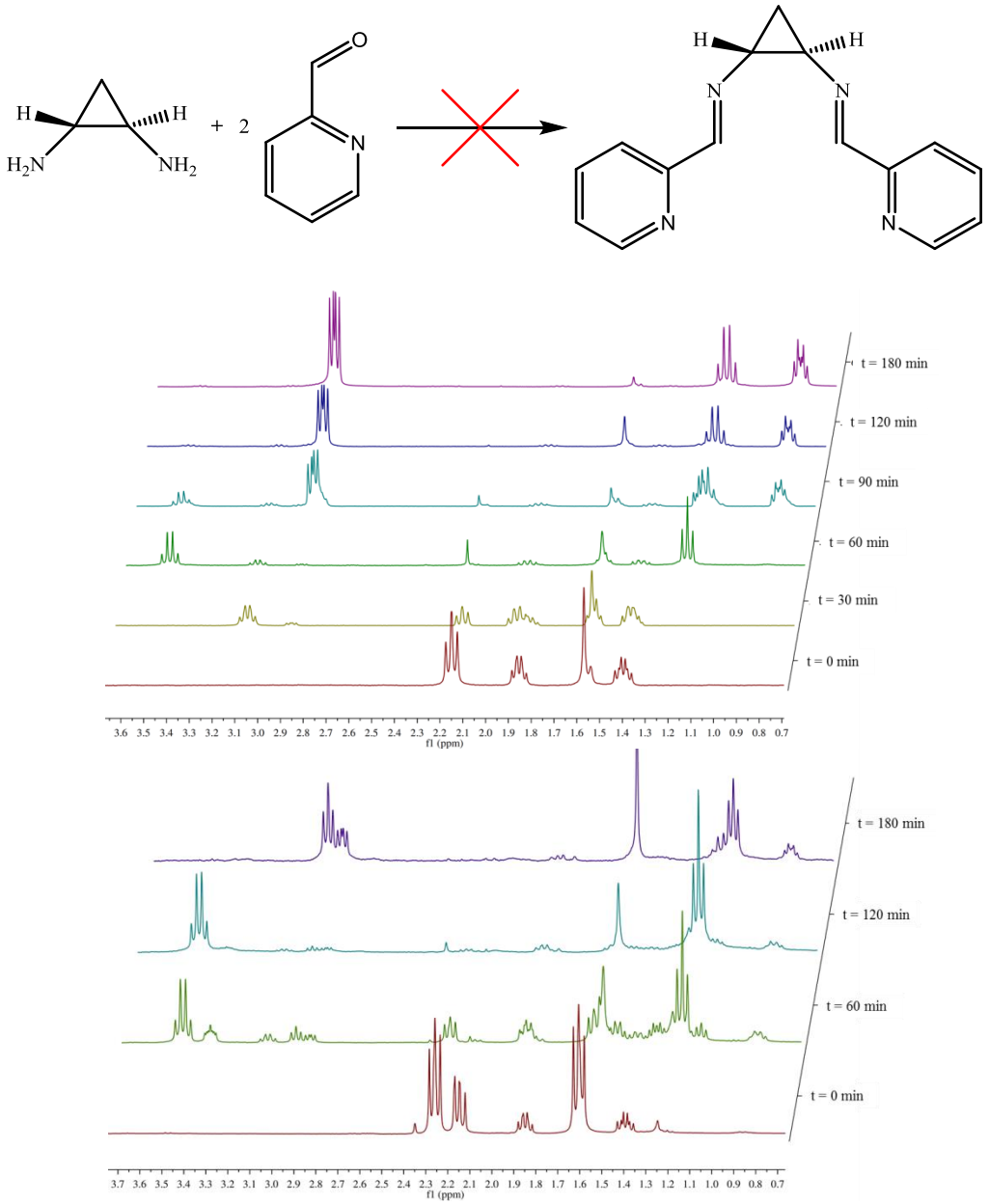

Figure A.1. *Top:* Reaction of *cis*-1,2-cyclopropanediarbonyl diazide to form *cis*-1,2-cyclopropane diisocyanate. Two different intermediates can be seen at t = 30 min and t = 60 min. *Bottom:* Thermolysis of a mixture of *cis* and *trans cis*-1,2-cyclopropanediarbonyl diazide. Both species seemingly pass through the same intermediate (t = 120 min) but stereochemistry is retained in the final product (t = 180 min).

conditions. Various ligand cyclizations have been observed in these laboratories where two imine moieties were in close proximity and able to interact. A recent example is

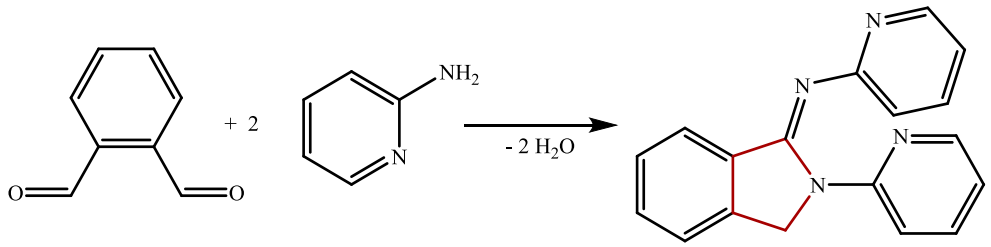

(A.3)

highlighted in Eq. A.3,[4] where the newly formed heterocycle is shown in red. One could envision that an analogous cyclization of the desired reaction product would result in cyclopropane ring-opening, which would in turn lead to nonspecific decomposition reactions to generate the intractable mixtures observed.

The synthesis of related [2-(benzoylamino)cyclopropylamino](2-pyridyl)formaldehyde *was* facile (Scheme A.1 *x*),[5] but attempts at metallation with 1st row transition metals generated complex product mixtures. This result is perhaps unsurprising, as the *trans* cyclopropane moiety was initially expected to ring-open upon metallation and clean reactivity out of the *trans* ligand system was hopeful at best.

A.2. Alternate Tetradentate Ligand Networks

To further explore the utility of various tetradentate ligands, a series of condensations were carried out to synthesize **L1** – **L6** (Scheme A.2, Scheme A.3). **L1** is analogous to the {dmp(PI)$_2$} ligand (*cf.* Chapter 2), and unsurprisingly, exhibits analogous reactivity with nickel. Unfortunately **L2**, where n = 5, did not metallate

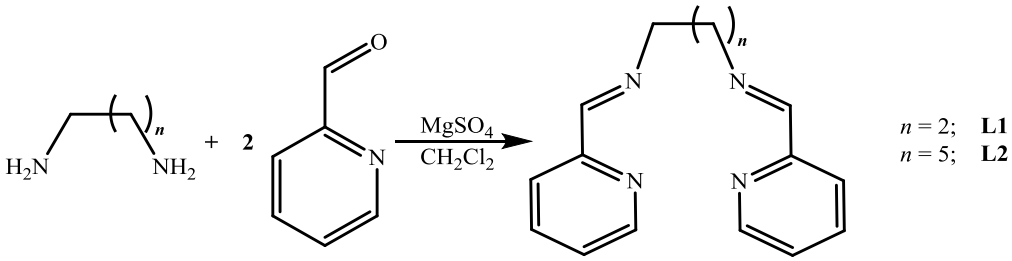

Scheme A.2. Synthesis of tetradentate pyridine imine-based ligands **L1** – **L2**.

cleanly. Presumably, the long alkyl chain in the ligand backbone allowed coordination to multiple metal centers and formation of oligomeric species.

To extend the chemistry of tetradentate diimine ligand systems that could impart pseudo square planar geometry about a metal center, 2,2-dimethyl-1,3-propanediamine was treated with various benzaldehyde derivatives to afford **L3** – **L6** (Scheme A.3). Initial metallation efforts focused on the preparation of $[Me_2C(CH{=}NCH_2Ph)_2]FeL_n$, $\{dmp(PhI)_2\}FeL_n$. The reaction of **L5** with 1.0 equiv

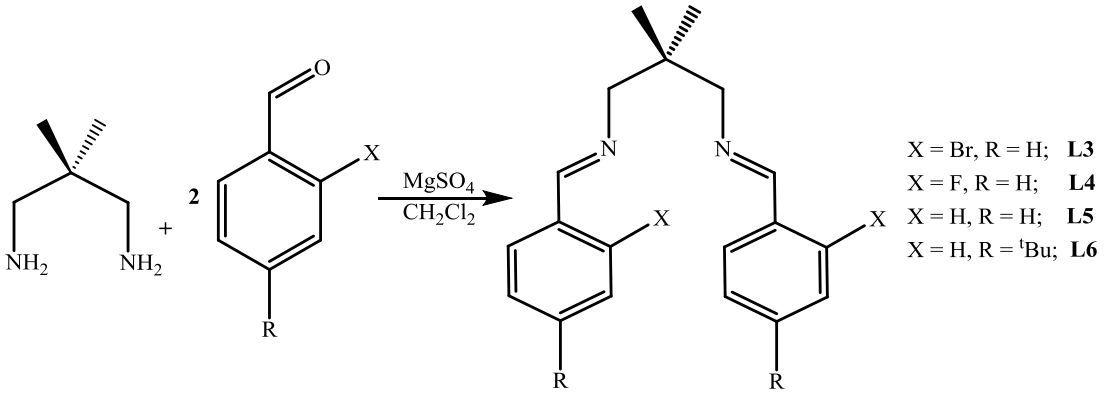

Scheme A.3. Synthesis of tetradentate phenyl imine-based ligands **L3** – **L6**.

$(Me_3P)_4FeMe_2$[6] resulted in a deep purple solution over 1 wk, although ^{1}H NMR spectral analysis only indicated the presence of starting materials. Over 3 wk a minor diamagnetic product started growing in and precipitation of solids was observed,

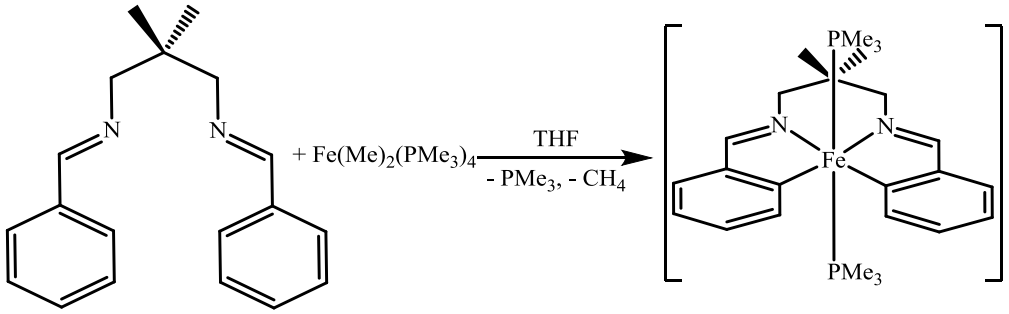

(A.4)

although the thermal sensitivity of $(Me_3P)_4FeMe_2$ precluded complete reaction to form the new product (Eq. A.4). Gratifyingly, treatment of **L3** with 2.0 equiv $Fe(PMe_3)_4$[7] afforded the same purple solution within minutes with concomitant precipitation of solid. The ^{1}H NMR spectrum of the reaction mixture was consistent with the diamagnetic product formed in Eq. A.4 and confirmed generation of $\{dmp(PhI)_2\}Fe(PMe_3)_2$, $\mathbf{L_A}$-$Fe(PMe_3)_2$ (Eq. A.5). The complex was isolable as a

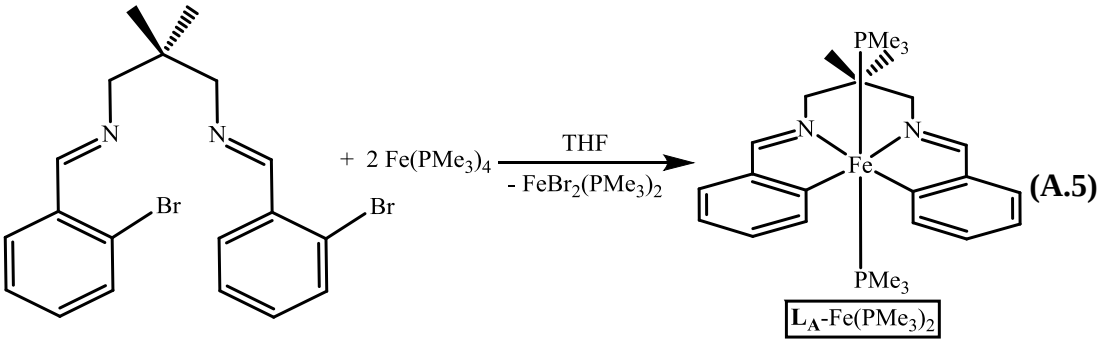

(A.5)

purple solid, but was prone to thermal degradation and darkened to brown over 4 h in the solid state at 23 °C. Nonetheless, $\mathbf{L_A}$-$Fe(PMe_3)_2$ could be crystallized from a saturated solution of pentane at -35 °C. The ^{1}H NMR spectrum of the isolated $\mathbf{L_A}$-$Fe(PMe_3)_2$ is illustrated in Figure A.2 and reveals a highly symmetric species with two bound phosphine ligands.

In the reaction shown in Eq. A.5, one equivalent of $Fe(PMe_3)_4$ was lost as $FeBr_2(PMe_3)_2$. To develop a more atom-economic synthesis of $\mathbf{L_A}$-$Fe(PMe_3)_2$ the fluorinated ligand **L4** was synthesized. In principle, reaction of **L4** with 1.0 equiv. $Fe(PMe_3)_4$ could afford the desired product and Me_3PF_2. Unfortunately, reaction of **L4** with either 1 or 2 equiv $Fe(PMe_3)_4$ did not produce $\mathbf{L_A}$-$Fe(PMe_3)_2$.

To further explore the chemistry of first-row transition metals with tetradentate diimine ligand systems with metal-carbon bonds, **L3** was treated with 2.0 equiv

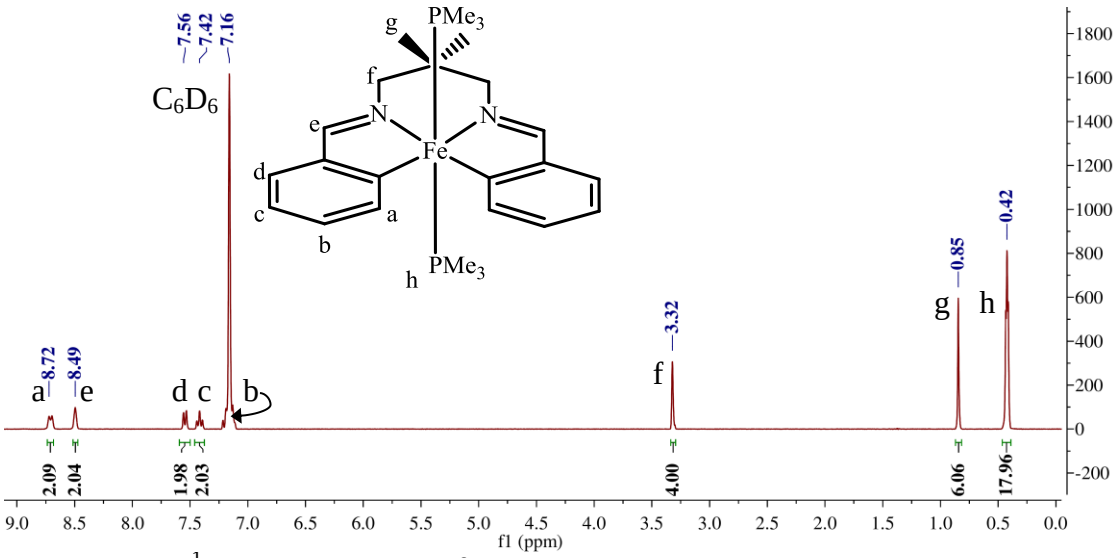

Figure A.2. ^{1}H NMR spectrum of {dmp(PhI)$_2$}Fe(PMe$_3$)$_2$ (**L$_A$**-Fe(PMe$_3$)$_2$) in C_6D_6.

Ni(COD)$_2$[8] to afford dark orange {dmp(PhI)$_2$}Ni, **L$_A$**-Ni (Eq. A.6). The ^{1}H NMR spectrum of **L$_A$**-Ni is illustrated in Figure A.3. The chemical shifts of **L$_A$**-Ni are quite

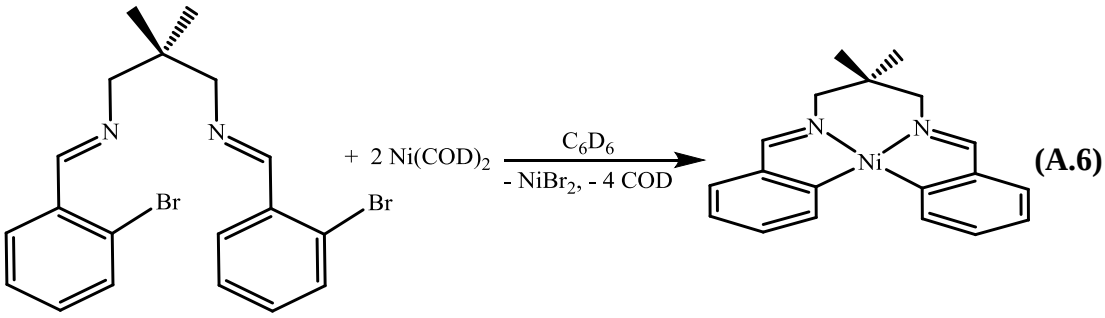

(A.6)

similar to those of {dmp(PI)$_2$}Ni, although the proton *ortho* to the metal center is shifted ~1.4 ppm downfield in {dmp(PI)$_2$}Ni due to the close proximity of a nitrogen atom on the pyridine ring.

To synthesize the analogous cobalt complex {dmp(PhI)$_2$}CoL$_n$, **L4** was allowed to react with 2 equiv Co(PMe$_3$)$_4$.[9] Upon addition of ligand to a solution of Co(PMe$_3$)$_4$, an immediate color change from light brown to deep blue-brown was observed with precipitation of a gold solid (Eq. A.7). By ^{1}H NMR spectroscopy consumption of starting materials was observed but no new soluble diamagnetic or

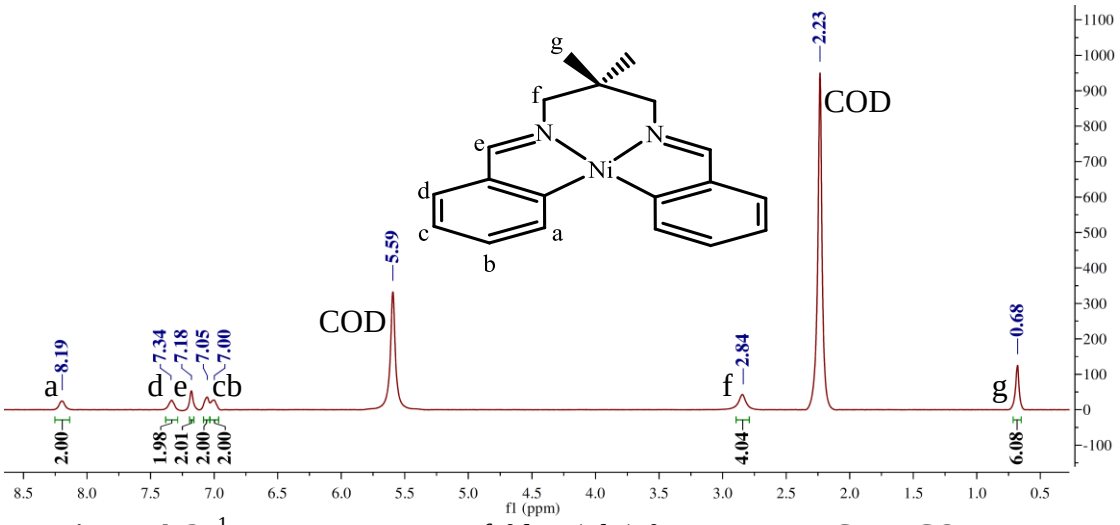

Figure A.3. ^{1}N NMR spectrum of {dmp(PhI)$_2$}Ni, $\mathbf{L_A}$-Ni in C_6D_6. COD = 1,4-cyclooctadiene.

paramagnetic products were seen, implying that the cobalt species formed was insoluble in organic solvents. Considering the relatively high solubilities of the analogous {dmp(PhI)}Fe(PMe$_3$)$_2$ and {dmp(PhI)$_2$}Ni complexes, it is unlikely that

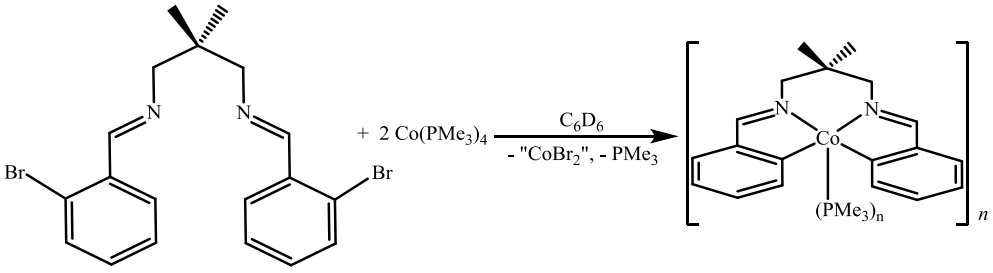

(A.7)

monomeric {dmp(PhI)}$_2$Co(PMe$_3$)$_n$ formed cleanly, but a dimeric or oligomeric cobalt species would be predicted as relatively insoluble. Attempts at obtaining crystals suitable for X-ray analysis of the gold precipitate to determine the molecular structure of the reaction product are ongoing.

Experimental

All manipulations were performed using glove box and high vacuum techniques under an inert atmosphere unless otherwise stated. Hydrocarbon and ethereal solvents were refluxed over sodium, and vacuum transferred from sodium benzophenone ketyl (with 3–6 mL tetraglyme/L added to hydrocarbons). Benzene-d_6 was heated to reflux over sodium to dry and vacuum transferred from freshly cut sodium. $(Me_3P)_4FeMe_2$,[6] $Fe(PMe_3)_4$,[7] $Ni(COD)_2$,[8] and $Co(PMe_3)_4$[9] were prepared according to literature procedures. Sodium methoxide was prepared fresh before use. All other chemicals were commercially available and used as received. All glassware was oven dried for a minimum of 2 h. Caution: ethyl acrylate has a very strong, characteristic acrid odor and MUST be used in a fume hood. ^{1}H NMR spectra were obtained on Varian INOVA 400, Varian Mercury 300, and Bruker ARX 300 spectrometers, and chemical shifts are reported relative to benzene-d_6 (^{1}H, δ 7.16), $CDCl_3$ (^{1}H, δ 7.26), D_2O (^{1}H, δ 4.79), and CD_3OD(^{1}H, δ 3.31).

Synthesis. 1. 1,2-Cyclopropanedicarboxylic acid diethyl ester. To a 250 mL flask charged with ethyl acrylate (86 mL, 0.808 mol) and ethyl chloroacetate (38.3 mL, 0.359 mol) at 0 °C was added solid sodium methoxide (19.4g, 0.359 mol) in portions over 20 min in air. The solution turned yellow and was allowed to stir 1 h at 0 °C. The reaction mixture was transferred to a 1 L flask containing 200 mL distilled water, and enough distilled water was added to completely dissolve the NaCl byproduct (~50 mL). The organic phase was separated, and the aqueous phase was extracted with three 20 mL portions of dichloromethane. The combined organics were washed with brine (2 x 50 mL) and dried over $MgSO_4$. Removal of volatiles *in vacuo*

yielded crude product. Pure 1,2-cyclopropanedicarboxylic acid diethyl ester isomers was obtained as a mixture of *cis* and *trans* (~ 2:1 ratio) through fractional distillation (b.p. 60 -79 °C, 26.01 g, 0.140 mol, 39%). ^{1}H NMR ($CDCl_3$, 300 MHz) δ 1.11 – 1.31 (mult, *cis* + *trans* C*H*$_3$; mult, *trans* ^{cy}Pro-C*H*$_2$; 10H), 1.36 – 1.43 (mult, *cis* ^{cy}Pro-C*H*$_2$, 1H), 1.59 – 1.68 (mult, *cis* ^{cy}Pro-C*H*$_2$, 1 H), 1.99 – 2.06 (mult, *cis* ^{cy}Pro-C*H*, 2 H), 2.09 – 2.16 (mult, *trans* ^{cy}Pro-C*H*, 1 H), 4.07 – 4.16 (mult, *cis* + *trans* C*H*$_2$, 6H).

2. 1,2-Cyclopropanedicarboxylic acid. To a 250 mL flask containing NaOH (16.76 g, 0.419 mol) in H_2O (112 mL) was added 1,2-cyclopropanedicarboxylic acid diethyl ester (*cis* + *trans*, 26.00 g, 0.140 mol) in air. The mixture was heated to reflux 3h and concentrated to 10 mL total volume. Concentrated HCl(aq) was added to neutralize until pH < 1 (35 mL). The mixture was filtered to remove NaCl, and the filtrate was continually extracted with Et_2O for 24h. The resulting organic portion was dried over $MgSO_4$ and concentrated to dryness to yield pure 1,2-cyclopropanedicarboxylic acid as a mixture of *cis* and *trans* isomers (~2:1 ratio). Yield = 16.94 g (0.130 mol, 93%). ^{1}H NMR ($CDCl_3$, 300 MHz, *cis*) δ 1.35 – 1.44 (mult, ^{cy}Pro-C*H*$_2$, 1H), 1.48 – 1.56 (mult, ^{cy}Pro-C*H*$_2$, 1 H), 2.21 – 2.28 (mult, ^{cy}Pro-C*H*, 2 H). ^{1}H NMR ($CDCl_3$, 300 MHz, *trans*) δ 1.48 – 1.54 (t, J = 7 Hz, ^{cy}Pro-C*H*$_2$, 2H), 2.16 – 2.23 (t, J = 7 Hz, ^{cy}Pro-C*H*, 2 H).

3. Separation of *cis* and *trans* 1,2-cyclopropanedicarboxylic acid. To a 250 mL flask charged with acetic anhydride (10.25 g, 0.100 mol) was added 1,2-cyclopropanedicarboxylic acid (16.94 g, 0.130 mol) as a mixture of *cis* and *trans* (~ 2:1) isomers in air. The reaction mixture was heated to 80 °C for 25 min then concentrated to a thick yellow oil. 1,2-cyclopropanedicarboxylic anhydride sublimed

out of the mixture under full dynamic vacuum at ~ 60 °C as a white crystalline powder. The material remaining in the sublimation apparatus was *trans*-1,2-cyclopropanedicarboxylic acid (> 95%), which could be recrystallized from hot acetonitrile (3.38 g, 0.26 mol, 60%). The sublimed 1,2-cyclopropanedicarboxylic anhydride was dissolved in 5 mL H_2O and heated to 80 °C for 10 min. Solvent was removed *in vacuo*, and the resulting *cis*-1,2-cyclopropanedicarboxylic acid was recrystallized from hot nitromethane (9.36 g, 0.72 mmol, 83%).

4. ***cis*-1,2-Cyclopropanedicarbonyl dichloride.** To a 25 mL flask charged with solid *cis*-1,2-cyclopropanedicarboxylic acid (6.7 g, 0.051 mol) was added solid PCl_5 (32.17 g, 0.154 mol) in portions at 23 °C in air over 10 min while stirring. The reaction was slightly exothermic upon addition and a small amount of liquid PCl_3 and cyclopropanedicarbonyl dichloride was formed. The reaction was heated to 100 °C for 5 h, and then filtered to remove excess PCl_5. *cis*-1,2-cyclopropanedicarbonyl dichloride was isolated from the filtrate via fractional distillation (35 – 51 °C, 10^{-4} torr, 7.04 g, 0.042 mol, 82%). ^{1}H NMR ($CDCl_3$, 300 MHz, *cis*) δ 1.60 – 1.69 (mult, ^{cy}Pro-C*H*$_2$, 1H), 2.02 – 2.10 (mult, ^{cy}Pro-C*H*$_2$, 1 H), 2.80 – 2.89 (mult, ^{cy}Pro-C*H*, 2 H). IR: ν_{CO} = 1794 cm^{-1}.

5. ***trans*-1,2-Cyclopropanedicarbonyl dichloride.** *Trans*-1,2-cyclopropanedicarbonyl dichloride was prepared via an analogous procedure to that given in **(4.)**. ^{1}H NMR ($CDCl_3$, 300 MHz, *trans*) δ 1.90 (t, J = 8 Hz, ^{cy}Pro-C*H*$_2$, 2H), 2.91 (t, J = 8 Hz, ^{cy}Pro-C*H*, 2 H).

6. ***cis*-1,2-Cyclopropanedicarbonyl diazide.** To a 25 mL flask charged with NaN_3 (1.58 g, 24.3 mmol) in H_2O (4.5 mL) was added *cis*-1,2-cyclopropanedicarbonyl

dichloride (1.35 g, 8.1 mmol) in acetone (3 mL) dropwise at 0 °C over 5 min in air. The mixture was allowed to stir at 0 °C for 2 h and then poured into ice H_2O (18 mL). Et_2O (4 mL) was added and the organic layer was separated. The aqueous layer was extracted with Et_2O (3 x 4 mL) and the combined organics were washed with H_2O (1 x 3 mL) and dried over $MgSO_4$. Volatiles were removed *in vacuo* to yield a thick yellow oil, and the oil was triturated twice with 10 mL hexanes to yield *cis*-1,2-cyclopropanedicarbonyl diazide (1.43 g, 7.9 mmol, 98%) as an off-white powder that was used without further purification. ^{1}H NMR ($CDCl_3$, 300 MHz, *cis*) δ 1.34 – 1.44 (mult, ^{cy}Pro-C*H*$_2$, 1H), 1.81 – 1.89 (mult, ^{cy}Pro-C*H*$_2$, 1 H), 2.10 – 2.18 (mult, ^{cy}Pro-C*H*, 2 H). IR: ν_{CO} = 1710 cm^{-1}, ν_{NNN} = 2144 cm^{-1}.

7. *cis*-1,2-Cyclopropanedicarbonyl diazide. *Trans*-1,2-cyclopropanedicarbonyl diazide was prepared via an analogous procedure to that given in **(6.)**. ^{1}H NMR ($CDCl_3$, 300 MHz, *trans*) δ 1.61 (t, J = 7 Hz, ^{cy}Pro-C*H*$_2$, 2H), 2.26 (t, J = 7 Hz, ^{cy}Pro-C*H*, 2 H).

8. ***cis*-1,2-Cyclopropane diisocyanate.** To a 25 ml flask charged with *cis*-1,2-cyclopropanedicarbonyl diazide (1.46 g, 8.1 mmol) was added toluene (15 mL) via vacuum transfer. The reaction mixture was heated to 80 °C under Ar. Upon initial evolution of N_2 the reaction mixture turned bright aqua blue and progressively turned green and then yellow as the reaction was heated to 80 °C for 3 h. Toluene was removed *in vacuo* to yield crude *cis*-1,2-cyclopropane diisocyanate as an off-white solid that was used without purification in subsequent reactions. ^{1}H NMR ($CDCl_3$, 300 MHz, *cis*) δ 0.80 – 0.89 (mult, ^{cy}Pro-C*H*$_2$, 1H), 1.12 – 1.22 (mult, ^{cy}Pro-C*H*$_2$, 1 H), 2.86 – 2.94 (mult, ^{cy}Pro-C*H*, 2 H). IR: ν_{NCO} = 2281 cm^{-1}.

9. *trans*-1,2-Cyclopropane diisocyanate. *Trans*-1,2-cyclopropane diisocyanate was prepared via an analogous procedure to that given in **(8.)**. ^{1}H NMR ($CDCl_3$, 300 MHz, *trans*) δ 1.12 (t, J = 6 Hz, ^{cy}Pro-CH_2, 2H), 2.96 (t, J = 6 Hz, ^{cy}Pro-C*H*, 2 H).

10. *trans*-1,2-Cyclopropane diamine dihydrochloride. To a 250 mL flask charged with concentrated HCl (6.93 mL, 28 mmol) in H_2O (50 mL) was added a solution of *trans*-1,2-cyclopropane diisocyanate (3.40 g, 27 mmol) in toluene (4 mL) dropwise at 23 °C while stirring. An orange-brown biphasic mixture formed and the reaction was allowed to stir 18 h. The reaction mixture was concentrated to dryness and methanol (45 mL) was added. The resulting solution was filtered and Et_2O (20 mL) was added to precipitate *trans*-1,2-cyclopropane diamine dihydrochloride as a white powder (3.19 g, 22 mmol, 79%). ^{1}H NMR (D_2O, 300 MHz, *trans*) δ 1.48 (t, J = 7 Hz, ^{cy}Pro-CH_2, 2H), 3.13 (t, J = 7 Hz, ^{cy}Pro-C*H*, 2 H).

11. *trans*-1,2-Cyclopropane diamine. To a 25 mL flask charged with *trans*-1,2-cyclopropane diamine dihydrochloride (300. mg, 2.07 mmol) in H_2O (2 mL) was added NaOH (170. mg, 4.25 mmol) in H_2O (2 mL) at 23 °C while stirring. The mixture was allowed to stir 10 min and was concentrated to dryness to yield crude pale pink *trans*-1,2-cyclopropane diamine as a mixture with NaCl. The similar solubility of the reaction product and NaCl precluded separation, but ^{1}H NMR spectral analysis indicated clean conversion to the desired *trans*-1,2-cyclopropane diamine. ^{1}H NMR (CD_3OD, 300 MHz, *trans*) δ 0.54 (t, J = 6 Hz, ^{cy}Pro-CH_2, 2H), 2.16 (t, J = 6 Hz, ^{cy}Pro-C*H*, 2 H).

12. [2-(Benzoylamino)cyclopropylamino](2-pyridyl)formaldehyde. To a 5

mL flask charged with a 1:1 mixture of *trans*-1,2-cyclopropane diamine and NaCl (151 mg, 0.83 mmol) was added pyridine (0.5 mL) in air. A solution of 2-picolic acid (205. mg, 1.67 mmol) in pyridine (0.8 mL) was added dropwise at 23 °C over 5 min, and a tan-brown precipitate formed. The reaction was stirred 15 min, and $P(OPh)_3$ (516 mg, 1.67 mmol) was added dropwise over 5 min. The reaction flask was equipped with a reflux condenser and the brown mixture was heated to reflux for 4 hr. After cooling to 23 °C the solution was filtered to remove NaCl, and the resulting dark brown mixture was concentrated to a thick brown oil and crystallized from hot chloroform to yield [2-(benzoylamino)cyclopropylamino](2-pyridyl)formaldehyde as a light brown powder. ^{1}H NMR ($CDCl_3$, 300 MHz) δ 1.37 (t, J = 6 Hz, ^{cy}Pro-C*H*$_2$, 2H), 3.07 – 3.13 (mult, ^{cy}Pro-C*H*, 2 H), 7.43 (td, J = 5, 2 Hz, py-C*H*, 2H), 7.85 (td, 8, 2 Hz, py-C*H*, 2H), 8.19 (d, J = 8 Hz, py-C*H*, 2H), 8.26 (br s, $\nu_{1/2}$ = 9.5 Hz, N*H*, 2 H), 8.54 (dt, 4, 1 Hz, py-C*H*, 2 H).

13. $H_2C(CH_2N{=}CHPy)_2$ (L1). To a 25 mL flask containing 1,3-diaminopropane (500. mg, 6.74 mmol), $MgSO_4$ (400. mg, 3.32 mmol), and CH_2Cl_2 (5 mL) was added a solution of 2-pyridinecarboxaldehyde (1.44 g, 13.44 mmol) in CH_2Cl_2 (5 mL) dropwise at 23 °C over 5 min. The reaction was allowed to stir at 23 °C for 4 h, filtered to remove $MgSO_4$, and volatiles was removed *in vacuo* to afford $H_2C(CH_2N{=}CHPy)_2$ as a pale golden oil (1.06 g, 4.2 mmol, 62%). ^{1}H NMR ($CDCl_3$, 300 MHz): δ 2.10 (quint, J = 7 Hz, C*H*$_2$, 2H), 3.73 (t, J = 6 Hz, C*H*$_2$, 4H), 7.23 (t, J = 6 Hz, py-C*H*, 2H), 7.66 (t, J = 8 Hz, py-C*H*, 2H), 7.92 (d, J = 8 Hz, py-C*H*, 2H), 8.35 (s, im-C*H*, 2H), 8.56 (d, J = 6 Hz, py-C*H*, 2H).

14. $(CH_2CH_2CH_2N=CHPy)_2$ (L2). To a 25 mL flask containing 1,6-diaminohexane (500. mg, 4.30 mmol), $MgSO_4$ (1.55g, 12.9 mmol), and CH_2Cl_2 (2 mL) was added a solution of 2-pyridinecarboxaldehyde (922 mg, 8.61 mmol) in CH_2Cl_2 (2 mL) dropwise at 23 °C over 5 min. The reaction was allowed to stir at 23 °C for 2 h, filtered to remove $MgSO_4$, and volatiles was removed *in vacuo* to afford $(CH_2CH_2CH_2N=CHPy)_2$ as an off-white oil (800. mg, 2.70 mmol, 63%). ^{1}H NMR (C_6D_6, 300 MHz): δ 1.25 – 1.31 (mult, C*H*$_2$, 4H), 1.56 – 1.65 (mult, C*H*$_2$, 4H), 3.45 (td, J = 7, 1 Hz, C*H*$_2$, 4H), 6.64 (ddd, J = 7, 5, 1 Hz, py-C*H*, 2H), 7.07 (td, J = 7, 2 Hz, py-C*H*, 2H), 8.17 (dt, J = 8, 1 Hz, py-C*H*, 2H), 8.48 (ddd, J = 5, 2, 1 Hz, py-C*H*, 2H), 8.54 (s, im-C*H*, 2H).

15. $Me_2C(CH_2N=CH\text{-}2\text{-}Br\text{-}Ph)_2$ (L3). To a 25 mL flask containing 2,2-dimethyl-1,3-propanediamine (400. mg, 3.91 mmol), $MgSO_4$ (236 mg, 1.96 mmol), and CH_2Cl_2 (2 mL) was added a solution of 2-bromobenzaldehyde (1.449 g, 7.83 mmol) in CH_2Cl_2 (2 mL) dropwise at 23 °C over 5 min. The reaction was allowed to stir at 23 °C for 2 h, filtered to remove $MgSO_4$, and volatiles was removed *in vacuo* to afford $Me_2C(CH_2N=CH\text{-}2\text{-}Br\text{-}Ph)_2$ as a viscous yellow oil (1.59 g, 3.65 mmol, 93%). ^{1}H NMR (C_6D_6, 300 MHz): δ 1.09 (s, C*H*$_3$, 6H), 3.46 (s, C*H*$_2$, 4H), 6.69 (t, J = 7 Hz, py-C*H*, 2H), 6.90 (t, J = 7 Hz, py-C*H*, 2H), 7.27 (d, J = 8 Hz, py-C*H*, 2H), 8.23 (d, J = 8 Hz, py-C*H*, 2H), 8.72 (s, im-C*H*, 2H).

16. $Me_2C(CH_2N=CH\text{-}2\text{-}F\text{-}Ph)_2$ (L4). To a 10 mL flask containing 2,2-dimethyl-1,3-propanediamine (206 mg, 2.02 mmol), $MgSO_4$ (121 mg, 1.01 mmol), and CH_2Cl_2 (10 mL) was added a solution of 2-fluorobenzaldehyde (500. mg, 4.03 mmol) in CH_2Cl_2 (5 mL) dropwise at 23 °C over 5 min. The reaction was allowed to

stir at 23 °C for 3 h, filtered to remove $MgSO_4$, and volatiles was removed *in vacuo* to afford $Me_2C(CH_2N{=}CH\text{-}2\text{-}F\text{-}Ph)_2$ as a viscous yellow oil (552 mg, 1.76 mmol, 87%). ^{1}H NMR (C_6D_6, 400 MHz): δ 1.08 (s, C*H*$_3$, 6H), 3.44 (s, C*H*$_2$, 4H), 6.71 – 6.91 (mult, py-C*H*, 6H), 8.20 (t, J = 7 Hz, py-C*H*, 2H), 8.59 (s, im-C*H*, 2H). ^{19}F NMR (C_6D_6, 400 MHz): δ -122.82 (dt, J = 11, 6 Hz, Ar-*F*).

17. $Me_2C(CH_2N{=}CHPh)_2$ (L5). To a 25 mL flask containing 2,2-dimethyl-1,3-propanediamine (500. mg, 4.89 mmol), $MgSO_4$ (294 mg, 2.44 mmol), and CH_2Cl_2 (3 mL) was added a solution of benzaldehyde (1.039 g, 9.79 mmol) in CH_2Cl_2 (2 mL) dropwise at 23 °C over 5 min. The reaction was allowed to stir at 23 °C for 2 h, filtered to remove $MgSO_4$, and volatiles was removed *in vacuo* to afford $Me_2C(CH_2N{=}CHPh)_2$ as a viscous pale yellow oil (1.20 g, 4.34 mmol, 89%). ^{1}H NMR (C_6D_6, 400 MHz): δ 1.23 (s, C*H*$_3$, 6H), 3.58 (s, C*H*$_2$, 4H), 7.17 – 7.22 (mult, py-C*H*, 6H), 7.81 (d, J = 7 Hz, py-C*H*, 4H), 8.12 (s, im-C*H*, 2H).

18. $Me_2C(CH_2N{=}CH\text{-}4\text{-}^tBu\text{-}Ph)_2$ (L6). To a 25 mL flask containing 2,2-dimethyl-1,3-propanediamine (500. mg, 4.89 mmol), $MgSO_4$ (294 mg, 2.44 mmol), and CH_2Cl_2 (3 mL) was added a solution of 4-*tert*-butylbenzaldehyde (1.588 g, 9.79 mmol) in CH_2Cl_2 (2 mL) dropwise at 23 °C over 5 min. The reaction was allowed to stir at 23 °C for 2.5 h, filtered to remove $MgSO_4$, and volatiles was removed *in vacuo* to afford $Me_2C(CH_2N{=}CH\text{-}4\text{-}^tBu\text{-}Ph)_2$ as an off-white viscous oil (1.6 g, 4.10 mmol, 84%). ^{1}H NMR (C_6D_6, 400 MHz): δ 0.74 (s, C(C*H*$_3$)$_3$, 18H), 0.85 (s, C*H*$_3$, 6H), 3.20 (s, C*H*$_2$, 4H), 6.78 (d, J = 7 Hz, py-C*H*, 4H), 7.79 (s, im-C*H*, 2H), 8.08 (d, J = 7 Hz, py-C*H*, 4H).

19. $[Me_2C(CH{=}NCH_2Ph)_2]Fe(PMe_3)_2$. To a 50 mL flask charged with

$Fe(PMe_3)_4$ (300. mg, 0.833 mmol) and THF (10 mL) was added a solution of $Me_2C(CH_2{=}NCH\text{-}2\text{-}Br\text{-}Ph)_2$ (**L4**, 182 mg, 0.42 mmol) in THF (10 mL) dropwise at 23 °C over 5 min. The solution turned deep indigo-purple and dark solid precipitated out of solution. The reaction mixture was stirred 2 h at 23 °C and solvent was removed *in vacuo* to yield a dark blue-purple film, and the residue was triturated twice with 10 mL portions of pentane. The thick oily material was taken up in 25 mL pentane and filtered, and the filter cake was washed with pentane (~ 30 x 10 mL). The filtrate was cooled to -78 °C and filtered to yield $[Me_2C(CH{=}NCH_2Ph)_2]Fe(PMe_3)_2$ as a thermally sensitive purple sticky solid (30. mg, 0.062 mmol, 15%). ^{1}H NMR (C_6D_6, 400 MHz): δ 0.42 (t, J = 3 Hz, **h**, 18H), 0.85 (s, **g**, 6H), 3.32 (s, **f**, 4H), 7.19 (t, J = 7 Hz, **c**, 2H), 7.42 (t, J = 7 Hz, **b**, 2 H), 7.54 (d, J = 8 Hz, **d**, 2 H), 8.71 (d, J = 8 Hz, **a**, 2 H). ^{31}P NMR (C_6D_6, 162 MHz): δ 10.02 (s, $\nu_{1/2}$ = 13 Hz, *P*Me_3).

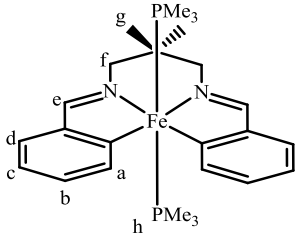

20. $[Me_2C(CH{=}NCH_2Ph)_2]Ni$. To a J. Young tube charged with $Me_2C(CH_2N{=}CH\text{-}2\text{-}Br\text{-}Ph)_2$ (**L3**, 15 mg, 0.034 mmol) and $Ni(COD)_2$ (19 mg, 0.069 mmol) was added C_6D_6 (0.4 mL) at 23 °C. The reaction mixture turned deep red over 15 min and solid precipitated out of solution. ^{1}H NMR analysis confirmed release of cyclooctadiene and formation of $[Me_2C(CH{=}NCH_2Ph)_2]Ni$. ^{1}H NMR ($C_6D_6$, 400 MHz): δ 0.68 (s, C*H*$_3$, 6H), 2.84 (s, C*H*$_2$, 4H), 7.00 (t, J ~ 6 Hz, py-C*H*, 2H), 7.05 (t, J ~ 7 Hz, py-C*H*, 2 H), 7.18 (s, im-C*H*, 2H), 7.34 (d, J ~ 7 Hz, py-C*H*, 2 H), 8.19 (d, J ~ 7 Hz, py-C*H*, 2 H).

REFERENCES

1. Hulley, E. B. Ph.D. Thesis, Cornell University, Ithaca, NY, **2011**.

2. McCoy, L. L. *J. Am. Chem. Soc.* **1958,** *80,* 6568 – 6572.

3. Witiak, D. T.; Lee, H. J.; Goldman, H. D.; Zwilling, B. S. *J. Med. Chem.* **1978,** *21,* 1194 – 1197.

4. Lindley, B. M. Ph.D. Thesis, Cornell University, Ithaca, NY, **2015**.

5. Barnes, D. J.; Chapman, R. L.; Vagg, R. S.; Watton, E. C. *J. Chem. Eng. Data* **1978,** *23*, 349 – 350.

6. Karsch, H. H. *Chem. Ber.* **1977**, *110*, 2699 – 2711.

7. Bhattacharya, P.; Krause, J. A.; Guan, H. *Organometallics*, **2011**, *30*, 4720 – 4729.

8. Schunn, R. A. *Inorg. Synth.* **1974,** *15*, 5 – 9.

9. Klein, H. -F.; Karsh, H. H. *Chem. Ber.* **1975,** *108,* 944 – 955.